Towards non-invasive measurements of ligament function: Implementation and advancement of ultrasound elastography techniques

Isabelle Kuder

October 2024

A thesis submitted for the degree of Doctor of Philosophy

Department of Mechanical Engineering
Imperial College London
London, SW7 2AZ

IMPERIAL

Statement of Originality

I hereby declare that the work described in this thesis is original and was produced by myself. All work contributed by others has been acknowledged throughout. Methods based on existing work have been appropriately referenced.

Copyright Declaration

The copyright of this thesis rests with the author. Unless otherwise indicated, its contents are licensed under a Creative Commons Attribution-Non Commercial 4.0 International Licence (CC BY-NC).

Under this licence, you may copy and redistribute the material in any medium or format. You may also create and distribute modified versions of the work. This is on the condition that: you credit the author and do not use it, or any derivative works, for a commercial purpose.

When reusing or sharing this work, ensure you make the licence terms clear to others by naming the licence and linking to the licence text. Where a work has been adapted, you should indicate that the work has been changed and describe those changes.

Please seek permission from the copyright holder for uses of this work that are not included in this licence or permitted under UK Copyright Law.

Abstract

Collateral ligament insufficiency due to injury or an imbalance after knee replacement surgery can lead to knee instability or stiffness. The aim of this PhD project was to develop ultrasound techniques that can non-invasively assess the health and function of these tissues by measuring their biomechanical properties. The key to implementing shear wave imaging for measuring material properties was adequate consideration of how shear wave propagation through the collateral ligaments is influenced by the viscous and thin nature of the tissue. *Ex vivo* tests on tissue-mimicking phantoms and the medial collateral ligaments of porcine joints showed that a Voigt model could effectively capture the viscous effects, while a Lamb wave model accounted for the guided wave phenomenon resulting from the structure's narrow boundaries. Analysing shear wave propagation with an incorrect model led to material properties that exhibited a dependency on the tissue's thickness and did not accurately reflect those from mechanical testing. The ultrasound speckle tracking technique, which was used to measure the strain behaviour of the ligaments, also required careful tuning of the post-processing algorithm to account for the complex anatomy and elongation pattern of ligaments. It was found that selection of the algorithmic settings, which conventionally requires a time-consuming trial-and-error approach and validation against ground truth data, could instead be automated by using an optimisation approach that verifies displacement field convergence, then minimises variance between repeat measurements. This optimisation routine was insensitive to anatomical variation and loading conditions, producing tuned algorithms that accurately and reliably measured strains in the medial ligaments of both *ex vivo* porcine and human knees, and for quasi-static and dynamic loading. Additionally, the non-uniform strain behaviour of *in vivo* medial ligamentous structures was measured with good reliability, detecting elongation of the anterior bundles and shortening of posterior bundles during knee flexion.

Acknowledgements

Before discussing the work accomplished in this PhD project, I would like to thank a number of people whose support and encouragement have been invaluable. First and foremost, I would like to thank my supervisor, Dr Richard van Arkel, who has been there to both celebrate the successes and navigate the challenges of this project. I have learned so much from you, not only through your vast technical knowledge, but also through your unwavering enthusiasm and ability to always see the bigger picture.

I am also grateful for the secondary support I have received: To Prof Andrew Amis, whose belief in the potential of non-invasive tools in orthopaedics has been so encouraging, and whose deep understanding of soft tissue mechanics has helped contextualise the findings. To Mr Gareth Jones - your willingness to trial the technique in practice made the clinical study possible. Your support and patience was invaluable, and I could not have asked for better collaboration on this study. To Dr Fred Cegla, for sharing your expertise on ultrasound and for granting me access to all the equipment in the NDE lab. And, finally, to Antonio De Sanctis, thank you for your extensive technical help when setting up the hydrophone experiments.

I would also like to recognise the financial support and help received from DePuy Synthes and the EPSRC (CASE studentship award ref: 2434418), without which the work of this project would not have come to fruition. In particular, thank you to Mick Rock at DePuy, for his continued encouragement and guidance throughout.

I would also like to express my gratitude to everyone in the Biomechanics group. The kindness and curiosity shared throughout the group truly made the office such a welcoming and inspiring place to work throughout the last four years.

To Joseff, thank you for helping me find the right balance between the work and my life beyond the project. And, finally, to my family - Mama, Papa, and Laura - you have always been my biggest supporters and I cannot thank you enough.

Table of Contents

List of Figures xiii

List of Tables xix

01 Introduction 2

1.1 Motivation 4

1.2 Aims and objectives 7

1.3 Thesis structure 8

02 Literature Review 10

2.1 Biomechanics and clinical background 12

2.1.1 Anatomy, composition and biomechanics of tendons and ligaments . 12

2.1.2 Techniques to measure biomechanical properties of tendons and ligaments 16

2.1.3 Role of the collateral ligaments in the knee 17

2.1.4 Summary of mechanical properties of collateral ligaments 18

2.1.5 Treatment of the collateral ligaments during knee replacement surgery 25

2.2 Ultrasound background 27

2.2.1 Fundamentals 27

2.2.2 Imaging modes 29

2.2.3 Quantitative ultrasound elastography 31

2.2.4 Shear wave imaging . . . 32
2.2.5 Speckle tracking . . . 45
2.3 Conclusion . . . 54

03 Shear Wave Imaging Implementation 57

3.1 Introduction . . . 58
3.2 Shear wave generation and ultrasound acquisition sequences . . . 60
3.2.1 Acoustic radiation force (ARF) . . . 60
3.2.2 External shaker . . . 62
3.2.3 Plane wave imaging (PWI) . . . 63
3.3 Post-processing algorithms . . . 65
3.3.1 Tissue motion calculation . . . 65
3.3.2 Filtering . . . 67
3.3.3 Evaluating material properties based on shear wave propagation . . . 71
3.4 Discussion . . . 83
3.4.1 Comparison to state-of-the-art . . . 83
3.4.2 Conclusion . . . 85

04 Speckle Tracking Implementation 87

4.1 Introduction . . . 88
4.2 Acquisition sequences . . . 90
4.3 Post-processing algorithms . . . 92
4.3.1 Speckle tracking algorithm . . . 92
4.3.2 Optimisation procedure to tune algorithmic settings . . . 97
4.4 Discussion . . . 101
4.4.1 Comparison to state-of-the-art . . . 101
4.4.2 Conclusion . . . 102

4A Strain calculation using deformation gradient decomposition 103

05 Ultrasound Safety 110

5.1 Introduction 112
5.2 Materials and Methods 115
5.2.1 Calculation of safety indices 115
5.2.2 Equipment & test setup 122
5.2.3 Tested ultrasound imaging modes 123
5.2.4 Shear wave measurements with varying transducer voltages in agar phantom specimens 125
5.3 Results 126
5.3.1 Validation of hydrophone measurement procedure 126
5.3.2 Acoustic outputs for the imaging modes of this project 127
5.3.3 Shear wave measurements with varying transducer voltages in agar phantom specimens 129
5.4 Discussion 130
5.4.1 Most important findings 130
5.4.2 Comparison to literature 131
5.4.3 Limitations 132
5.4.4 Conclusion 133

06 Validation: *Ex Vivo* Specimens 134

6.1 Introduction 136
6.2 Materials and Methods 138
6.2.1 Shear wave imaging: agar phantom specimens 138
6.2.2 Shear wave imaging: porcine specimens 144
6.2.3 Speckle tracking: porcine specimens 148

6.2.4 Speckle tracking: cadaveric human specimens . . . 155
6.3 Results . . . 159
6.3.1 Shear wave imaging: agar phantom specimens . . . 159
6.3.2 Shear wave imaging: porcine specimens . . . 167
6.3.3 Speckle tracking: porcine specimens . . . 173
6.3.4 Speckle tracking: cadaveric human specimens . . . 177
6.4 Discussion . . . 179
6.4.1 Shear wave imaging: most important findings . . . 179
6.4.2 Shear wave imaging: comparison to literature . . . 180
6.4.3 Shear wave imaging: limitations . . . 182
6.4.4 Speckle tracking: most important findings . . . 185
6.4.5 Speckle tracking: comparison to literature . . . 186
6.4.6 Speckle tracking: limitations . . . 187
6.4.7 Conclusion . . . 190

07 Validation: *In Vivo* 192

7.1 Introduction . . . 194
7.2 Materials and Methods . . . 197
7.2.1 Knee brace design . . . 197
7.2.2 Speckle tracking: healthy volunteers . . . 202
7.2.3 Speckle tracking: clinical pilot study . . . 207
7.3 Results . . . 209
7.3.1 Speckle tracking: healthy volunteers . . . 209
7.3.2 Speckle tracking: clinical pilot study . . . 220
7.4 Discussion . . . 221
7.4.1 Most important findings . . . 221
7.4.2 Comparison to literature . . . 222
7.4.3 Limitations . . . 223

7.4.4 Conclusion 226

08 Conclusions and Future Work 228

8.1 Discussion. 230

8.1.1 Most important findings 230

8.1.2 Clinical relevance 231

8.1.3 Limitations 233

8.1.4 Final conclusions 234

8.2 Recommendations for future work 235

8.2.1 Shear wave imaging. 235

8.2.2 Speckle tracking. 240

09 References 245

10 Appendices 270

A ICREC letter of favourable opinion for the study with healthy volunteers 272

B REC letter of favourable opinion for the clinical study 273

C HRA letter of approval for the clinical study 280

List of Figures

2.1 Hierarchical structure of ligaments and tendons. 13

2.2 Literature review on the relative strain or length change of the medial ligament bundles of the knee during knee flexion from 0° to 75°. 24

2.3 Ultrasound transducer coordinate system. 29

2.4 Simulated beam profiles for conventional scanline imaging, plane wave imaging, and the acoustic radiation force (ARF) push pulse. 30

2.5 Ultrasound elastography steps. 32

2.6 Diagrams for the shear wave imaging methods. 34

3.1 Shear wave generation and tracking sequences when using an acoustic radiation force (ARF) push. 61

3.2 Shear wave generation and tracking sequences when using an external shaker. 62

3.3 Summary of the shear wave imaging post-processing procedure. 66

3.4 3D Fourier domain filter mask to remove high-frequency jitter, low-frequency motion from user and shear wave reflections/reverberations travelling against the main direction of propagation. 69

3.5 Time-of-flight (TOF) analysis using the linear regression algorithm. 74

3.6 Time-of-flight (TOF) analysis using the radon transform algorithm. 75

3.7 Method to obtain the shear wave phase velocity from the Fourier transform of the axial velocity data. 75

3.8 Post-processing steps for the viscoelastic dispersion analysis. 78

3.9 Illustration of Lamb wave propagation. 79

3.10 Example dispersion maps for thin-layered samples, obtained with acoustic radiation force (ARF) excitation and external shaker excitation. 80

4.1 Flowchart of the custom 2D speckle tracking algorithm to calculate soft tissue strain. 93

4.2 Depiction of how longitudinal ligament strains were calculated, which was based on the change of distance between neighbouring nodes within a nodal grid that follows the shape of the ligament. 96
4.3 Example convergence analysis to find minimum settings for the NRIR method. 98
4.4 Steps of the to-be-minimised objective function of the optimisation, which calculates the normalised standard deviation of the strain maps of repeat measurements. 100
4A.1 Principal strains within the ligament calculated for an example measurement for which there was relative sliding between the different layers of the ligament. 106
4A.2 Deformation gradient decomposition scheme, which allows evaluation of the stretch tensor that contains the longitudinal and transverse strains along and across the ligament. 106
4A.3 Longitudinal ligament strains obtained using the proposed ligament stretch tensor definition. 108

5.1 Pressure and intensity waveforms for a point in the insonified field. 117
5.2 Test setup for the hydrophone measurements to characterise the acoustic wave-field of the ultrasound imaging modes used in this project. 123
5.3 Acoustic outputs measured for the validation imaging mode with known peak pressure and MI values. 126
5.4 Acoustic output safety indices for different transducer voltages, calculated for three imaging modes used in this project. 127
5.5 Convergence of the calculated shear wave velocities with increased transducer voltage. 129

6.1 Experimental setup for the agar cube mechanical compression test. 139
6.2 Experimental setup for the agar plate shear wave imaging measurements. . 140
6.3 Experimental setup for the porcine MCL shear wave imaging measurements. 145
6.4 Experimental setup for the porcine MCL strain measurements. 149

6.5 Flowchart of the *ex vivo* ultrasound speckle tracking measurements taken for the porcine and human specimens, illustrating the training/test split for the optimisation routine. 151
6.6 Experimental setup for the human ligament strain measurements. 156
6.7 Quasi-static stress-strain curves during the initial response to loading for the large homogeneous agar cube samples of varying agar concentrations. . . . 160
6.8 Bar chart of the measured material properties for the agar cube specimens, obtained using ultrasound shear wave imaging (four post-processing techniques), and quasi-static material testing. 161
6.9 Radon transform (TOF) post-processing example for an agar cube specimen. 162
6.10 Linear regression (TOF) post-processing example for an agar cube specimen. 162
6.11 Phase velocity method post-processing example for an agar cube specimen. 162
6.12 Viscoelastic dispersion analysis post-processing example for an agar cube specimen. 163
6.13 Material properties for the thin-layered agar plate specimens of varying thickness, obtained using ultrasound shear wave imaging (six post-processing techniques).. 165
6.14 Dispersion analysis post-processing example for an agar plate specimen (thickness $= 7.2\,\mathrm{mm}$). 166
6.15 Sensitivity analysis for the multi-variable dispersion models applied to the agar plate measurements. 167
6.16 Viscoelastic behaviour of the porcine MCL specimens, measured using a dynamic tensile loading test.. 169
6.17 Example of how the shear modulus, obtained from shear wave imaging time-of-flight (TOF) or phase velocity post-processing methods, varied with different shear wave excitation frequencies.. 169
6.18 Scatter plot of the measured material properties for the porcine MCL specimens obtained using ultrasound shear wave imaging (six post-processing techniques), and dynamic sinusoidal tensile testing.. 170

6.19 Dispersion analysis post-processing example for a porcine MCL specimen (thickness $= 6.7\,\mathrm{mm}$). 171
6.20 Sensitivity analysis for the multi-variable dispersion models applied to the porcine MCL measurements. 171
6.21 Displacement convergence results for the porcine and human training measurements. 174
6.22 Convergence of the surrogate optimisation for the porcine measurements and example strain maps of repeats for different quality penalties. 175
6.23 Porcine MCL surface strains measured by the tuned ultrasound speckle tracking algorithm (test set) and optical DIC. 175
6.24 Example porcine strain maps at maximum loading obtained using DIC and ultrasound.. 176
6.25 Strains in the medial ligaments of the cadaveric human knee during extension-flexion, as measured by the tuned speckle tracking algorithm. 178
6.26 Example strain map for the posterior bundle of the MCL at 100° of flexion (AP position $= -0.35$). 178

7.1 Iterations of the knee brace design for *in vivo* measurements of medial knee ligament strain during extension-flexion using ultrasound.. 200
7.2 Flowchart of the *in vivo* ultrasound speckle tracking measurements taken for the healthy participants, illustrating the training group for tuning the speckle tracking algorithm, and the test group for the inter-rater and intra-rater reliability study. 205
7.3 Spatial registration of the *in vivo* ultrasound acquisitions obtained at the three different sessions for each participant. 206
7.4 Displacement convergence results for the *in vivo* training measurements of the healthy participants. 210
7.5 Inter-rater and intra-rater reliabilities for the *in vivo* ultrasound strain measurements of the medial ligaments of healthy participants. 211

7.6 Correlation and Bland-Altman plot showing the agreement of the inter-rater and intra-rater *in vivo* ultrasound strain measurements when a ligament region of interest of 10 mm length and 0 mm proximal offset from the distal femur is selected. 212
7.7 Correlation and Bland-Altman plot showing the agreement of the inter-rater and intra-rater *in vivo* ultrasound strain measurements when a ligament region of interest of 15 mm length and 0 mm proximal offset from the distal femur is selected. 213
7.8 Strains that developed in the medial knee ligaments of 12 healthy participants during 20° to 75° of flexion, as measured by the tuned *in vivo* speckle tracking algorithm for a region of interest extending 10 mm proximally from the distal femur 214
7.9 Strains that developed in the medial knee ligaments of 12 healthy participants during 20° to 75° of flexion, as measured by the tuned *in vivo* speckle tracking algorithm for a region of interest extending 15 mm proximally from the distal femur.. 216
7.10 Example *in vivo* strain map for the anterior bundle of the medial ligament complex after knee flexion from 20° to 75° for a ligament region of interest extending 10 mm proximally from the distal femur, and the strain curve showing how average strains in this region of interest evolved throughout knee flexion. 218
7.11 Example *in vivo* strain map for the anterior bundle of the medial ligament complex after knee flexion from 20° to 75° for a ligament region of interest extending 15 mm proximally from the distal femur, and the strain curve showing how average strains in this region of interest evolved throughout knee flexion. 219
7.12 Pre-operative strains in the medial ligaments during extension-flexion in a knee replacement patient, as measured by the tuned speckle tracking algorithm. 220

List of Tables

2.1 Collateral ligament material properties. 20

2.2 Advantages and disadvantages of generating shear waves using vibrations from external shakers vs acoustic radiation forces. 33

2.3 Shear wave imaging methods using acoustic radiation forces, summarising first implementations in the literature as well as commercial systems using the techniques. 34

2.4 *Ex vivo* and *in vivo* shear wave imaging implementations. 38

2.5 *Ex vivo* and *in vivo* speckle tracking implementations to measure deformation or strain in tendons and ligaments. 48

3.1 Parameters for generating shear waves with a single push beam ARF. 61

3.2 Parameters for plane wave tracking of the shear wave and the Verasonics beamforming procedure. 63

3.3 Settings for the filter applied to the Fourier domain. 68

4.1 Transmission, acquisition and beamforming parameters for the conventional scanline imaging and coherent plane-wave compounding (CPWC) mode implemented on the Verasonics research ultrasound system. 91

4.2 Main settings selected in the 'Clarius Ultrasound App' when using the wireless Clarius ultrasound scanner during the clinical pilot study. 91

5.1 Thresholds for the ultrasound safety indices. 112

5.2 Acoustic outputs for the imaging modes of this project implemented on the Verasonics ultrasound machine with an L11-5v transducer. 128

6.1 Parameters of the speckle tracking algorithm that were tuned for all applications of this project, showing the settings used in previous studies, the range of settings tested here, and the final settings found by the surrogate optimisation routine (after 1500 iterations) for the *ex vivo* porcine, *ex vivo* human, and *in vivo* human ligaments. 153

6.2 Dimensions and weights of the agar cube specimens, as measured using a Vernier calliper. 159
6.3 Summary of the measured material properties for the agar cube specimens, obtained using ultrasound shear wave imaging and quasi-static material testing.. 161
6.4 Thicknesses of the agar plate specimens, as measured using a Vernier calliper. 163
6.5 Summary of the measured material properties for the agar plate specimens, obtained using ultrasound shear wave imaging.. 164
6.6 Thicknesses of the porcine MCL specimens, as measured from the ultrasound images. 167
6.7 Summary of the measured material properties for the porcine MCL specimens, obtained using ultrasound shear wave imaging and dynamic material tensile testing.. 168
6.8 Results for the pre-optimisation convergence check on the porcine and human training sets, showing the settings for which convergence was tested, and the settings for which the lateral displacement field had converged to within relative errors of 5 %.. 173
6.9 Strain results for the three porcine specimens, obtained from the tuned ultrasound speckle tracking algorithm and the DIC measurements. 176

7.1 Number of measurements captured during the *in vivo* study with healthy participants for different knee flexion ranges. 204
7.2 Results for the pre-optimisation convergence check on the *in vivo* optimisation training set, showing the settings for which convergence was tested, and the settings for which the lateral displacement field had converged to within relative errors of 5 %.. 209

01

Introduction

1.1 Motivation 4
1.2 Aims and objectives 7
1.3 Thesis structure 8

List of Abbreviations

QUS	Quantitative ultrasound
TKR	Total knee replacement

1.1 Motivation

Total knee replacement (TKR) is a surgical procedure during which an artificial knee joint replaces a knee that has become impaired due to, for example, osteoarthritis. This procedure has the potential to significantly reduce pain and restore joint range of motion and strength [1, 2]. In the UK alone, around 100,000 patients require TKR every year, making up over 50 % of all primary surgical joint procedures [3]. However, despite advancements in implant design and surgical technique, around 20 % of patients are dissatisfied with their TKR [4] and experience 30 % worse knee function during activities of daily living [5].

Knee instability and stiffness are some of the main complications following knee arthroplasty and will often significantly reduce the quality of life of affected patients [3, 6, 7]. Falls or fear of falling due to implant instability reduces the confidence of patients and leads to increasing immobility [8, 9]. Likewise, patients in our Patient and Public Involvement (PPI) group report that implant stiffness can lead to pain and reduced range of motion, preventing them from performing daily activities such as putting on their socks/shoes or playing with grandchildren on the floor. These are significant challenges considering the primary aims of the surgery are to relieve pain and restore function.

One source of knee instability or stiffness is improper balancing of the collateral ligaments during the knee replacement surgery [3, 6]. The collateral ligaments are flat bands of fibrous tissue that connect the femur in the upper leg to the tibia and fibula of the lower leg. They play an important role in stabilising the knee. Leaving the ligaments too slack

can lead to instability, while if they are too tight, a patient can experience stiffness or pain. It is therefore crucial that these ligaments remain properly tensioned over the full range of motion after the placement of the implant [10, 11]. However, despite a rise in assistive technologies that facilitate intra-operative collateral ligament balancing [12], knee instability and stiffness are still prevalent and result in around $20 - 35\,\%$ of revision surgeries, a figure that has not changed in the last 10 years [3, 13].

It remains unclear what happens to the collateral ligaments after surgery: could post-operative healing and adaptation change the mechanical properties of the ligaments and cause a balanced knee to become unbalanced [7]?

Clinically, the integrity of the collateral ligaments is most often assessed with a varus/valgus stress test. However, this test is very subjective and offers poor reliability. Recent research has explored the use of a video-fluoroscopy system to obtain a more quantitative assessment of post-operative ligament function by measuring the strain behaviour of the ligament: the motion of ligament attachment sites is tracked throughout knee extension and flexion and the ligament strain during this motion is obtained from the estimated ligament length change [14, 15]. However, fluoroscopy is an invasive research method, exposing patients to radiation.

Instead, ultrasound technology could provide a safe, quick, non-invasive, and more widely available tool to monitor the integrity of the collateral ligaments after surgery: in the past two decades, quantitative ultrasound (QUS) techniques have become increasingly important medical diagnostic tools, which have enabled the biomechanics and properties of soft tissues to be measured objectively and non-invasively [16, 17]. Two techniques that could prove particularly useful in the clinical assessment of ligaments are (1) shear wave imaging to measure viscoelastic material properties, and (2) speckle-tracking to measure the strain behaviour of the ligaments. These quantitative metrics can be used as diagnostic parameters to detect abnormal ligament adaptations, and provide an insight into collateral ligament function in knee stability [18, 19]. Changes in material properties could, for example, indicate potential tightening due to recovery at surgical incisions or stress-relaxation and tearing of overly tight ligaments. Changes in how much the ligaments

strain during certain knee movements could warn of increased or decreased engagement of the ligament due to inadequate tensioning.

Various commercial systems have already implemented the above ultrasound elastography techniques, such as for the detection of liver fibrosis [20–23] or malignant tumours in the breast [24–27]. However, commercial implementations are often designed and validated for large, homogeneous tissue and do not provide accurate results in tissue structures with complex anatomy or material properties such as, for example, the thin, viscoelastic fibrous structure of ligaments [28–30].

Consequently, there is considerable interest in expanding these techniques for new applications involving more complex soft tissue. This requires understanding of how intricate material behaviours and anatomical variations impact the ultrasound acquisition and post-processing requirements. From this understanding, a set of frameworks and tools can be developed to facilitate the transfer of these techniques to novel applications. In the field of orthopaedics, this could open up new opportunities to better understand post-operative changes in collateral ligament function and could guide the development of surgical techniques and implant design to reduce complications related to the collateral ligaments.

1.2 Aims and objectives

The aim of this PhD thesis was to develop non-invasive diagnostic tools for monitoring the health and function of fibrous connective tissue. To achieve this, the following objectives were defined:

1. Develop ultrasonic acquisition and post-processing techniques to measure the material properties and strain behaviour of thin-layered, viscoelastic soft tissue.
2. Validate these techniques using reference data of strain and material properties, obtained from *ex vivo* specimen measurements in a materials testing lab.
3. Gain insight into the *in vivo* strain behaviour of the medial ligaments in healthy knees, and determine the reliability of quantifying this behaviour using non-invasive ultrasound measurements.

1.3 Thesis structure

This thesis is structured as follows: **Chapter 2** provides a review of the literature, discussing both the biomechanical behaviour of collateral ligaments and their role after knee replacement surgeries, as well as the fundamental principles of ultrasound and quantitative ultrasound (QUS) techniques. In **Chapter 3** and **Chapter 4**, the implementation of the shear wave imaging and speckle tracking techniques is outlined, including ultrasound acquisition methods and custom post-processing algorithms. The acoustic output levels of both ultrasound techniques are measured in **Chapter 5** to verify whether these are safe for *in vivo* applications. In **Chapter 6**, the shear wave imaging and speckle tracking techniques are validated on tissue-mimicking phantom specimens, as well as *ex vivo* porcine and human cadaveric medial knee ligaments. **Chapter 7** explores the use of the speckle tracking algorithm for *in vivo* applications, investigating the reliability (inter-rater and intra-rater) of measurements performed on healthy volunteers, and presenting the results for the first patient of a clinical pilot study. The thesis concludes with a discussion of the potential future direction of this work in **Chapter 8**.

02

Literature Review

2.1 Biomechanics and clinical background 12

2.2 Ultrasound background 27

2.3 Conclusion 54

List of Abbreviations

ACL	Anterior cruciate ligament
ARF	Acoustic radiation force
CPWC	Coherent plane-wave compounding
CUSE	Comb-push ultrasound shear elastography
HIFU	High intensity focused ultrasound
LCL	Lateral collateral ligament
LVDT	Linear variable displacement transducer
MCL	Medial collateral ligament
POL	Posterior oblique ligament
PWI	Plane wave imaging
QUS	Quantitative ultrasound
RF	Radio frequency
SMURF	Spatially modulated ultrasonic radiation force
SSI	Supersonic shear imaging
SWEI	Shear wave elastography imaging
TKR	Total knee replacement
TOF	Time-of-flight

2.1 Biomechanics and clinical background

2.1.1 Anatomy, composition and biomechanics of tendons and ligaments

The musculoskeletal system forms the foundation of the human body, providing structure, stability, and enabling controlled movement [31]. Tendons and ligaments are essential fibrous connective tissues within this system, each playing distinct yet complementary roles. Tendons connect muscles to bones, transmitting forces to move the skeleton, while ligaments connect bones to one another, stabilising joints and preventing excessive movement [31–33]. The shape and size of these structures can vary greatly depending on their specific role and location in the body, ranging from fat tendons that transfer forces from large muscle bodies (e.g., the Achilles tendon), to mid-size ligaments that provide stability and constraint (e.g., collateral ligaments), and finally thin, delicate connective tissue where space is limited (e.g., annular ligaments or flexor digitorum tendons of the hand) [34].

Tendons and ligaments share a unique hierarchical structure that allows them to bear significant mechanical loads while maintaining flexibility (Figure 2.1) [32]. At the largest level, they consist of fascicles separated by a fascicular membrane. Each fascicle is in turn made up of individual fibres ($1 - 12\,\mu m$) running through a fascicular matrix; fibres can be further broken down into fibrils, subfibrils, and microfibrils ($3.5 - 100\,nm$) [31, 36].

The mechanical properties of tendons and ligaments are also influenced by their

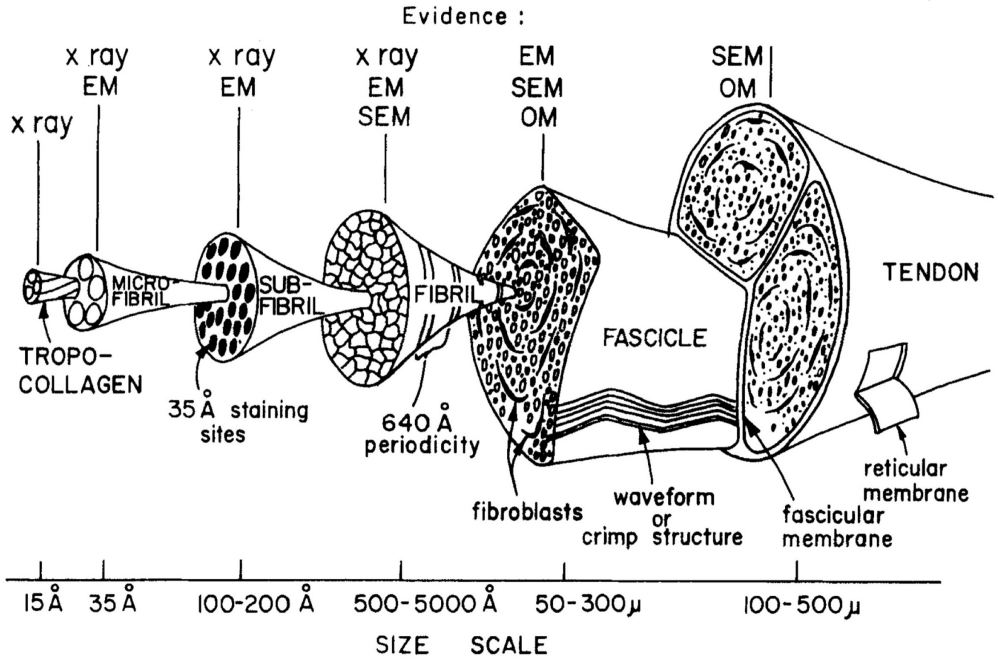


FIGURE 2.1 Hierarchical structure of ligaments and tendons, reproduced with permission from Kastelic et al. [35].

biochemical composition. Collagen, the predominant component of fibrils, constitutes for $70 - 80\,\%$ of the dry weight and is responsible for their tensile strength and load-bearing capabilities, making them among the strongest soft tissues in the body. Elastin, composing $1 - 2\,\%$ of dry weight, contributes elasticity, allowing these tissues to stretch. Proteins such as proteoglycans ($<1\,\%$) bind the water to form a gel, providing stability and strength between fibres [31, 33, 37].

The interplay of the hierarchical structure and composition of tendons and ligaments leads to finely tuned mechanical properties that provide both strength and flexibility, with nonlinear, anisotropic, and viscoelastic behaviour.

Non-linearity

Non-linearity is mainly caused by the “crimped” structure of fibrils: in their relaxed state, fibrils take on a wavy, zigzag formation [36]. Thus, these tissues are relatively compliant during initial loading while the fibrils uncrimp [31, 33]. Resistance to loading gradually increases as the fibrils straighten and become parallel to the direction of loading, resulting in a concave stress-strain curve during the first $1.5 - 4\,\%$ of straining [31, 36]. This region of

the curve has been termed the “toe” region [31]. This is followed by a mostly linear region until the tissue’s yield point [33]. Non-linearity is especially important in ligament function, since the lower elastic modulus at small loads provides freedom of joint movement, while the higher modulus at large loads restricts excessive, unstable movement.

Anisotropy

The mechanical properties of connective tissue varies with the direction of loading [32]. For example, the strength and elasticity of the medial collateral ligament (MCL) has been found to be 30 times higher in the longitudinal direction compared to its transverse direction [38]. This anisotropy is linked to the arrangement and orientation of fibres. In tendons, fibres generally run parallel to each other in line with the direction of muscle pull, providing great strength in this direction, but less resilience against loads across the fibres [31]. In contrast, ligaments have a more complex structure with an irregular distribution of fibres of varying thickness and length. These fibres are often arranged in spiral or oblique patterns, oriented at an angle of $0 – 30°$ relative to the longitudinal axis. Depending on the joint movement and the constraint needed during different activities, ligaments can be subjected to forces in various directions and, thus, this more complex fibre arrangement enables ligaments to transmit or resist these forces [31, 33].

Viscoelasticity

Viscous effects are present as well, caused by the complex interaction of collagen, elastin, proteins, and water, as well as the interaction of fibre bundles as they slide along each other [33]. Viscosity causes the mechanical behaviour to be time-dependent, resulting in (1) hysteresis in the stress-strain curve due to internal energy dissipation, i.e. different paths of loading and unloading, (2) static creep, i.e. straining under constant stress, (3) static stress relaxation, i.e. decrease in stress under constant strain, (4) strain rate dependent stress-strain response, and (5) time lag between the stress and strain response during dynamic loading [32, 39, 40]. These characteristics manifest multiple practical benefits in tendons and ligaments: stress relaxation reduces the peak stress during extended or cyclic

loading, such as during walking, thus reducing the risk of fatigue failure. Additionally, due to the strain rate dependency, ligaments and tendons exhibit a higher elastic modulus during rapid loading, enabling them to absorb and resist large impact forces more effectively [33].

Rheological models are often used to describe the viscoelastic behaviour of connective tissue in terms of dashpots and springs [31]. For example, the Kelvin-Voigt model (or often simply referred to as Voigt model) approximates the mechanical behaviour of the tissue with a parallel arrangement of a spring and dashpot [39]. This model is particularly effective in simulating creep behaviour, where tissue gradually deforms until reaching an equilibrium under a constant load. This model has previously been applied to the Achilles and hamstring tendons [30, 41]. Alternatively, the spring and dashpot can be combined in series to give the Maxwell model [31]. Both the Kelvin-Voigt and Maxwell models characterise the viscoelastic behaviour using two constants: an elastic modulus and a viscous coefficient. While this simplification means that certain viscoelastic characteristics are not modelled appropriately, such as stress relaxation in the Voigt model and creep in the Maxwell model [42], it facilitates their implementation in further mathematical formulations. For instance, these simplified models are often applied when modelling shear wave propagation through viscoelastic materials. In fact, Zhou et al. [43] demonstrated that the Voigt model outperformed more complex models, such as the standard linear solid or spring-pot models, when applied to shear wave propagation in tissue-mimicking phantoms.

Strength

The strength of tendons and ligaments is mainly influenced by the number and diameter of fibrils, as well as their collagen content. Tendons usually have a greater cross-sectional area with more and larger fibrils to carry loads. Furthermore, they often have a higher proportion of collagen compared to ligaments [31]. Thus, these structures tend to have higher failure loads, reflecting their role in handling large muscle forces. Strength can also vary within a single structure. For instance, the anterior bundles of the collateral ligaments have been found to have a higher collagen content than the posterior bundles [33].

2.1.2 Techniques to measure biomechanical properties of tendons and ligaments

Mechanical properties of *ex vivo* ligaments and tendon specimens are calculated from the static or dynamic stress-strain response measured with a material testing machine. These tests are generally performed in tension, since this tends to be the principal mechanism of loading these structures are subjected to *in vivo* [32]. Performing these uniaxial tensile tests can be challenging: tendons and ligaments that have been isolated from the bone/muscle are difficult to mount in the testing machine. Generally, a clamping mechanism is used; however, this can damage the specimen, lead to stress concentrations or result in slipping from the clamps at large tensile forces [32]. Instead, ligaments and tendons are often tested with bone insertions intact, and the specimen is mounted with clamps or custom fixtures holding on to the bone. The stress-strain curve obtained from these tests provides insight into the large-scale material properties of the entire connective tissue. Material properties that can be read from the quasi-static stress-strain curve include tangent modulus of the linear response region, instantaneous modulus during initial loading, ultimate tensile strength, and ultimate tensile strain [32]. From dynamic stress-strain measurements, the viscoelastic strain rate dependency of modulus and strength, as well as the viscoelastic phase lag between the stress and strain responses, can be determined [39].

In vivo measurement of mechanical properties is more challenging. Most commonly, manual examinations such as palpation or laxity tests are used to assess tendon or ligament function. For example, tendon or ligament thickening or swelling may be detected through palpation if the soft tissue of interest lies close to the skin, such as the patellar or Achilles tendon [44]. Knee laxity tests, including the varus-valgus stress test and Lachman test, are commonly used to assess knee stability and provide valuable insight into the integrity of the collateral ligaments or anterior cruciate ligament (ACL), respectively. However, these tests are often very subjective [45, 46].

Some quantitative imaging-based methods for *in vivo* measurements have therefore been proposed. For example, fluoroscopy can be used to track the motion of ligament

attachment sites during joint motion, from which the strain within the ligament or its elongation pattern can be estimated, which indicates the ligament's contribution to stability [14, 19, 47]. However, the ionising radiation of fluoroscopy makes this technique unsuitable for routine application [48]. Instead, quantitative ultrasound (QUS) techniques have been trialled, such as speckle tracking to measure the strain behaviour, or shear wave imaging to measure viscoelastic properties [30, 49, 50]. However, concerns exist regarding the reliability of these techniques when applied to thin fibrous tissue, due to its non-elastic material behaviour and the difficulty in obtaining clear images of such structures [30, 48, 51].

2.1.3 Role of the collateral ligaments in the knee

The collateral ligaments are flat bands of fibrous connective tissue that connect the femur in the upper leg to the tibia and fibula of the lower leg. They play a vital role in stabilising the knee and maintaining the bone and joint geometry [52]. The viscoelastic properties of collateral ligaments are optimised such that they can stretch within their elastic limit to provide freedom of knee movement, while providing sufficient constraint through resistive forces to provide stability and prevent, for example, over-extension or over-flexion [33].

The lateral collateral ligament (LCL) is a cord-like structure located on the outside of the knee and its main function is to restrict excessive varus rotation, i.e. inwards angulation of the tibia, while also providing some resistance to external rotation. It attaches inferior to the lateral epicondyle of the femur and to the fibular head [52–54].

The medial collateral ligament (MCL) is located on the inside of the knee and consists of two separate structures. The longitudinal fibres of the superficial MCL have a femoral attachment near the medial epicondyle, and two tibial attachments located approximately 12 and 60 mm distal to the tibial plateau [52, 54, 55]. The shorter fibres of the deep MCL, on the other hand, are located beneath the superficial MCL and attach to the femur and tibia just above and below the joint line, with an additional intermediate attachment to the medial meniscus [54, 55].

The posterior oblique ligament (POL) lies posterior to the superficial MCL and is part of the medial ligament complex [55]. Some consider it to be a distinct structure, while others describe it to be part of the posterior bundle of the superficial MCL. Its proximal attachment is posterior to the femoral attachment of the superficial MCL, from where it extends fanlike towards the tibia: while anterior fibres of the POL run parallel to and merge with the superficial MCL, posterior fibres are oriented obliquely, running to a more posterior attachment on the tibia [46].

Anterior and superficial structures of the medial ligament complex act as primary valgus stabilisers, while posterior structures prevent excessive internal rotation. The deep MCL provides additional restraint against internal rotation while also stabilising the meniscus [54].

After the ACL, the MCL is the ligament in the knee most susceptible to injury [56]. Ligaments and tendons can often heal and regenerate themselves after small injuries with a regiment of bracing, rest and physiotherapy [57]. However, full ruptures require surgical reconstruction. The degree of damage and progression of healing is difficult to detect, and is often estimated based on structural changes on MRI images, abnormalities at bone insertion cites on CT scans, or using laxity tests [54, 57–59].

2.1.4 Summary of mechanical properties of collateral ligaments

An extensive literature review was conducted on the dimensions as well as quasi-static and dynamic viscoelastic material properties of collateral ligaments (Table 2.1). In summary, the human LCL is approximately $50\,\mathrm{mm}$ long [52, 60–62], with a width of around $4-5\,\mathrm{mm}$ at its mid-substance [60, 63] and $6.8-8.8\,\mathrm{mm}$ at the attachment sites [52]. Large differences are reported for the lengths of the human MCL $(30-112\,\mathrm{mm})$ [55, 60, 63], with notable variations between bundles, i.e. $\sim 80\,\mathrm{mm}$ for anterior superficial fibres [52], $\sim 90\,\mathrm{mm}$ for posterior superficial fibres [52], and $\sim 30\,\mathrm{mm}$ for deep fibres [55]. The width of the MCL is $\sim 10\,\mathrm{mm}$ [52, 55, 60] although it can decrease to $5\,\mathrm{mm}$ for the deep MCL [55]. Reported

thicknesses were between $2 - 3\,\mathrm{mm}$ for both ligaments in humans.

The elastic moduli of the human collateral ligaments ranged between $94 - 626\,\mathrm{MPa}$. While, generally, elastic moduli increased with strain rate [64], values were inconsistent between studies. For example, Kerrigan et al. [64] reports elastic moduli for the MCL of $\sim 94\,\mathrm{MPa}$ at low strain rates $< 2\,\%/\mathrm{s}$, which increase to $\sim 180\,\mathrm{MPa}$ for strain rates $> 1000\,\%/\mathrm{s}$. However, this high strain rate measurement is lower than the quasi-static values reported by other studies [38, 60, 65, 66]. Similarly, for the LCL, the quasi-static elastic modulus of $\sim 500\,\mathrm{MPa}$ reported by Cho et al. [60] was notably higher than those measured at higher strain rates by other studies (e.g., $180 - 380\,\mathrm{MPa}$ at $100\,\%/\mathrm{s}$) [61, 62]. The elastic moduli of the ligaments of animal models typically used for *ex vivo* experiments were mostly within the large range of variation of human ligaments ($\sim 100 - 1000\,\mathrm{MPa}$).

A wide range of factors have been found to affect the material properties of tendons and ligaments, which could explain the large variation in the reported material properties of these tissues. For example, connective tissue can remodel when subjected to increased loading and, thus, regular activity can increase strength and Young's modulus, and reduce hysteresis [33]. On the other hand, prolonged immobilisation and disuse of the tissue can significantly reduce strength and stiffness [67]. Stretching can reduce viscosity, hysteresis, and stiffness [40]. Ageing has been found to deteriorate material properties, with decreased stiffness, ultimate stress, and energy absorption [68–71].

Abnormal material properties in tendons and ligaments can also be a sign of pathological tissue changes due to injury [32, 33]. Injuries can be caused by sudden eccentric loading, with ACL and MCL tears being a common sports injury (e.g., in footballers and skiers) when the knee undergoes non-physiological internal rotation [33]. Damage can also be caused by an accumulation of small tears induced by repetitive straining and overuse, which in tendons is often referred to as tendinopathy [32]. Alternatively, soft tissues can be damaged during surgical procedures. For instance, in knee replacement surgery, the collateral ligaments may be resected accidentally, particularly in smaller knees, or they

TABLE 2.1 Collateral ligament material properties. Values taken from graphs are approximated and indicated with the "$\sim$" symbol. Where available, standard deviations ($\pm$) and ranges ([ ]) are reported.

Reference	Species	MCL/ LCL	Age	Length (mm)	Width (mm)	Thickness (mm)	Cross-sectional area (mm^2)	Elastic modulus (MPa) (strain rate given in brackets)	Viscoelastic properties
Butler 1986 [61]	Human	LCL	27 ± 5.2 [21 – 30] years	50.8 ± 2.1 [48.7 – 52.9]	-	-	2.75 ± 1.11 [1.54 – 3.73]	$\sim 380 \pm 40$ (100 %/s)	-
Kerrigan 2003 [64]	Human	LCL	55.1 ± 11.9 [40 – 66] years	-	-	-	15.28 ± 7.93 [7.01 – 26.64]	366.8 ± 146.0 [230.4 – 538.5] (1.41 $\pm$ 0.07 %/s) 626.0 ± 130.6 [485.0 – 742.8] (1908.01 $\pm$ 770.99 %/s)	-
LaPrade 2005 [62]	Human	LCL	57.5 [40 – 77] years	57.8 ± 5.5	-	-	11.9 ± 2.9	183.5 ± 110.7 (100 %/s)	-
Otake 2007 [52]	Human	LCL	79.5 ± 9.5 [64 – 98] years	**anterior bundle:** 52.9 ± 7.3 [35.6 – 70.0] **posterior bundle:** 54.6 ± 7.2 [37.8 – 73.0]	**proximal attachment:** 8.8 ± 0.9 [7.0 – 10.0] **distal attachment:** 6.8 ± 1.0 [5.0 – 10.0]	-	-	-	-
Wilson 2012 [63]	Human	LCL	81 [62 – 92] years	69.9 ± 6.4	4.7 ± 1.1	2.6 ± 0.3	-	-	-
Smeets 2017 [66]	Human	LCL	74 ± 7 years	-	-	-	-	289.0 ± 159.7 [127.7 – 611.7] (2 %/s)	-
Cho 2020 [60]	Human	LCL	79.1 [62 – 93] years	48.15 ± 5.79	3.96 ± 0.98	2.58 ± 0.95	8.76 ± 3.77	493.86 ± 98.97 (0.167 mm/s)	-
Quapp 1998 [38]	Human	MCL	62 ± 18 years	-	-	-	-	332.15 ± 58.27 (1 %/s)	-
Kerrigan 2003 [64]	Human	MCL	55.1 ± 11.9 [40 – 66] years	-	-	-	88.79 ± 38.46 [58.34 – 162.57]	94.0 ± 68.2 [40.1 – 170.7] (1.78 $\pm$ 0.35 %/s) 182.5 ± 78.2 [108.5 – 264.4] (1204.63 $\pm$ 306.07 %/s)	-
Robinson 2004 [55]	Human	MCL	75 – 93 years	**superficial:** 80 – 112 **deep:** 29 – 33	**superficial:** 10 – 13 **deep:** 5 – 9	-	-	-	-
Bonifasi-Lista 2005 [72]	Human	MCL	53.6 ± 10.3 years	-	-	-	-	-	**static stress relaxation (after 1000 s):** 60 – 80 % of the initial stress **dynamic phase difference between stress and strain:** 0.10 – 0.35 radians
Lujan 2007 [65]	Human	MCL	57 ± 5 years	-	-	-	-	202 ± 37 (1 %/s)	-

Otake 2007 [52]	Human	MCL	$79.5 \pm 9.5\ [64-98]$ years	**anterior bundle:** $80.1 \pm 7.4\ [70.0-100.0]$ **posterior bundle:** $92.8 \pm 8.0\ [76.8-110.0]$	**proximal attachment:** $11.3 \pm 1.0\ [9.7-14.0]$ **distal attachment:** $9.5 \pm 1.6\ [7.0-15.0]$	-	-	-	-
Wilson 2012 [63]	Human	MCL	$81\ [62-92]$ years	112.1 ± 5.9	32.1 ± 3.1	2.1 ± 0.6	-	-	-
Smeets 2017 [66]	Human	MCL	74 ± 7 years	-	-	-	-	$441.8 \pm 117.2\ [281.2-617.5]$ (2 %/s)	-
Cho 2020 [60]	Human	MCL	$79.1\ [62-93]$ years	68.99 ± 19.01	11.19 ± 2.78	2.14 ± 0.70	24.52 ± 11.94	326.75 ± 225.22 (0.167 mm/s)	-
Ristaniemi 2018 [73]	Bovine	LCL	$14-22$ months	-	-	-	-	**ramp loading:** $\sim 254 \pm 136$ (0.005 mm/s) **sinusoidal loading:** 181.66 ± 135.26 (0.1 Hz) 187.80 ± 140.20 (0.5 Hz) 190.08 ± 142.14 (1 Hz) **initial elastic modulus at 0% strain:** 1.20 ± 21.04	**dynamic phase difference between stress and strain:** $\sim 5.0 \pm 1.4°$ (0.1 Hz) $\sim 5.8 \pm 1.4°$ (0.5 Hz) $\sim 6.4 \pm 2.1°$ (1 Hz)
Chawla 2009 [74]	Bovine	MCL	-	36.29 ± 5.85	-	-	72.11 ± 18.37	235.66 ± 84.18 (0.023 ± 0.010 %/s) 601.33 ± 210.50 (9223 ± 843 %/s) 1217.66 ± 243.52 (11983 ± 1419 %/s)	-
Ristaniemi 2018 [73]	Bovine	MCL	$14-22$ months	-	-	-	-	**ramp loading:** $\sim 333 \pm 60$ (0.005 mm/s) **sinusoidal loading:** 288.51 ± 102.56 (0.1 Hz) 296.60 ± 105.48 (0.5 Hz) 298.56 ± 105.96 (1 Hz) **initial elastic modulus at 0% strain:** 2.9 ± 10.6	**dynamic phase difference between stress and strain:** $\sim 4.4 \pm 1.1°$ (0.1 Hz) $\sim 4.7 \pm 1.4°$ (0.5 Hz) $\sim 5.5 \pm 2.4°$ (1 Hz)

Cone 2019 [75]	Porcine	LCL	$0-18$ months	**0 months:** $7.8 \pm 1.1\ [6.6-9.0]$ **1.5 months:** $12.5 \pm 0.8\ [11.7-13.3]$ **3 months:** $22.2 \pm 4.5\ [17.5-26.9]$ **4.5 months:** $29.4 \pm 2.1\ [27.2-31.5]$ **6 months:** $34.5 \pm 4.1\ [30.3-38.8]$ **18 months:** $35.6 \pm 3.3\ [32.2-39.0]$	-	-	**0 months:** $1.7 \pm 0.4\ [1.2-2.1]$ **1.5 months:** $6.3 \pm 1.6\ [4.6-7.9]$ **3 months:** $13.3 \pm 1.9\ [11.3-15.2]$ **4.5 months:** $18.5 \pm 4.3\ [13.9-23.0]$ **6 months:** $26.3 \pm 3.6\ [22.6-30.0]$ **18 months:** $31.3 \pm 5.1\ [25.9-36.7]$	-	-
Blank 2020 [76]	Porcine	LCL	6 months	24.5 ± 4.5	-	-	32.9 ± 7.3	-	-
Peck 2010 [77]	Porcine	MCL	-	36.60 ± 6.12	-	-	13.78 ± 9.88	-	-
Germscheid 2011 [78]	Porcine	MCL	$6-8$ months	**YK, R:** 66.0 ± 3.3 **YK, L:** 64.4 ± 3.2 **RD, R:** 68.5 ± 5.0 **RD, L:** 71.5 ± 5.2	**YK, R:** 7.5 ± 0.8 **YK, L:** 7.5 ± 0.7 **RD, R:** 8.4 ± 0.9 **RD, L:** 8.2 ± 1.1	**YK, R:** 1.8 ± 0.2 **YK, L:** 1.6 ± 0.3 **RD, R:** 2.1 ± 0.2 **RD, L:** 1.8 ± 0.2	**YK, R:** 13.5 **YK, L:** 12.0 **RD, R:** 17.6 **RD, L:** 14.8	**YK, R:** 400.0 ± 47.5 **YK, L:** 477.8 ± 110.7 **RD, R:** 327.6 ± 54.4 **RD, L:** 390.0 ± 109.9 $(0.333\ \mathrm{mm/s})$	**cyclic creep strain (100 N, 1 Hz, 30 cycles):** **YK, R:** $0.24 \pm 0.03\ \%$ **YK, L:** $0.26 \pm 0.06\ \%$ **RD, R:** $0.23 \pm 0.05\ \%$ **RD, L:** $0.26 \pm 0.05\ \%$ **static creep strain (100 N, 20 minutes):** **YK, R:** $1.16 \pm 0.08\ \%$ **YK, L:** $1.35 \pm 0.15\ \%$ **RD, R:** $1.32 \pm 0.26\ \%$ **RD, L:** $1.38 \pm 0.21\ \%$
Cone 2019 [75]	Porcine	MCL	$0-18$ months	**0 months:** $7.7 \pm 1.8\ [5.9-9.6]$ **1.5 months:** $12.5 \pm 2.2\ [10.2-14.8]$ **3 months:** $20.8 \pm 2.1\ [18.6-23.0]$ **4.5 months:** $33.0 \pm 3.2\ [29.7-36.3]$ **6 months:** $34.2 \pm 2.6\ [31.5-36.9]$ **18 months:** $38.7 \pm 3.4\ [35.1-42.3]$	-	-	**0 months:** $0.9 \pm 0.3\ [0.6-1.2]$ **1.5 months:** $3.7 \pm 1.2\ [2.5-5.0]$ **3 months:** $9.3 \pm 1.8\ [7.4-11.2]$ **4.5 months:** $14.0 \pm 2.3\ [11.7-16.4]$ **6 months:** $19.8 \pm 2.9\ [16.7-22.9]$ **18 months:** $22.5 \pm 3.5\ [18.7-26.2]$	-	-
Blank 2020 [76]	Porcine	MCL	6 months	23.3 ± 8.3	-	-	29.0 ± 8.9	-	-

Thornton 2007 [79]	Rabbit	MCL	12 months	21.34 ± 0.94	-	-	3.90 ± 0.51	613 ± 63 (0.333 mm/s or 1.5 %/s)	-
Wan 2014 [70]	Rabbit	MCL	$1.5 - 13$ months	-	-	-	**1.5 months:** 0.85 ± 0.26 **4 − 5 months:** 2.01 ± 0.54 **6 − 7 months:** 1.86 ± 0.61 **12 − 13 months:** 2.80 ± 0.83	**1.5 months:** 469.50 ± 85.23 **4 − 5 months:** 735.00 ± 41.57 **6 − 7 months:** 872.10 ± 183.40 **12 − 13 months:** 1037.00 ± 72.43 (0.1 mm/s)	-
Thornton 2015 [80]	Rabbit	MCL	$1 - 3$ years	-	-	-	-	**1 year:** ~ 695 $[570 - 840]$ **3 years:** ~ 630 $[440 - 680]$ (0.333 mm/s)	-
Strickland 2003 [81]	Sheep	MCL	-	-	-	-	$\sim 8.0 \pm 1.5$	-	-

YK: Yorkshire breed
RD: Red Duroc breed
L: Left
R: Right

may be partially or fully released intentionally if implant placement results in excessive joint stiffness [82, 83]. These ruptures or tears can cause a reduction in elastic modulus and viscosity [41, 84–87].

Biomechanical function of tendons and ligaments can also be assessed from their strain or length change behaviour. For example, in the Achilles and patellar tendon, abnormal length change behaviour can show reduced subtendon sliding, which limits efficient muscle activation, and has been linked to ageing, tendinopathy and ruptures [88–95].

In the collateral ligaments, the length change behaviour has already been studied for healthy knees. During knee flexion from full extension to $75°$, the LCL slackens to approximately $-4\,\%$ [47]. The MCL and POL, on the other hand, experience non-uniform length change patterns (Figure 2.2). The anterior fibres elongate, with the maximum reported length change after $75°$ of knee flexion occurring in the anterior fibres of the deep MCL during squatting, at around $30\,\%$ [96]. As the attachment of the fibres progresses posteriorly, strains decrease, with the lowest reported strains being around $-30\,\%$ for the posterior fibres of the POL [18].

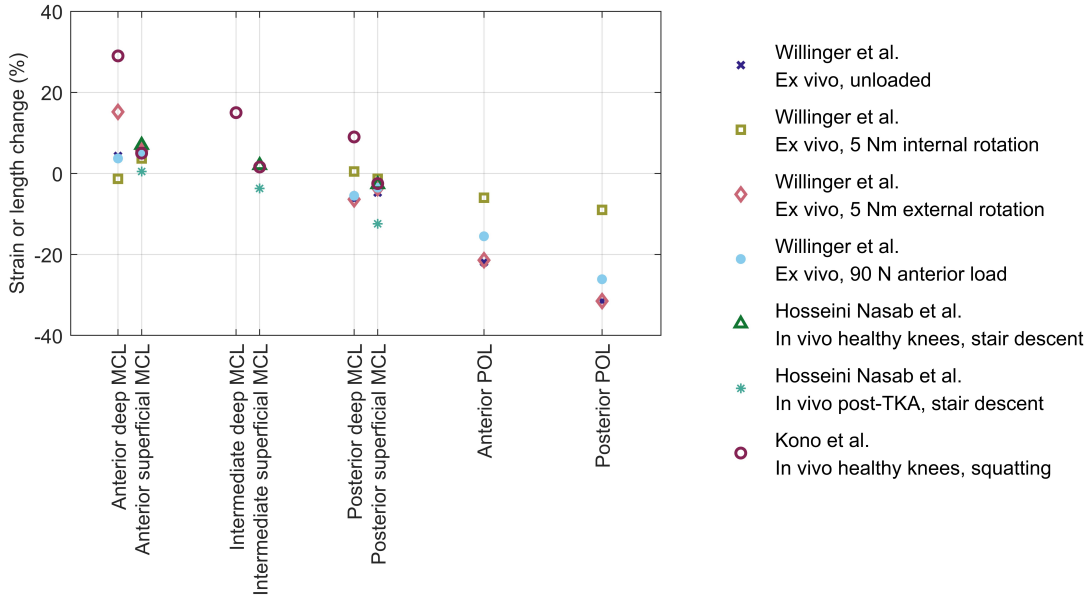


FIGURE 2.2 Literature review on the relative strain or length change of the medial ligament bundles of the knee during knee flexion from $0°$ to $75°$. Willinger et al. [18] measured length change values in *ex vivo* cadaveric knees using linear variable displacement transducers (LVDTs). Hosseini Nasab et al. [14, 47] and Kono et al. [96] estimated ligament length changes by tracking the bony attachment sites in fluoroscopic images. All values were read off the graphs presented in these studies.

As with the Achilles tendon, altered strain mechanisms in the collateral ligaments may be indicative of damage. Alternatively, these changes could suggest that the collateral ligaments are not being properly engaged following knee replacement surgery due to altered knee biomechanics. A fluoroscopy study by Hosseini Nasab et al. [14] revealed that total knee replacement (TKR) surgery leads to altered elongation behaviours in the MCL. In the healthy knees, anterior fibres continuously elongate, while posterior fibres shorten. In TKR patients, the behaviour is similar for the first $40 - 50^{\circ}$ of flexion; however, for increased flexion, anterior fibres slacken again and posterior fibres experience more pronounced shortening than in the healthy knees [14, 19, 47]. This leads to overall lower strains after 75° of flexion (Figure 2.2).

2.1.5 Treatment of the collateral ligaments during knee replacement surgery

The collateral ligaments play a vital role in stabilising the knee and maintaining the bone and joint geometry. Therefore, preserving these ligaments during knee replacement surgery is preferred and surgeons perform a procedure known as “ligament balancing” to ensure that ligament tension remains properly balanced throughout the procedure [10, 11]. Unsuccessful balancing of the ligaments at the time of surgery has been linked to poor post-operative outcomes: overly tightening the ligaments reduces range of motion and can cause pain, while loose ligaments can lead to implant instability, causing the patient to feel unstable when performing daily activities [8, 9]. Furthermore, tightness can lead to overstraining of the ligaments which can cause plastic deformation, tears and cell death, while laxity can impair the healing response mechanism [15].

The most common recommendation for ligament balancing during knee replacement surgery is to achieve a rectangular and equal gap between the femoral and tibial implant components both in extension and flexion [8]. Two main surgical methods exist for achieving this. 1) During the measured resection technique, bony landmarks are used as reference points for tibial and femoral resections. Bone cuts are then followed by soft-tissue release to

obtain equal flexion and extension gaps. 2) During the gap-balancing technique, ligament structures are released first to obtain neutral alignment. The femoral component is then positioned parallel to the resected tibia, resulting in symmetric gaps and equally tensioned ligaments [97–99].

Historically, optimal ligament balancing has often been judged subjectively by the surgeon, with no measurable intra-operative guidelines [8]: the knee is moved through a range of motion, and the stability, stiffness and movement pattern is assessed. Thus, there has been great research interest in improving and establishing quantitative metrics for the balancing of ligaments. One of the major advancements seen in the last years is the development of a sensor-assisted device called Verasense by Orthosensor. This device replaces the tibial spacer that is traditionally used to measure the gaps between the tibial and femoral components. Instead, the Verasense provides surgeons with the magnitude and position of loads on the medial and lateral side, allowing for more informed and objective decisions during soft tissue release and implant positioning [12]. With the use of this device, the success rate for balancing has been shown to increase from 50% to over 90% [100].

However, despite the improved intra-operative success rate, complications related to a ligament unbalance remain high [3, 13]. While it is well understood how ligaments contribute to stability during surgery, little information is available on how post-operative healing or adaption can compromise this stability. Currently, the only non-invasive way to monitor post-operative collateral ligament function is with manual laxity tests, such as the varus-valgus stress test, or by measuring the elongation pattern using a video-fluoroscopy system [14, 15]. However, laxity tests are very subjective and fluoroscopy comes with the risks associated with radiation.

2.2 Ultrasound background

Ultrasound has established an indispensable role in the field of diagnostic medicine due to its non-invasive nature, real-time imaging capabilities, and versatility in assessing soft tissue appearance and mechanics [101]. Its ability to provide detailed information on soft tissues, blood flow, and movement, combined with its safety and cost-effectiveness, makes it a critical tool in a wide range of clinical applications, from obstetrics and cardiology to musculoskeletal and abdominal assessments [101].

2.2.1 Fundamentals

Sound is acoustic pressure waves travelling through a medium. Acoustic waves with frequencies between $20\,\mathrm{Hz}$ and $20\,\mathrm{kHz}$ are audible, whereas ultrasound waves, with higher frequencies, fall within an inaudible spectrum. The medium through which sound travels determines various characteristics of propagation, such as the speed of the waves or its attenuation, i.e. how much energy is absorbed by the medium [101]. For example, in the human body, speeds and attenuation coefficients range from $\sim 1500\,\mathrm{m/s}$ and $<1\,\mathrm{dB/cm/MHz}$ in fat, blood and soft tissue, to $\sim 4000\,\mathrm{m/s}$ and $\sim 5\,\mathrm{dB/cm/MHz}$ in bone [102, 103]. Furthermore, the acoustic impedance of the medium plays a vital role in medical ultrasound imaging. Impedance is the product of the density of the medium and the speed of sound in the medium. Ultrasound waves reflect and refract when there is a change in acoustic impedance, and the detection of these backscattered reflections

gives rise to ultrasound images. Thus, boundaries of structures with a large difference in impedance, such as soft tissue and bone, are characterised by a large spike in the reflected signal, resulting in bright features in the ultrasound image. However, even small changes in impedance due to the heterogeneity of soft tissue are visible, as they result in a speckled appearance in the background of the image. This speckle pattern is often unique to specific types of tissues and, while it appears to be noisy, remains stable over consecutive acquisitions [102, 103].

Ultrasound transducers used in medical imaging are usually composed of a 1D linear or curved array of individual piezoelectric elements. These elements convert electrical pulses to mechanical vibrations that generate ultrasonic pressure waves that propagate through the skin and into the body [104]. The same ultrasound transducer can be used to measure the backscattered ultrasound echoes: the piezoelectric elements output a raw electrical radio frequency (RF) signal proportional to the measured acoustic pressure [104]. Next, a beamforming procedure is applied to convert the time-varying signal from each element into 2D-spatial data representing the contribution of reflected signal from each point in the field of view. Beamforming considers the time that the reflections from each point in space take to return to each transducer element, based on the speed of sound in the tissue. Thus, the signal from each element is delayed and summed accordingly to calculate the contributions from each point in the field [101, 105].

Beamformed ultrasound images are often described in the transducer coordinate system (Figure 2.3): the lateral dimension refers to the direction along the long axis of the ultrasound transducer face, i.e. along the piezoelectric elements of a 1D array. The axial dimension is parallel to the direction of ultrasound wave propagation, i.e. perpendicular to the transducer face and into the depth of the tissue. Lastly, the elevational dimension is along the short axis of the ultrasound transducer face, i.e. perpendicular to the 2D image slice [101]. Throughout this thesis, directional descriptions will be made in this coordinate system.

The resolution of the beamformed ultrasound images is determined by the smallest distance between scatterers at which their reflections can still be distinguished during

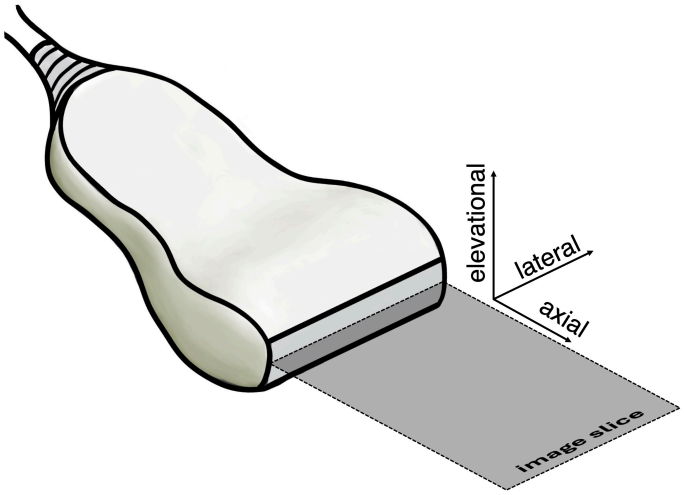


FIGURE 2.3 Ultrasound transducer coordinate system.

the beamforming process [105, 106]. In the axial image direction, this is equal to half of the spatial pulse length, i.e. the product of the wavelength and the cycles per pulse. Thus, axial resolution can be improved by using high-frequency ultrasound transducers, since these produce waves of shorter wavelength [49]. However, since higher frequency waves are also attenuated more quickly, only superficial structures can be visualised with high-frequency waves [106].

Usually, multiple transducer elements are activated during each transmission to produce an ultrasound beam of higher intensity. The lateral resolution is related to the width of this beam, which varies with distance from the transducer. Without any focusing, the beam converges within a “near-zone”, gradually decreasing from the width of the transducer to half this width; in the “far-zone”, the beam diverges again. Lateral resolution can be improved by using a narrower, focused beam, which is achieved by activating the transducer elements with slight delays [106].

2.2.2 Imaging modes

A wide range of imaging modes exist that aim to strike a balance between spatial and temporal resolution, as well as penetration depth (Figure 2.4).

The most common imaging mode implemented by commercial ultrasound scanners is a conventional scanline mode. Each vertical line of the image (into the depth of the imaged tissue) is obtained one at a time with a narrow focused beam centred on the line. These beams are created using a sub-aperture of the transducer, i.e. a small subset of the ultrasound transducer elements. Since the image is created line by line, multiple transmissions are required to obtain one full image, with each transmission shifting the focused beam laterally along the transducer. The main disadvantage of this imaging mode is that it limits the achievable frame rate. However, due to the narrow, focused beams, spatial resolution and penetration depth is increased [49, 105, 107].

Plane wave imaging (PWI) is an ultrafast imaging mode that was developed to capture rapid tissue motion, such as cardiac contractions or shear wave propagation through the tissue. To achieve these high frame rates, all transducer elements are activated simultaneously to produce a single unfocused beam that insonifies the entire field of view. Thus, the ultrasound image can be obtained with as a little as one transmission, in which case the frame rate is only limited by the speed of the ultrasound waves through the medium, the desired image depth and the processing time to create the image [105]. This allows for frame rates of up to several thousand frames per second. However, this comes at the cost of reduced spatial resolution and contrast since no beam focusing is used.

Coherent plane-wave compounding (CPWC) is an extension of the PWI mode. In this case, beam steering is applied to transmit the unfocused beams at several angles. By

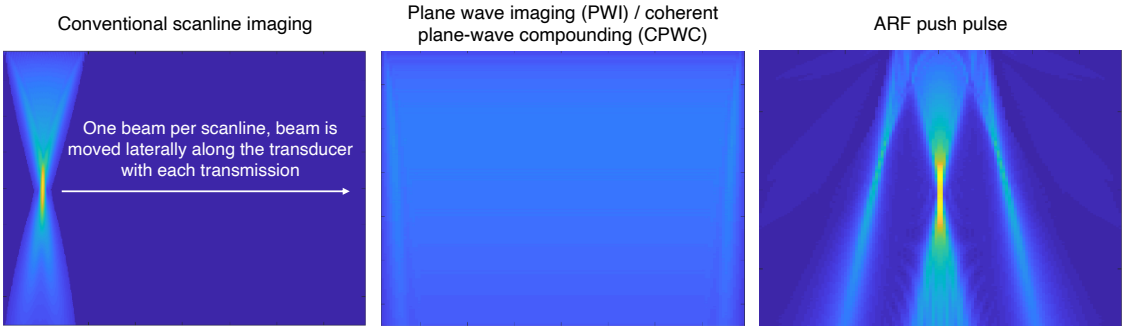


FIGURE 2.4 Simulated beam profiles for conventional scanline imaging, plane wave imaging, and the acoustic radiation force (ARF) push pulse. The colour map illustrates the relative pressures in the field. As can be seen, focusing produces narrower beams with a more concentrated intensity distribution, thereby enhancing resolution.

averaging the beamformed signal obtained at the different angles, an overall image with improved quality can be obtained. This averaging process is called coherent compounding [105, 108]. Even though each individual beam has a low and wide intensity distribution, a synthetic focusing technique for transmission and receive can be used to obtain equally high axial and lateral resolutions in the entire field of view [109, 110].

Ultrasound transmissions can also be used to generate acoustic radiation forces (ARFs) through a transfer of momentum within the soft tissue. These forces can be used to generate shear waves whose propagation behaviour can give diagnostic insights or, alternatively, for therapeutic high intensity focused ultrasound (HIFU) applications (e.g., destruction of pathological tissue) [103, 111]. While this momentum transfer also occurs during regular B-mode imaging, the forces involved are minimal. Forces produced by the ultrasound pulse can be elevated by focusing the ultrasound beam, extending the duration of the pulse (i.e., microseconds vs nanoseconds), increasing the transducer voltage or a combination of these [103, 112].

2.2.3 Quantitative ultrasound elastography

The diagnostic importance of assessing soft tissue mechanical properties has long been recognised. Pathological changes, such as tumours, are frequently associated with increased stiffness and, for centuries, palpation has been employed to identify these stiff masses within the body [113]. However, manual assessment is often very subjective and depends on the experience of the clinician. Quantitative ultrasound (QUS) elastography, first introduced by Ophir et al. in 1991 [114], has enabled a non-invasive and objective measurement of the function and material characteristics of soft tissue, such as its strain behaviour or elastic modulus. This allows for a more complete assessment of tissue health and helps clinicians identify pathological changes in the underlying microstructure of the tissue that are not palpable or visually detectable from B-mode ultrasound images [86, 101, 108].

There exist several branches of ultrasound elastography, and most are linked by the

same fundamental steps depicted in Figure 2.5 [101]. The objective is to analyse tissue displacement due to an excitation source, which in turn provides information about the tissue's mechanical properties. Two common elastography techniques are shear wave and speckle tracking imaging, and a detailed description of these is given in the following sections.

Some approaches that are not based on tissue motion exist as well. For example, acoustoelasticity techniques measure tissue stiffness from the intensity of reflected ultrasound waves [115]. Thus, by comparing the echo intensity of B-mode images, changes in stiffness may be detected. In orthopaedics, this technique has been applied to tendons to quantify stiffness changes with loading [116], or due to damage and healing [117, 118].

2.2.4 Shear wave imaging

The evolution of shear wave imaging

The ultrasonic technique of shear wave imaging is based on the principle that the propagation speed of a shear wave in a medium is related to the elastic shear modulus [16]. Shear waves can be generated using two types of excitation sources, either (1) an external vibration source that taps the skin near the soft tissue of interest [41, 119], or (2) using a highly focused beam from the ultrasound transducer itself, which produces an acoustic radiation force (ARF) at the focus through a momentum transfer from the beam to the tissue [120, 121]. The tissue motion due to the shear wave propagation is subsequently tracked using ultrafast ultrasound imaging. The advantages and disadvantages of using an external shaker vs ARF-based technique are summarised in Table 2.2. Ultimately, the

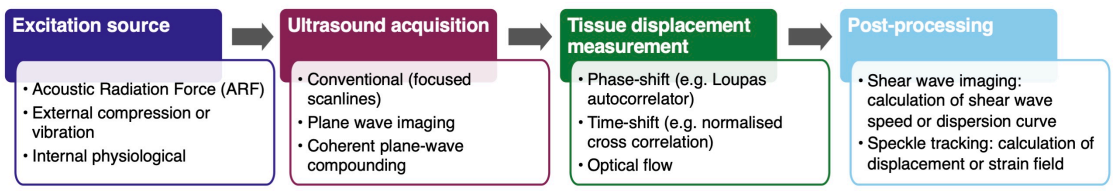


FIGURE 2.5 Ultrasound elastography steps.

TABLE 2.2 Advantages and disadvantages of generating shear waves using vibrations from external shakers vs acoustic radiation forces (ARFs).

Aspect	External shaker	ARF-based technique
Safety	No risk of thermal or mechanical damage has been reported (vibration forces are generally less than those of commercial massage guns)	Potential for thermal and mechanical tissue damage due to high acoustic pressures and intensities [103]
Patient comfort	May be uncomfortable due to physical vibrations	ARF cannot be felt and thus may be more comfortable for patients
Setup	Requires bulky, external equipment [112]	Integrated into ultrasound systems, thus more suitable in clinical settings
Hardware	Less expensive and simpler hardware	Requires a powerful ultrasound system that can support high transducer voltages [108]
Precision	Shear waves are generated at the surface of skin and, thus, cannot be localised to deeper tissue structures	Shear wave generation can be targeted to tissue of interest, which can be better for small areas
Shear wave frequency	Results in controlled shear wave frequencies with a narrow bandwidth, allowing precise measurements over a wide range of frequencies, which is especially useful for dispersion analysis [41, 43]	Results in shear waves with a broad range of frequencies that depend on the interaction of the ARF with the soft tissue, i.e. less control over frequencies [41]
Shear wave amplitude	Shear waves with higher amplitude can be generated, leading to more accurate shear wave tracking [122]	Stronger shear waves require larger acoustic radiation forces, which increases the risk of thermal or mechanical damage due to acoustic pressures [103]

choice of the most suitable method will depend on the specific application requirements.

Shear wave imaging, initially referred to as “sonoelasticity”, was first implemented by Lerner and Parker [119, 123] in the late 1980s using externally generated shear waves. Methods utilising ARF-generated waves soon followed, with various versions being developed over the next decade. These methods employed different techniques for both excitation and tracking of tissue displacement. Table 2.3 and Figure 2.6 describe these methods.

In 1998, Sarvazyan et al. [120] were the first to propose that ultrasound can be used for both shear wave generation and tracking, presenting the physical and mathematical theory behind shear wave formation due to an acoustic radiation force. Later in 2003, Nightingale et al. [121] published their experimental work based on this idea, establishing the shear wave elastography imaging (SWEI) method where the same transducer is used to induce a shear wave at a single location and track the subsequent tissue motion at multiple lateral positions.

In 2004, Bercoff et al. [112] introduced the supersonic shear imaging (SSI) method: multiple shear waves are generated in quick succession at different focal depths. If these shear sources move at supersonic speed, i.e. faster than the shear waves, a Mach cone is created, resulting in two quasi-plane shear waves. This method provides

TABLE 2.3 Shear wave imaging methods using acoustic radiation forces, summarising first implementations in the literature as well as commercial systems using the techniques.

Name	Excitation	Lateral tracking location	Commercial system	First implementation
Shear wave elastography imaging (SWEI)	Single ARF	Multiple tracking locations	Acuson VTIQ (Siemens) ElastPQ (Philips) Aplio (Toshiba)	Sarvazyan et al. 1998 [120] Nightingale et al. 2003 [121]
Supersonic shear imaging (SSI)	Multiple axial ARF	Multiple tracking locations	Aixplorer (SuperSonic Imagine)	Bercoff et al. [112]
Spatially modulated ultrasonic radiation force (SMURF)	Multiple lateral ARF	Single tracking location	-	McAleavy et al. 2007 [124]
Comb-push ultrasound shear elastography (CUSE)	Multiple lateral ARF	Multiple tracking locations	LOGIQ E9 (GE) [125]	Zhao et al. 2011 [126]

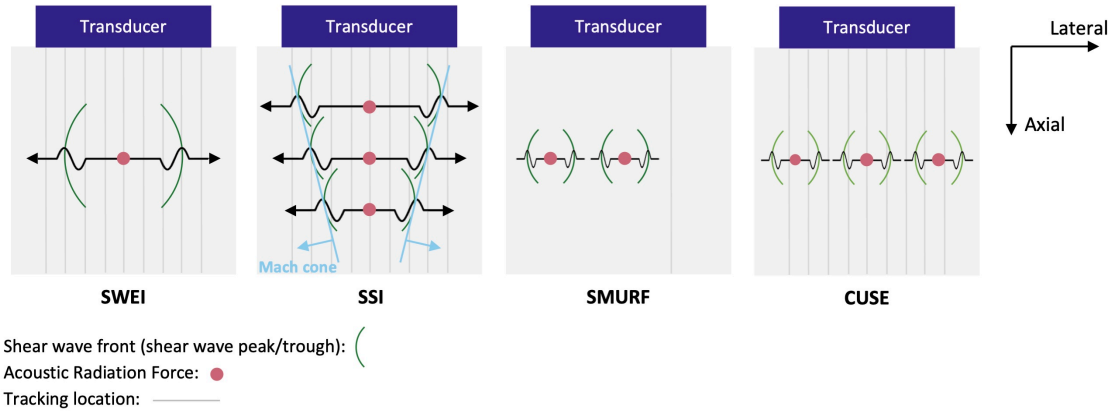


FIGURE 2.6 Diagrams for the shear wave imaging methods.

higher displacement amplitudes and a plane wave front (as opposed to spherical wave propagation [127]), allowing a larger area to be covered and shear wave velocities to be estimated with higher accuracy [112, 128].

The spatially modulated ultrasonic radiation force (SMURF) technique was developed by McAleavey et al. [124] in 2007. In this case, an ARF force is applied at several lateral positions, thus generating a shear wave with a known wavelength. The frequency of the shear wave is then measured at the tracking location. Thus, the shear wave speed can be calculated from the wavelength and frequency [124]. Comb-push ultrasound shear elastography (CUSE) is an extension of this method presented by Zhao et al. [126]. This method usually uses unfocused instead of focused push beams to reduce the complexity of the push protocol, allowing for a larger number of simultaneous focus points; furthermore, tracking is often performed at multiple locations [126, 129].

Core principles of shear wave imaging

The external vibration or ARF produces both compressional and shear waves. The speed of compressional waves is related to the bulk modulus of the material, while the speed of the shear waves is related to the shear modulus [120, 121]. Since the bulk modulus in biological soft tissue is far greater than the shear modulus, the compressional waves travel very quickly through the tissue and are difficult to detect, while the shear waves travel at a slower speed and can be captured with high frame-rate ultrasound systems [130, 131].

The velocity of shear waves depends on the viscoelastic properties and density of the tissue and, when using the Voigt viscoelastic model, is governed by Equation 2.1.

$$c_p = \sqrt{\frac{2}{\rho}\frac{\mu^2 + (\omega\eta)^2}{\sqrt{\mu^2 + (\omega\eta)^2} + \mu}} \tag{2.1}$$

$c_p =$ phase velocity of the shear wave

$\eta =$ Voigt shear viscosity

$\mu =$ Voigt shear modulus

$\rho =$ material density

$\omega =$ angular temporal frequency

Two types of velocities can be used to describe the propagation of shear waves: phase and group velocity. Phase velocity describes the speed of individual frequency components of the wave. The superposition of multiple frequency components can lead to the formation of wave packets, i.e. groups with large amplitude, and the speed of propagation of these packets is termed the group velocity. Therefore, while phase velocity is related to the material properties (Equation 2.1), group velocity usually represents the speed at which information or energy is transferred; these are only equivalent for elastic material where phase velocity does not vary with frequency, i.e. $\omega/k = d\omega/dk =$ constant [132, 133].

$$c_g(\omega) = \frac{d\omega}{dk} \tag{2.2}$$

$$c_p(\omega) = \frac{\omega}{k} \tag{2.3}$$

c_g = group velocity of the shear wave

k = shear wavenumber

Most shear wave imaging implementations use so-called time-of-flight (TOF) algorithms which track the movement of the overall wave packet through the field of view. This gives a measure of the shear wave's group velocity [132], thus assuming that the tissue is elastic and non-dispersive ($\eta = 0$ and $c_p = c_g$), leading to the following simplification of Equation 2.1: $\mu = \rho c_p^2 = \rho c_g^2$. Furthermore, the Young's modulus (E) is sometimes reported instead of shear modulus by assuming that the soft tissue is incompressible and isotropic, i.e. $E \approx 3\mu$ [71, 86, 134].

However, shear waves travelling through biological material with non-negligble viscous effects will experience dispersion, leading to frequency dependent phase and group velocities. Thus, to allow for full characterisation of tissue properties using Equation 2.1, the shear wave phase velocity must be measured at a range of frequencies. Failure to do so will result in inaccurate material property measurements and inconsistencies in the results of studies that use shear waves of different frequencies.

Another source of dispersion is the geometry of the soft tissue. Soft tissues often consist of layered structures of different thicknesses and mechanical properties [28, 135]. If the shear wave is induced in a layer of thickness less than the shear wavelength, the bulk wave theory is no longer applicable [135, 136]. Instead, reflections of the shear wave at boundaries of heterogeneous soft tissue can lead to complex propagation patterns. This occurs, for example, in thin-layered tendons and ligaments, where shear waves bounce between the internal boundaries of the structure. The interference of the shear wave reflections results in a new, dispersive "guided" wave with frequency-dependent phase and group velocity [30, 135, 136]. While conventional shear wave imaging systems have been used for thin-layered tissue structures [71, 86, 137, 138], the calculated wave velocity does not correspond to the bulk shear wave velocity, but instead gives the guided wave group velocity at the centre frequency [30]. This value is not very meaningful when attempting to determine mechanical properties and, when used as the shear wave velocity (c_p) value in

the aforementioned relationship, significantly underestimates the shear modulus [28–30]. Instead, more complex guided wave models have been established, for example the Lamb wave dispersion model, that describe how the guided wave speed is linked to both the tissue geometry and its material properties [30, 139, 140].

Shear wave imaging applications

Shear wave imaging is being used or developed for a wide range of clinical applications to scan for changes in tissue stiffness, which can signify a pathological condition (Table 2.4). It has allowed for the detection of liver fibrosis [20–22], malignant tumours in the breast [24, 25, 112], cardiovascular diseases through changes in the arterial walls [139, 141], and skin diseases through changes in the dermis layer of skin [28, 137, 142].

The shear or Young's elastic moduli obtained from ultrasound shear wave imaging can also provide valuable information about the health and function of soft tissue in the musculoskeletal system: (1) firstly, activity has been found to increase the elastic modulus, both temporarily after exertion and in the long term. For example, the shear modulus of leg muscles increased by around $3\,\%$ immediately after running [143], and the modulus of the ulnar collateral ligaments of baseball pitchers was found to be around eight times higher than those of non-throwing healthy individuals [86]. (2) injury, on the other hand, can lead to a drop in shear modulus, with reports in the literature indicating drops of $20 - 50\,\%$ in injured ulnar collateral ligaments and hamstring tendons [41, 86]. Furthermore, elastic moduli of the ulnar collateral ligament dropped by around $40 - 50\,\%$ from pre-season to season-end in professional baseball and football players, possibly indicating injury due to overstraining [87]. (3) lastly, ageing also decreases stiffness. In a study by Wu et al. [71], subjects aged over 50 had around $24\,\%$ lower Young's moduli in muscles and around $28\,\%$ lower moduli in tendons and ligaments compared to subjects aged $21 - 30$.

Shear or Young's modulus can also indicate the amount of load on the soft tissue, with higher values measured for increased loading. For example, Ahmadzadeh et al. [144] showed that shear wave velocity increased more than threefold for an *ex vivo* patellar tendon loaded to $\sim 900\,\mathrm{N}$ in a tensile testing machine. Similarly, *in vivo* measurements of

TABLE 2.4 *Ex vivo* and *in vivo* shear wave imaging implementations. The first entries in the table are studies that assume that dispersive effects are negligible and use an elastic tissue model, both for large homogeneous structures, but also for thin layered soft tissue or tissue-mimicking phantoms. Next, a review of studies considering dispersion is provided. These either consider dispersion due to viscoelasticity, the thin tissue geometry, or a combination of both. Overall, the review mainly focused on ligament and tendon applications.

Reference	US system & transducer	Excitation method	ARF push pulse	Imaging mode	PRF (kHz)	SF (MHz)	Tissue motion calculation	Post-processing	Material property model	Results
Large, elastic model applied to homogeneous soft tissue or tissue-mimicking phantoms										
Bercoff 2004 [112]	L4	ARF SWEI ARF SSI	-	PWI	3	50	1D correlation algorithm on RF (correlated with reference echo)	-	Inversion algorithm: $\mu = \frac{\rho}{N}\sum_{\omega}\frac{F\left(\frac{\partial^2 u_x}{\partial t^2}\right)}{F\left(\frac{\partial^2 u_x}{2\partial x^2}+\frac{\partial^2 u_x}{\partial z^2}\right)}$	**Gelatin-agar phantom** SWEI on 3 %-3 % gelatin-agar: $\mathrm{SWV} = 1.5\,\mathrm{m/s}$ SSI on 5 %-1 % gelatin-agar: $\mu = 6\,\mathrm{kPa}$ ***In vivo* breast** $\mu = 1\,\mathrm{kPa}$
Xie 2012 [145]	Verasonics L7-4	ARF SWEI	400 µs	PWI	4	-	-	TOF SWV calculation	Large, elastic, isotropic medium ($E = 3\rho\,\mathrm{SWV}^2$)	**Elastography phantom (CIRS)** Provided by phantom manufacturer: $E = 5.0 \pm 1.6, 5.8 \pm 2.0, 9.7 \pm 3.0, 15.0 \pm 3.0, 25.0 \pm 5.0, 60.0 \pm 8.0\,\mathrm{kPa}$ SWEI: $E = 5.31, 6.93, 11.17, 11.76, 19.20, 55.47\,\mathrm{kPa}$
Nordenfur 2013 [146]	Verasonics L7-4	ARF SWEI ARF SSI ARF unfocused push ARF unfocused CUSE	480 cycles 5 MHz 96 µs	CPWC 5 MHz	10	20	Loupas 2D autocorrelator	Directional filter TOF SWV calculation Median filter (applied to shear wave arrival times)	-	**10 % PVA phantom, 2 freeze-thaw cycles** SWEI: $\mathrm{SWV} = 3.3 \pm 0.2\,\mathrm{m/s}$ SSI: $\mathrm{SWV} = 3.3 \pm 0.3\,\mathrm{m/s}$ Unfocused push: $\mathrm{SWV} = 3.2 \pm 0.3\,\mathrm{m/s}$ Unfocused CUSE: $\mathrm{SWV} = 3.3 \pm 0.4\,\mathrm{m/s}$ **10 % PVA phantom, 5 freeze-thaw cycles** SWEI: $\mathrm{SWV} = 6.1 \pm 1.0\,\mathrm{m/s}$ SSI: $\mathrm{SWV} = 5.7 \pm 1.2\,\mathrm{m/s}$ Unfocused push: $\mathrm{SWV} = 5.9 \pm 1.7\,\mathrm{m/s}$ Unfocused CUSE: $\mathrm{SWV} = 5.9 \pm 1.7\,\mathrm{m/s}$
Cortes 2015 [41]	Ultrasonix L14-5/38	External shaker $f =$ 208 – 624 Hz	-	PWI 10 MHz	6.24	40	Phase-shift algorithm on RF using Fourier transforms	Median filter Directional filter Low-pass Butterworth filter SWV calculation using local frequency estimation method	-	**Agar phantoms** 1 % agar: $\mathrm{SWV} \approx 5.5\,\mathrm{m/s}$ 1.5 % agar: $\mathrm{SWV} \approx 7\,\mathrm{m/s}$ 2 % agar: $\mathrm{SWV} \approx 11\,\mathrm{m/s}$
Jang 2015 [147]	Aixplorer SL15-4	ARF SSI	7.5 MHz 150 µs	-	10	-	2D correlation algorithm on IQ	TOF SWV calculation	-	**Agar phantoms** 1.5 % agar: $\mathrm{SWV} = 5.30 \pm 0.27\,\mathrm{m/s}$ 2 % agar: $\mathrm{SWV} = 7.30 \pm 0.54\,\mathrm{m/s}$
Khalitov 2016 [148]	Verasonics L7-4	ARF SWEI	5 MHz	PWI 5 MHz	-	-	Correlation algorithm (correlated with reference echo)	TOF SWV calculation	Large, elastic, isotropic medium ($E = 3\rho\,\mathrm{SWV}^2$)	**049 elastography phantom (CIRS)** Provided by phantom manufacturer: $E = 10.00 \pm 3.85, 18.00 \pm 5.15, 28.0 \pm 4.5, 58.0 \pm 5.8\,\mathrm{kPa}$ SWEI: $\mathrm{SWV} = 1.67, 2.14, 3.17, 4.29\,\mathrm{m/s}$, $E = 8.4, 13.7, 30.1, 55.2\,\mathrm{kPa}$
Carbente 2019 [149]	Verasonics L11-4v	ARF SSI	1000 cycles 5 MHz 192 µs	CPWC 5 MHz	10	20	Loupas 2D autocorrelator	Directional filter Median filter TOF SWV estimation Low-pass Butterworth, spectral inversion or median filter	Large, elastic, isotropic medium ($E = 3\rho\,\mathrm{SWV}^2$)	**049A elastography phantom (CIRS)** Provided by phantom manufacturer: $E = 8 \pm 3, 14 \pm 4, 25 \pm 6, 45 \pm 8, 80 \pm 12\,\mathrm{kPa}$ Using SSI: $E = 10.26 \pm 0.05, 15.64 \pm 0.09, 29.18 \pm 0.10, 45.81 \pm 0.11, 85.21 \pm 0.13\,\mathrm{kPa}$

Sadeghi 2019 [150]	Verasonics L7-4	ARF SSI	500 cycles 5.2 MHz 96 µs	-	10	-	Loupas 2D autocorrelator	Directional filter TOF SWV calculation	Large, elastic, isotropic medium ($\mu = \rho\,\mathrm{SWV}^2$)	**0.9 % – 2.7 % Agar phantoms** $\mu = 12.89 \pm 0.75$ kPa – 153.26 ± 5.34 kPa
Large, elastic model applied to thin-layered structures										
Aubry 2013 [134]	Aixplorer	ARF SSI	12 MHz	PWI 12 MHz	-	-	-	-	Large, elastic, isotropic medium ($E = 3\rho\,\mathrm{SWV}^2$)	***In vivo* Achilles tendon** Maximal plantar flexion: $\mathrm{SWV} = 6.8 \pm 1.4$ m/s, $E = 147.6 \pm 62.6$ kPa 45° plantar flexion: $\mathrm{SWV} = 10.7 \pm 2.4$ m/s, $E = 359.1 \pm 16.0$ kPa 0° flexion: $\mathrm{SWV} = 15.5 \pm 0.9$ m/s, $E = 723.1 \pm 78.7$ kPa 45° dorsiflexion: $\mathrm{SWV} = 16.1 \pm 0.7$ m/s, $E = 779.5 \pm 57.1$ kPa
Luo 2015 [142]	Aixplorer SL15-4	ARF SSI	-	-	-	-	-	-	Large, elastic, isotropic medium ($\mu = \rho\,\mathrm{SWV}^2$)	***In vivo* dermis** Forearm: $\mu = 2.7 – 5.7$ kPa
Haen 2017 [137]	Aixplorer	ARF SSI	-	-	-	-	-	-	Large, elastic, isotropic medium ($\mu = \rho\,\mathrm{SWV}^2$)	***Ex vivo* Achilles tendon** 25° plantar flexion: $\mu \approx 40$ kPa 0° flexion: $\mu \approx 90$ kPa Maximal dorsiflexion: $\mu \approx 130$ kPa
Xiang 2017 [137]	Aixplorer SL15-4	ARF SSI	-	-	-	-	-	-	Large, elastic, isotropic medium ($E = 3\rho\,\mathrm{SWV}^2$)	***In vivo* dermis** Middle finger: $E \approx 34$ kPa Forearm: $E \approx 16$ kPa Chest: $E \approx 16$ kPa Abdomen: $E \approx 11$ kPa
Lin 2018 [86]	Verasonics L11-5v	ARF SSI	500 cycles 7.8 MHz 100 µs	PWI	10	-	-	-	Large, elastic, isotropic medium ($\mu = \rho\,\mathrm{SWV}^2$)	***In vivo* ulnar collateral ligament** Healthy: $\mu = 110.2 \pm 37.7$ kPa Injured elbow of baseball pitcher: $\mathrm{SWV} = 13.65$ m/s, $\mu = 186.45$ kPa Uninjured elbow of baseball pitcher: $\mathrm{SWV} = 29.66$ m/s, $\mu = 879.59$ kPa
Payne 2018 [138]	Acuson S3000 9L4	ARF SWEI	-	-	-	-	-	-	-	***In vivo* Achilles tendon** 0° flexion: $\mathrm{SWV} = 9.00 – 9.43$ m/s
Zhang 2018 [151]	Verasonics L11-4	ARF SWEI	500 cycles 4 MHz 125 µs	PWI 6.25 MHz	13.3	-	KANSI algorithm (correlation with reference echo)	TOF SWV calculation	Large, elastic, isotropic medium ($E = 3\rho\,\mathrm{SWV}^2$)	***In vivo* crystalline lens of rabbit eyes** 60 days old: $\mathrm{SWV} = 1.38 \pm 0.02$ m/s, $E = 15.82 \pm 1.75$ kPa 90 days old: $\mathrm{SWV} = 2.06 \pm 0.30$ m/s, $E = 13.00 \pm 4.01$ kPa 120 days old: $\mathrm{SWV} = 2.07 \pm 0.29$ m/s, $E = 13.03 \pm 3.90$ kPa 150 days old: $\mathrm{SWV} = 2.30 \pm 0.28$ m/s, $E = 16.07 \pm 4.05$ kPa
Ahmadzadeh 2019 [144]	Verasonics L7-4	ARF SWEI	500 cycles 5 MHz 100 µs	PWI 5 MHz	20	-	Loupas 2D autocorrelator	TOF SWV calculation	-	***Ex vivo* patellar tendon** $\mathrm{SWV} = 10 – 36$ m/s (tensile loading: 8 – 935 N, 0 – 7 MPa)

Sadeghi 2018-2020 [87, 135, 143, 150, 152–155]	Verasonics L11-4v, L11-5, L7-4, C5-2	ARF SSI ARF focused CUSE	500 cycles 3.1 – 7.8 MHz 80 – 161 µs	CPWC	10	-	Loupas 2D autocorrelator	Directional filter TOF SWV calculation	Large, elastic, isotropic medium ($\mu = \rho\,\mathrm{SWV}^2$)	**0.9 % – 2.7 % 1 mm-thin agar phantoms** $\mu = 8.35 \pm 0.17$ kPa – 18.66 ± 1.61 kPa ***In vivo* tibialis anterior muscle** Before running: $\mu = 14.12 \pm 2.11$ kPa After running: $\mu = 17.74 \pm 5.58$ kPa For varying intramuscular pressure: $\mu = 15.83 \pm 2.46$ kPa – 21.88 ± 4.33 kPa (blood pressure cuff inflation: 0 – 120 mmHg) ***In vivo* peroneus longus muscle** Before running: $\mu = 8.56 \pm 1.71$ kPa After running: $\mu = 11.81 \pm 3.95$ kPa For varying intramuscular pressure: $\mu = 9.64 \pm 1.97$ kPa – 12.88 ± 5.99 kPa (blood pressure cuff inflation: 0 – 120 mmHg) ***In vivo* ulnar collateral ligament of baseball players** Dominant arm, pre-season: $\mu = 347.64 \pm 420.05$ kPa Dominant arm, season-end: $\mu = 210.83 \pm 209.44$ kPa Non-dominant arm, pre-season: $\mu = 503.95 \pm 590.59$ kPa Non-dominant arm, season-end: $\mu = 312.67 \pm 240.66$ kPa ***In vivo* ulnar collateral ligament of football quarterbacks** Dominant arm, pre-season: $\mu = 447.56 \pm 339.13$ kPa Dominant arm, season-end: $\mu = 207.02 \pm 277.18$ kPa Non-dominant arm, pre-season: $\mu = 808.15 \pm 578.34$ kPa Non-dominant arm, season-end: $\mu = 491.42 \pm 420.03$ kPa ***In vivo* lumbar multifidus muscle** ***(prone, sitting up, sitting up & arm lifted)*** Healthy (avg. age = 35): $\mu = 16.15 \pm 6.69, 27.28 \pm 25.72, 45.02 \pm 25.27$ kPa Healthy (avg. age = 60): $\mu = 16.08 \pm 11.85, 28.11 \pm 3.87, 37.26 \pm 11.87$ kPa After radio frequency neurotomy: $\mu = 14.44 \pm 6.62, 16.57 \pm 9.59, 20.07 \pm 10.96$ kPa After posterior lumbar fusion: $\mu = 9.81 \pm 3.75, 17.26 \pm 8.68, 21.85 \pm 13.83$ kPa **Thin fascia of tibialis anterior** $\mathrm{SWV} = 3.90 \pm 0.16$ m/s, $\mu = 16.12 \pm 0.44$ kPa
Wu 2020 [71]	Aixplorer SL10-2	ARF SSI	-	-	-	-	-	-	Large, elastic, isotropic medium ($E = 3\rho\,\mathrm{SWV}^2$)	*Min values corresponded to females* > 51 *years old and max values corresponded to males* 21 – 30 *years old, except for the medial patellar retinaculum where the trend was reversed* ***In vivo* leg muscles** $E = 7.60 \pm 0.59$ kPa – 35.75 ± 1.43 kPa ***In vivo* quadriceps tendon** $E = 47.22 \pm 1.38$ kPa – 63.50 ± 1.72 kPa ***In vivo* MCL** $E = 23.44 \pm 1.29$ kPa – 35.51 ± 1.41 kPa ***In vivo* LCL** $E = 64.22 \pm 2.65$ kPa – 90.92 ± 2.76 kPa ***In vivo* patellar tendon** $E = 49.60 \pm 1.45$ kPa – 73.26 ± 1.67 kPa ***In vivo* medial patellar retinaculum** $E = 13.00 \pm 0.60$ kPa – 22.20 ± 0.85 kPa ***In vivo* lateral patellar retinaculum** $E = 24.06 \pm 1.52$ kPa – 49.02 ± 1.18 kPa

Viscoelastic model applied to soft tissue or tissue-mimicking phantoms										
Cortes 2015 [41]	Ultrasonix L14-5/38	External shaker $f =$ 208 – 624 Hz	-	PWI 10 MHz	6.24	40	Phase-shift algorithm on RF using Fourier transforms	Median filter Directional filter Low-pass Butterworth filter SWV calculation using local frequency estimation method	Viscoelastic dispersion model (Voigt)	***In vivo* Achilles tendon** Healthy: $\mathrm{SWV} \approx 10 - 20\,\mathrm{m/s}$ (208 – 624 Hz), $\mu = 71.7 \pm 49.2\,\mathrm{kPa}$, $\eta = 64.6 \pm 13.3\,\mathrm{Pa\,s}$ Injured: $\mu = 105.5\,\mathrm{kPa}$, $\eta = 35.5\,\mathrm{Pa\,s}$ ***In vivo* hamstring tendon** Healthy: $\mu = 59.1\,\mathrm{kPa}$, $\eta = 18.4\,\mathrm{Pa\,s}$ Regrowing after it was used as graft: $\mu = 32.4\,\mathrm{kPa}$, $\eta = 8.9\,\mathrm{Pa\,s}$
Zhou 2018 [43]	Verasonics L11-5v	External shaker $f =$ 100 – 300 Hz	-	PWI 6.4 MHz	2	-	Correlation algorithm	TOF SWV calculation	Viscoelastic dispersion model (Maxwell, Voigt, SLS, spring-pot, and fractional Voigt)	**Tissue-mimicking phantom (CIRS)** Voigt: $\mu = 1.55\,\mathrm{kPa}$, $\eta = 5.68\,\mathrm{Pa\,s}$ Maxwell: $\mu = 7.87\,\mathrm{kPa}$, $\eta = 9.19\,\mathrm{Pa\,s}$ SLS: $\mu_0 = 1.62\,\mathrm{kPa}$, $\mu_1 = 88.00\,\mathrm{kPa}$, $\eta = 5.96\,\mathrm{Pa\,s}$ Spring-pot: $\mu_\alpha = 0.00\,\mathrm{kPa}$, $\alpha = 1.00\,\mathrm{Pa\,s}$ Fractional Voigt: $\mu_0 = 1.55\,\mathrm{kPa}$, $\mu_{alpha} = 0.01\,\mathrm{kPa}$, $\alpha = 1.00\,\mathrm{Pa\,s}$
Guided wave dispersion model applied to thin-layered structures										
Bernal 2011 [140]	Spherically focused transducer for ARF, single element transducer for tracking	ARF SWEI	3 MHz 200 µs	7.5 MHz	4	-	Cross-spectral correlation	TOF SWV calculation Guided wave dispersion analysis in Fourier domain For dispersion analysis: threshold filter removing signal with $< 7.5\,\%$ of maximum intensity (applied to wavenumber-frequency)	Lamb wave dispersion model	**Urethane tube phantom** $\mathrm{SWV} \approx 2.5 - 15\,\mathrm{m/s}$ (50 – 1900 Hz), $\mu = 187\,\mathrm{kPa}$ ***Ex vivo* porcine carotid artery** $\mathrm{SWV} \approx 2.5 - 7\,\mathrm{m/s}$ (50 – 1900 Hz), $\mu = 24 - 45\,\mathrm{kPa}$ at 10 – 100 mmHg
Widman 2015 [141]	Aixplorer SL15-4	ARF SSI	6 MHz 150 µs	PWI 7.5 MHz	8	-	Loupas 2D autocorrelator	Directional filter TOF SWV calculation Guided wave dispersion analysis in Fourier domain For dispersion analysis: threshold filter removing signal with $< 10\,\%$ of maximum intensity (applied to wavenumber-frequency) and bandpass filter (applied to phase velocity - frequency space)	Lamb wave dispersion model	**10 % PVA phantom** Mechanical testing, soft plaque: $\mu = 3.3 \pm 0.5\,\mathrm{kPa}$ Mechanical testing, hard plaque: $\mu = 98.3 \pm 3.4\,\mathrm{kPa}$ Large elastic model, soft plaque: $\mu = 5.2\,\mathrm{kPa}$ Large elastic model, hard plaque: $\mu = 26.8 \pm 0.3\,\mathrm{kPa}$ Lamb wave dispersion model, soft plaque: $\mu = 5.9 \pm 0.6\,\mathrm{kPa}$ Lamb wave dispersion model, hard plaque: $\mu = 106.2 \pm 17.2\,\mathrm{kPa}$
Helfenstein-Didier 2016 [29]	Aixplorer SL15-4	ARF SWEI	-	-	17	-	-	Guided wave dispersion analysis in Fourier domain	Dispersion model	***In vivo* Achilles tendon** 45° plantar flexion: $\mu = 118.01 \pm 67.88\,\mathrm{kPa}$ 35° plantar flexion: $\mu = 258.65 \pm 124.88\,\mathrm{kPa}$ 25° plantar flexion: $\mu = 509.14 \pm 148.51\,\mathrm{kPa}$
Maksuti 2016 [139]	Aixplorer SL15-4	ARF SSI	5 MHz 150 µs	PWI 7.5 MHz	8	-	Loupas 2D autocorrelator	TOF SWV calculation Guided wave dispersion analysis in Fourier domain For dispersion analysis: threshold filter removing signal with $< 10\,\%$ of maximum intensity (applied to wavenumber-frequency) and bandpass filter (applied to phase velocity - frequency space)	Lamb wave dispersion model	**10 % PVA arterial phantoms (hollow cylinder)** Mechanical testing: $\mu = 30.5 \pm 0.4\,\mathrm{kPa}$ Large elastic model: $\mu = 6.7\,\mathrm{kPa}$ Lamb wave dispersion model: $\mu = 30.6 \pm 3.2\,\mathrm{kPa}$
Li 2019 [28]	Verasonics L9-4	ARF SWEI	1000 cycles 6.5 MHz	PWI 6.5 MHz	10	-	Loupas 2D autocorrelator	TOF SWV calculation Dispersion analysis in Fourier domain	Lamb wave dispersion model	***In vivo* dermis of forearm** Large elastic model: $E = 20.8 \pm 4.4\,\mathrm{kPa}$ Lamb wave dispersion model: $E = 69.6 \pm 7.9\,\mathrm{kPa}$

Combined viscoelastic and Lamb wave dispersion model applied to thin-layered structures										
Nenadic 2011 [156]	Single element transducer	External shaker $f =$ 50 – 500 Hz	-	7.5 MHz	4	-	Cross-spectral correlation	TOF SWV estimation for each shaker frequency Guided wave dispersion analysis	Viscoelastic (Voigt) & Lamb wave dispersion model	**10% gelatin phantoms** $\mathrm{SWV} \approx 1 - 4\,\mathrm{m/s}$ (50 – 500 Hz), $\mu = 10\,\mathrm{kPa}$, $\eta = 4\,\mathrm{Pa\,s}$ ***Ex vivo* porcine spleen** $\mathrm{SWV} \approx 1 - 2.5\,\mathrm{m/s}$ (50 – 500 Hz), $\mu = 3.6\,\mathrm{kPa}$, $\eta = 2.8\,\mathrm{Pa\,s}$ ***Ex vivo* porcine myocardium** $\mathrm{SWV} \approx 2 - 6\,\mathrm{m/s}$ (50 – 500 Hz), $\mu = 11\,\mathrm{kPa}$, $\eta = 10\,\mathrm{Pa\,s}$
Urban 2013 [157]	Ultrasonics RP L9-4	External shaker $f =$ 50 – 400 Hz	-	-	2-2.5	-	Cross-spectral correlation	TOF SWV estimation for each shaker frequency Guided wave dispersion analysis	Viscoelastic (Voigt) & Lamb wave dispersion model	***In vivo* porcine myocardium** Diastole: $\mathrm{SWV} \approx 1 - 2.5\,\mathrm{m/s}$ (50 – 500 Hz), $\mu = 1.81 \pm 0.80\,\mathrm{kPa}$, $\eta = 2.76 \pm 0.56\,\mathrm{Pa\,s}$ Systole: $\mathrm{SWV} \approx 3 - 5\,\mathrm{m/s}$ (50 – 500 Hz), $\mu = 21.14 \pm 7.72\,\mathrm{kPa}$, $\eta = 4.16 \pm 4.32\,\mathrm{Pa\,s}$
Brum 2014 [30]	Aixplorer SL15-4	ARF SSI	8 MHz 150 µs	PWI	11 & 18	-	Correlation algorithm on RF data	Average filter across consecutive measurements Guided wave dispersion analysis in Fourier domain	Viscoelastic (Voigt) & Lamb wave dispersion model	***In vivo* Achilles tendon** Along fibres: $\mathrm{SWV} = 11.7 \pm 1.6\,\mathrm{m/s} - 15.5 \pm 2.0\,\mathrm{m/s}$ (300 – 700 Hz), $\mu = 920 \pm 330\,\mathrm{kPa}$ Across fibres: $\mathrm{SWV} = 2.85 \pm 0.49\,\mathrm{m/s} - 2.86 \pm 0.49\,\mathrm{m/s}$ (300 – 700 Hz), $\mu = 16.4 \pm 2.3\,\mathrm{kPa}$, $\eta = 3.09 \pm 0.92\,\mathrm{Pa\,s}$

ARF: acoustic radiation force
CPWC: coherent plane-wave compounding
CUSE: comb-push ultrasound shear elastography
IQ: in-phase and quadrature
PWI: plane wave imaging
RF: radio frequency
US: ultrasound
SSI: supersonic shear imaging
SWEI: shear wave elastography imaging
SWV: shear wave velocity
TOF: time-of-flight

the Achilles tendon demonstrate that the shear modulus can increase by around $3-5$ times from maximal plantar flexion to maximal dorsiflexion [29, 134, 158]. In the lumbar multifidus muscle of the back, shear moduli doubled when moving from a prone position to sitting up and tripled when sitting up with the arm lifted [154]. In the myocardium of a porcine heart, shear moduli increased more than tenfold from the diastole to systole phase [157]. This demonstrates that shear wave imaging can be used to estimate soft tissue loading during different states, which can be diagnostically insightful in itself. However, if the objective is to assess changes in ligament function due to, for example, activity, injury or ageing, it is crucial that shear wave imaging is performed with the same soft tissue loading conditions each time.

The tissue model used during post-processing is also important. The additional viscous material property obtained by using a viscoelastic dispersion model can provide further insight into the health and function of the tissue. Cortes et al. [41] demonstrated that Voigt viscosity drops by half for an injured Achilles or hamstring tendon. However, there is no evidence that considering viscous dispersion improves the elastic material property measurements. For the Achilles tendon during neutral ankle position, the shear elastic modulus of $\sim 70\,\mathrm{kPa}$ measured by Cortes et al. [41] with a Voigt viscoelastic model was only slightly outside the range of $\sim 80-240\,\mathrm{kPa}$ measured by studies using an elastic model. However, when considering the thin geometry of the tendon with a Lamb wave model, shear elastic modulus measurements were notably higher, with values around five times higher in tissue-mimicking phantoms [139, 141], three times higher in the dermis [28] and up to ten times higher in the Achilles tendon [30, 41, 138, 158].

Challenges in applying shear wave imaging to tendons and ligaments

The diagnostic value of measuring shear or Young's modulus of soft tissue using shear wave imaging is evident. It is furthermore reassuring that the observed relationship between modulus and tissue health is in line with previous observations based on mechanical tensile tests, which found that remodelling due to increased activity leads to increased stiffness [33], while ageing or injury causes tissue weakening with decreased

stiffness [32, 68]. However, the Young's modulus of tendons and ligaments measured by shear wave imaging are often three orders of magnitude lower than those measured during mechanical tensile testing. As was summarised in Table 2.1, the Young's modulus obtained from the stress-strain response of human collateral ligaments ranged between $94 - 626\,\mathrm{MPa}$, while Wu et al. [71] measured Young's moduli less than $100\,\mathrm{kPa}$ using shear wave imaging.

There are three factors that may contribute to this discrepancy between the material properties obtained from tensile testing and shear wave imaging. Firstly, as noted above, analysing shear wave propagation using an incorrect tissue model can lead to underestimation of the shear modulus. Most shear wave imaging implementations approximate soft tissue as a homogeneous and elastic medium. While this may be valid for larger tissues such as the liver or breast, it appears to be unsuitable for thin, viscoelastic structures like tendons and ligaments.

Another factor may be that the Young's moduli reported for tensile testing are usually calculated from the linear region of the stress-strain curve. However, Brandão et al. [159] have shown that the modulus measured using shear wave imaging represents the instantaneous elasticity of the tissue. For tendons and ligaments, the instantaneous elastic modulus (i.e., the gradient of the stress-strain curve) is much lower during initial loading and gradually increases throughout the toe-region as the fibres uncrimp. This may also explain the increase in measured shear modulus with tissue loading observed by previous studies [134, 144, 157, 158]. However, even after considering this variation in modulus with loading, simultaneous ultrasound and tensile testing by Brandão et al. still demonstrated a 5- to 20-fold difference between the measured instantaneous moduli in the Achilles tendon. The behaviour is likely to be similar in the collateral ligaments: the initial elastic modulus of $\sim 1\,\mathrm{MPa}$ reported by Ristaniemi et al. [73] for bovine LCLs is still ten times higher than the maximum Young's modulus of $\sim 100\,\mathrm{kPa}$ measured for the human LCL with shear wave imaging [71].

Lastly, while soft tissue can normally be assumed to be isotropic and incompressible, tendons and ligaments display highly anisotropic behaviour due to their complex

hierarchical structure, thus violating the approximation of $E \approx 3\mu$, which is used to obtain Young's modulus from the shear modulus. Instead, tendons and ligaments are more accurately represented by a transversely isotropic model. Royer et al. [160] were able to show that, for this type of model, the approximation of $E \approx 3\mu$ still provides a good estimate for the transverse Young's modulus when using shear waves propagating perpendicular to the fibre direction; however, the shear modulus obtained from waves propagating parallel to the fibre direction is not enough to determine the longitudinal Young's modulus.

2.2.5 Speckle tracking

The evolution of speckle tracking

The speckle tracking technique is used to measure larger tissue deformations. In the first implementations of this technique, tissue motion tracking relied on manual identification of anatomical landmarks in each frame of the ultrasound cine acquisition, based on the unique speckle pattern of the landmarks. For example, in the field of orthopaedics, Maganaris and Paul first demonstrated this approach in the 1990s to measure muscle-tendon mechanics [161].

Automated speckle tracking algorithms soon followed, with displacement fields calculated from the phase or cross correlation of the ultrasound data [26, 162, 163]. In the first algorithms, tissue tracking was constrained to the axial dimension with 1D correlation of the ultrasound data [26, 114, 162]. In fact, even nowadays, most commercial speckle tracking systems are a one dimensional implementation and only output the axial displacement or strain map [164]. This is due to lack of phase information and low resolution in the lateral direction: while axial resolution is only limited by the transducer and sampling frequency, providing a large number of axial data points, lateral resolution is limited by the spacing of transducer elements. Hence, accurately tracking the displacement of the speckle pattern in the lateral direction is much more challenging [109, 164, 165].

However, many applications benefit from motion tracking in the lateral dimension, for example when the primary strain is in the lateral direction (e.g., collateral ligaments [49, 166]), when shear strains need to be calculated (e.g., to help distinguish between different tumours [167]) or when motion needs to be represented in a different coordinate system (e.g., radial and circumferential in cardiovascular imaging [168–170]). Hence, recent research has focused on developing techniques that will allow accurate determination of displacements in two and even three dimensions [167, 168, 171].

Core principles of speckle tracking

Ultrasound speckle tracking follows the main steps that were outlined in Figure 2.5. The tissue is subjected to loading from an excitation source, and the resulting deformation is tracked using a series of ultrasound acquisitions [172]. Local strains can also be computed by taking the gradient of the measured displacement field [172–174]. In many applications, the strain field is subsequently used to determine relative tissue stiffness in the field of view: assuming that the entire region is subjected to equal loading, stiffer tissue will deform less than softer tissue [172, 174].

The excitation source can fall into one of two categories: external or internal physiological [169, 173]. External refers to loading applied to the outside of the body, for example by pushing the transducer down on the tissue during the strain imaging procedure [173]. Alternatively, tissue deformation due to an internal physiological strain source can be measured, such as contraction of cardiac muscle tissue [170, 173] or, as will be used in this project, the straining of the collateral ligaments due to the natural loading during knee movement [49, 51, 166].

At the core of speckle tracking techniques is a displacement calculation algorithm, typically based on block-matching or non-rigid image registration. This algorithm tracks the unique speckle patterns in ultrasound images from frame to frame, enabling the measurement of tissue motion throughout the entire loading cycle. The speckles arise naturally in the background of an ultrasound image due to the interference of reflections from randomly distributed acoustic scatterers, thus allowing differentiation between different areas of the

tissue [172, 175].

During block-matching, the ultrasound image is divided into small kernels, each encompassing a small area of the unique speckle pattern. These reference kernels are then searched for in a larger kernel in the next frame, and the displacement that provides the best match based on a similarity metric, e.g. normalised cross-correlation, is found [26, 109, 114].

Non-rigid image registration techniques are based on optical flow algorithms, which assume that the pixel intensity remains constant during motion. These algorithms compute the displacement of each pixel by aligning it with the pixel of most similar intensity in the next frame. The overall displacement field is determined through an optimisation process, where the to-be-minimised objective function consists of a cost term and a regularisation function. The cost term represents the intensity difference between the two frames after the first frame has been deformed by the displacement field. The regularisation function penalises large strains or discontinuities in the displacement field, ensuring that non-rigid deformations are captured with local variations, while maintaining an adjustable level of smoothness [176–178].

Speckle tracking applications

Speckle tracking imaging is most commonly used to screen for stiff pathological tissue (e.g., tumours or fibrosis) in the breast [26, 27, 179–182], liver [23, 179, 183, 184], thyroid [185, 186] or prostate [187]. In these applications, tissue motion is induced through external compression, such as pressing the transducer against the tissue during imaging. Typically, a 1D speckle tracking algorithm suffices, since the tissue principally deforms in the axial direction. Relative stiffness maps can subsequently be constructed from the tissue motion, since stiff pathological tissue will deform less than the surrounding tissue.

Speckle tracking has also been investigated as a method for measuring the deformation or strain of orthopaedic soft tissues in response to physiological loading (Table 2.5). While the primary research focus has been on the Achilles tendon [50, 88–95, 177, 188–195], it

TABLE 2.5 *Ex vivo* and *in vivo* speckle tracking implementations to measure deformation or strain in tendons and ligaments.

Reference	US system & transducer	Displacement calculation method	Regularisation method	Data type	Tissue	Tissue excitation method	Main findings
Farron 2009 [196]	Sonoline Antares VFX13-5	Block-matching	Linear least square fit to 1D displacement results	RF	*In vivo* healthy tibialis anterior tendon	Electrical muscle stimulation with preloads of $0-50\,\%$ of MVIC	Peak tendon strains due to electrical stimulation: $0.06-0.80\,\%$
Korstanje 2010 [197]	Philips iE33 L9-3	Block-matching	-	B-mode	*Ex vivo* porcine, *ex vivo* human and *in vivo* flexor digitorum superficialis tendon	*Ex vivo*: elongation in materials testing machine of $5-15\,\mathrm{mm}$ at $4-16\,\mathrm{mm/s}$ *In vivo*: extension-flexion of fingers	*Ex vivo* error in tracked displacements: $1.0-1.3\,\%$ *In vivo* error in tracked displacements: $1.6\,\%$
Chernak Slane 2012 [198]	Ultrasonix L14-5	Block-matching	Median filter	RF	*Ex vivo* porcine flexor tendon	Cyclic stretching in materials testing machine ($4\,\%$ strain at 0.5 Hz)	Correlation of longitudinal US and crosshead displacements: $R^2 > 0.8$ US transverse strains: -2.5 to $-8.5\,\%$
Slane 2014 [50]	Ultrasonix L14-5	Block-matching	Median filter Low-order polynomial surface fit	RF B-mode	*Ex vivo* porcine flexor tendon	Cyclic stretching in materials testing machine ($4\,\%$ strain at 0.5 Hz)	Correlation of US and DIC displacements: $R^2 = 0.98 \pm 0.03$ and 0.92 ± 0.16 for RF and B-mode data, respectively Correlation of US and DIC strains: $R^2 = 0.77 \pm 0.26$ and 0.63 ± 0.31 for RF and B-mode data, respectively Average difference between US and DIC strains: $-0.4\,\%$ and $-1.1\,\%$ for RF and B-mode data, respectively
Slane 2014 [199]	-	Block-matching	2^{nd} order polynomial surface fit	RF	*In vivo* healthy Achilles tendon	$0-30^\circ$ plantar flexion at 0.5 Hz with 30° and 90° knee flexion angle (passive and with eccentric loading)	Deep fibres of the Achilles tendon displaced more than superficial fibres (on average $0.9-2.6\,\mathrm{mm}$ more). Displacements decreased with eccentric loading in all tendon regions, except for the superficial tendon in a flexed knee posture. Displacements increased with more extended knee posture.
Franz 2015 [188]	Ultrasonix L14-5	Block-matching	Median filter	RF	*In vivo* healthy Achilles tendon	Walking at $0.75,\ 1.00$ and $1.25\,\mathrm{m/s}$	Achilles tendon experienced non-uniform deformation, with $16-29\,\%$ higher peak elongation in superficial fibres compared to deep fibres during walking. Non-uniformity was more pronounced with faster walking speed.
Franz 2015 [95]	Ultrasonix L14-5	Block-matching	-	RF	*In vivo* healthy Achilles tendon	Walking at $0.75,\ 1.00$ and $1.25\,\mathrm{m/s}$ Passive plantar flexion at 0.5 Hz with 0° and 90° knee flexion angle	Non-uniformity of Achilles tendon deformation and strain was not significantly different for young and old adults at slow walking speeds. However, at a walking speed of $1.25\,\mathrm{m/s}$, the tendons of old adults had $41\,\%$ less deformation and strain variations.
Slane 2015 [94]	Ultrasonix L14-5	Block-matching	2^{nd} order polynomial surface fit	RF	*In vivo* healthy Achilles tendon	$0-30^\circ$ plantar flexion with eccentric loading	Deep fibres of the Achilles tendon displaced significantly more than superficial fibres. Overall displacement throughout the tendon decreased with eccentric loading, but increased with ageing. However, ageing reduced non-uniformity.
Chimenti 2016 [177]	Ultrasonix L9-4	NRIR	Regularisation performed within NRIR algorithm	RF	*In vivo* healthy Achilles tendon	Heel lowering Partial squat Heel lowering & partial squat	Compressive strains across the fibres of the Achilles tendon was higher in deep fibres compared to superficial fibres. The largest compressive strains occurred during combined heel lowering and partial squat ($-20.7 \pm 8.1\,\%$).
Chimenti 2017 [189]	Ultrasonix L9-4	NRIR	-	-	*In vivo* Achilles tendon with insertional Achilles tendinopathy (IAT) and healthy control group	Heel lowering Partial squat	Longitudinal tensile strains ranged from $1.36\,\%$ in the deep fibres of tendinopathic tendons during heel lowering to $10.4\,\%$ in the deep fibres of healthy tendons during partial squats. Transverse compressive strains ranged from $-4.90\,\%$ in the superficial fibres of tendinopathic tendons during heel lowering to $-20.1\,\%$ in the deep fibres of healthy tendons during partial squats.

Bogaerts 2017 [190]	Ultrasonix and Vevo 2100 L14-5 and MS250	NRIR	Regularisation performed within NRIR algorithm	B-mode	*In vivo* healthy Achilles tendon	MVIC at neutral ankle position Passive ankle flexion from 10° plantar flexion to 10° dorsiflexion	Achilles tendon experienced non-uniform deformation/strain, with higher displacements in the deep fibres (passive flexion: $3.03\,\mathrm{mm}$; MVIC: $2.59\,\mathrm{mm}$) and higher strains in the superficial fibres (passive flexion: $0.33\,\%$; MVIC: $0.29\,\%$). Intra-day reliability: ICC $= 0.86$ Inter-day reliability: ICC $= 0.72$
Slane 2017 [51]	Ultrasonix L14-5	Block-matching	Median filter Low-order polynomial surface fit	RF	*Ex vivo* healthy MCL *Ex vivo* healthy LCL	10 Nm varus (LCL) / valgus (MCL)	Current implementation of the speckle tracking algorithm led to strain measurements with large standard deviations and, for the MCL, unexpected negative strains during valgus loading. Average US strains: 1.2 ± 3.9 and $= -3.6 \pm 5.4$ for LCL and MCL, respectively
Beyer 2018 [93]	HI Vision Ascendus	Block-matching	-	B-mode	*In vivo* surgically treated Achilles tendon rupture and healthy contralateral	Heel-raises (20° plantar flexion) with 0°, 40° and 100° knee flexion angle	Deep fibres of the Achilles tendon displaced significantly more than superficial fibres in the healthy tendon, but not in the surgically repaired Achilles tendon. This displacement difference was significantly greater when performing heel rises with the knee flexed 100° compared to 40°.
Clark 2018 [191]	Ultrasonix L14-5	Block-matching	2^{nd} order polynomial surface fit	RF	*In vivo* healthy Achilles tendon	MVIC at different ankle joint angles (10° dorsiflexion to 30° plantar flexion	Deep fibres of the Achilles tendon displaced $51\,\%$ more than superficial fibres. Tendon displacement was correlated with gastrocnemius and soleus muscle shortening.
Gijsbertse 2018 [49]	Philips iE33 and Visualsonics 2100 L11-3 and MS250s	Block-matching	Median filter	RF	*Ex vivo* LCL	Cyclic stretching in materials testing machine ($5\,\%$ strain at 1 Hz)	Correlation of US and DIC strains: $R^2 = 0.93$ and 0.71 for transducer frequency of 20 MHz and 7 MHz, respectively Average difference between US and DIC strains: $-0.49\,\%$ and $-0.67\,\%$ for transducer frequency of 7 MHz and 20 MHz, respectively
Slane 2018 [200]	Ultrasonix L14-5	Block-matching	-	RF	*In vivo* healthy patellar tendon	Knee flexion 50 – 90°	Patellar tendon experienced significant superficial-to-deep non-uniformity, with males exhibiting more non-uniformity than females.
Slane 2018 [201]	Ultrasonix L14-5	Block-matching	-	RF	*In vivo* healthy patellar tendon	Knee flexion 50 – 90°	The distal patellar tendon elongated ($5.6 \pm 5.7\,\%$) while the proximal region shortened ($-1.7 \pm 3.1\,\%$) during knee flexion. In the distal tendon, displacement was mostly uniform, while the deep and superficial fibres of the proximal tendon displaced in opposite directions (distal vs proximal).
Schrier 2019 [202]	Philips iE33 15L7	Block-matching	-	-	*In vivo* superficial flexor digitorum superficialis tendon (FDS) and subsynovial connective tissue, in patients with carpal tunnel syndrome (CTS) and healthy control group	Extension-flexion of third digit	Control group US displacements: $6.8 \pm 2.4\,\mathrm{cm}$ and $1.5 \pm 0.7\,\mathrm{cm}$ for FDS and SSCT, respectively CTS group US displacements: $8.4 \pm 2.5\,\mathrm{cm}$ and $2.1 \pm 0.8\,\mathrm{cm}$ for FDS and SSCT, respectively Inter-rater reliability: ICC $= 0.74 – 0.95$ and $0.66 – 0.82$ for the control and CTS group, respectively Intra-rater reliability: ICC $= 0.87 – 0.94$ and $0.81 – 0.98$ for the control and CTS group, respectively
Stenroth 2019 [192]	Ultrasonix L14-5	Block-matching	-	RF	*In vivo* healthy Achilles tendon	MVIC	Deep (anterior) fibres displaced more than superficial (posterior) fibres, and medial fibres displaced more than lateral fibres, with the highest displacements of $\sim 7\,\mathrm{mm}$ occurring in the anteromedial region
Clark 2020 [88]	Ultrasonix L14-5	Block-matching	2^{nd} order polynomial surface fit	RF	*In vivo* healthy Achilles tendon	MVIC at different ankle joint angles ($0 – 30^\circ$ plantar flexion	Achilles tendon non-uniformity decreased with age. In young adults, the soleus subtendon displaced $51\,\%$ more than the gastrocnemius subtendon. The difference reduced to $31\,\%$ in older adults. This may be due to changes in muscle contractile behaviour, i.e. smaller differences between gastrocnemius and soleus peak shortening during isometric force generation.
Couppé 2020 [89]	HI Vision Ascendus L14-6	Block-matching	-	B-mode	*In vivo* Achilles tendon with unilateral tendinopathy and healthy contralateral	Heel raises in standing and seated position ($0 – 20^\circ$ plantar flexion)	Superficial fibres of the Achilles tendon experienced less displacement than deep fibres in all conditions except for standing on the tendinopathic leg. In general, the difference in displacement was lower in the tendinopathic Achilles tendon ($0.52 \pm 0.16\,\mathrm{mm}$ vs. $1.02 \pm 0.18\,\mathrm{mm}$).

Clark 2021 [90]	Ultrasonix L14-5	Block-matching	Median filter 2^{nd} order polynomial surface fit	RF	*In vivo* healthy Achilles tendon	Walking at $0.8,\ 1.0$ and $1.2\,\mathrm{m/s}$ Walking at $1.2\,\mathrm{m/s}$ with a horizontal impeding/aiding force of $5\,\%$ body weight	Achilles tendon non-uniformity increased with walking speed and with impeding horizontal force, but decreased with age. Deep fibres displaced more than superficial fibres, with differences lying between $1.14 \pm 0.37\,\mathrm{mm}$ (subjects aged $65-80$ years walking at $0.8\,\mathrm{m/s}$) and $4.38 \pm 0.81\,\mathrm{mm}$ (subjects aged $18-35$ years walking at $1.2\,\mathrm{m/s}$ with impeding force).
Dandois 2021 [166]	Ultrasonix	Block-matching	Median filter	RF	*Ex vivo* healthy MCL *Ex vivo* healthy LCL (*in situ* in cadaveric knee)	Knee varus (LCL) / valgus (MCL) motion applied by dynamometer	Correlation of US and DIC strains: $R^2 = 0.97 \pm 0.03$ and 0.63 ± 0.54 for LCL and MCL, respectively Average absolute difference between US and DIC strains: 0.37 ± 0.16 and $= 0.38 \pm 0.11$ for LCL and MCL, respectively Average US strains: $2.99 \pm 1.16\,\%$ and $= 1.65 \pm 1.69\,\%$ for LCL and MCL, respectively
Khair 2021 [91]	UST-5411	Block-matching	-	B-mode	*In vivo* ruptured and healthy contralateral Achilles tendon	Isometric ramp contraction up to $30\,\%$ of uninjured limb's MVIC	Peak relative displacement of different anteroposterior points in the Achilles tendon was higher in uninjured tendons ($1.29 \pm 0.87\,\mathrm{mm}$) compared to injured tendons ($0.69 \pm 0.68\,\mathrm{mm}$).
Lehr 2021 [193]	Ultrasonix L14-5	Block-matching	-	RF	*In vivo* healthy Achilles tendon	MVIC at different ankle joint angles (-20° dorsiflexion to 20° plantar flexion) with electrical muscle stimulation of the medial gastrocnemius and soleus	Stimulation of the soleus resulted in $49\,\%$ larger tendon non-uniformity compared to stimulation of the medial gastrocnemius. Peak tendon non-uniformity decreased by $61\,\%$ from plantar flexion to dorsiflexion.
Aggouras 2022 [194]	Ultrasonix L9-4	NRIR	-	-	*In vivo* Achilles tendon with insertional Achilles tendinopathy (IAT)	Passive ankle flexion	Impingement could be detected based on changes in tendon curvature. Increased tendon thickness due to insertional Achilles tendinopathy caused impingement across a larger range of ankle angles.
Khair 2022 [92]	Aloka Prosound Alpha 10 UST-5411	Block-matching	Low-order polynomial surface fit	B-mode	*In vivo* ruptured and healthy contralateral Achilles tendon	Isometric ramp contraction up to $30\,\%$ of uninjured limb's MVIC with electrical muscle stimulation of the medial and lateral gastrocnemius	Achilles tendon non-uniformity was higher in uninjured tendons compared with injured tendons.
Mora 2022 [195]	Vevo 3100	NRIR	-	RF	*Ex vivo* murine Achilles tendon	Passive ankle dorsiflexion	Achilles tendon experienced increasing compressive strains across the fibres and increasing tensile strains along the fibres ($\sim 5\,\%$ after 20° of flexion) during ankle dorsiflexion. Transverse compressive strains were significantly higher at the insertion compared to the midsubstance ($\sim -12\,\%$ vs $\sim -5\,\%$ after 20° of flexion). Test-retest reliability across fibres: $R = 0.97$ Test-retest reliability along fibres: $R = 0.79$

MVIC: maximum voluntary isometric contraction

NRIR: non-rigid image registration

RF: radio frequency

US: ultrasound

has also been applied to muscle [26, 171], tibialis anterior tendons [196], flexor digitorum superficialis tendons [197, 202], patellar tendons [200, 201] and the collateral ligaments [49, 51, 166].

In most applications, the applied physiological loading resulted in tensile strains along fibres and compressive strains across the fibres. Reported longitudinal strains varied across different tissues, with maximum values of $0.8\,\%$ in the tibialis anterior tendon during electrical muscle stimulation [196], $\sim 3\,\%$ in the collateral ligaments during varus-valgus knee motion [166], $\sim 6\,\%$ in the distal patellar tendon during knee flexion [201], and $\sim 10\,\%$ in the Achilles tendon during partial squats [189]. Interestingly, while distal fibres of the patellar tendon lengthened during knee flexion, the proximal fibres shortened by $-1.7\,\%$ during the same measurements [201]. Compressive transverse strains were as low as approximately $-20\,\%$ in the Achilles tendon during simultaneous heel lowering and partial squatting [177].

Healthy Achilles and patellar tendons are characterised by a non-uniform strain or displacement behaviour. In the Achilles tendon, longitudinal strains are higher in superficial fibres [188, 190], while longitudinal displacements and transverse strains are higher in deep fibres [88, 89, 93, 94, 177, 190–192, 199]. During knee flexion, the distal patellar tendon elongates with uniform displacement across its fibres. In contrast, the proximal patellar tendon shortens, and its deep and superficial fibres displace in opposite directions [200, 201].

Changes in the strain or displacement behaviour can indicate tissue damage or weakening. For example, in the Achilles tendon, non-uniformity was found to decrease with age and injury [88–95]. Speckle tracking can also detect changes in the tendon curvature during loading, which can indicate bone impingement [194].

Challenges in applying speckle tracking to tendons and ligaments

As with shear wave imaging, applying speckle tracking to tendons and ligaments presents several challenges compared to larger, more homogeneous soft tissues. Consequently,

commercially available speckle tracking systems have been found to be unreliable for these tissues [197, 203].

Firstly, commercial systems are often based on block-matching algorithms where the size of the kernels has been optimised to the speckle pattern of larger, homogeneous tissue. The striated pattern of tendons and ligaments requires more elongated blocks that are sized to the shape and thickness of the fascicles of connective tissue [197].

Secondly, when measuring tendon or ligament motion during physiological loading, most of the tissue displacement is in the lateral direction of the ultrasound images. Due to the lower resolution and lack of phase information in this direction, speckle correlation is more challenging for this type of motion [173, 198, 203].

Furthermore, since strain is not an inherent mechanical property but rather a functional assessment of the tissue under specific loading scenarios, results can be highly dependent on the measurement conditions. When using quasi-static external excitation, such as compression applied to the soft tissue by the clinician, it is challenging to control the stress applied to the tissue and, thus, the resulting strain map usually only provides a qualitative assessment of tissue stiffness. For dynamic physiological motion, such as measuring collateral ligament strain during knee movement, it is essential that the same movement is performed for each measurement. This consistency is crucial for comparing data across different patients and time points [51].

Dynamic movements also introduce the additional challenge of maintaining proper alignment between the transducer and the tissue of interest. As tendons and ligaments shift relative to the skin during joint movement, manually keeping the transducer over the tissue is difficult. Out-of-plane movements can lead to the capture of different structures with varying strain behaviour, resulting in measurements that represent a combination of multiple tissues. Additionally, significant out-of-plane movement between frames can lead to rapidly changing speckle patterns that cannot be tracked accurately [51, 203, 204].

Despite these challenges, speckle tracking has already been demonstrated for large energy-storing tendons, such as the Achilles or patellar tendon. However, the above

challenges are exacerbated when imaging the collateral ligaments: (1) their smaller geometry makes them more difficult to identify on ultrasound images, (2) the way they stretch around the bone and closeness to the skin leads to an uneven imaging surface, (3) the complex wrapping behaviour results in non-uniform strain behaviour within the ligament and, lastly, (4) to capture notable changes in strains, a large dynamic range of motion, such as knee extension-flexion, is required, making the measurements more susceptible to out-of-plane motion due to the difficulty of keeping the transducer aligned to the ligaments throughout the motion [51, 166].

2.3 Conclusion

In summary, this literature review gave an overview of how the hierarchical anatomy and biochemical composition of tendons and ligaments leads to a complex mechanical behaviour. Changes in the mechanical properties can indicate a functional change or damage. Specifically, review of the literature revealed the following relationships:

- Elastic modulus can increase due to tissue remodelling after an increase in activity, while injury, prolonged inactivity or ageing can cause a drop in stiffness.
- Viscosity and hysteresis decreases with injury or stretching.
- The strain behaviour changes with injury, age and, in the collateral ligaments, after knee replacement surgery.

However, existing methods to assess *in vivo* ligament or tendon function are either imprecise, e.g. palpation or joint laxity tests, or rely on ionising imaging modalities, such as fluoroscopy-based strain measurements. Since ultrasound is one of the least expensive and most widely available imaging modalities, quantitative ultrasound techniques, such as shear wave imaging and speckle tracking, are an attractive alternative. These techniques can measure the viscoelastic properties, i.e. modulus and viscosity, and strain behaviour of soft tissue, which, as outlined above, could provide valuable insights into the function of tendons and ligaments. However, while these techniques have already been applied to large, homogeneous soft tissues, obtaining reliable measurements in connective tissue is more challenging, especially in very thin ligaments with complex deformation behaviour.

03

Shear Wave Imaging Implementation

3.1 Introduction **58**

3.2 Shear wave generation and ultrasound acquisition sequences **60**

3.3 Post-processing algorithms **65**

3.4 Discussion **83**

List of Abbreviations

ARF	Acoustic radiation force
IQ	In-phase and quadrature
PRF	Pulse repetition frequency
PWI	Plane wave imaging
RF	Radio frequency
RANSAC	Random sample consensus
SNR	Signal-to-noise ratio
SWEI	Shear wave elastography imaging
TOF	Time-of-flight

3.1 Introduction

Soft tissue material properties are an important marker of tissue health and function [205], and ultrasound shear wave imaging has emerged as a powerful, non-invasive tool that can quantitatively measure these properties [120]. In clinical practice, this technique is most commonly used to detect pathological tissue changes, such as fibrosis or tumours, in the liver [20–22], muscle and breast [24, 25].

Commercial implementations of shear wave imaging have been predominantly developed with the assumption that tissues are large, linearly elastic, and homogeneous, relying on simplified models that directly calculate the elastic modulus from shear wave velocities [139]. However, this approach overlooks the complex, heterogeneous and viscoelastic nature of most soft tissues [206], leading to potential inaccuracies.

Applying a simplified elastic model to viscoelastic tissue has two consequences. Firstly, neglecting viscous contributions can cause bias in the elastic moduli measurements [207]. Secondly, the diagnostic value of the viscous component is lost: in the liver, viscosity has been found to be an important differentiator of fibrosis or steatosis disease state, as well as benign or malignant tumours [85, 208–211]. In tendons, changes in viscosity can signal the presence of injury [41].

In addition to the intrinsic material properties of the tissue, the geometry of the tissue itself plays a pivotal role in shear wave propagation. Many clinically relevant applications in a wide range of fields involve thin tissue structures, such as tendons and ligaments in

orthopaedics [30, 41], the walls of the heart and blood vessels in cardiology [140, 156], skin in dermatology [28, 137, 142], and the cornea or crystalline lens in optometry [151, 212, 213]. The thin geometry of these tissues can lead to guided shear wave propagation, where the wave interacts with tissue boundaries, creating complex wave patterns [139]. Conventional shear wave imaging will measure the velocity of the guided wave, which is often much slower than the underlying shear wave velocity. Failure to account for this will result in inaccurate measures of material properties.

Given these complexities, it is essential to accurately model shear wave propagation by considering both viscoelasticity and the influence of tissue geometry. Viscoelastic models have already been used for tissue-mimicking phantoms [43], the liver [85, 210, 214], the kidney [214], and the Achilles tendon [41]. Guided wave models have been applied to tissue-mimicking phantoms [139, 141], the skin [28], the bladder wall [215], the carotid artery [140, 216], the cornea [212], and the Achilles tendon [29]. However, the simultaneous consideration of both effects has only been addressed in a limited number of studies by Brum et al. (Achilles tendon) [30], and by Urban and Nenadic et al. [156, 157] (cardiac applications).

This chapter aims to provide a comprehensive overview of the most suitable post-processing methods for different types of tissues. As the models become more sophisticated to account for viscosity and thin tissue geometry, they also become more computationally demanding. Therefore, to facilitate their broader application, this chapter emphasises practical guidance on implementing these models using common Matlab functions, making these advanced techniques more accessible to researchers new to the field.

3.2 Shear wave generation and ultrasound acquisition sequences

Throughout this project, shear waves were generated using either an acoustic radiation force (ARF) emitted by the ultrasound probe itself or by using an external shaker. The propagation of the shear wave through phantom samples or ligamentous soft tissue was subsequently captured using ultrasound plane wave imaging (PWI). All ultrasound sequences were implemented on a Verasonics Vantage 128 research ultrasound system (Verasonics Inc., Kirkland, WA, USA).

3.2.1 Acoustic radiation force (ARF)

The ARF-based shear wave imaging procedure followed the shear wave elastography imaging (SWEI) scheme by Sarvazyan et al. [120] and Nightingale et al. [121], i.e. shear waves were generated using a single focused push beam of extended duration (Figure 3.1). A broad range of transmission settings have been used in the literature for producing the push beam, and those used for this work fell within these ranges (Table 3.1).

When designing the transmission protocol, it should be noted that stronger shear waves with a higher signal-to-noise ratio (SNR) can be obtained when using settings that produce high acoustic pressures with strongly focused beams. However, pressures that are too high can cause structural damage due to cavitation within the tissue (i.e., formation and bursting

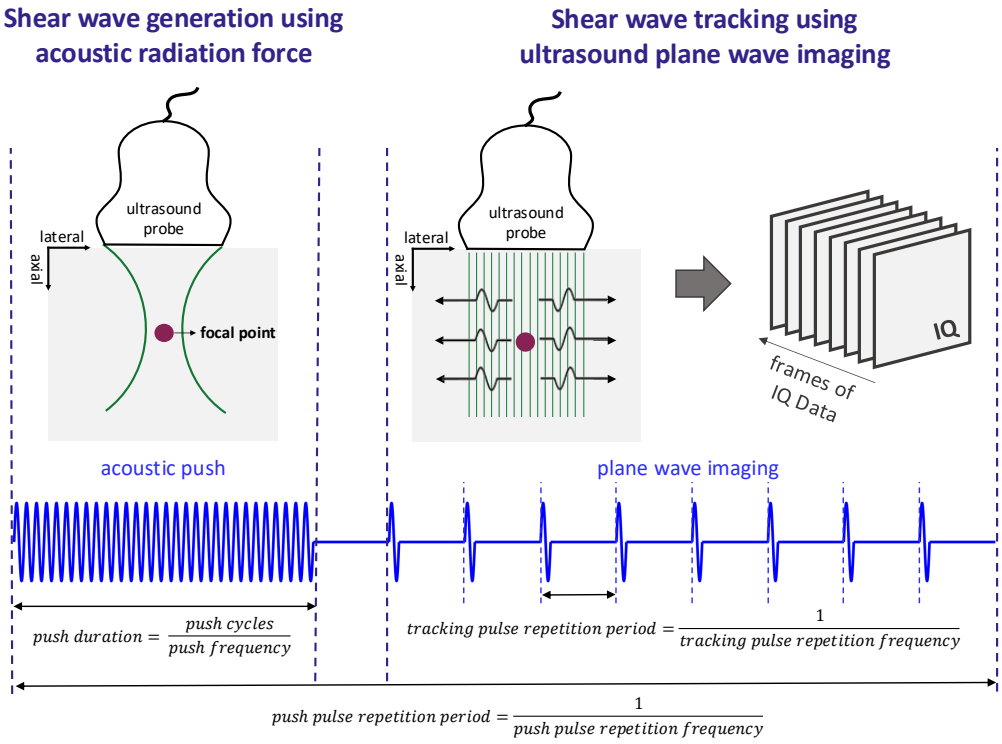


FIGURE 3.1 Shear wave generation and tracking sequences when using an acoustic radiation force (ARF) push.

TABLE 3.1 Parameters for generating shear waves with a single push beam ARF. The Matlab structures through which these parameters are defined in the Verasonics script are indicated in the second column.

Parameter	Verasonics Matlab structure	Values used in literature	Selected Values
Push pulse repetition period	`SeqControl (timeToNextEB)`	2 Hz [150]	2 Hz
Push cycles	`TW.Parameters`	400 – 1000 cycles [86, 112, 144, 146, 149, 152]	1000 cycles
Transducer push frequency	`TW.Parameters`	3.1 – 7.8 MHz [86, 112, 139, 141, 144, 146, 149, 151, 152, 217]	7.8 MHz
Push duration	`TW.Parameters`	96 – 192 µs [86, 108, 112, 139, 141, 144, 146, 149, 151, 152, 217]	128 µs
Transducer push elements	`TX.pushElements`	32 – 110 elements [86, 108, 144, 146, 151, 152]	32 elements
Focal depth	`TX.focus`	14.8 – 15.4 mm [144, 146, 149]	Using the real-time ultrasound feed, the focal depth was positioned in the centre of the specimen.

of bubbles in the tissue) as well as thermal damage. Therefore, for *in vivo* applications, the right balance needs to be found, with the ARF acoustic pressures high enough to generate visible shear waves that can be tracked, but without exceeding the recommended safety limits [218, 219]. Measurement of the safety indices is discussed in more detail in Chapter 5: Ultrasound Safety.

The push frequency was set to the transducer centre frequency in order to maximise the transmission amplitude, resulting in the most efficient transfer of ARF to the tissue [108, 150].

3.2.2 External shaker

Shear waves were also generated using a mini-shaker (Type 4810, Bruel & Kjaer, Norcross, GA) that has a vibrating element which, when in contact with the sample or the skin near the soft tissue of interest, can generate continuous shear waves at controlled frequencies between $0 - 18$ kHz (Figure 3.2).

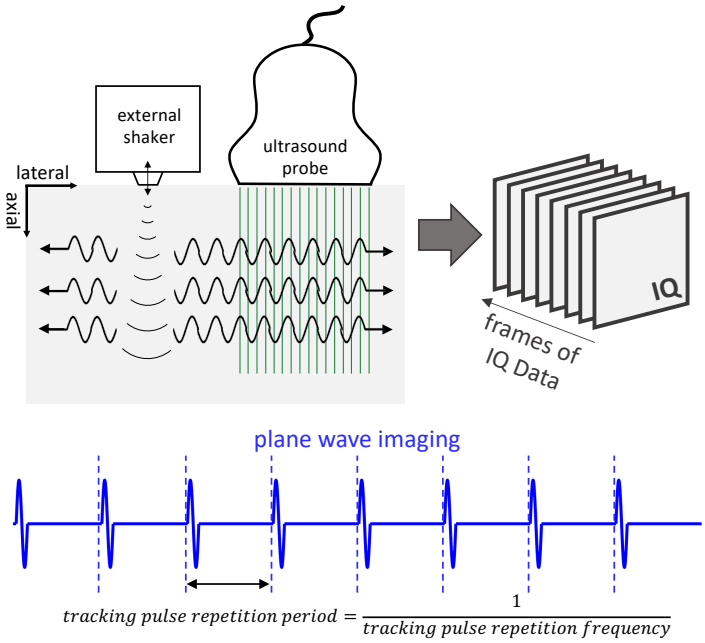


FIGURE 3.2 Shear wave generation and tracking sequences when using an external shaker.

3.2.3 Plane wave imaging (PWI)

An ultrafast PWI sequence was implemented to capture the rapid propagation of the shear wave across the field of view.

Table 3.2 summarises how PWI has previously been implemented to track shear waves, as well as the settings used in this project.

The pulse repetition frequency (PRF) was initially set to $10\,\mathrm{kHz}$ for the phantom samples. However, this PRF was found to be too low for the ligamentous specimen, since the shear wave velocities for these were higher (SWV $\approx 5.5 - 13\,\mathrm{m/s}$) than in the agar phantom specimen (SWV $\approx 2.5 - 5.5\,\mathrm{m/s}$). Due to attenuation, the shear wave is best tracked in the first $10\,\mathrm{mm}$ of propagation before the SNR becomes too low. Thus, for shear wave velocities over $10\,\mathrm{m/s}$, a PRF of $10\,\mathrm{kHz}$ results in fewer than 10 frames during which the shear wave is visible for tracking.

Therefore, for the experiments on ligaments, the acquisition sequence was optimised to maximise the PRF of the Verasonics system. The main limiting factor was found to be the imaging depth [105]: ultrasound images are created by transmitting ultrasound waves and then waiting for their reflections to return to the transducer elements. Reflections

TABLE 3.2 Parameters for plane wave tracking of the shear wave and the Verasonics beamforming procedure. The Matlab structures through which these parameters are defined in the Verasonics script are indicated in the second column.

Parameter	Verasonics Matlab structure	Values used in literature	Selected Values
Tracking pulse repetition frequency (PRF)	`SeqControl (timeToNextAcq)`	3 – 20 kHz [86, 112, 139, 141, 144, 146, 149, 151, 152]	10 – 15 kHz
Transducer tracking frequency	`TW.Parameters`	5 – 7.5 MHz [43, 139, 141, 144, 146, 148, 149, 151]	7.8 MHz
Transducer tracking elements	`TX.Apod`	-	128 elements (full aperture)
Temporal sampling frequency	`Receive.sampleMode`	20 – 50 MHz [41, 112, 146, 149]	31.25 MHz `Receive.sampleMode = 'NS200BW'`
Beamforming lateral sampling frequency	`PData.PDelta`	-	$0.5\,\lambda$ $(0.10\,\mathrm{mm})$
Beamforming axial sampling frequency	`PData.PDelta`	$0.25\,\lambda$ [108]	$0.25\,\lambda$ $(0.05\,\mathrm{mm})$

λ: ultrasound wavelength ($\frac{\text{speed of ultrasound}}{\text{transducer frequency}}$)

from further away in the field will take longer to return to the transducer. Thus, since the transducer elements can only produce the next transmission sequence once the reflections from the furthest desired imaging depth have been acquired, increasing the PRF will require the imaging depth to be minimised. Here, the imaging depth was set to $30\,\mathrm{mm}$, which allowed the PRF to be increased to $15\,\mathrm{kHz}$ before the Verasonics script produced an error message, informing the user that the time between the pulses was too short.

The Verasonics pixel-based beamforming technique was applied to convert the raw radio frequency (RF) data captured during the PWI acquisitions to beamformed in-phase and quadrature (IQ) data for a pre-defined region of interest next to the ARF focus or the tapping location of the external shaker.

When using ARF excitation, the shear wave push and PWI tracking sequences were both implemented with a single ultrasound probe and, thus, ultrasound transmissions alternated between these two sequences (Figure 3.1). When using the external shaker, shear waves were continuously generated by the shaker while the ultrasound system simultaneously operated in the PWI acquisition mode (Figure 3.2).

3.3 Post-processing algorithms

The following sections describe how the collected in-phase and quadrature (IQ) ultrasound data was post-processed to, firstly, visualise the shear wave propagation and, secondly, determine the material properties based on the shear wave propagation. These steps have been summarised in Figure 3.3.

3.3.1 Tissue motion calculation

The Doppler effect is widely used in the field of ultrasound to measure the velocity of the contents that are being imaged: by determining how the frequency changes between the transmitted and received pulse, the velocity of the reflector (along the direction of the ultrasound beam) can be estimated. One widely known application is pulsed wave Doppler imaging, which is used to measure the velocity of blood.

The Doppler effect is also relevant when tracking shear waves. Shear waves are transverse waves; thus, even though they travel laterally through the ultrasound field of view, the local displacement of the tissue is in the axial direction, i.e. along the direction of the ultrasound beam. Thus, various algorithms have been developed based on the Doppler effect, which calculate the axial tissue velocity by estimating the ratio between the transmitted and received frequency.

The algorithm adopted in this work was the Loupas 2D-autocorrelation algorithm

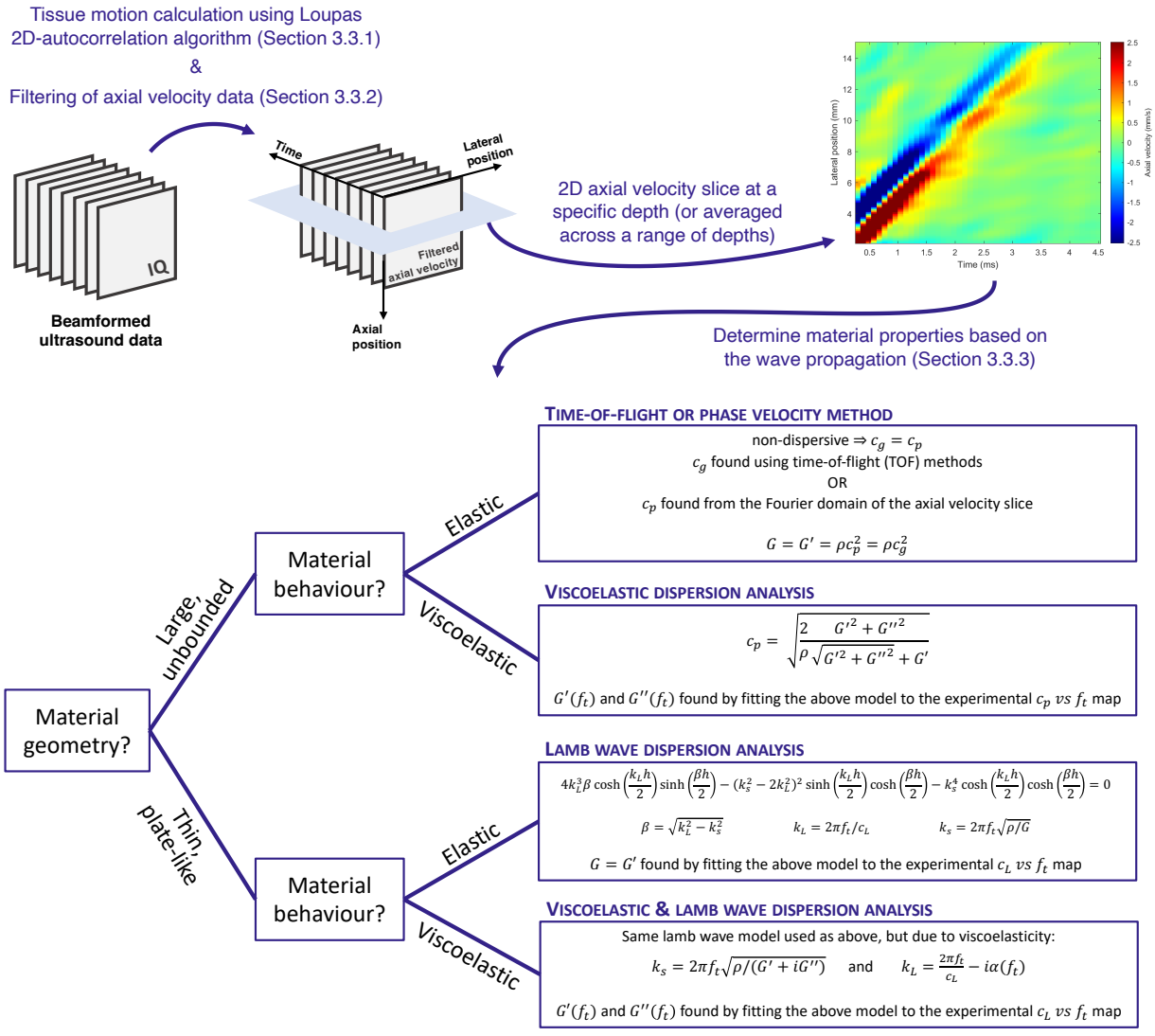


FIGURE 3.3 Summary of the shear wave imaging post-processing procedure. With the help of the decision tree, the most appropriate post-processing method can be identified for a given application. All methods and variables are outlined in further detail in Sections 3.3.1-3.3.3.

(Equation 3.1), a phase-shift algorithm that corrects for local variations of the centre frequency [108, 220]. This algorithm has been shown to provide accurate results at little computational cost [108, 139, 149].

$$v = \frac{c\, F_{PRF}}{2F_s} \frac{arctan\left[\frac{\sum_{m=0}^{M-1}\sum_{n=0}^{N-2}\{Q(m,n)I(m,n+1) - I(m,n)Q(m,n+1)\}}{\sum_{m=0}^{M-1}\sum_{n=0}^{N-2}\{I(m,n)I(m,n+1) + Q(m,n)Q(m,n+1)\}}\right]}{2\pi\frac{F_c}{F_s} + arctan\left[\frac{\sum_{m=0}^{M-1}\sum_{n=0}^{N-2}\{Q(m,n)I(m+1,n) - I(m,n)Q(m+1,n)\}}{\sum_{m=0}^{M-1}\sum_{n=0}^{N-2}\{I(m,n)I(m+1,n) + Q(m,n)Q(m+1,n)\}}\right]} \tag{3.1}$$

c = speed of sound in the medium

F_c = transducer centre frequency

F_{PRF} = pulse repetition frequency

F_s = sampling frequency

I = in-phase signal

M = axial window size

N = temporal window size

Q = quadrature signal

v = axial tissue velocity

The algorithm is based on the IQ data obtained from the Verasonics beamforming procedure. Here, the axial and temporal window size was set to $M = 5$ and $N = 5$, respectively. The resulting axial velocity data is a 3D matrix (lateral position $\times$ axial position $\times$ time).

3.3.2 Filtering

Axial velocity data is often prone to several sources of noise, such as reverberations from the ARF or signal decorrelation [108]. When the SNR is low, it becomes difficult to discern the shear wave from the noise and, thus, accurately track its motion through the medium. Here, the following steps were taken to reduce this noise.

Removal of reverberation frames due to the acoustic radiation force (ARF)

When using an ARF push beam to generate shear waves, there is a spike in axial velocities in the field of view for the first few frames, possibly due to reverberations in the field caused by the push pulse [108]. Therefore, when using this excitation method, the first $0.3\,\text{ms}$ were removed from the axial velocity data.

Median filter

A $3\times3\times3$ median filter, i.e. $0.15\,\text{mm} \times 0.30\,\text{mm} \times 0.3\,\text{ms}$ (axial $\times$ lateral $\times$ time), was applied using the Matlab function `medfilt3`, which effectively removed large outliers within the data [149].

Butterworth and directional filter

Lastly, a 3D mask combining a 4$^{\text{th}}$ order Butterworth and directional filter was applied to the Fourier transform of the data (Figure 3.4). The 3D axial velocity data was Fourier transformed using the Matlab function `fftn` with the zero-padding settings defined in Table 3.3 (higher zero-padding was used in the temporal frequency dimension since higher resolution was needed for the low cut-off frequency of $50\,\text{Hz}$).

The first component of the filter mask applied to the Fourier domain of the signal was a bandpass 4$^{\text{th}}$ order Butterworth filter, i.e. a filter consisting of both a high- and low-pass component (Figure 3.4, top row). The low-pass component had a cut-off frequency in all three dimensions (lateral and axial wavenumber, and temporal frequency) to eliminate any

TABLE 3.3 Settings for the filter applied to the Fourier domain.

Fourier domain frequency	fftn zero-padding	Butterworth low-pass cut-off frequency	Butterworth high-pass cut-off frequency
Temporal frequency (f_t)	6	$C_{t,low} = 2000\,\text{Hz}$	$C_{t,high} = 50\,\text{Hz}$
Axial wavenumber (ν_{ax})	2	$C_{ax} = 1000\,\text{m}^{-1}$	-
Lateral wavenumber (ν_{lat})	2	$C_{lat} = 1000\,\text{m}^{-1}$	-

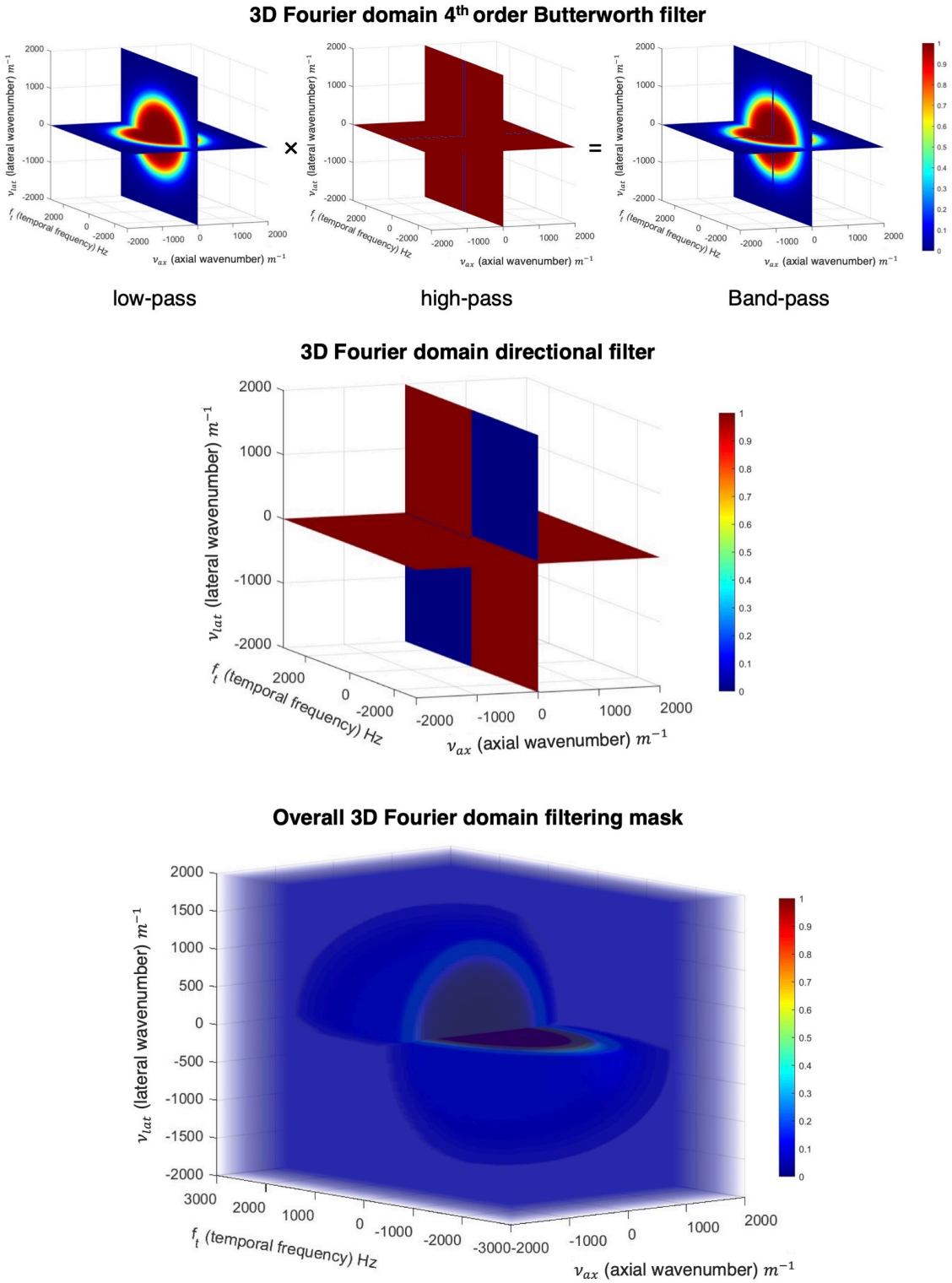


FIGURE 3.4 3D Fourier domain filter mask to remove high-frequency jitter, low-frequency motion from user and shear wave reflections/reverberations travelling against the main direction of propagation. The Fourier domain of the signal is multiplied by the filter mask, i.e. frequencies where the mask value is close to zero (dark blue) are removed, while frequencies where the mask value is close to one (dark red) are kept. A 4th order bandpass Butterworth filter mask **(top)** removes high frequencies in all dimensions, as well as very low temporal frequencies. The directional filter **(middle)** removes two quadrants of the ν_{lat}-f_t Fourier domain, only preserving waves moving in the main direction of propagation. The overall mask **(bottom)** is obtained by multiplying together the individual masks. For clarity, the top two rows only show two slices of the 3D filter at $\nu_{lat} = 0$ and $\nu_{ax} = 0$. To help visualise the overall 3D effect of the filter, the bottom figure shows the full 3D map, with increased transparency for values approaching zero (dark blue regions) [221].

high-frequency jitter or noise [149]. The high-pass component only had a temporal cut-off frequency of 50 Hz to remove any motion caused by movement of the ultrasound probe by the user [108]. Equations 3.2-3.3 were used to define the filter [222, 223]. The cut-off frequencies for the Butterworth filter are summarised in Table 3.3.

$$H_{low\text{-}pass}(\nu_{lat}, \nu_{ax}, f_t) = \frac{1}{1 + \left({\frac{\nu_{lat}}{C_{lat}}}^2 + {\frac{\nu_{ax}}{C_{ax}}}^2 + {\frac{f_t}{C_{t,low}}}^2 \right)^n} \tag{3.2}$$

$$H_{high\text{-}pass}(f_t) = 1 - \frac{1}{1 + {\frac{f_t}{C_{t,high}}}^{2n}} \tag{3.3}$$

C_{ax} = axial low-pass cut-off frequency

C_{lat} = lateral low-pass cut-off frequency

$C_{t,high}$ = temporal high-pass cut-off frequency

$C_{t,low}$ = temporal low-pass cut-off frequency

f_t = temporal frequency

$H_{high\text{-}pass}$ = high-pass Butterworth transfer function

$H_{low\text{-}pass}$ = low-pass Butterworth transfer function

n = Butterworth order

ν_{ax} = linear axial wavenumber

ν_{lat} = linear lateral wavenumber

The aim of the directional filter was to remove any interference from waves travelling in the opposite direction from the main shear wave propagation. These waves may occur due to reflections or refractions of the main shear wave when it encounters boundaries or other discontinuities in the medium. Signal corresponding to waves moving in a certain direction can be isolated by removing certain quadrants of the ν_{lat}-f_t domain. For example, for waves moving in the positive lateral direction, the lateral wavenumber and temporal frequencies will either be both positive or both negative. Hence, the quadrants where these have opposing signs can be set to zero to remove waves moving in the opposite direction (Figure 3.4, middle) [108, 149, 221].

The final mask that was ultimately applied to the Fourier transform was obtained by multiplying together the low-pass Butterworth filter, high-pass Butterworth filter and directional filter.

3.3.3 Evaluating material properties based on shear wave propagation

The shear wave velocity is closely linked to the material properties of the medium, as governed by Equations 3.4-3.7 below [132, 207, 224].

The shear modulus can be expressed as a complex number consisting of a storage and loss component:

$$G^*(\omega) = G^{'}(\omega) + iG^{''}(\omega) \tag{3.4}$$

G^* = complex shear modulus
$G^{'}$ = shear elastic storage modulus
$G^{''}$ = shear loss modulus (viscous component)
ω = angular temporal frequency

The complex shear wavenumber describes the shear wave propagation:

$$k_s^*(\omega) = \frac{\omega}{c_p(\omega)} - i\alpha_s(\omega) \tag{3.5}$$

c_p = phase velocity of the shear wave
k_s^* = angular complex shear wavenumber
α_s = attenuation of the shear wave

The complex shear modulus is related to the complex wavenumber through:

$$G^*(\omega) = \frac{\rho\omega^2}{k_s^{*2}(\omega)} \tag{3.6}$$

ρ = material density

For an incompressible and isotropic medium with Poisson's ratio approximately equal to 0.5, the following equation can be used to link the extensional elastic modulus to the shear elastic modulus (storage components) [225]:

$$E^{'}(\omega) = 2G^{'}(\omega)(1+\upsilon) = 3G^{'}(\omega) \tag{3.7}$$

$E^{'}$ = extensional elastic storage modulus (i.e., Young's modulus)

υ = Poisson's ratio

Lastly, while the above theoretical equations taken from the literature are typically expressed in angular frequencies (ω in $\mathrm{rad/s}$) and angular wavenumbers (k in $\mathrm{rad/m}$), experimental data is typically displayed in linear frequencies (f in Hz) and linear wavenumbers (ν in m^{-1}). For consistency, this convention will be used here as well, but to highlight this difference and avoid confusion, the angular to linear relationships are summarised below:

$$k = 2\pi\nu \tag{3.8}$$

$$\omega = 2\pi f_t \tag{3.9}$$

f_t = temporal frequency

k = angular wavenumber

ν = linear wavenumber

Care has to be taken that the right method is used to obtain the phase velocity of the shear wave and the correct equation is subsequently used to calculate the elastic or viscoelastic material properties. Often, so-called time-of-flight (TOF) algorithms are applied to determine the shear wave velocity, from which the shear modulus is then calculated using $G = \rho c^2$. However, as will be demonstrated below, this simplified post-processing protocol is only applicable for large, unbounded, elastic material. Due to an effect called dispersion which causes the shear wave velocity to be frequency-dependent, more in-depth analysis is required when the material is viscoelastic and/or thin-layered, which is often the case for tendons and ligaments. The post-processing steps for the different

material and geometry conditions are outlined in detail below.

Large, unbounded elastic material

Since elastic material does not have a loss modulus, the shear modulus and shear wavenumber are both real and Equation 3.6 simplifies to $G = \rho c_p^2$. With the density known (for soft tissue $\rho \approx 1000\,\mathrm{kg/m^3}$ [108]), only the shear wave phase velocity is needed to determine the shear modulus. Typically, TOF algorithms are used to find the velocity of the shear wave. While these technically calculate the group velocity of the wave [30, 132], i.e. the velocity of the wave packet rather than individual wave phases, phase and group velocity can be shown to be equal in elastic material due to its non-dispersive nature, i.e. shear wave velocity is not frequency-dependent (Equations 3.10-3.13) [132].

$$c_g(\omega) = \frac{d\omega}{dk_s} = \frac{df_t}{d\nu_s} \tag{3.10}$$

$$c_p(\omega) = \frac{\omega}{k_s} = \frac{f_t}{\nu_s} \tag{3.11}$$

$c_g =$ group velocity of the shear wave

For non-dispersive material, ω is linearly related to k_s:

$$\omega = c\ k_s \tag{3.12}$$

Therefore:

$$c_g = \frac{d\omega}{dk_s} = \frac{\omega}{k_s} = c_p \tag{3.13}$$

Two different TOF algorithms were implemented in this project.

1. In the linear regression method, the shear wave is tracked by determining its 'arrival time' for each lateral position. The shear wave propagation through each lateral position can be visualised by looking at how the axial velocity at these positions varies sinusoidally with time (Figure 3.5, left). The shear wave arrival time can then be defined as the time at which the axial velocity reaches either a peak or trough. By plotting the shear wave arrival

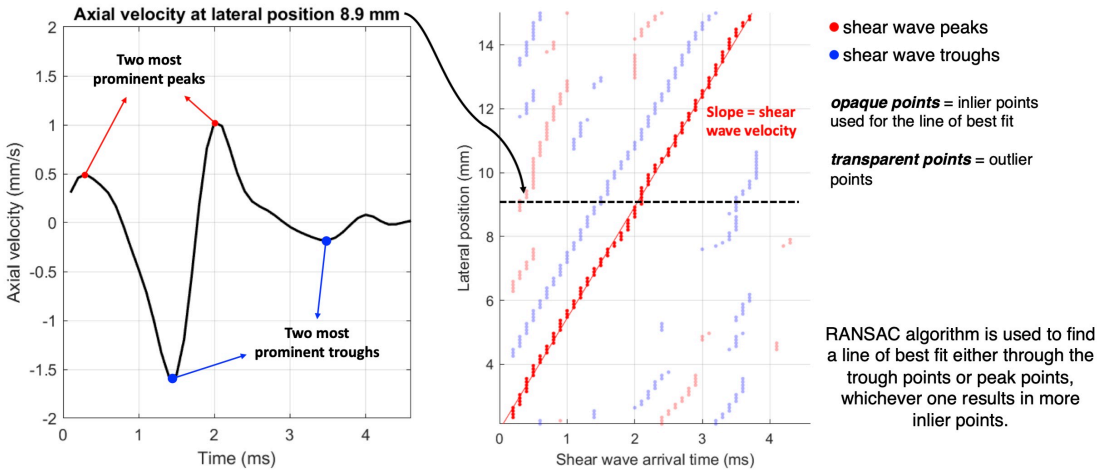


FIGURE 3.5 Time-of-flight (TOF) analysis using the linear regression algorithm.

time against lateral position, a linear trend becomes visible, the slope of which is equal to the shear wave velocity (Figure 3.5, right).

If SNR is low, determining the peaks and troughs in the axial velocity vs time plot that correspond to the shear wave is challenging. Thus, at each lateral position the two most prominent peaks and troughs, i.e. four points overall, are plotted. Subsequently, a random sample consensus (RANSAC) algorithm (Matlab function `ransac`) is used to find a line of best fit for both the peak and trough points. The RANSAC algorithm uses the following steps to find the line of best fit in the presence of outliers: 1) a random subset of the data is selected, 2) the Matlab `fit` function finds the line of best fit for this subset, 3) the number of inlier points is calculated, i.e. the number of points from the entire original data set which lie within a pre-defined maximum distance from the line, and 4) this process is iteratively repeated to find the line of best fit with the most inlier points [226].

After the two lines of best fit have been found (one for the peak points and one for the trough points), the line with the most inlier points is used to calculate the shear wave velocity.

2. The radon transform method is best understood by depicting the axial velocity vs lateral position vs time data as a colour plot (Figure 3.6). The red and blue streaks through the plot correspond to maximum and minimum axial velocity, respectively, thus representing the

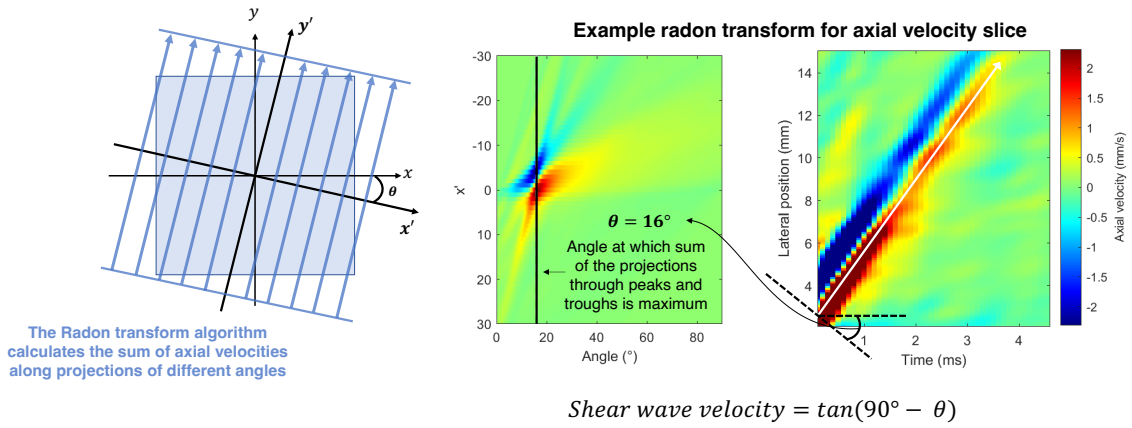


FIGURE 3.6 Time-of-flight (TOF) analysis using the radon transform algorithm.

shear wave peak and trough. Using the Matlab `radon` function, the sum of axial velocities for projections at different angles and different x' positions is calculated. This sum along the projections reaches a maximum and minimum for the projections running exactly through the red and blue streaks. The corresponding angle of the maximum/minimum projection is used to determine the slope of the streaks and, thus, the shear wave velocity.

An additional algorithm, which will be referred to as the phase velocity method, was developed for this study (Figure 3.7). Unlike the TOF methods that calculate the group velocity, this method directly finds the phase velocity of the shear wave by taking the 2D Fourier transform of a lateral position vs time slice of the axial velocity data. The point at which the Fourier transform magnitude map reaches a maximum is located. By dividing

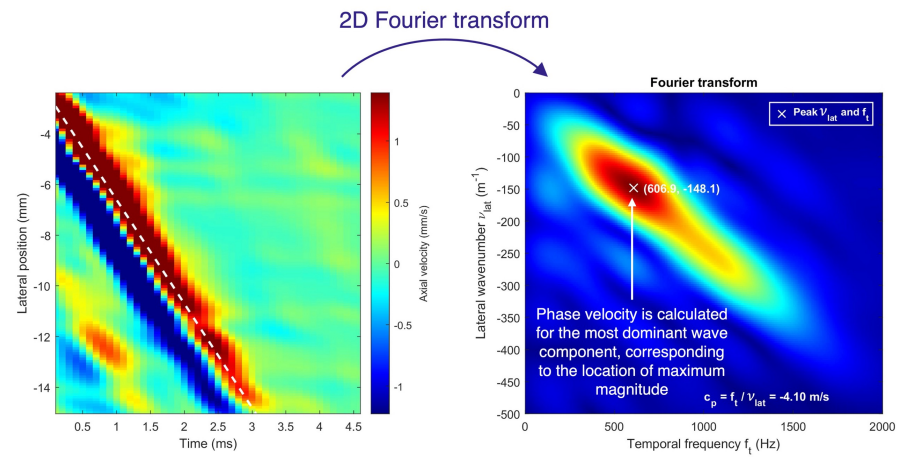


FIGURE 3.7 Method to obtain the shear wave phase velocity from the Fourier transform of the axial velocity data.

the corresponding wavenumber by the frequency, the phase velocity of the most dominant frequency component of the wave is obtained (Equation 3.11).

Large, unbounded viscoelastic material (viscoelastic dispersion analysis)

For viscoelastic material, the shear modulus and shear wavenumber are complex and frequency dependent. This means that viscoelastic materials are dispersive, i.e. shear waves of different frequencies will travel at different velocities. Following on from Equations 3.4-3.7, the shear wave phase velocity can be related to the shear loss and storage moduli using the following steps [43, 207, 224].

Rearranging Equation 3.6 and multiplying the numerator and denominator within the square root by the conjugate $G^{'} - iG^{''}$:

$$k_s^* = \omega\sqrt{\frac{\rho}{G^{'} + iG^{''}}} = \omega\sqrt{\frac{\rho(G^{'} - iG^{''})}{G^{'2} + G^{''2}}} \tag{3.14}$$

The real and imaginary parts of the above equation can be separated using the following theorem for the square root of a complex number [227]:

$$\sqrt{a + bi} = \sqrt{\frac{\sqrt{a^2 + b^2} + a}{2}} + i\frac{b}{|b|}\sqrt{\frac{\sqrt{a^2 + b^2} - a}{2}} \tag{3.15}$$

Therefore:

$$k_s^* = \omega\sqrt{\frac{\rho}{G^{'2} + G^{''2}}}\left[\sqrt{\frac{\sqrt{G^{'2} + G^{''2}} + G^{'}}{2}} - i\sqrt{\frac{\sqrt{G^{'2} + G^{''2}} - G^{'}}{2}}\right] \tag{3.16}$$

Finally, since shear wave phase velocity is related to the real part of the complex wavenumber (Equation 3.5) [43, 132]:

$$Re(k_s^*) = \frac{\omega}{c_p} = \omega\sqrt{\frac{\rho}{2}\frac{\sqrt{G^{'2} + G^{''2}} + G^{'}}{G^{'2} + G^{''2}}} \tag{3.17}$$

$$c_p = \sqrt{\frac{2}{\rho}\frac{G^{'2} + G^{''2}}{\sqrt{G^{'2} + G^{''2}} + G^{'}}} \tag{3.18}$$

A wide range of viscoelastic models exist, with each one defining the storage and loss modulus differently [43]. For soft biological tissue, the Voigt model has previously been

found to provide a good fit [30, 41, 43, 156, 205]:

$$G^{'} = \mu \tag{3.19}$$

$$G^{''} = \omega\eta = 2\pi f_t\, \eta \tag{3.20}$$

$\eta =$ Voigt shear viscosity

$\mu =$ Voigt shear modulus

Therefore, for the Voigt model, the dispersion curve (c_p vs f_t) is defined using the following equation:

$$c_p = \sqrt{\frac{2}{\rho}\frac{\mu^2 + (2\pi f_t \eta)^2}{\sqrt{\mu^2 + (2\pi f_t \eta)^2} + \mu}} \tag{3.21}$$

It can now be seen from Equation 3.21 how the frequency-dependency of the loss modulus will result in a frequency-dependent shear wave phase velocity. By fitting this Voigt dispersion model to experimentally obtained dispersion data, the Voigt material properties (μ and η) can be determined.

It should be noted that, due to the dispersion effect, group velocity will no longer be equal to phase velocity. Therefore, for viscoelastic materials, it is crucial that the experimentally obtained dispersion data is based on the phase velocity.

The fitting process involved the following steps (Figure 3.8). First, a 2D lateral position vs time slice was extracted from the experimental axial velocity data, which either corresponded to the data at a specific axial depth or the average over a range of depths. Next, a 2D fast Fourier transform was applied to this spatio-temporal axial velocity field to convert it into its wavenumber vs frequency representation. Next, by using the $c_p = f_t/\nu$ relationship, this plot was transformed into a phase velocity vs frequency map. Finally, the theoretical Voigt dispersion curve (Equation 3.21) was fitted to this experimental dispersion map.

This curve of best fit was found using the Matlab optimisation function `fmincon`, which aimed to find the Voigt material properties for which the theoretical dispersion curve best crossed through the region of maximum magnitude of the experimental phase velocity vs

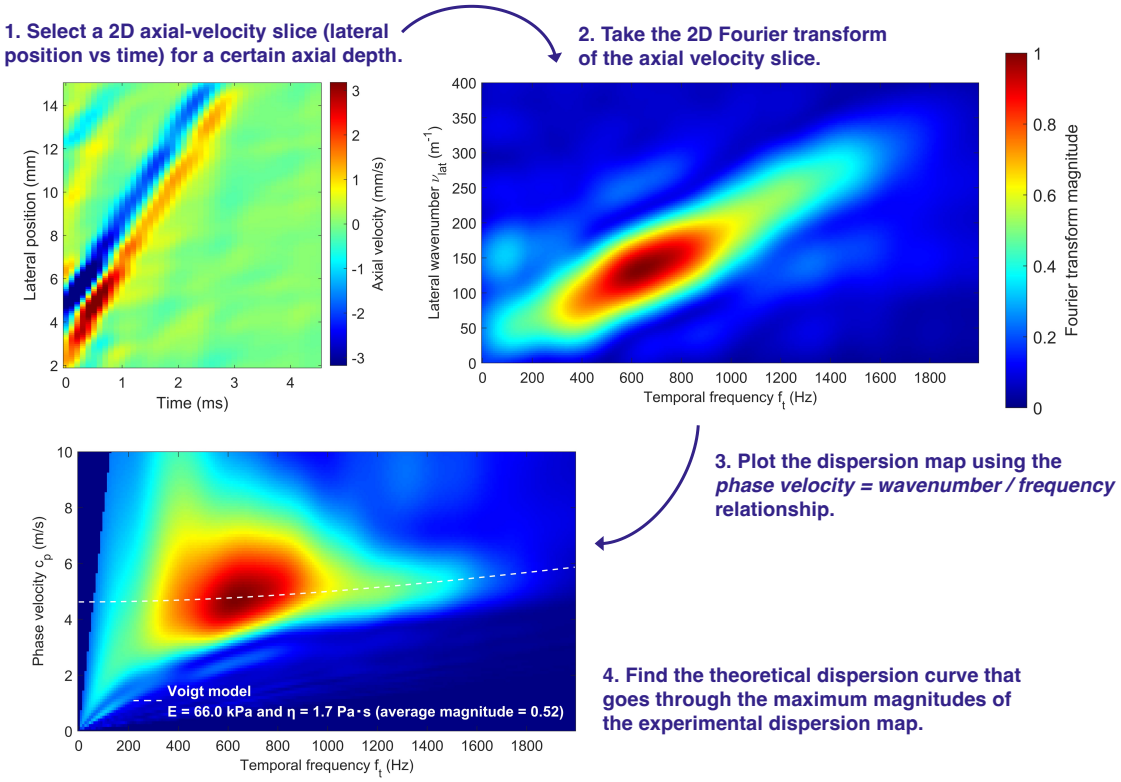


FIGURE 3.8 Post-processing steps for the viscoelastic dispersion analysis. Viscoelastic material properties are obtained by fitting the theoretical dispersion model to the experimental dispersion map (bottom left).

frequency map. The goodness-of-fit was thus defined as the average magnitude of the dispersion map along the fitted curve: at each iteration of the optimisation, the Matlab function `interp2` was used to find the magnitude at each frequency along the theoretical dispersion curve, and the average of these values was taken as the to-be-optimised goodness-of-fit. To allow results of different measurements to be compared more easily, the Fourier transform magnitudes were normalised to range from $0-1$; thus, average magnitude values of the fitted dispersion curve closer to one indicated a better fit.

The experimental shear wave dispersion map can be obtained using both the ARF excitation and external shaker methods. Shear waves generated using ARF excitation naturally have a large bandwidth, with detectable frequencies in the Fourier domain across several hundred hertz. Thus, phase velocities over a range of frequencies can be measured with a single shear wave. On the other hand, the external shaker creates shear waves with a low bandwidth, meaning that with each shear wave, the phase velocity is obtained for only a specific frequency. However, specific frequencies can be targeted more

accurately and, even though each frequency needs to be excited separately, ultimately a wider range of frequencies can be investigated. The Fourier transforms of the acquisitions at the different frequencies are then combined to obtain one overall dispersion map.

Thin, elastic material (Lamb wave dispersion analysis)

The geometry of the material can be another source of dispersion: when a shear wave travels through a thin-layered structure, it will reflect at the internal boundaries and will propagate as a so-called guided wave [30, 140]. The resulting overall wave is a combination of these internal reflections, and its phase velocity is frequency-dependent and different to the velocity of the underlying shear wave (Figure 3.9). Different models exist that describe the formation and propagation of guided waves, each considering different geometries and boundary conditions. For guided waves travelling through ligaments and tendons, the below antisymmetric Lamb wave model has been shown to be effective, which approximates the tissue as a thin, infinitely large and isotropic plate surrounded by a medium of similar density [30, 139, 140, 156].

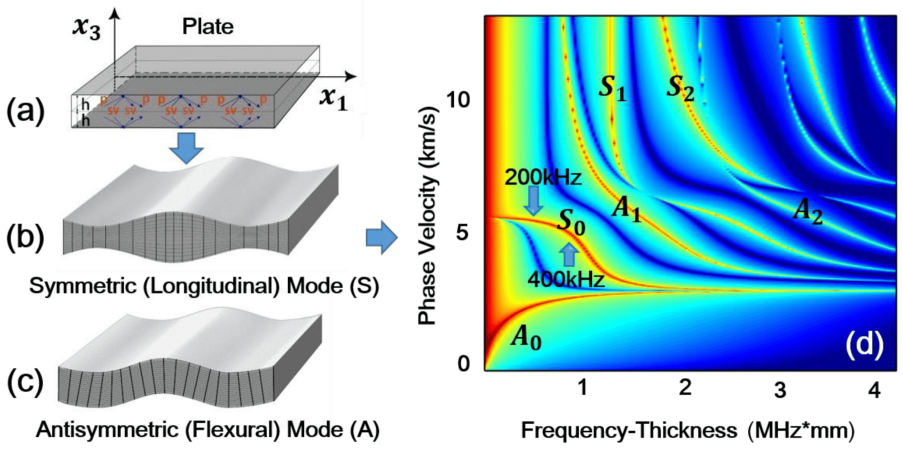


FIGURE 3.9 Illustration of Lamb wave propagation, reproduced from Sun et al. [228], licensed under CC BY. **(a)** Longitudinal (P) and shear (S) waves are reflected at the internal plate boundaries and are thus guided along the plate. **(b)** Antisymmetric modes of the Lamb wave. **(c)** Symmetric modes of the Lamb wave. **(d)** Dispersion curves of the Lamb wave for an aluminium plate.

$$4{k_L}^3\beta\, cosh(\frac{k_L h}{2})sinh(\frac{\beta h}{2}) - ({k_s}^2 - 2{k_L}^2)^2 sinh(\frac{k_L h}{2})cosh(\frac{\beta h}{2}) - {k_s}^4 cosh(\frac{k_L h}{2})cosh(\frac{\beta h}{2}) = 0 \tag{3.22}$$

$$\beta = \sqrt{{k_L}^2 - {k_s}^2}$$

$$k_L = \omega / c_L$$

For elastic materials, $G'' = 0$ is real and Equation 3.14 reduces to:

$$k_s = \omega\sqrt{\rho / G} \tag{3.23}$$

c_L = Lamb wave phase velocity

h = height of the thin-layered structure

k_L = Lamb wavenumber

Similar to the viscoelastic post-processing approach described in the previous section, the Lamb wave model can be fitted to the experimental dispersion map obtained from the Fourier domain of the axial velocity data (Figure 3.10). In this case, the phase velocity of

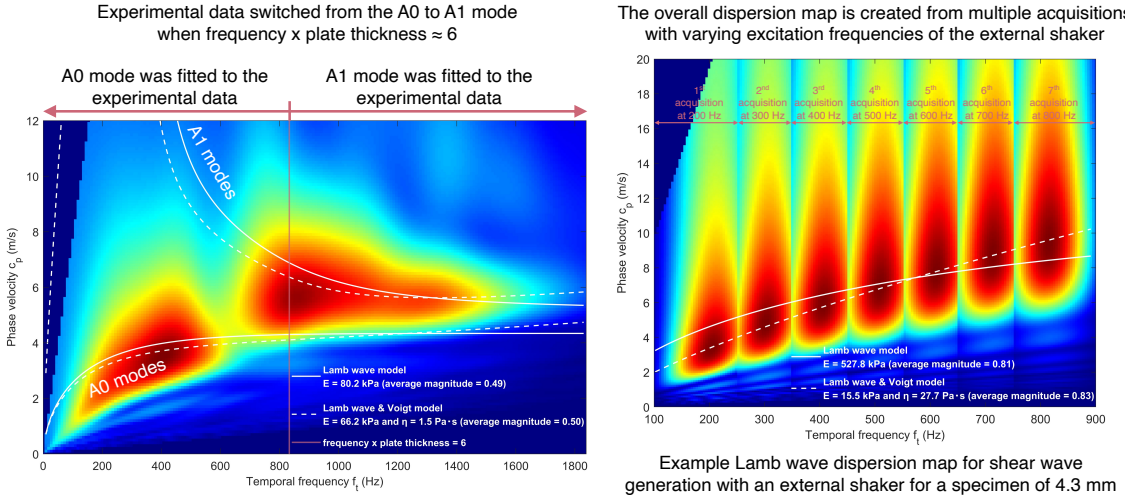


FIGURE 3.10 Example dispersion maps for thin-layered samples, obtained with acoustic radiation force (ARF) excitation **(left)** and external shaker excitation **(right)**. Lamb wave dispersion models describe the propagation of guided waves, which result from the superposition of the internal reflections of the shear wave between the boundaries of thin, plate-like structures. Note that the two dispersion maps were obtained for different materials (**left:** tissue-mimicking agar phantom, **right:** porcine collateral ligament).

the experimental dispersion map is the velocity of the Lamb wave (c_L). Since the height of the medium can be measured either using vernier callipers in *ex vivo* experiments or from the ultrasound images, the only unknown is the shear modulus G.

The Matlab optimisation function `fmincon` was again used to find the theoretical Lamb wave dispersion curve that best matched the maximum magnitude region of the experimental dispersion map. However, since the Lamb wave equation (Equation 3.22) is an implicit function (i.e., the dependent variable c_L cannot be isolated), finding the Lamb wave dispersion curve at each iteration for new trial values of shear modulus was more challenging and computationally expensive. Here, the Matlab function `fsolve` was used to find a solution of the implicit equation at a range of frequencies between $0 - 1500$ Hz.

An additional challenge was the multi-modal nature of Lamb wave propagation, which results in multiple possible function solutions at every frequency, each corresponding to a different mode of the Lamb wave (Figure 3.9). Thus, to obtain the curves of different modes, the 'initial point' input variable of `fsolve` was varied until the different solutions were found [229]. Here, only the first two modes (A0 and A1) were evaluated, since these were found to be the dominant modes for the frequency range used throughout this study ($<$1500 Hz). Furthermore, it was found that the experimental dispersion data switched from the A0 to the A1 mode for frequencies $\gtrsim 6/\text{plate thickness}$. Therefore, when fitting the model to the experimental data, the A0 mode was used for frequencies below this threshold and the A1 mode for frequencies above this threshold.

Thin, viscoelastic material (viscoelastic & Lamb wave dispersion analysis)

If the material is both thin and viscoelastic, both sources of dispersion have to be accounted for. Viscoelasticity will result in a complex shear wavenumber k_s^* (Equation 3.14) and a complex Lamb wavenumber k_L^* (Equation 3.24). Thus, the left-hand side of the Lamb wave equation (Equation 3.22) will have a real and imaginary part and, when solving for c_L, it has to be ensured that both the real and imaginary parts of the equation equal to zero [229]. The Matlab function `fsolve` is able to solve these types of complex equations, and thus the same approach as above was implemented (Figure 3.10); however, in this case,

two material property variables were input into the optimisation function of `fmincon`, i.e. the Voigt shear modulus and viscosity (μ and η).

$$k_L^*(\omega) = \frac{\omega}{c_L(\omega)} - i\alpha_L(\omega) \tag{3.24}$$

c_L = phase velocity of the Lamb wave

k_L^* = angular complex Lamb wavenumber

α_L = attenuation of the Lamb wave

3.4 Discussion

3.4.1 Comparison to state-of-the-art

The post-processing procedures outlined in this chapter combine established methods from the literature (as referenced throughout) with novel advancements developed during this project. The following summary aims to distinguish new contributions from previously implemented methods.

1. **Shear wave generation**: the effectiveness of using an external shaker to investigate phase velocity dispersion due to viscoelasticity has been demonstrated in a wide range of soft tissue, such as the liver [210, 214], kidney [214] and tendons [41]. However, it has not seen much use for investigating guided wave dispersion in thin structures, with the main research focus in cardiac applications [156, 157]. Since an external shaker allows more controlled generation of shear waves at a wider range of frequencies, there is a clear argument for its use for any form of frequency dispersion analysis. Here, the process for obtaining the dispersion maps for both ARF and external-shaker induced shear waves has been outlined, to which either a viscoelastic and/or guided wave dispersion model can be fitted.

2. **Filter design:** in most previous implementations of shear wave imaging, a 2D (lateral $\times$ temporal) median filter and/or directional filter was used to reduce noise in the calculated axial velocities [146, 149, 150]. Incorporating a bandpass filter into the design has been shown to effectively mitigate both low-frequency background noise

and high-frequency jitter [41, 108]. Additionally, Lipman et al. [221] demonstrated that a 3D directional filter (lateral $\times$ axial $\times$ temporal) significantly outperformed traditional 2D filters. To leverage both these improvements, a 3D filter with combined directional and bandpass filtering has been implemented. This approach not only enhanced noise reduction but also reduced computational costs. Instead of applying a 2D filter to each axial velocity slice individually, the 3D filter can be applied to the entire 3D axial velocity matrix, streamlining the process.

3. **Large, elastic model:** the time-of-flight methods to calculate group velocity were based on previous work [108, 144, 149, 151, 230]. However, some improvements were made. Linear regression methods typically find a single "shear wave arrival time", i.e. axial velocity peak/trough, at each lateral position [108]. When SNR was low, distinguishing between peaks/troughs corresponding to the shear wave vs ones that are introduced by noise was challenging, leading to poor linear regression between arrival time and lateral position. Using a RANSAC algorithm, as suggested by Wang et al. [230], can improve the fit. Here, multiple peaks and troughs were extracted per lateral position, further increasing the likelihood that the true shear wave flight is detected by the RANSAC algorithm.

   In addition to the time-of-flight methods, a new technique was proposed, i.e. the phase velocity method based on the Fourier transform. Since this method requires less processing steps and directly finds the most dominant wave component in the Fourier domain, it is hypothesised that it is more robust against noise and artefacts. Furthermore, by implementing an efficient Fast Fourier Transform (FFT), computational times are further reduced.

4. **Dispersion models:** the steps to obtain the experimental dispersion map from the axial velocity data have been previously described [30, 139]. However, here a new algorithm for fitting the theoretical dispersion curves was proposed. Previous methods obtain an experimental dispersion curve by finding the phase velocity at each frequency that corresponds to the maximum magnitude on the experimental dispersion map [30, 139]. As a result, the objective during curve fitting is to minimise

the distance between the theoretical and experimental curves. In this project, on the other hand, optimisation was based on maximising the magnitude of the points on the dispersion map that the theoretical curve passes through. The high magnitude region of the experimental dispersion map can have a large spread, and not reducing this experimental data to a single curve can be advantageous. For example, as will be shown in Chapter 6, by assessing the sensitivity of the objective function to variations in the material properties, the confidence in the measured properties can be evaluated.

Furthermore, while previous implementations of the combined viscoelastic and Lamb wave model consider that the shear wavenumber is complex, they do not account for the complex nature of the Lamb wavenumber, which includes the attenuation component (Equation 3.24) [30, 156, 157]. Assuming that the Lamb wavenumber is real allows for the Lamb wave velocity to be determined by considering only the real components of the equation (Equation 3.22). However, when the complex contribution from attenuation is considered, there are two unknown variables: the Lamb wave velocity and attenuation. Decomposing the Lamb wave equation shows that both the real and imaginary parts contain both variables. Thus, real and imaginary parts have to be solved to find the two unknowns. This illustrates that the assumption of a real Lamb wavenumber will alter the dispersion curve [229].

3.4.2 Conclusion

The ultrasound shear wave imaging post-processing pipeline presented in this chapter can be used to analyse shear wave propagation across a range of soft tissues, from a large and elastic medium, to thin-layered and viscoelastic structures. It guides the selection of an appropriate shear wave propagation model that best represents the underlying material properties. This will enable more consistent and comparable measurements of material properties across tissues with varying viscosities and thicknesses.

04

Speckle Tracking Implementation

4.1 Introduction **88**

4.2 Acquisition sequences **90**

4.3 Post-processing algorithms **92**

4.4 Discussion **101**

4A Strain calculation using deformation gradient decomposition **103**

The contents of this chapter formed part of a journal article published in Ultrasound in Medicine and Biology [231]. All co-authors played a supervisory role in this work. Additionally, while I wrote the initial draft, co-authors contributed amendments to the text.

List of Abbreviations

CPWC	Coherent plane-wave compounding
DIC	Digital image correlation
IQ	In-phase and quadrature
NRIR	Non-rigid image registration
QUS	Quantitative ultrasound
SE	Strain elastography
SNR	Signal-to-noise ratio
STE	Speckle tracking echocardiography

4.1 Introduction

Many existing quantitative ultrasound (QUS) techniques are underpinned by speckle tracking algorithms that measure tissue deformation under external or physiological loading [114]. Strain elastography (SE), for instance, is used to detect stiff pathological tissue such as tumours and lesions, in large homogeneous tissues such as the breast [180–182], liver [183, 184], prostate [187], and thyroid [186]. In the field of cardiology, speckle tracking echocardiography (STE) is used to quantitatively evaluate cardiac function by measuring myocardial velocities, deformation, and strain [232–234].

There is much scope for further impact, as for most fields the technique is nascent and not in routine use. For example, in orthopaedics, measuring the deformation or strain behaviour of connective tissue such as tendons and ligaments could help diagnose abnormal tissue changes due to ruptures, tissue pathologies or surgical procedures [89, 91, 189, 235, 236]. In optometry, monitoring strain in the sclera could provide early detection of elevated intraocular pressure, the primary risk factor for glaucoma [237].

However, the technology has not penetrated this field clinically, since applying the speckle tracking algorithm to new fields presents challenges. Commercial systems have often proven unreliable for novel applications, particularly those involving thin or complex soft tissues [203]. Instead, there is a need for advanced implementations of speckle tracking algorithms that are specifically tailored for the unique characteristics of each tissue type, such as their specific ultrasound speckle patterns and strain rates [51, 204]. Finding suitable settings is challenging due to the lack of guidelines and systematic

comparisons of existing algorithms [204]. Furthermore, the equipment-specific nature of images limits transferability of settings between different research centres and clinics with different equipment. This is a significant barrier to adoption as creating application-specific algorithms classically requires a known gold standard result, and these data are either not available for many possible biomechanical applications or can only be obtained at specialist centres who have access to expensive laboratory equipment.

Here, a novel approach for identifying optimal application-specific speckle tracking algorithms and machine settings is presented, which does not need gold standard reference data. The approach is centred on the signal-to-noise ratio (SNR) principle: with suitable algorithmic settings the noise in the calculated displacement field should be low while the signal, i.e., the true underlying tissue displacement, should be high. Since signal is inherently repeatable while noise is inherently random, a tuned algorithm should lead to repeatable results for repeated acquisitions, while for a suboptimal algorithm the accumulation of random frame-to-frame displacement errors leads to non-repeatable inaccuracies in tracking. Hence, it was hypothesised that the variance between repeated acquisitions for otherwise identical tissue and loading conditions could be used as a quality penalty for optimisation.

This chapter provides a detailed overview of the development of the speckle tracking algorithm and the accompanying optimisation routine for adjusting the algorithmic settings. The main objective was to develop an accessible speckle tracking framework which, using the optimisation routine, can be tuned for a wide range of applications.

4.2 Acquisition sequences

The design of an ultrasound speckle tracking procedure does not start with the post-processing algorithm. Instead, accurate tracking of tissue motion greatly depends on the quality of the collected images and, therefore, selecting a suitable ultrasound acquisition method is of great importance. As a general rule, there exists a trade-off between image resolution, frame rate and imaging depth. While high image resolutions are better able to capture the details of the speckle pattern and, thus, facilitate accurate speckle tracking, resolution will have to be limited when imaging deeper or fast-moving tissue structures.

Here, a conventional scanline and coherent plane-wave compounding (CPWC) imaging mode were implemented on the Verasonics Vantage 128 research ultrasound system with a L11-5v transducer (linear, $38\,\mathrm{mm}$, $5-11\,\mathrm{MHz}$ bandwidth) (Verasonics Inc., Kirkland, WA, USA). The specific settings used are summarised in Table 4.1. The optimisation routine of this study, discussed in more detail in Section 4.3.2, was then used to find which mode was more suitable for the tested applications.

During the final clinical pilot study of this project, a commercial wireless Clarius ultrasound scanner was used (linear, $38.5\,\mathrm{mm}$, $4-13\,\mathrm{MHz}$ bandwidth) (1st generation L7-38, Clarius Mobile Health, Vancouver, BC, Canada). Images are collected via the 'Clarius Ultrasound App' which is available for phones or tablets. The acquisition method on this scanner was a conventional imaging mode, and the main settings defined in the user interface of the Clarius application are given in Table 4.2.

TABLE 4.1 Transmission, acquisition and beamforming parameters for the conventional scanline imaging and coherent plane-wave compounding (CPWC) mode implemented on the Verasonics research ultrasound system. The Matlab structures through which these parameters are defined in the Verasonics script are indicated in the second column.

Parameter	Verasonics Matlab structure	Values used in literature	Selected Values
Frame rate	`SeqControl (timeToNextAcq)`	10 – 155 Hz [109, 193, 197, 236, 238–240]	30 Hz
Transducer frequency	`TW.Parameters`	3.5 – 21 MHz [49, 109, 168, 193, 197, 198, 236, 238–242]	7.8 MHz
Temporal sampling frequency	`Receive.sampleMode`	20.8 – 50 MHz [109, 168, 241]	31.25 MHz `Receive.sampleMode = 'NS200BW'`
Conventional scanline transducer elements (for each focused beam)	`TX.Apod`	-	32 elements
Conventional scanline focal depth	`TX.focus`	6 – 22 mm [109, 243, 244]	10.1 mm
CPWC transducer elements	`TX.Apod`	-	128 elements (full aperture)
CPWC beam steering angles	`TX.Steer`	7 – 121 angles between ± 14 – 45° [109, 168, 233, 241]	30 angles between $\pm 36^\circ$
Beamforming lateral sampling frequency	`PData.PDelta`	0.025 – 0.297 mm [197, 198, 236, 240]	0.25 λ (0.05 mm)
Beamforming axial sampling frequency	`PData.PDelta`	0.019 – 0.067 mm [197, 198, 236, 240]	0.25 λ (0.05 mm)

TABLE 4.2 Main settings selected in the 'Clarius Ultrasound App' when using the wireless Clarius ultrasound scanner during the clinical pilot study.

Parameter	Selected Values
Imaging mode	B-mode
Gain	50 %
Dynamic range	50 %
Screen calibration level	12
Image export format	DICOM JPEG Lossless, Nonheirarchical (Process 14)

4.3 Post-processing algorithms

All algorithms in this study were developed in Matlab (MATLAB R2021b, The MathWorks, Inc., Natick, MA, USA).

4.3.1 Speckle tracking algorithm

Flexibility and configurability were the focus when designing the 2D speckle tracking algorithm to calculate soft tissue strain, so that the optimisation routine could then automatically test different combinations of the large range of algorithmic settings used in previous speckle tracking studies. Thus, the algorithm was uniquely structured so that settings ranging from acquisition to speckle tracking to post-processing could all be varied during the optimisation (Figure 4.1). The steps of this algorithm were:

Placement of nodes

Most speckle tracking algorithms calculate strain from a uniform nodal grid and assume that the tissue under investigation primarily displaces in the lateral or axial direction. The strain is then simply obtained by differentiating the lateral or axial displacements with respect to the original nodal positions. However, this assumption does not hold true for all types of tissue. For instance, ligaments often wrap around bone and thus tend to be curved, with their shape changing throughout the loading cycle. This effect is amplified

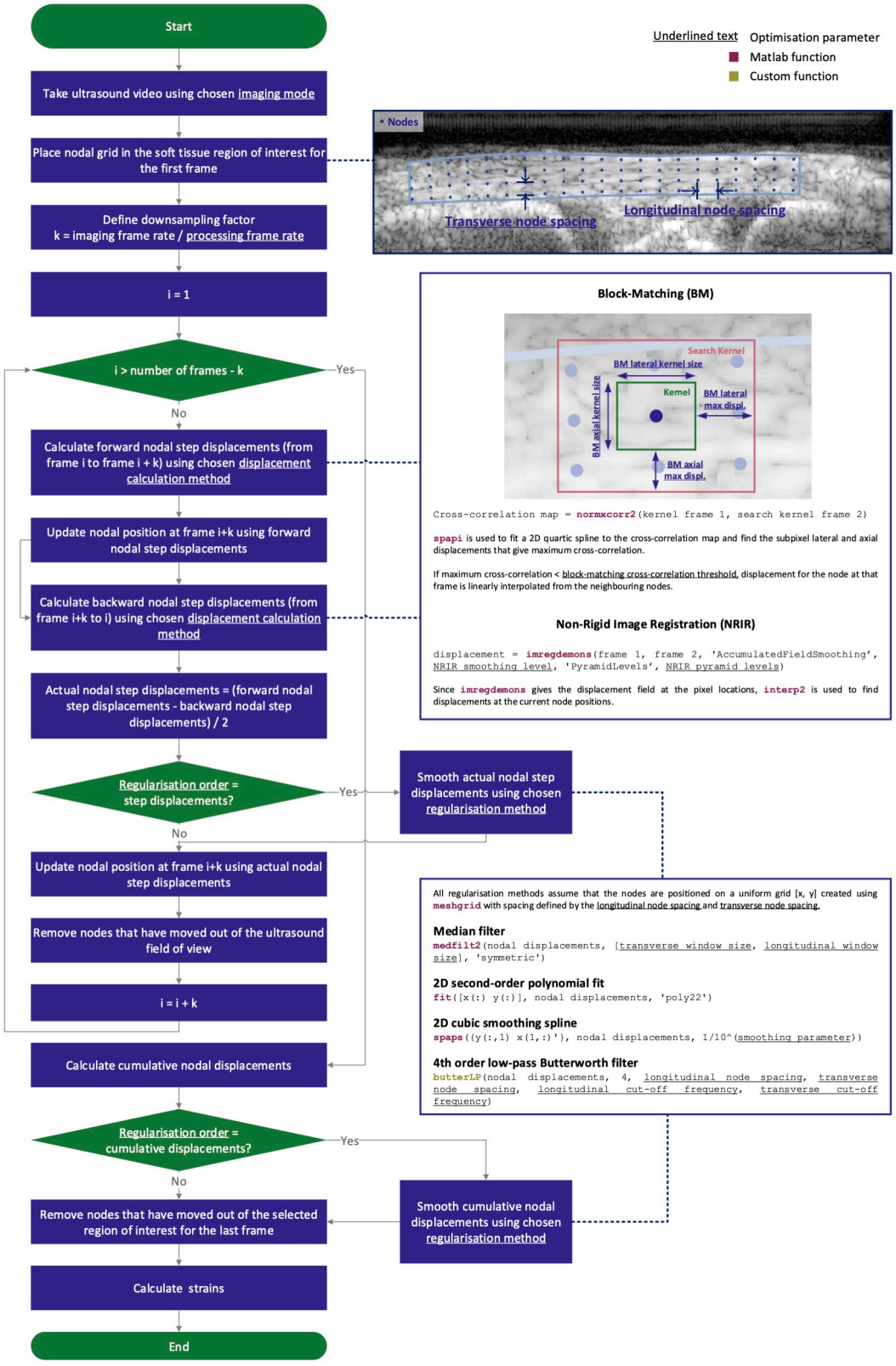


FIGURE 4.1 Flowchart of the custom 2D speckle tracking algorithm to calculate soft tissue strain. Inbuilt Matlab functions are dark red, custom functions olive, and parameters that can be varied in the optimisation are underlined.

in situ when certain regions of the ligament may slacken or even buckle under certain loading conditions [51]. Therefore, placing a uniform rectangular nodal grid on such tissues with complex geometries inevitably means that some nodes will be located outside the region of interest. During smoothing, displacements at these nodes may invalidate the displacements measured at nodes located within the bounds of the tissue, especially when there are large displacement field discontinuities at the boundary due to, for example, relative tissue sliding.

Instead, a nodal grid which follows the tissue geometry was used, which ensured that all nodes were within the bounds of the ligament. This nodal grid was defined by manually selecting the tissue region of interest in the B-mode image of the first frame, and then automatically populating it with a grid of nodes that aligned to the selected region.

Displacement field calculation

The frame-to-frame nodal displacements were tracked using either a block-matching [173, 197, 198] or non-rigid image registration (NRIR) [177, 190] algorithm applied to the envelope of the ultrasound signal, which was calculated from the in-phase and quadrature (IQ) data.

For the block-matching method, kernels were centred on the nodes and searched for in a larger search kernel in the subsequent frame by calculating the normalised cross-correlation map between the two kernels. Subpixel displacements were subsequently obtained by fitting a 2D quartic spline to the cross-correlation map and finding the position of maximum correlation [245]. If the normalised cross-correlation was below a pre-defined threshold, the displacement for the node at that frame was linearly interpolated from the neighbouring nodes [196].

For the NRIR method, frame-to-frame displacements were found using the Matlab function `imregdemons` (Image Processing Toolbox). This function allowed the smoothness of the calculated displacement field and level of detectable displacements to be specified using the “Accumulated Field Smoothing” and “Pyramid Levels” input arguments. Since this

function gives the displacements for each pixel location, cubic spline interpolation was used to find the displacements at the predefined nodes.

For both approaches, to improve accuracy, a combination of forward and backward tracking was used to calculate the frame-to-frame step displacements: first, the forward step displacements were calculated from the current frame to the next frame using one of the above methods. The nodal positions were then updated with these displacements, and the backward step displacements of these nodes back to the current frame were calculated. The actual nodal step displacements were then taken to be the average of the forward and backward displacements.

Displacement field regularisation

Any noise in the displacement field is amplified when differentiating to obtain strain. The displacement field was therefore regularised using either a median filter [188, 198], 2D second-order polynomial fit [94, 191], 2D cubic smoothing spline [246], a fourth order low-pass Butterworth filter, or a combination of these methods. Regularisation was either applied to the nodal step displacements before updating the nodal position at each frame, or to the final cumulative displacements.

Removal of stray nodes

At each frame, any nodes that moved out of the ultrasound field of view were removed. Furthermore, after calculating the displacements for all frames, any nodes that moved out of a manually selected region of interest in the B-mode image of the last frame were removed. This assured that nodes that strayed away from the tissue of interest did not invalidate the measured strain.

Strain calculation

Since the nodal grid was aligned with the gross tissue geometry in the initial position and, assuming that this corresponded to the ligament fibre alignment, the longitudinal strains

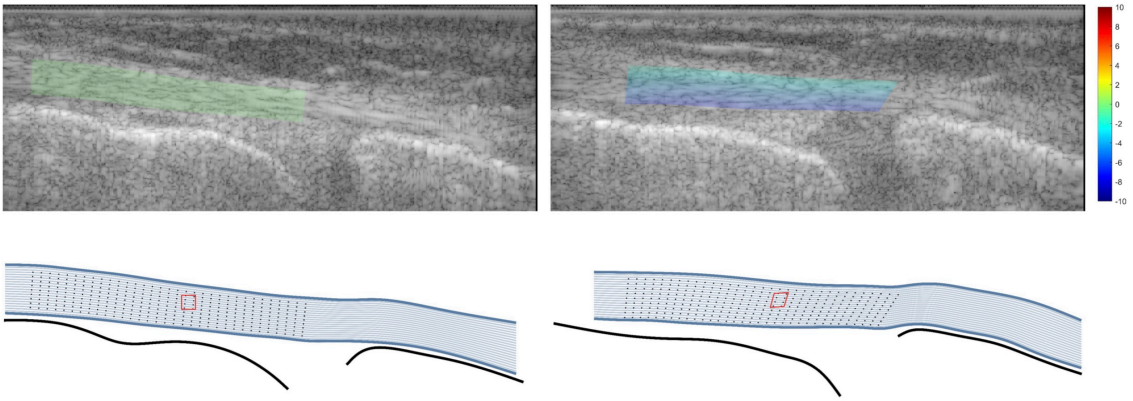


FIGURE 4.2 Depiction of how longitudinal ligament strains were calculated, which was based on the change of distance between neighbouring nodes within a nodal grid that follows the shape of the ligament. The top row shows how the selected region of interest strains from the first **(top left)** to the last **(top right)** frame for an example ligament measurement. The sketches below show how the region of interest was populated with a nodal grid **(bottom left)** and how this grid deformed from the first to the last frame **(bottom right)**. The red box illustrates how a small kernel within the ligament deforms, undergoing both longitudinal and transverse strains, as well as shear strain due to relative sliding of different layers of the ligament; as shown in Addendum 4A, this shear component has a significant impact on the principal strains.

along the fibre direction could be calculated by dividing the change in distance between nodes by the original nodal spacing of the first frame (Equation 4.1) (Figure 4.2). It should be noted that this gave a relative tissue strain measurement with respect to the tissue state in the first frame, which is only equal to the absolute strain if the tissue is initially unloaded. Alternatively, the stretch tensor can be computed via deformation gradient decomposition, from which the principal strains within the ligament can be determined, as demonstrated in Addendum 4A of this chapter. Addendum 4A also describes a new deformation gradient decomposition method which allows the longitudinal ligament strain to be calculated for different initial ligament fibre orientations. Since the ligament fibre orientation has to be manually defined based on the ultrasound images, this tool can help assess how errors during ligament selection affect the calculated strain.

$$E_L\Big|_{i,j} = \frac{D2\Big|_{i,j} - D1\Big|_{i,j}}{D1\Big|_{i,j}} \tag{4.1}$$

$D1\Big|_{i,j}$ = distance between $node|_{i,j-1}$ and $node|_{i,j+1}$ in the first frame

$D2\Big|_{i,j}$ = distance between $node|_{i,j-1}$ and $node|_{i,j+1}$ in the final frame

$E_L\Big|_{i,j}$ = longitudinal strain along the ligament at $node|_{i,j}$

4.3.2 Optimisation procedure to tune algorithmic settings

The aim of the optimisation procedure was to create application-specific implementations of the speckle tracking algorithm outlined above by finding algorithmic settings with which the full tissue motion is captured and repeatability is maximised. This optimisation routine consisted of two steps: a displacement field convergence analysis and a surrogate optimisation scheme based on repeatability of repeated measurements.

Displacement field convergence analysis

Certain settings, such as, for example, frame rates which are too slow to capture the underlying tissue motion, can lead to underestimation of the displacement or strain levels, as some of the motion is not captured. However, these settings may still produce repeatable measurements as, on average, the same amount of data is lost across each of the repeated acquisitions. This is problematic since the main optimisation scheme (described in the next section) is based on maximising repeatability. Thus, a pre-optimisation convergence analysis was performed to find the minimum settings for which the full underlying tissue motion is captured.

Here, it was found that the following settings of the implemented speckle tracking algorithm (Figure 4.1) required a pre-optimisation convergence check.

1. Frame rate: the rate at which the frames of the ultrasound video are collected. It has previously been shown that the measured tissue strain can depend on the used frame rate [51].

2. NRIR pyramid levels: a setting of the Matlab non-rigid image registration algorithm (`imregdemons`), which defines the number of multi-resolution image pyramid levels. Larger frame-to-frame displacements are better captured with higher pyramid levels.

3. Block-matching axial/lateral maximum displacement: this parameter defines how much larger the search kernel is compared to the reference kernel when using the block-matching displacement calculation method (Figure 4.1). A larger size difference

allows for larger frame-to-frame displacements to be measured, but also increases the risk of false matching of the kernels.

The convergence check was based on the lateral displacements since, in the applications of this project, most of the tissue motion was in this direction. The nodal displacement field was calculated using the block-matching and NRIR methods with varying frame rates and NRIR pyramid levels or block-matching axial/lateral maximum displacement settings. To allow for regular frame rate spacing during the convergence analysis, the original ultrasound videos were downsampled from 30 Hz using the Matlab function `resample`, which uses interpolation between frames to produce the desired frame rates.

Next, the mean absolute lateral displacement across the entire nodal grid was calculated for the different combinations of settings (Figure 4.3). As the settings were increased, the measured lateral tissue motion plateaued, indicating the point at which convergence was reached and the tissue motion was fully captured. Subsequently, relative errors in the lateral displacement measurements were calculated, both with respect to frame rate and

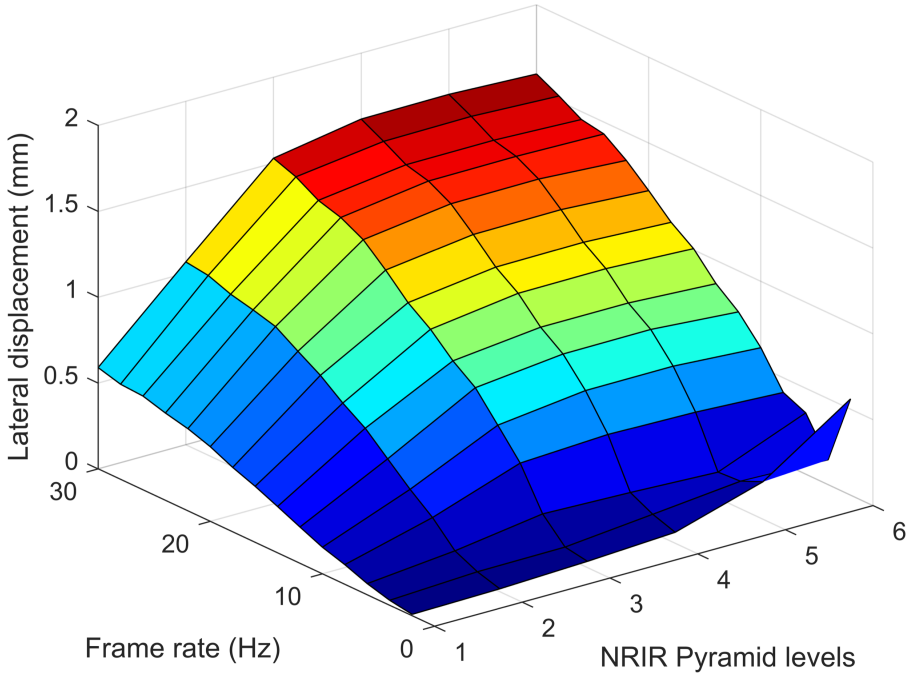


FIGURE 4.3 Example convergence analysis to find minimum settings for the NRIR method. The average lateral displacement in the imaged medium was calculated for a one-second interval with different combinations of NRIR pyramid levels and processing frame rates. As can be seen, displacements are underestimated for settings that are too low, but converge as the settings are increased.

with respect to NRIR pyramid levels or block-matching axial/lateral maximum displacement. Settings were said to be converged if the averages of both relative errors were below $5\,\%$ (Equations 4.2-4.3).

$$\epsilon_{i,j}\Big|_{\text{w.r.t } i} = \frac{u_{i,j} - u_{i-1,j}}{u_{i,j}} \tag{4.2}$$

$$\epsilon_{i,j}\Big|_{\text{w.r.t } j} = \frac{u_{i,j} - u_{i,j-1}}{u_{i,j}} \tag{4.3}$$

i = ultrasound processing frame rate

j = NRIR pyramid level or block-matching axial/lateral maximum displacement

u = lateral displacement

ϵ = relative error

Only converged settings for these parameters were then used in the second step of the optimisation routine.

Surrogate optimisation scheme

Next, settings were optimised for repeatability with a surrogate optimisation scheme (Matlab function `surrogateopt`), an efficient solver that is able to find function minima with fewer function evaluations, making it particularly useful for applications with expensive objective functions. In short, this algorithm initially solves the objective function at random sample points, then creates a "surrogate" of the objective function by interpolating through these points, and subsequently searches for the minimum of the objective function by solving at new adaptive points, updating the surrogate with each new function evaluation. These adaptive points are chosen based on a merit function, which predicts at which location a new objective function evaluation will be most beneficial in the search for minimum. Once the optimisation converges to a minimum value, the surrogate resets, i.e., a new surrogate with new random sample points is constructed and the search for

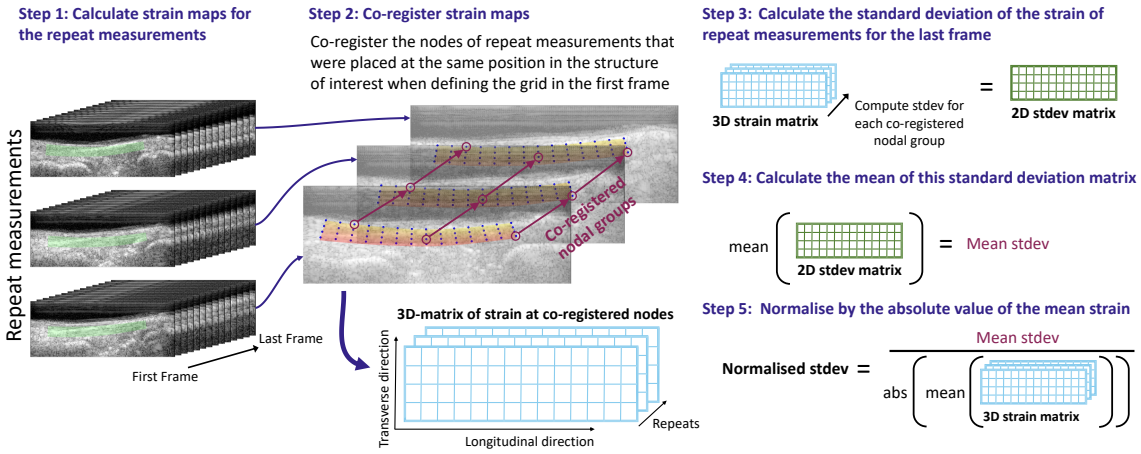


FIGURE 4.4 Steps of the to-be-minimised objective function of the optimisation, which calculates the normalised standard deviation of the strain maps of repeat measurements.

minimum is repeated.

Here, the to-be-minimised objective function was set to the normalised standard deviation of repeat strain maps, which from now on will be referred to as the "quality penalty" (Figure 4.4). This was computed by: (i) calculating the strain maps for repeat measurements with the current sample settings, (ii) co-registering nodes to align repeat strain maps, (iii) calculating the standard deviation of strain for each of the co-registered nodal groups at the end of the loading cycle (last frame), (iv) calculating the mean of this standard deviation of all nodal groups and (v) normalising this by the absolute value of the mean strain.

The optimisation was performed on 30 AMD Rome CPUs with up to 200 GB RAM. The convergence criterion for a surrogate reset was defined to be fulfilled if a minimum of the objective function has been found, with all the immediately neighbouring points having been evaluated. The stopping criterion for a surrogate optimisation is typically set to a total number of iterations; here, this was set to 1500 iterations.

The specific range of settings for each parameter of the algorithm that should be trialled during the optimisation can be adapted based on, for example, the results of the pre-optimisation convergence check and the capabilities of the used ultrasound acquisition system. The range of settings tested for the applications of this project will be outlined in Chapter 6.

4.4 Discussion

4.4.1 Comparison to state-of-the-art

The work in this chapter demonstrates several new contributions to the field of ultrasound speckle tracking:

1. **Speckle tracking framework:** a flowchart for the speckle tracking algorithm was presented (Figure 4.1), which was structured such that settings could be easily varied depending on the application. This framework enables the integration of various features from existing speckle tracking algorithms, allowing them to be combined into new versions of the algorithm. For example, a new implementation could use a NRIR-based method together with displacement field regularisation techniques that have previously only been tested with the block-matching method [198, 246].

2. **Non-uniform 2D nodal grid:** ligaments are often curved as they wrap around bone, with the orientation changing throughout joint movement. Thus far, *in situ* speckle tracking in ligaments has only been trialled with a 1D line of nodes positioned at the centre of the ligament [51, 166]. Here, an algorithm was developed that populates the region of interest with a 2D non-uniform grid that conforms to the tissue geometry.

3. **Strain calculation:** for tendons and ligaments, the longitudinal/transverse strains along/across fibres are of greatest interest. In previous applications of the speckle tracking algorithm to tendons, the fibres were mostly straight and parallel to the

lateral axis of the ultrasound images. As a result, longitudinal and transverse strains could be approximated by the lateral and axial strains, which were easily obtained by differentiating the lateral and axial displacement field [198]. However, for curved ligaments, calculating strains along and across the non-uniform grid provides a more accurate measure. Here, two methods for calculating these longitudinal and transverse strains were developed. Firstly, strains can be obtained by evaluating the change in distance between neighbouring nodes. Alternatively, a set of equations (Equation 4A.11-4A.14) were derived based on a novel deformation gradient decomposition method. These equations can additionally assess how the calculated strains vary for different fibre orientation angles (Addendum 4A).

4. **Optimisation routine:** optimising the settings of the speckle tracking algorithm based on displacement field convergence and repeatability is a new concept, and its ability to produce well-tuned, application-specific algorithms is demonstrated in Chapter 6. Since it allows algorithmic settings to be adjusted without prior knowledge about the speckle tracking algorithm and without ground truth data, this tool will enable new research groups to adopt the ultrasound technique more easily, thereby accelerating its application to a wider range of uses.

4.4.2 Conclusion

In summary, the proposed speckle tracking framework together with the novel optimisation routine facilitates the development of new, application-specific versions of the algorithm that leverage the most suitable features from previous implementations. This approach does not rely on ground-truth data, which can often only be obtained with *ex vivo* specimens and expensive digital image correlation (DIC) equipment. Additionally, it was designed to be compatible with ultrasound images regardless of data type or acquisition method, making it adaptable to various ultrasound machines. Thus, this non-invasive technology can be trialled more easily in new fields where assessing tissue deformation or strain can provide valuable insights into the tissue's biomechanical functions.

Addendum A: Strain calculation using deformation gradient decomposition

In the speckle tracking implementation used throughout this project, the strain along the ligament was determined by calculating the change in distance between nodes that follow the shape of the ligament, as discussed in Section 4.3.1. Alternatively, the deformation gradient $\boldsymbol{F}$ (Equation 4A.1) can be decomposed to separate the motion into rigid body rotations and deformations.

The methods below will demonstrate how the principal strains in the ligament can be extracted from the displacement field using a common decomposition method. Additionally, a custom decomposition method will be proposed, which allows the longitudinal and transverse strains along and across the ligament to be obtained.

The deformation gradient can be derived from the displacement field gradients using the following equation [247].

$$\boldsymbol{F} = \boldsymbol{I} + \frac{\partial \boldsymbol{u}}{\partial \boldsymbol{x}} = \begin{bmatrix} 1 + \frac{\partial u}{\partial x} & \frac{\partial u}{\partial y} \\ \frac{\partial v}{\partial x} & 1 + \frac{\partial v}{\partial y} \end{bmatrix} \tag{4A.1}$$

$\boldsymbol{F}$ = deformation gradient

$\boldsymbol{I}$ = identity matrix

$\boldsymbol{u}$ = displacement vector

$\boldsymbol{x}$ = position vector

Obtaining the displacement field gradients with respect to x and y is straightforward for a uniform grid. Equation 4A.2 can be applied when using a non-uniform grid, such as the ones used for the ligaments in this study (Figure 4.2).

$$\begin{bmatrix} \frac{\partial u}{\partial x} & \frac{\partial u}{\partial y} \\ \frac{\partial v}{\partial x} & \frac{\partial v}{\partial y} \end{bmatrix} = \begin{bmatrix} \frac{\partial u}{\partial i} & \frac{\partial u}{\partial j} \\ \frac{\partial v}{\partial i} & \frac{\partial v}{\partial j} \end{bmatrix} \begin{bmatrix} \frac{\partial x}{\partial i} & \frac{\partial x}{\partial j} \\ \frac{\partial y}{\partial i} & \frac{\partial y}{\partial j} \end{bmatrix}^{-1} \tag{4A.2}$$

$i =$ rows of the non-uniform grid

$j =$ columns of the non-uniform grid

The method presented here to obtain principal strains is based on the works of Bob McGinty [247]. First, polar decomposition is used to split the deformation gradient $\boldsymbol{F}$ into an orthogonal matrix multiplied by a symmetric matrix, i.e. a two-step process of deformation with equal shear components followed by rigid body rotation:

$$\boldsymbol{F} = \boldsymbol{R} \cdot \boldsymbol{U} \tag{4A.3}$$

$\boldsymbol{R} =$ rigid body rotation matrix

$\boldsymbol{U} =$ right stretch tensor

Note, that the order can also be reversed, i.e. rotation followed by deformation, but for brevity the workings here will focus on deformation followed by rotation.

Polar decomposition allows the rigid body rotation and right stretch tensor to be determined in the following manner:

$$\boldsymbol{F}^T \cdot \boldsymbol{F} = (\boldsymbol{R} \cdot \boldsymbol{U})^T \cdot (\boldsymbol{R} \cdot \boldsymbol{U}) = \boldsymbol{U}^T \cdot \boldsymbol{R}^T \cdot \boldsymbol{R} \cdot \boldsymbol{U} \tag{4A.4}$$

Since rotation matrices are orthogonal matrices, $\boldsymbol{R}^T = \boldsymbol{R}^{-1}$. After substitution:

$$\boldsymbol{F}^T \cdot \boldsymbol{F} = \boldsymbol{U}^T \cdot \boldsymbol{R}^{-1} \cdot \boldsymbol{R} \cdot \boldsymbol{U} = \boldsymbol{U}^T \cdot \boldsymbol{U} \tag{4A.5}$$

Next, since $\boldsymbol{U}$ is symmetric:

$$\boldsymbol{U}^T \cdot \boldsymbol{U} = \boldsymbol{U} \cdot \boldsymbol{U} = \boldsymbol{U}^2 \tag{4A.6}$$

And thus, the final decomposed equations to obtain the rigid body rotation and right stretch tensor are given below:

$$\boldsymbol{U}^2 = \boldsymbol{F}^T \cdot \boldsymbol{F} \tag{4A.7}$$

$$\boldsymbol{R} = \boldsymbol{F} \cdot \boldsymbol{U}^{-1} \tag{4A.8}$$

The process for finding the square root of symmetric matrices has previously been demonstrated [247]. In Matlab, the function `sqrtm` can be used.

The principal strains and directions can then be calculated by determining the eigenvalues and eigenvectors of $\boldsymbol{U} - \boldsymbol{I}$.

However, principal strains may not be the most meaningful metric when looking at the deformation of ligaments. If, for example, there is relative movement of the different layers of the ligament, the stretch tensor will contain shear components. Since principal strains occur along the principal axes where shear strains are zero, the principal strain directions will point diagonally across the ligament rather than along the longitudinal and transverse directions of the ligament. An example of this is shown in Figure 4A.1, where the principal strains and principal strain directions have been calculated for the same measurement as in the previous example of Figure 4.2 in Section 4.3.1.

Instead, an alternative decomposition of the deformation gradient $\boldsymbol{F}$ is proposed here, which splits it into steps of deformation and rigid body rotations that are more meaningful in the context of ligament motion.

Consider how the small kernel that was highlighted in Figure 4.2 deforms from the initial to the final state. The values of interest are E_L and E_T, the longitudinal and transverse strains along and across the ligament fibres. A shear component E_S that allows for relative sliding between layers of the ligament will also be included in the decomposition. The stretch tensor consisting of these strains will be called the ligament stretch tensor, $\boldsymbol{U_{LIG}}$. Unlike the right stretch tensor $\boldsymbol{U}$ of the polar decomposition, symmetry is not assumed, but rather it is assumed that there is no relative sliding across fibres, i.e. $U_{LIG,21} = 0$.

Figure 4A.2 shows the transformations applied to the kernel. Since the normal and shear

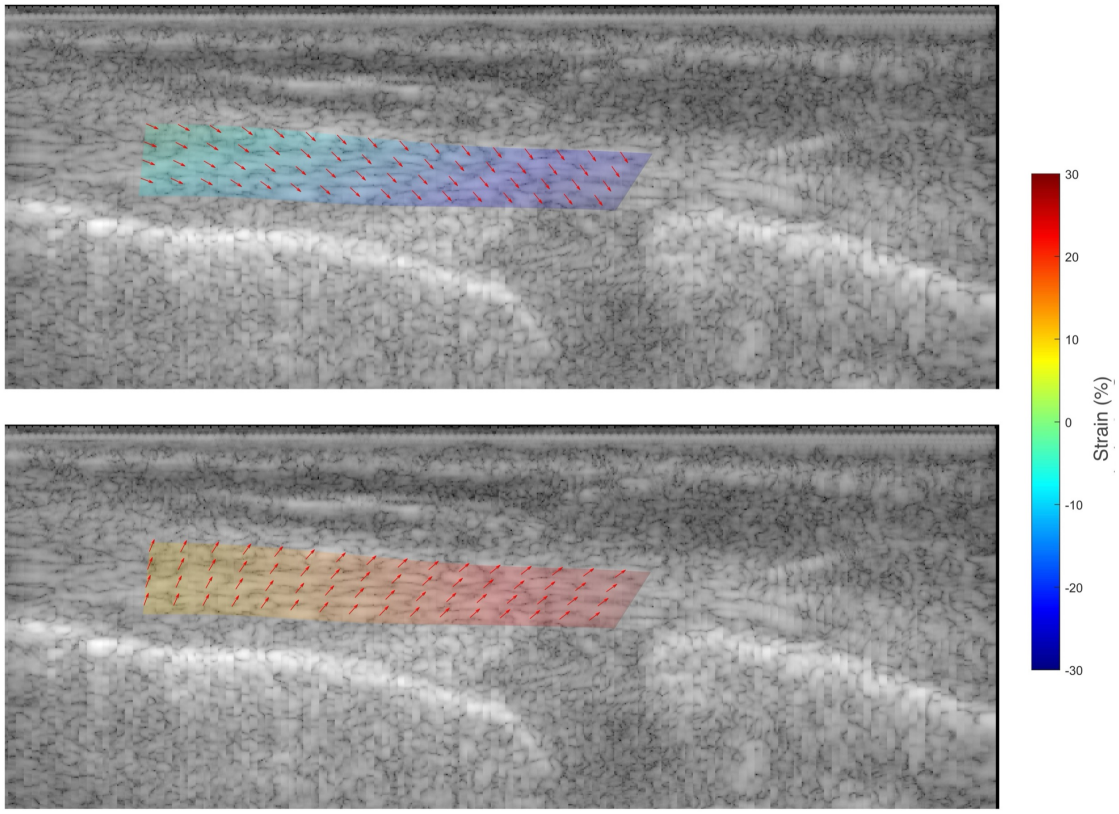


FIGURE 4A.1 Principal strains within the ligament calculated for an example measurement for which there was relative sliding between the different layers of the ligament. Principal strains and directions were obtained by calculating the eigenvalues and eigenvectors of the right stretch tensor.

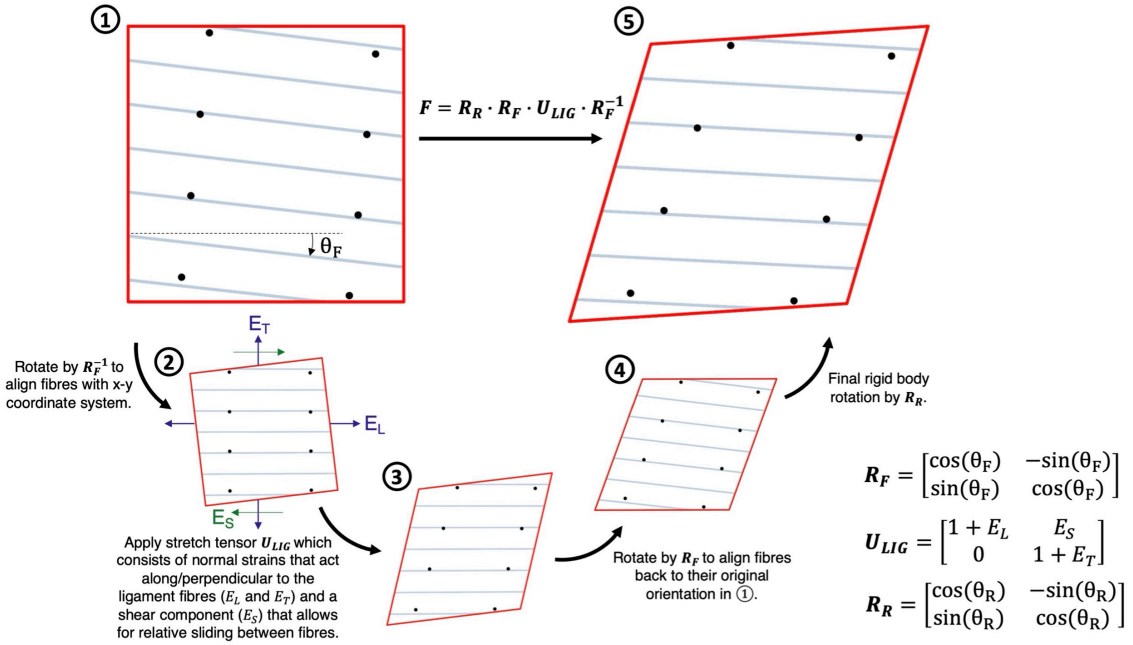


FIGURE 4A.2 Deformation gradient decomposition scheme, which allows evaluation of the stretch tensor (U_{LIG}) that contains the longitudinal and transverse strains along and across the ligament. These strain metrics are more relevant when analysing the ligament strain behaviour.

components of the stretch tensor $\boldsymbol{U_{LIG}}$ act in the $x-y$ coordinate system, the kernel first needs to be rotated so that the fibres are aligned with the x-axis ($\boldsymbol{R_F}^{-1}$). Next, the stretch tensor is applied, after which the kernel is rotated back so that the fibres are aligned to their original orientation ($\boldsymbol{R_F}$). Lastly, a final rigid body rotation is applied ($\boldsymbol{R_R}$).

This results in the following decomposition of the deformation gradient:

$$\boldsymbol{F} = \boldsymbol{R_R} \cdot \boldsymbol{R_F} \cdot \boldsymbol{U_{LIG}} \cdot \boldsymbol{R_F}^{-1} \tag{4A.9}$$

$\boldsymbol{R_R}$ = rigid body rotation matrix

$\boldsymbol{R_F}$ = fibre angle rotation matrix

$\boldsymbol{U_{LIG}}$ = ligament stretch tensor

After rearranging:

$$\boldsymbol{U_{LIG}} = \boldsymbol{R_F}^{-1} \cdot \boldsymbol{R_R}^{-1} \cdot \boldsymbol{F} \cdot \boldsymbol{R_F} \tag{4A.10}$$

After simplifying:

$$\theta_R = \arctan\left(-\frac{F_{11}\tan(\theta_F) + F_{12}\tan^2(\theta_F) - F_{21} - F_{22}\tan(\theta_F)}{F_{11} + F_{12}\tan(\theta_F) + F_{21}\tan(\theta_F) + F_{22}\tan^2(\theta_F)}\right) \tag{4A.11}$$

$$\begin{aligned} E_L = {} & F_{11}\left\{\cos^2(\theta_F)\cos(\theta_R) - \sin(\theta_F)\cos(\theta_F)\sin(\theta_R)\right\} \\ & + F_{12}\left\{\sin(\theta_F)\cos(\theta_F)\cos(\theta_R) - \sin^2(\theta_F)\sin(\theta_R)\right\} \\ & + F_{21}\left\{\sin(\theta_F)\cos(\theta_F)\cos(\theta_R) + \cos^2(\theta_F)\sin(\theta_R)\right\} \\ & + F_{22}\left\{\sin^2(\theta_F)\cos(\theta_R) + \sin(\theta_F)\cos(\theta_F)\sin(\theta_R)\right\} - 1 \end{aligned} \tag{4A.12}$$

$$\begin{aligned} E_T = {} & F_{11}\left\{\sin^2(\theta_F)\cos(\theta_R) + \sin(\theta_F)\cos(\theta_F)\sin(\theta_R)\right\} \\ & + F_{12}\left\{-\sin(\theta_F)\cos(\theta_F)\cos(\theta_R) - \cos^2(\theta_F)\sin(\theta_R)\right\} \\ & + F_{21}\left\{-\sin(\theta_F)\cos(\theta_F)\cos(\theta_R) + \sin^2(\theta_F)\sin(\theta_R)\right\} \\ & + F_{22}\left\{\cos^2(\theta_F)\cos(\theta_R) - \sin(\theta_F)\cos(\theta_F)\sin(\theta_R)\right\} - 1 \end{aligned} \tag{4A.13}$$

$$
\begin{aligned}
E_S = F_{11} &\left\{-\sin(\theta_F)\cos(\theta_F)\cos(\theta_R) + \sin^2(\theta_F)\sin(\theta_R)\right\} \\
&+ F_{12}\left\{\cos^2(\theta_F)\cos(\theta_R) - \sin(\theta_F)\cos(\theta_F)\sin(\theta_R)\right\} \\
&+ F_{21}\left\{-\sin^2(\theta_F)\cos(\theta_R) - \sin(\theta_F)\cos(\theta_F)\sin(\theta_R)\right\} \\
&+ F_{22}\left\{\sin(\theta_F)\cos(\theta_F)\cos(\theta_R) + \cos^2(\theta_F)\sin(\theta_R)\right\}
\end{aligned}
\tag{4A.14}
$$

$E_L =$ longitudinal strain along the ligament

$E_T =$ transverse strain across the ligament

$E_S =$ shear strain

$\theta_F =$ ligament fibre orientation angle

$\theta_R =$ rigid body rotation angle

Equations 4A.11-4A.14 can be applied to the example measurement from Figure 4.2. The fibre orientation angle is taken to be the angle between neighbouring nodes. Figure 4A.3 shows the results for the longitudinal strain E_L. The results are identical to the strains obtained using the first strain calculation method demonstrated in Figure 4.2 (RMSE $= 2.6 \times 10^{-4}\,\%$). Due to its simplicity, the first method was used in this study. However, the second method facilitates analysis of how the initial fibre orientation affects the calculated strains. Since this fibre angle is based on the shape and orientation of the manually selected ligament region of interest, future analysis could use this second method to investigate how human error during ligament selection affects the final results.

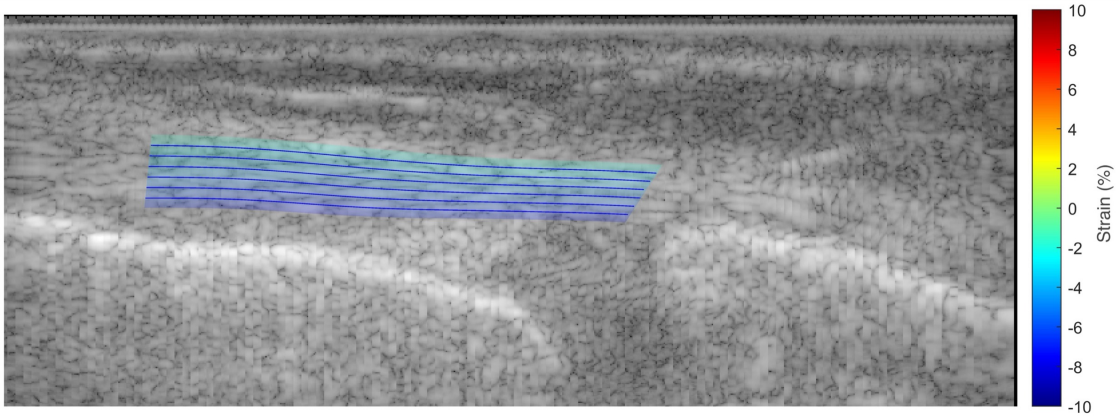


FIGURE 4A.3 Longitudinal ligament strains obtained using the proposed ligament stretch tensor definition. The blue lines show the ligament fibres in the final frame, obtained by computing the streamlines of the vector field of the final fibre orientations (initial fibre orientation angle + rigid body rotation angles).

05

Ultrasound Safety

5.1 Introduction **112**
5.2 Materials and Methods **115**
5.3 Results **126**
5.4 Discussion **130**

I would like to acknowledge the help received by Antonio De Sanctis, the NDE lab technician, in helping to set up the hydrophone wave tank experiment. Specifically, the control of the 3D motorised positioning system was based on Matlab scripts kindly provided by Antonio.

List of Abbreviations

ARF	Acoustic radiation force
BMUS	British Medical Ultrasound Society
CPWC	Coherent plane-wave compounding
FDA	Food and Drug Administration
MI	Mechanical index
SNR	Signal-to-noise ratio
SSI	Supersonic shear imaging
SWEI	Shear wave elastography imaging
TOF	Time-of-flight
TI	Thermal index
TIB	Thermal index bone

5.1 Introduction

All ultrasound transmission modes were implemented using custom scripts on the Verasonics Vantage 128 ultrasound system. As a non-CE/non-UKCA marked research system, the Verasonics machine does not have any inbuilt acoustic output limits for safe clinical use. Excessive acoustic outputs can cause mechanical tissue damage through inertial cavitation or thermal tissue damage through heating, which can, for example, result in tissue lesions, necrosis, and apoptosis [102, 248].

The acoustic outputs can vary significantly between different imaging modes, even when the same ultrasound system and transducer is used [249]. For example, acoustic pressures and intensities can be increased through beam focusing, extending the duration of the

TABLE 5.1 Thresholds for the ultrasound safety indices. British Medical Ultrasound Society (BMUS) values are taken from Table 2 in reference [218] (Guidelines for the safe use of diagnostic ultrasound equipment). Food and Drug Administration (FDA) values are taken from section 5.2.4 and 5.2.8.1.4 in reference [219] (Marketing clearance of diagnostic ultrasound systems and transducers).

Safety index	British Medical Ultrasound Society (BMUS) [218]	Food and Drug Administration (FDA) [219]
MI	0.7 ($\mathrm{MI}>0.7$ can be used without contrast agents, but with increased risk of cavitation)	1.9
TI	1 (For $1 < \mathrm{TI} < 6$, exposure time should be limited depending on TI magnitude, e.g. 4 min for a $\mathrm{TI} = 3$)	6 (Not an upper limit, but manufacturers have to provide a justification for $\mathrm{TI}>6$)
I_{sppa}	-	$190\ \mathrm{W/cm^2}$
I_{spta}	-	$720\ \mathrm{mW/cm^2}$

transmitted pulse, increasing the frame rate or increasing the transducer voltage [102]. Therefore, it is crucial that the acoustic field is characterised for each imaging mode that is to be used for *in vivo* applications. The following four safety metrics are most widely used to quantify the risk of mechanical and thermal damage. Thresholds for these acoustic safety indices are provided by regulatory bodies such as the US Food and Drug Administration (FDA) and British Medical Ultrasound Society (BMUS) (Table 5.1). To date, no adverse bio-effects have been reported when using ultrasound at diagnostic acoustic output levels that are below these thresholds [250].

1. Mechanical index (MI): this metric quantifies the risk of mechanical bio-effects due to inertial cavitation. The pressure variation due to ultrasound wave propagation can cause expansion and contraction of gas bubbles within the tissue. Inertial cavitation can occur when the pressure variation is so high that the bubbles collapse catastrophically, leading to tissue damage [250]. Bubble formation and cavitation is more likely to occur in liquid media (e.g., blood or cysts) or tissue containing gas (e.g., lung or intestines), or when gas-bubble contrast agents are used [102, 103]. Furthermore, cavitation is less likely to occur with high-frequency ultrasound transmissions, since the shorter time period of the pulse reduces the time during which bubbles can form and grow [102].

2. Thermal index (TI): this metric is an indicator of the expected temperature increase within the tissue due to the ultrasound transmissions. It provides the ratio between the power emitted by the transducer to the power needed to raise the tissue temperature by $1\,^{\circ}\mathrm{C}$. Soft-tissue will absorb acoustic energy from the ultrasound waves travelling through it. If the rate of energy dissipation is less than the rate of energy absorption, the tissue will heat up [102, 103].

3. Spatial-peak pulse-average intensity (I_{sppa}): this is a secondary metric to assess the likelihood of mechanical damage due to cavitation. The pulse-average intensity measures the average over a single pulse and therefore detects the instantaneous peaks in intensity that may lead to mechanical damage [102].

4. Spatial-peak temporal-average intensity (I_{spta}): this is an additional metric to assess the risk of thermal damage [102]. Intensity measures the average power over time flowing per unit cross-sectional area and, thus, better measures the likelihood of localised tissue temperature rise that may occur when the beam area is small and acoustic energy is dissipated less rapidly [102]. By taking the temporal-average of the intensity, which includes the "off" period between frames when there is a short pause between transmissions, the balance between energy deposition and dissipation within the tissue can be assessed.

All safety metrics can be calculated from the acoustic pressure distribution of the insonified field. These pressures are most commonly measured using a needle hydrophone, a high frequency underwater microphone that generates a voltage waveform when subjected to an acoustic pressure [103]. To get the pressure map for the entire insonified field, the hydrophone is incrementally moved through the field using a 3D mechanical translation stage, capturing the pressure variation with time for the full ultrasound transmission sequence at each location [150, 249]. Alternatively, for more accurate acoustic power measurements, which are used in the calculation of the thermal index, a radiation force balance can be used. This is a highly absorbent target which measures the acoustic radiation force due to the incident ultrasound waves [102, 251]. However, these can only give the spatial-average power at a certain distance from the transducer and, thus, cannot measure how the beam varies spatially, which is required for the calculation of the mechanical index or the spatial-peak intensities [251].

The following work shows the measurement and post-processing procedure to characterise the acoustic fields for the imaging modes implemented in this study, both for the shear wave imaging and speckle tracking techniques, ensuring that these are safe for *in vivo* applications.

5.2 Materials and Methods

5.2.1 Calculation of safety indices

The safety indices were calculated from the measured hydrophone voltages using Equations 5.1-5.18, which follow the IEC 62359 standard [250] (*Ultrasonics - Field characterization - Test methods for the determination of thermal and mechanical indices related to medical diagnostic ultrasonic fields*) and IEC 62127 standard [252] (*Ultrasonics - Hydrophones*).

All safety indices are related to the acoustic pressure in the insonified field, which can be calculated from the measured hydrophone voltages using the hydrophone sensitivity:

$$p(x, y, z, t) = \frac{V(x, y, z, t)}{M_L(f_c)} \tag{5.1}$$

f_c = transducer transmission centre frequency

M_L = hydrophone sensitivity

p = instantaneous acoustic pressure

t = time

V = measured hydrophone voltage

x = lateral position (along the transducer face)

y = elevational position (out of the imaging plane)

z = axial position (distance away from the transducer face)

The sensitivity of the hydrophone is frequency-dependent and is defined by calibration data, which was provided by the hydrophone supplier for frequencies between 1 and $30\,\mathrm{MHz}$; interpolation was used to obtain the sensitivity at the centre frequency of the transmitted ultrasound waves.

As the transmitted ultrasound waves travel through the soft tissue, some energy is deposited in the tissue, resulting in a decrease in acoustic pressures with increased distance from the transducer. This attenuation is not only depth-dependent, but also frequency-dependent, with high-frequency ultrasound waves being subject to greater attenuation [102, 103].

Compared to the attenuation in soft tissue, ultrasonic waves undergo almost no attenuation in water ($\alpha = 0.5 - 1.0$ vs $0.0022\,\mathrm{dB/cm/MHz}$, respectively) [102, 103]. Thus, to estimate the pressure field that would exist in soft tissue, the acoustic pressure field obtained from the hydrophone measurements performed in water are "derated" using Equation 5.2 below. To be conservative and ensure that pressures are not underestimated, a lower attenuation of $0.3\,\mathrm{dB/cm/MHz}$ is used for deration, as defined in IEC 62359 [250].

$$p_\alpha(x, y, z, t) = p(x, y, z, t) \times 10^{\frac{-\alpha z f_c}{20dB}} \tag{5.2}$$

p_α = derated instantaneous acoustic pressure

α = acoustic attenuation coefficient

Mechanical index

The risk of cavitation is related to the derated peak rarefaction pressure, i.e. the minimum derated pressure that occurs in the medium due to the transmitted ultrasound beam, both with respect to space and time [103] (Figure 5.1). Thus, the mechanical index is based on this value. When using focused beams, the peak rarefaction pressure will be located in the focal region [103].

$$p_{r,\alpha} = |min\left[p_\alpha(x, y, z, t)\right]| \tag{5.3}$$

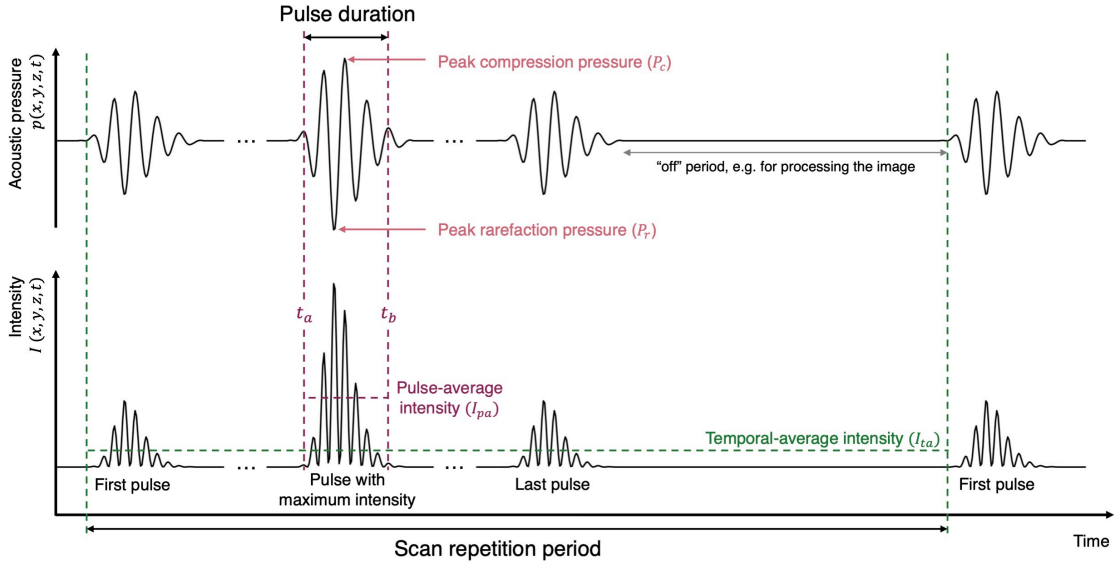


FIGURE 5.1 Pressure and intensity waveforms for a point in the insonified field (based on illustrations produced by Haar et al. [103]). The peak compression and rarefaction pressure are the maximum and minimum pressures during the full scan repetition period. Temporal-average intensity is the average intensity over the scan repetition period. Pulse-average intensity is the average intensity over the pulse of maximum intensity.

$$\mathrm{MI} = \frac{p_{r,\alpha}}{C_{\mathrm{MI}}\sqrt{f_c}} \tag{5.4}$$

$C_{\mathrm{MI}} = 1\,\mathrm{MPa}/\sqrt{\mathrm{MHz}}$

MI = mechanical index

$p_{r,\alpha}$ = derated peak rarefaction pressure

Intensity metrics

The derated intensity of the ultrasound beam is calculated using Equation 5.5.

$$I_\alpha(x, y, z, t) = \frac{{p_\alpha}^2(x, y, z, t)}{\rho c} \tag{5.5}$$

I_α = derated instantaneous intensity

c = velocity of sound in water ($1500\,\mathrm{m/s}$)

ρ = density of water ($1000\,\mathrm{kg/m^3}$)

To obtain the pulse-average and temporal-average intensities, the intensity is either

averaged across a single pulse or across the entire scan repetition period, respectively (Figure 5.1). For scanning imaging modes for which a sequence of different transmissions that do not follow the same acoustic path is used, the scan repetition period spans from the start of the first transmitted pulse of the sequence to the start of the first pulse of the next sequence [250, 252]. Here, the push pulse of shear wave imaging is a non-scanning imaging mode and, thus, the scan repetition period is simply equal to the time between the transmission of one push beam and the next push beam, i.e. the reciprocal of the pulse repetition rate. However, conventional and coherent plane-wave compounding (CPWC) imaging are scanning modes and, therefore, the scan repetition period is the reciprocal of the frame rate, encompassing all the transmissions that make up one frame as well as the "off" period during which the frames are processed [103]. The pulse-average intensity, on the other hand, is only calculated for the duration of the one pulse for which the intensity is highest. The spatial-peak values are subsequently obtained by finding the maximum of the pulse- and temporal-average intensities in the entire field.

$$I_{sppa,\alpha} = max\left[\frac{\int {p_{pulse,\alpha}}^2(x,y,z,t)\,dt}{\rho c \times \mathrm{PD}}\right] \tag{5.6}$$

$$\mathrm{PD} = 1.25(t_b - t_a) \tag{5.7}$$

$$I_{spta,\alpha} = max\left[\frac{\int {p_\alpha}^2(x,y,z,t)\,dt}{\rho c \times \mathrm{SRP}}\right] \tag{5.8}$$

$I_{sppa,\alpha}$ = derated spatial-peak pulse-average intensity

$I_{spta,\alpha}$ = derated spatial-peak temporal-average intensity

PD = pulse duration

$p_{pulse,\alpha}$ = derated instantaneous acoustic pressure for the pulse of maximum intensity

SRP = scan repetition period

t_a = the time at which the time integral is 10 % of the full integral

t_b = the time at which the time integral is 90 % of the full integral

Thermal index

Lastly, the thermal index is calculated, which gives the ratio of the total power over the ultrasound transmissions to the power required to raise the temperature of the soft tissue by $1\,^{\circ}\mathrm{C}$:

$$\mathrm{TI} = P_0 / P_{deg} \tag{5.9}$$

TI = thermal index

P_0 = output power of the ultrasound machine

P_{deg} = power required to raise tissue temperature by $1\,^{\circ}\mathrm{C}$

Different models are used to estimate P_{deg}, which take into account the type of tissue that is within the insonified field and whether a scanning or non-scanning imaging mode is used. When imaging tendons and ligaments, the main intended application of this project, one has to consider that the bone to which the ligaments/tendons attach to will likely be located within the ultrasonic beam. Thus, for non-scanning imaging modes (e.g., the acoustic radiation force (ARF) push pulse), the thermal index bone (TIB) model should be used as specified in IEC 62359 [250]. For scanning imaging modes (e.g., conventional imaging or CPWC), on the other hand, the temperature rise near the transducer surface is typically greater than or similar to the temperature rise at the bone; therefore, the soft-tissue thermal index (TIS) model should be used instead [250]. By using an appropriate heat transfer model for the given tissue types, which considers factors such as thermal conductivity, acoustic absorption, perfusion-related cooling effects, and beam area, the power required to raise the tissue temperature by $1\,^{\circ}\mathrm{C}$ (P_{deg}) can be estimated (refer to section C.3.3 of IEC 62359 [250] for a detailed derivation of the heat transfer models). Thus, the specific thermal indices for the different tissue models can be computed.

The bone thermal index is calculated using Equation 5.10:

$$\mathrm{TIB} = min\left[\frac{\sqrt{P_\alpha(z_b) I_{spta,\alpha}(z_b)}}{C_{\mathrm{TIB1}}}, \frac{P_\alpha(z_b)}{C_{\mathrm{TIB2}}}\right] \tag{5.10}$$

$C_{\mathrm{TIB1}} = 50\,\mathrm{mW/cm}$

$C_{\mathrm{TIB2}} = 4.4\,\mathrm{mW}$

P_α = attenuated output power

TIB = bone thermal index

z_b = depth at which the product of P_α and $I_{spta,\alpha}$ is maximum

The calculation for spatial-peak temporal-average intensity has been shown in the previous section, but note that instead of determining one spatial-peak for the entire insonified field, a spatial-peak is calculated for each of the axial positions scanned by the hydrophone. Next, to estimate the attenuated output power, Equation 5.11 can be used [249, 250]:

$$P_\alpha(z) = I_{spta,\alpha}(z) \times A_{eq}(z) \tag{5.11}$$

The equivalent beam area at different axial positions was estimated from the theoretical beam width and height of an ultrasonic Gaussian beam for the given focal configurations [253]:

$$w(z) = w_a \sqrt{\frac{\left[\frac{z}{F_{lat}}(1+\beta_{lat}^2) - 1\right]^2 + \beta_{lat}^2}{1+\beta_{lat}^2}} \tag{5.12}$$

$$\beta_{lat} = \frac{\lambda F_{lat}}{\pi (w_a/2)^2} \tag{5.13}$$

$$h(z) = h_a \sqrt{\frac{\left[\frac{z}{F_{elev}}(1+\beta_{elev}^2) - 1\right]^2 + \beta_{elev}^2}{1+\beta_{elev}^2}} \tag{5.14}$$

$$\beta_{elev} = \frac{\lambda F_{elev}}{\pi (h_a/2)^2} \tag{5.15}$$

$$A_{eq} = w(z) \times h(z) \tag{5.16}$$

h = beam height

h_a = sub-aperture height (height of transducer elements)

F_{elev} = elevational focal depth

F_{lat} = lateral focal depth

w = beam width

w_a = sub-aperture width (# of transducer push elements $\times$ transducer pitch)

λ = wavelength of the ultrasound waves

Here, for the ARF push pulse, the sub-aperture width was $9.6\,\mathrm{mm}$ (32 transducer elements $\times 0.3\,\mathrm{mm}$ pitch), the sub-aperture height was $5\,\mathrm{mm}$, the elevational focal depth was $18\,\mathrm{mm}$ and the lateral focal depth was $10.1\,\mathrm{mm}$.

The bone thermal index is ultimately calculated for the axial position at which the product of the attenuated spatial-peak temporal-average intensity and power is maximum.

The soft-tissue thermal index for the scanning imaging modes is calculated using Equation 5.17 [250]:

$$\mathrm{TIS} = \frac{P_1 f_c}{C_{\mathrm{TIS1}}} \tag{5.17}$$

$$P_1 = \iint I_{ta}(x, y, z = 0)\, dx\, dy \tag{5.18}$$

$C_{\mathrm{TIS1}} = 210\,\mathrm{mW\ MHz}$

I_{ta} = temporal-average intensity

P_1 = bounded output power at the transducer surface (non-attenuated)

TIS = soft-tissue thermal index

The bounded output power is the non-attenuated power transmitted from the $10\,\mathrm{mm}$ linear length of the transducer that transmits the most power [250]. It is calculated from 2D lateral-elevational hydrophone data which is collected as close to the transducer face as possible. Power is obtained by integrating the temporal-average intensities with respect to space.

5.2.2 Equipment & test setup

Acoustic pressure measurements were performed in a tank filled with room temperature water, which was degassed using a handheld ultrasonic cleaner. The ultrasound transducer was held in place with a clamp such that the radiating transducer face was just submerged below the water and the ultrasound beams were transmitted vertically down into the tank (Figure 5.2). Acoustic pressures were measured using a calibrated NH0200 $0.2\,\mathrm{mm}$ needle hydrophone with a submersible preamplifier and DC coupler (Precision Acoustics, UK). A 3D motorised positioning system, controlled through a Matlab script, located the hydrophone in the water tank below the transducer, with the needle pointing vertically upwards. The output voltage from the hydrophone was recorded at a sampling frequency of $100\,\mathrm{MHz}$ using a portable USB-oscilloscope (Handyscope HS5, TiePie Engineering, Netherlands), which was connected to the hydrophone system with an inline $50\,\Omega$ terminator. The recording length was adjusted to capture all transmissions of one sequence, e.g. all 128 scanlines of the conventional imaging mode or all 30 beam-steered plane-waves of the CPWC mode. The voltage waveforms were filtered post-collection using a bandpass finite impulse response filter (Matlab function `designfilt`; filter order: 60, low- and high-pass cut-off frequencies: 3 and $11\,\mathrm{MPa}$).

To start, the hydrophone was placed at a manually found position of maximum acoustic pressure by incrementally moving it with the motorised positioning system until the output on the oscilloscope was approximately maximised. Next, an automised 3D scanning sequence was started, which moved the hydrophone in small spatial increments in the axial, lateral and elevational direction, pausing briefly at each position to record the pressure waveform. For the imaging modes with focused transmissions, the measurement region was constrained to a small area around the focus ($\sim 0.3 \times 0.5 \times 1\,\mathrm{mm}$) to allow smaller step sizes ($\sim 0.02 \times 0.05 \times 0.1\,\mathrm{mm}$) to be used; thus, the rapidly changing pressure within the focal zone could be captured, ensuring that the point of maximum intensity and mechanical index was measured. For the CPWC imaging mode, a larger region ($\sim 39 \times 2 \times 8\,\mathrm{mm}$) was scanned with larger step sizes ($\sim 1 \times 0.1 \times 1\,\mathrm{mm}$) to capture the wider plane-wave beams.

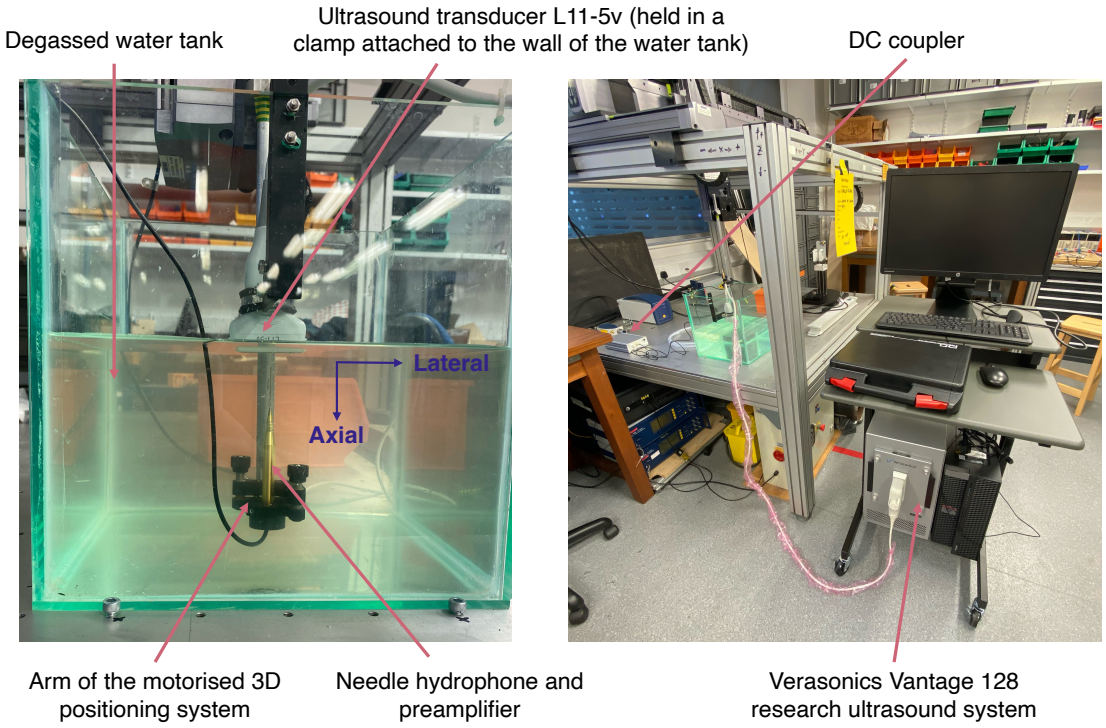


FIGURE 5.2 Test setup for the hydrophone measurements to characterise the acoustic wave-field of the ultrasound imaging modes used in this project.

Additionally, for the scanning imaging modes, a 2D scan capturing the bounded output power from a $10\,\mathrm{mm}$ strip immediately in front of the transducer was required for the calculation of TI [250]. An electronic mask was implemented in the Verasonics script such that only the elements in the central $10\,\mathrm{mm}$ region remained active and hydrophone measurements were taken in front of this region as close to the transducer surface as possible ($\sim 11 \times 5\,\mathrm{mm}$ 2D scan with $\sim 0.1 \times 0.1\,\mathrm{mm}$ increments).

5.2.3 Tested ultrasound imaging modes

Imaging mode with known acoustic outputs (validation of hydrophone measurement procedure)

The complete hydrophone wave tank setup and post-processing procedure was validated for an imaging mode with known acoustic outputs: in the documentation provided by Verasonics, the manufacturer of the research ultrasound system, peak compression

pressure, peak rarefaction, and mechanical index measurements were provided for an example wide-beam imaging mode when used with the L11-5v transducer [254]. Therefore, the acoustic outputs measured using the described experimental setup were validated against these values provided by Verasonics. These acoustic outputs were calculated from 14 repeat hydrophone measurements at the maximum pressure location in the ultrasound field.

Imaging modes of this project

The acoustic outputs were measured for the three main imaging modes implemented on the Verasonics Vantage 128 ultrasound machine (Verasonics Inc., Kirkland, WA, USA). All imaging modes were performed using a L11-5v transducer, with a centre frequency of 7.8 MHz. To summarise, the imaging modes were: (1) the ARF push pulse used for shear wave imaging (Table 3.1, cycles $= 1000$, push duration $= 128\,\mu s$, push pulse repetition rate $= 2$ Hz), (2) conventional scanline imaging (Table 4.1, focal depth $= 10.1$ mm, scanlines $= 128$, frame rate $= 30$ Hz), and (3) CPWC (Table 4.1, number of beam-steered plane waves $= 30$, frame rate $= 30$ Hz). For the ARF push beam used in the *ex vivo* experiments of this project, the focal depth was varied such that the focus was centred on the specimen. Here, for the acoustic output measurements, the focal depth was set to 10.1 mm.

For the speckle-tracking imaging modes, the acoustic wave-field was first characterised for a transducer voltage of 15 V, but was then reduced to 10 V for the conventional imaging mode to lower the pulse-average intensity to below the recommended thresholds. For the ARF push pulse, it was more important to find the transducer voltage that maximises the acoustic outputs while remaining below the recommended thresholds and, thus, the acoustic field was characterised for voltages between $5 - 60$ V in 5 V increments.

5.2.4 Shear wave measurements with varying transducer voltages in agar phantom specimens

From the hydrophone measurements, a safe transducer voltage limit can be defined for the ARF push pulse for which acoustic outputs remain below the recommended thresholds. To verify whether shear waves with sufficient signal-to-noise ratio (SNR) can be generated with this limit, the shear wave imaging procedure was tested in an agar phantom specimen ($2\,\%$ w/w) at the transducer voltages tested with the hydrophone setup. For each voltage, the shear wave velocity was calculated using the time-of-flight (TOF) methods and phase velocity method. The transducer voltage for which the calculated shear wave velocities converged was determined, with the convergence criteria defined as a relative error $<5\,\%$.

5.3 Results

5.3.1 Validation of hydrophone measurement procedure

The peak rarefaction pressure, peak compression pressure and mechanical index obtained for the wide-beam imaging mode were in good agreement with the values provided in the

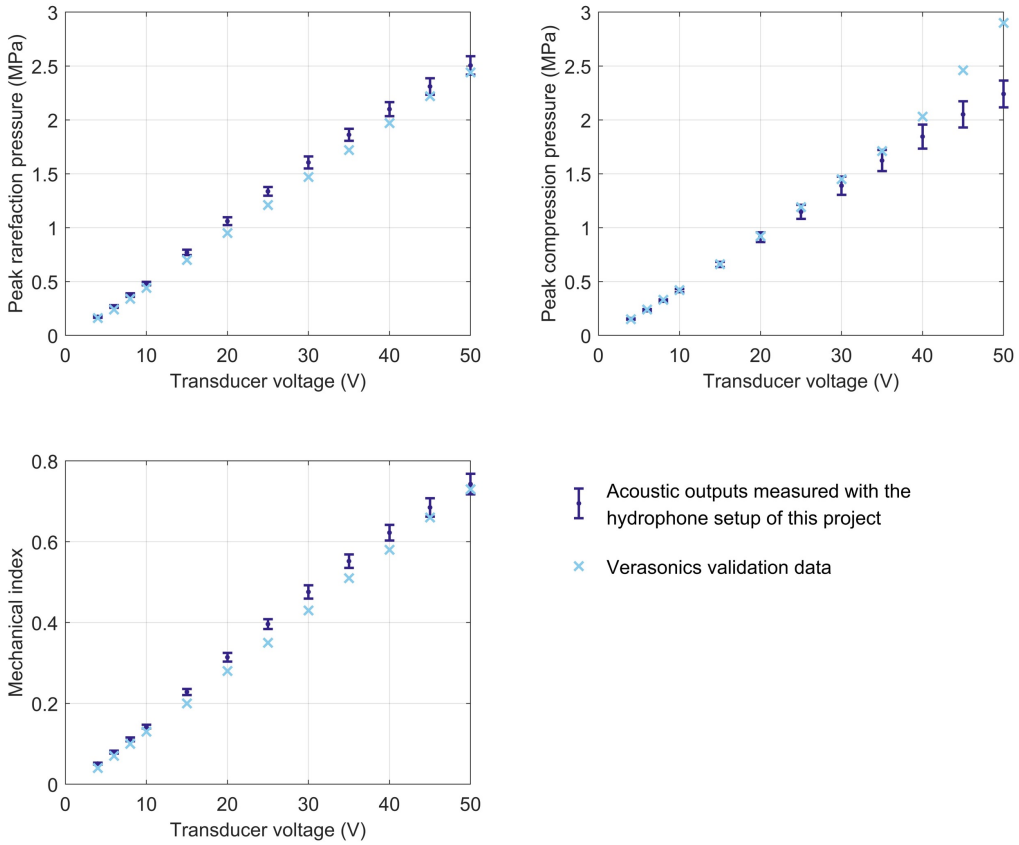


FIGURE 5.3 Acoustic outputs measured for the validation imaging mode with known peak pressure and MI values.

Verasonics documentation for transducer voltages between 4 – 50 V (Figure 5.3) (RMSE $=$ 0.09 MPa, 0.23 MPa and 0.03, respectively; R $>$ 0.99 for all). The main deviation occurred for the peak compression pressure at high transducer voltages (maximum error of $-23\,\%$ at 50 V).

5.3.2 Acoustic outputs for the imaging modes of this project

The measured MI, TI, I_{sppa}, and I_{spta} for the three imaging modes are summarised in Table 5.2. The results show that using focused beams can lead to acoustic outputs that are close to or exceed the safety indices that are related to mechanical risk (Figure 5.4): for the

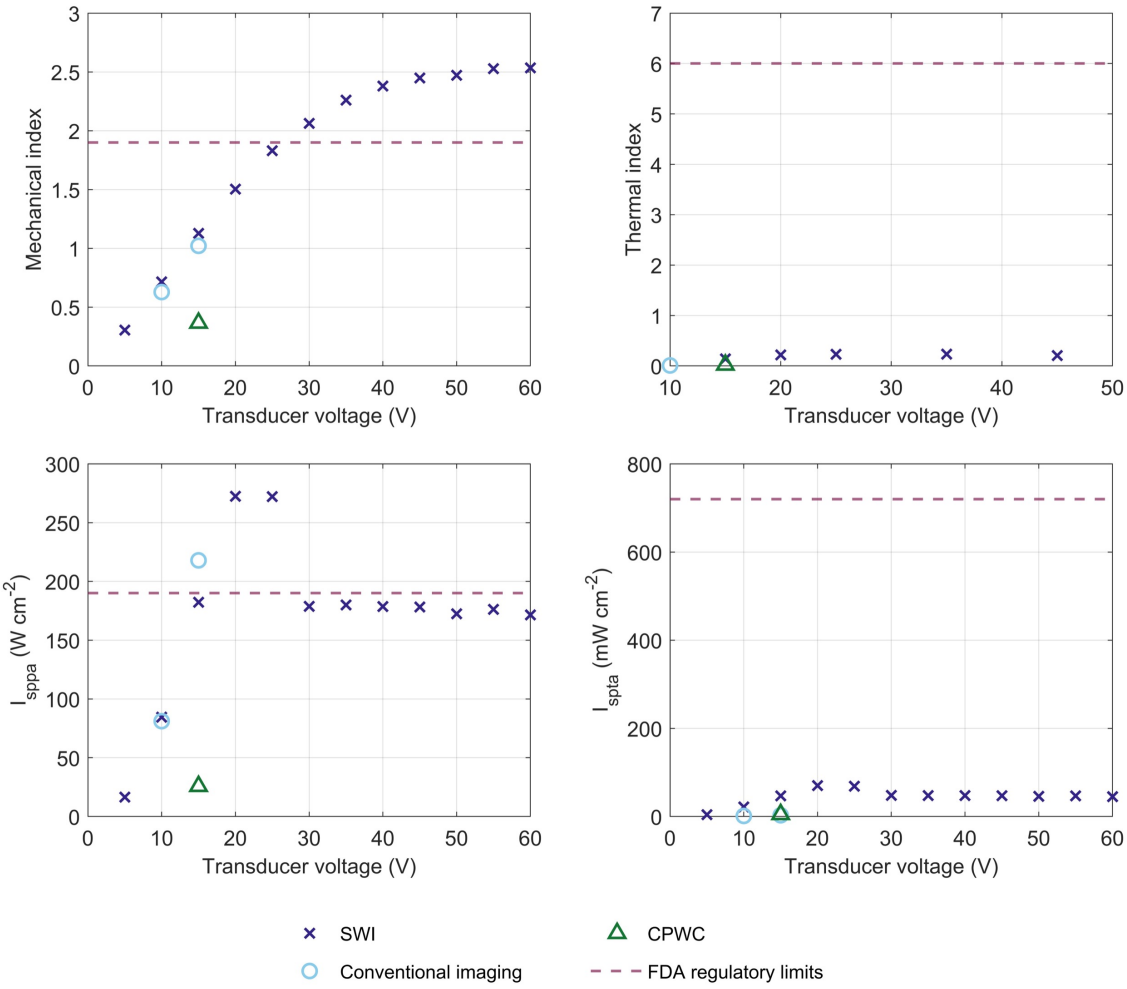


FIGURE 5.4 Acoustic output safety indices for different transducer voltages, calculated for three imaging modes used in this project. The dashed pink line shows the limits defined by the FDA.

ARF push pulse used in shear wave imaging, the MI exceeded the FDA safety thresholds for transducer voltages greater than 25 V, and the I_{sppa} exceeded the thresholds for 20 and 25 V. For the conventional imaging mode, the I_{sppa} was above the safety threshold at a transducer voltage of 15 V.

For all imaging modes, the safety metrics assessing thermal risk were well within safe thresholds, with the TI and I_{spta} remaining below $10\,\%$ of the recommended limits at all times.

TABLE 5.2 Acoustic outputs for the imaging modes of this project implemented on the Verasonics ultrasound machine with an L11-5v transducer. Thresholds defined by the FDA are MI ≤ 1.9, TI ≤ 6, $I_{sppa} \leq 190\,\mathrm{W/cm^2}$, and $I_{spta} \leq 720\,\mathrm{mW/cm^2}$.

	Transducer voltage	Mechanical index (MI)	Thermal index (TI)	Spatial-peak pulse-average intensity ($I_{sppa,0.3}$) (W/cm^2)	Spatial-peak temporal-average intensity ($I_{spta,0.3}$) (mW/cm^2)
ARF push beam (shear wave imaging)	5 V	0.30	-	16.46	4.22
	10 V	0.71	-	84.50	21.70
	15 V	1.13	0.141	182.22	46.88
	20 V	1.50	0.218	272.33	70.23
	25 V	1.83	0.230	272.09	68.81
	30 V	2.06	-	178.67	47.87
	35 V	2.26	0.235	179.85	47.65
	40 V	2.38	-	178.62	47.45
	45 V	2.45	0.205	178.15	47.22
	50 V	2.47	-	172.32	45.78
	55 V	2.53	-	176.10	46.89
	60 V	2.53	-	171.46	45.03
Conventional imaging (speckle tracking)	10 V	0.63	-	81.09	1.23
	15 V	1.02	0.009	217.91	2.79
CPWC (speckle tracking)	15 V	0.37	0.020	25.74	4.91

5.3.3 Shear wave measurements with varying transducer voltages in agar phantom specimens

The shear wave imaging measurements in agar phantom specimens showed that the calculated shear wave speeds converge for transducer voltages greater than $30\,\mathrm{V}$ for all TOF and phase velocity post-processing techniques. For lower transducer voltages, the calculated shear wave velocities were up to twice as high as the converged shear wave velocity when using the TOF methods ($10.6\,\mathrm{m/s}$ vs $4.8\,\mathrm{m/s}$). Furthermore, the standard deviation of the measured shear wave velocity (obtained from tracking the same shear wave at different axial depths $2\,\mathrm{mm}$ above and below the focus) was up to $16\,\mathrm{m/s}$ before convergence, but remained below $1\,\mathrm{m/s}$ for transducer voltages greater than $30\,\mathrm{V}$.

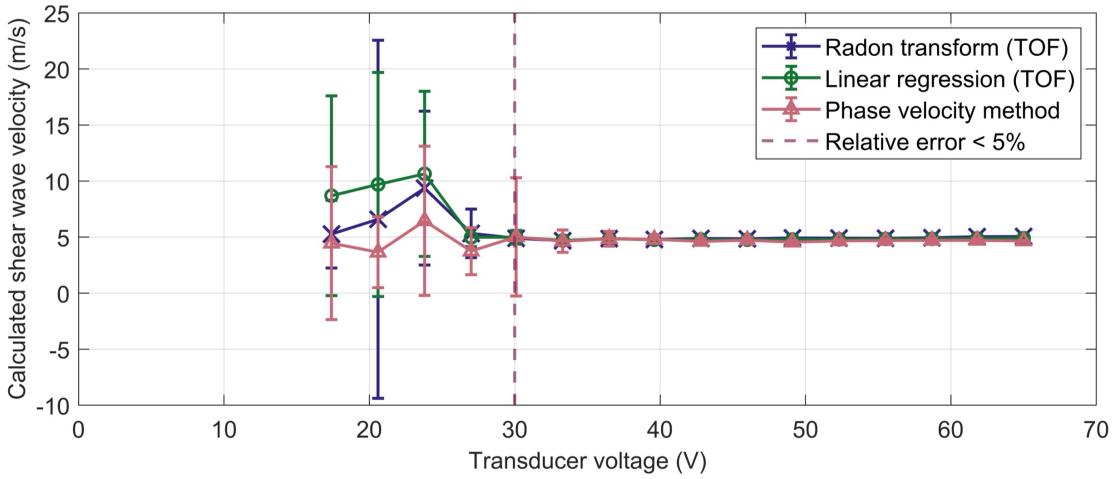


FIGURE 5.5 Convergence of the calculated shear wave velocities with increased transducer voltage. Higher acoustic pressures generate stronger shear waves that can be tracked more easily.

5.4 Discussion

5.4.1 Most important findings

This study confirmed that the speckle tracking technique can be safely implemented *in vivo*; however, shear waves for shear wave elastography imaging (SWEI) cannot be produced safely and reliably with the current transmission settings. While sufficiently clear images can be obtained for speckle tracking using the conventional and CPWC imaging modes within the found safe range of transducer voltages ($<10\,\mathrm{V}$ and $<15\,\mathrm{V}$, respectively), a convergence test found that a much larger transducer voltage of $>30\,\mathrm{V}$ was required to reliably track shear waves produced by the push pulse. Below this, the calculated shear wave velocities varied greatly, likely due to low SNR resulting in inaccurate tracking of the shear wave front. However, at these larger transducer voltages, the possibility of mechanical tissue damage exceeds acceptable levels of risk, as defined by the FDA.

In general, it was found that mechanical effects were a greater concern than thermal effects for the imaging modes implemented in this study: while thermal safety indices (TI and I_{spta}) remained low for all imaging modes, safety indices measuring risk of cavitation (MI and I_{sppa}) exceeded the safety limits for transducer voltages greater than $\sim 15\,\mathrm{V}$ when using imaging modes with focused transmissions, i.e. conventional imaging or the ARF push pulse of shear wave imaging. Furthermore, the mechanical safety indices were remarkably similar for both focusing imaging modes. This demonstrates that the mechanical risk primarily depends on the focal settings, as both imaging modes used the same sub-

aperture and focal depth. The key difference is that the ARF push pulse uses a single, long, uninterrupted transmission, whereas conventional imaging transmits multiple short, focused pulses that scan the field of view. This difference is evident in the thermal outputs: the reduced downtime in the extended push pulse allows for greater heat accumulation, which led to slightly higher temporal-average intensities; however, these were still well below the recommended safety thresholds. The unfocused transmissions of the CPWC imaging mode resulted in consistently low acoustic output metrics all around.

Acoustic outputs measured for the validation imaging mode using the protocol of this study were in excellent agreement with the example data provided by Verasonics ($R > 0.99$). These results give confidence that the experimental setup and post-processing calculations correctly followed the IEC standard. Furthermore, it suggests that slight variations in ultrasound and test equipment do not affect the acoustic outputs, since the values reported by Verasonics were obtained with a different ultrasound machine and transducer (i.e. same models, but not the exact same devices) and measured with a different hydrophone.

5.4.2 Comparison to literature

The Verasonics machine has already been used for *in vivo* imaging on human participants [28, 150, 216, 255]. These studies limit their acoustic exposure to adhere to the FDA recommendations. Thus, the same was done here, despite the more conservative recommendations by the BMUS. This is because the lower MI limit of 0.7 only applies when contrast agents containing gas micro-spheres are being used. Without contrast agents, cavitation due to diagnostic ultrasound is only a theoretical possibility [218]; a study conducted by Smallcomb and Simon [111] showed that a MI above 14.7 is needed for bubble formation and cavitation in collagenous tissue such as tendons and ligaments; even the more lenient FDA threshold is still almost 8 times lower than this. Additionally, while the BMUS threshold for thermal index (<1) is also much more restrictive, this was no concern here, since all thermal index measures were below this value.

Acoustic outputs of this study ($\mathrm{MI} = 2.38$, $I_{sppa} = 179\,\mathrm{mW/cm^2}$, $I_{spta} = 47\,\mathrm{mW/cm^2}$) were comparable to those measured by Sadeghi et al. [150] for their supersonic shear imaging (SSI) push pulse produced by the Verasonics ultrasound machine with C5-2 and L7-4 transducers operating at $40\,\mathrm{V}$ ($\mathrm{MI} = 1.72 - 2.63$, $I_{sppa} = 150 - 200\,\mathrm{W/cm^2}$, $I_{spta} = 521 - 648\,\mathrm{mW/cm^2}$). The lower spatial-peak temporal-average intensities measured here may be attributed to a longer break between successive push pulses, since here the shear wave propagation was calculated and visualised in real-time, which required more time between pulses for processing ($0.5\,\mathrm{s}$).

Another interesting observation was that at high transducer voltages, the MI and pulse-average intensities approached constant values. Inspection of the pressure waveform at these voltages revealed a nonlinear distortion, with the sinusoidal response taking on a skewed, asymmetrical shape. This indicates that the observed saturation effect is caused by the formation of shock waves; indeed, Karzova et al. [256] report an almost identical response, with shock waves first developing at $30\,\mathrm{V}$ and resulting pressure saturation at $45 - 90\,\mathrm{V}$. Saturation could also indicate that the maximum power-capabilities of the ultrasound machine have been reached [150].

5.4.3 Limitations

Mechanical indices are derived from acoustic intensity, whereas thermal indices depend on acoustic power. In this study, acoustic power was estimated by spatially integrating the intensity distribution. However, more precise power measurements could be achieved in the future using an acoustic radiation force balance. Given that the estimated thermal outputs for the imaging modes in this project were well within safety limits, the added accuracy provided by an acoustic radiation force balance was deemed unnecessary. Nonetheless, if the downtime between transmissions is shortened in future implementations, such as by increasing the frame rate or reducing the time between shear wave generations, thermal indices could approach safety thresholds. In such cases, the use of an acoustic radiation force balance would ensure more reliable power measurements.

Here, the acoustic outputs of focused transmissions were only characterised for a single focal depth of 10 mm, as it was estimated that the collateral ligaments would lie at around this depth. This focal depth was kept constant for all *in vivo* measurements of this project. However, it would be useful to be able to adjust the focal depth to guarantee that it does, in fact, coincide with the tissue of interest, ensuring that the tissue is captured with optimum resolution. Future work could explore how acoustic outputs vary with focal configurations, investigating at which focal depths the maximum outputs occur.

The time-consuming nature of this measurement procedure is an additional limitation, with each 3D hydrophone scan taking approximately half a day. For imaging modes where maximising the acoustic outputs is critical, such as for shear wave imaging, multiple iterations of transmission settings may need to be tested; thus, developing the transmission sequence could take several weeks. Simulations of the acoustic pressure field could help with this, enabling more efficient optimisation of *in vivo* transmission sequences [249]. By simulating the acoustic behaviour for a given transducer and transmission settings, researchers can predict the pressure fields and acoustic radiation forces that meet safety limits while still generating strong shear waves. This method can help narrow down settings such as the transducer frequency, push duration and focal depth, thus significantly reducing the time and effort required for trial-and-error approaches, where each iteration requires time-consuming 3D hydrophone scans in a wave tank.

5.4.4 Conclusion

The imaging modes used for speckle tracking can be used with safe acoustic output levels. The ARF push pulse, on the other hand, needs adaptation before it can be used safely and reliably *in vivo* for shear wave imaging. Overall, it was found that the risk of mechanical tissue damage was mainly determined by the focal configurations, while the risk of thermal damage was influenced by the length of and time between pulses. Further research is needed to understand the relationship between mechanical safety indices and specific focal configurations in order to find suitable settings for the ARF push pulse.

06

Validation: *Ex Vivo* Specimens

6.1 Introduction **136**
6.2 Materials and Methods **138**
6.3 Results **159**
6.4 Discussion **179**

The methods, results and discussion of the speckle tracking experiments have previously been published in Ultrasound in Medicine and Biology [231]. All co-authors played a supervisory role in this work. Additionally, while I wrote the initial draft, co-authors contributed amendments to the text.

I would like to acknowledge that the shear wave imaging experiment performed on the porcine ligaments was planned and conducted by Stephen Prashant as part of his final year project of his undergraduate degree. All analyses were conducted by myself using the post-processing techniques developed in this PhD project.

Lastly, I would like to thank Dr Catrin Davies for the loan of the DIC equipment, as well as Mick Rock and Joe Lawton at DePuy for arranging a training session with the manufacturer of the equipment.

List of Abbreviations

AP	Anterior/posterior
ARF	Acoustic radiation force
CV	Coefficient of variation
CPWC	Coherent plane-wave compounding
DIC	Digital image correlation
IQ	In-phase and quadrature
LVDT	Linear variable displacement transducer
MCL	Medial collateral ligament
NRIR	Non-rigid image registration
PMMA	Polymethyl-methacrylate
POL	Posterior oblique ligament
PRF	Pulse repetition frequency
PWI	Plane wave imaging
QUS	Quantitative ultrasound
RF	Radio frequency
RMSE	Root mean square error
TOF	Time-of-flight

6.1 Introduction

Orthopaedic connective tissues are crucial to the body's biomechanics. Tendons connect muscles to bones, transmitting forces that control joint movements, while ligaments connect bones to each other, stabilising joints [32, 206]. The mechanical properties and strain behaviour of these tissues are essential to their function. Elasticity reflects the tissue's ability to stretch and store energy, influencing range of motion and efficiency of energy transfer during locomotion. Viscosity, on the other hand, indicates the tissue's ability to absorb energy, preventing damage by dampening impact loads, and its ability to stress relax under prolonged loading, reducing risk of fatigue failure [30, 32, 257]. Lastly, the strain behaviour of connective tissue during joint movements can indicate its level of engagement [18, 47].

Using the quantitative ultrasound (QUS) techniques discussed in Chapters 3 and 4, these properties could be measured non-invasively, providing valuable insights into connective tissue health and function. This diagnostic power has already been demonstrated in tendons: changes in the strain behaviour and viscoelastic properties measured using speckle tracking or shear wave imaging can indicate ruptures [85, 91, 258, 259], tendinopathies [41, 84, 89, 189, 260, 261], increased activity [262, 263], and healing after surgical procedures [235, 264]. Additionally, tendon forces can be estimated from activation-dependent changes of instantaneous Young's modulus [144, 159]. These techniques could be equally effective in evaluating ligament integrity, ensuring that they are fulfilling their role in providing stability [14]. For example, monitoring of the collateral

ligaments after knee replacement surgery could indicate how post-operative ligament healing or adaptation contributes to complications such as knee instability or stiffness.

The unique anatomy and material properties of ligaments require careful consideration when applying the techniques. For shear wave imaging, the viscous nature and thin structure of ligaments lead to dispersion, which affects how shear waves propagate through them. Previous shear wave imaging studies have demonstrated the capability to generate and track shear waves in ligaments [71, 86, 87]. However, ligaments were approximated as elastic, homogeneous and non-dispersive media, which may result in inaccuracies in measuring their elastic moduli.

Several challenges have also been identified when applying the speckle tracking algorithm to ligaments: ligaments exhibit a unique speckle appearance and frame-to-frame movement, which can vary between ligaments and under different loading conditions due to their highly evolved anatomy and wrapping behaviour. Therefore, the speckle tracking algorithm must be adapted for each application [51, 204]. Indeed, Dandois et al. [166] recently found that even for equivalent varus-valgus movement to generate tensile strain in the lateral/medial collateral ligament, respectively, tracking required different algorithm settings for each side.

Due to the clinical relevance and aforementioned challenges of measuring ligament function using ultrasound, the quantitative ultrasound methods outlined in Chapters 3 and 4 will be applied and validated using orthopaedic tissue-mimicking phantoms, as well as medial ligamentous structures of the knee. The shear wave imaging technique will be evaluated with the different post-processing approaches corresponding to various tissue approximations (i.e., thin vs unbounded, elastic vs viscoelastic) to determine whether a more complex model yields more accurate material property estimations. Additionally, the optimisation routine for tuning the speckle tracking algorithm will be validated, a novel concept that could broaden the application of speckle tracking to new areas.

6.2 Materials and Methods

6.2.1 Shear wave imaging: agar phantom specimens

Initial validation of the shear wave imaging procedure was conducted on viscoelastic tissue-mimicking phantom specimens. The aim was to verify whether the accuracy of measured material properties can be improved by considering dispersion of the shear wave due to viscoelasticity or a thin-layered geometry. For this, two types of samples were used: cube samples and thin plates of varying thicknesses. It was hypothesised that the viscoelastic dispersion analysis would be most suitable for the larger cube samples, while a combination of Lamb wave and viscoelastic dispersion analysis would provide better results for the thin tissue-mimicking plate samples.

Specimens & test setup

Phantom specimens were made using agar, a gelatin-like substance obtained from seaweed with similar density and viscoelastic properties to soft tissue. Samples were prepared using the following procedure. Agar powder was weighed out with kitchen scales to give the desired agar to water concentration by weight ($\%\mathrm{w/w}$), and was added to lightly boiling water together with $1-2$ teaspoons of flour. The addition of flour has been shown to improve echogenicity of the phantoms [265], providing a clearer speckle pattern and thus enhancing tissue motion calculation. Once the agar and flour had dissolved completely, the mixture was poured into the phantom moulds. After cooling to room temperature, the

specimens set into a jelly-like material and were kept refrigerated until testing. Different agar concentrations resulted in specimens of different material properties, with higher concentrations resulting in larger Young's moduli.

For the agar cube specimens, a silicone mould of $\sim 4 \times 4 \times 4\,\mathrm{cm}$ was used. Four specimens with three different agar concentrations were produced ($2\times\ 2\,\%$ w/w, $1\times\ 3\,\%$ w/w, and $1\times\ 5\,\%$ w/w) (Figure 6.1). Note that two cubes had the same concentration to quantify the repeatability of the phantom production procedure. The dimensions of the cubes were measured using a Vernier calliper. Furthermore, the specimens were weighed using kitchen scales to allow for calculation of the density.

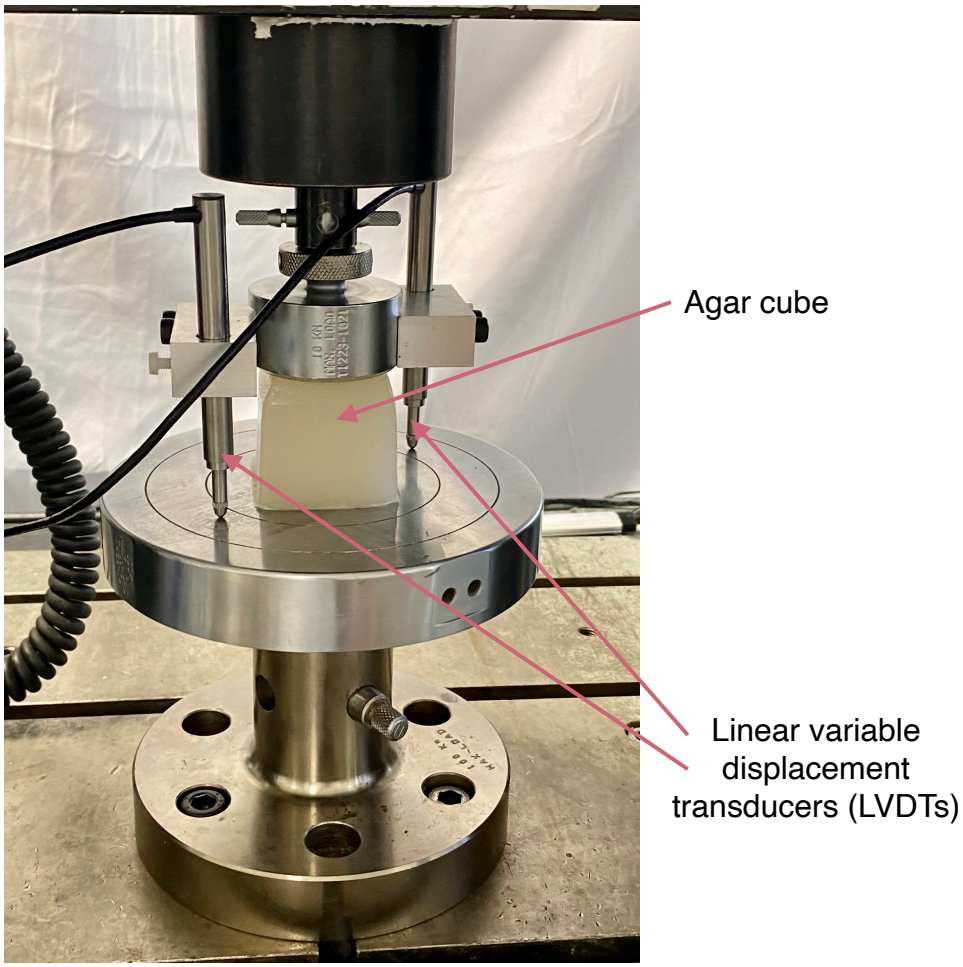


FIGURE 6.1 Experimental setup for the agar cube mechanical compression test. Specimens were quasi-statically compressed by $15\,\%$, and their height change was measured by two linear variable displacement transducer (LVDTs).

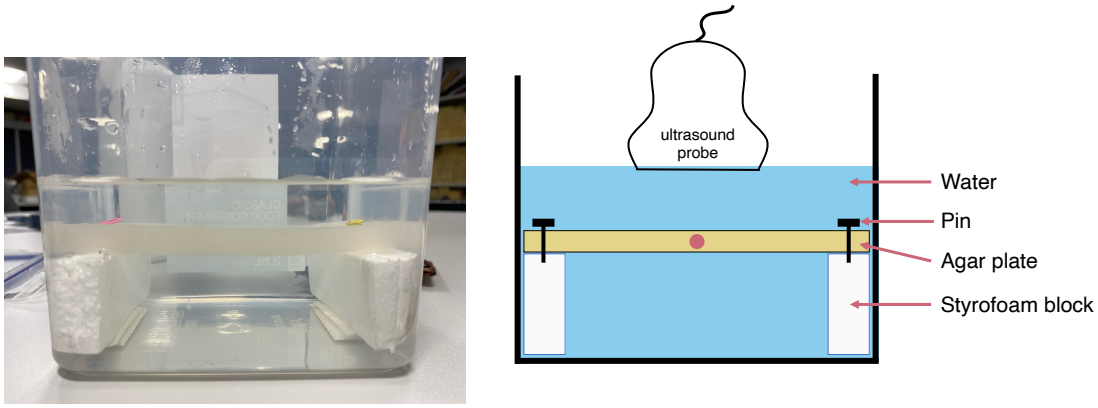


FIGURE 6.2 Experimental setup for the agar plate shear wave imaging measurements. The specimens were pinned to two styrofoam blocks to prevent them from floating and keep them submerged in the water tank. Ultrasound measurements were taken with the transmitting face of the transducer just below the water surface.

For the agar plate specimens, a $5\,\%$ w/w agar mixture was poured into a large plastic container ($\sim 15 \times 15 \times 25\,\text{cm}$), from which six plates of varying thicknesses were cut using a knife ($3 - 8\,\text{mm}$ with $\sim 1\,\text{mm}$ spacing) (Figure 6.2). The thicknesses of the plates were measured using a Vernier calliper.

Ultrasound measurements

For all agar phantom measurements, shear waves were generated using an acoustic radiation force (ARF) produced by the ultrasound transducer itself. Ultrasound shear wave generation and tracking was performed using the settings outlined in Tables 3.1 and 3.2 in Section 3.2 (page 61). In short, a research ultrasound system (Vantage 128, Verasonics Inc., Kirkland, WA, USA) with a L11-5v transducer (linear, $38\,\text{mm}$, $5 - 11\,\text{MHz}$ bandwidth) was used. In a window showing the real-time ultrasound images, the location of the focal point of the ARF was selected to be at the centre of the agar cubes or plates, and a rectangular region of interest was placed next to the focus. The ultrasound transducer alternated between the shear wave generation sequence, i.e. an extended push pulse of $128\,\mu\text{s}$ at the transducer central frequency of $7.6\,\text{MHz}$, and the shear wave tracking sequence, i.e. ultrafast plane wave imaging (PWI) at a pulse repetition frequency (PRF) of $10\,\text{kHz}$. The Verasonics pixel-based beamforming technique was used to reconstruct the radio frequency (RF) signal of the region of interest with a grid spacing of $0.05 \times 0.10\,\text{mm}$

(axial $\times$ lateral) and the data were saved in in-phase and quadrature (IQ) format.

In the case of the agar cube measurements, ultrasound gel was applied to the surface of the cubes and the ultrasound transducer was placed in contact with the samples by hand, taking care not to apply any load. Six repeat measurements were collected per specimen, with the transducer removed and placed back on the specimen for each measurement.

Since the Lamb wave dispersion model used in this study assumes that the sample of interest is surrounded by a medium of similar density, the agar plates were submerged in water (Figure 6.2); the agar specimens were over $95\,\%$ water by weight and thus their density was almost identical to that of water ($\sim$1000 $\mathrm{kg/m^3}$). For these measurements, the transducer was not placed in contact with the specimens, but was instead held such that the transmitting surface was just submerged in the water. Three repeat measurements were taken per specimen, and the transducer was again repositioned between each repeat.

Material mechanical testing

To validate the Young's moduli obtained from ultrasound shear wave imaging, mechanical compression tests were performed on the larger agar cube specimens of varying agar concentration (Figure 6.1). The specimens were placed in a material testing machine (Model 5565, Instron, Norwood, MA) and a $3\,\mathrm{N}$ preload ensured that the entire top surface of the specimens was in contact with the compression platen. Two $10\,\mathrm{mm}$ stroke linear variable displacement transducers (LVDTs) (Model D6/05000A, RDP Electronics Ltd, Wolverhampton, United Kingdom) were set up such that the base was attached to the top platen and the piston head was in contact with the bottom platen; this allowed accurate measurement of the vertical displacement between the platens. The specimens were subsequently pre-conditioned with 10 quasi-static ($1\,\mathrm{mm/min}$ or $0.038\,\%/\mathrm{s}$) ramp compressive loading and unloading cycles of $0-15\,\%$ strain (estimated from the specimen height and crosshead displacement), followed by one more quasi-static compression cycle for which the force-displacement data was recorded.

Data analysis

For the ultrasound measurements, axial velocities were calculated from the IQ data and filtered using the methods described in Section 3.3. For the larger cube specimens, the material properties were calculated using four post-processing techniques: the radon transform time-of-flight (TOF), linear regression TOF, phase velocity, and viscoelastic dispersion analysis methods. For the thin plate specimens, the material properties were additionally calculated using the Lamb wave dispersion and the combined Lamb wave & viscoelastic dispersion analysis methods. By assuming that the agar specimen were isotropic and incompressible, the Young's modulus was calculated using $E \approx 3\mu$, thus enabling comparison to the results from the compression tests. For the methods that produced values for both the shear/Young's elastic modulus and Voigt shear viscosity, the viscoelastic Voigt time constant was additionally computed using Equation 6.1:

$$\tau = \frac{\eta}{\mu} = \frac{3\eta}{E'} \tag{6.1}$$

$E^{'}$ = extensional elastic storage modulus (i.e., Young's modulus)

η = Voigt shear viscosity

μ = Voigt shear modulus

τ = Voigt time constant

For the mechanical compression tests, stress was calculated by dividing the force data by the sample cross-sectional area, while the strain was calculated by dividing the displacement by the measured sample height. It has been shown that the shear/Young's modulus obtained from the shear wave propagation is related to the apparent modulus of the material at its current load state [144, 159]. For a viscoelastic material which exhibits a non-linear stress-strain curve with increasing gradient, the apparent Young's modulus increases with increased loading. Since the ultrasound measurements were taken with the agar samples unloaded, the initial apparent Young's modulus was computed from the mechanical testing data by fitting a line to the stress-strain curve below $10\,\%$ strain. The standard error (SE) of the linear regression gradient was used to quantify the uncertainty

of the estimated Young's modulus.

The highest source of uncertainty in the mechanical Young's modulus measurements was deemed to be the measurement of the dimensions of the cubes. Due to the flexibility of the moulds, each sample had slightly different dimensions. Furthermore, even though Vernier caliper measurements usually have an accuracy of $\pm 0.02\,\mathrm{mm}$, the non-rigidity of the samples made it challenging to take measurements without slightly compressing the samples. Thus, analysis will account for measurement errors of up to $\pm 1\,\mathrm{mm}$. Using these lower and upper limits of sample cross-sectional area and height, an upper and lower bound of the stress-strain curve was obtained. The maximum and minimum Young's moduli were determined by fitting new lines to these curves.

For the agar cube specimens, the Young's moduli obtained using shear wave imaging and the quasi-static compression tests were quantitatively compared via the root mean square error (RMSE), i.e. the error between the ultrasound and mechanical testing results was calculated for each of the four specimens, and the root-mean-squared value of these four errors was computed. Additionally, the Pearson's correlation coefficient (R) between the ultrasound and validation data was calculated. Furthermore, the repeatability for phantoms of the same agar concentration was assessed by calculating the percentage difference between the material properties obtained for the two $2\,\%\,\mathrm{w/w}$ agar cube specimens.

For the agar plate specimens, the shear wave imaging Young's moduli were compared to the Young's modulus found for the agar cube specimen of equal agar concentration ($5\,\%\,\mathrm{w/w}$) by, again, evaluating the RMSE. Furthermore, robustness of the measured properties against changes in plate thickness was assessed using the coefficient of variation (CV) and Pearson's correlation coefficient (R). Since properties should be independent of specimen geometry, lower values for both would indicate better reliability.

Lastly, a sensitivity analysis was performed for the shear moduli and viscosities found using the viscoelastic and the combined viscoelastic & Lamb wave dispersion analyses. Since these methods use models with two unknown input variables (Voigt shear modulus and viscosity), they may be subject to a higher level of uncertainty associated with the

fitted models. The following analysis aimed to quantify this uncertainty: dispersion curves were computed for shear moduli and viscosities around the "optimum" material properties that were found from the curve of best fit. This allowed a "confidence region" to be defined, which encompassed the combinations of shear moduli and viscosities for which the goodness-of-fit of the dispersion curves remained within $1\,\%$ of the goodness-of-fit of the curve of best fit. Larger confidence regions indicate greater uncertainty in the estimated shear modulus and viscosity, as a wide range of material properties can result in similarly good fits to the experimental dispersion data.

6.2.2 Shear wave imaging: porcine specimens

Given the highlighted challenges in measuring ligament mechanical properties and the potential for clinical impact, the technique was also tested on porcine medial collateral ligament (MCL) specimens. Several challenges were anticipated: (1) compared to the agar plate specimen, porcine MCLs have a higher elastic modulus, leading to faster shear waves; (2) the porcine MCLs were thinner and would likely have stronger viscous effects than the tested agar plates, leading to more dispersion; and (3) higher viscoelasticity also results in faster attenuation of the shear waves, reducing the time window during which shear waves are visible for tracking.

To capture the dispersive behaviour in more detail, shear waves for this experiment were generated using an external shaker; thus, more shear wave frequencies could be targeted, providing a larger range of experimental shear wave phase velocity vs frequency data for fitting the theoretical dispersion models. Furthermore, since the acoustic output measurements in Chapter 5 revealed that the current implementation of the ARF push pulse is not safe for *in vivo* use, validating a protocol using an external shaker will facilitate the use of this technique for *in vivo* applications.

Specimens & test setup

All research with animal tissue acquired from the food-chain did not require prior ethical approval, rather was registered in the principal investigator's annual declaration, in accordance with the host institution's policies.

Four fresh-frozen porcine stifle ("knee") joints were defrosted at room temperature. The joints were dissected to remove all soft tissue except for the MCL. The ligament was sprayed regularly with water to prevent dehydration.

Ultrasound measurements

The same Verasonics ultrasound system and transducer was used as for the agar phantom experiments. Since the external shaker was used for this experiment, the ARF push pulse was excluded from the ultrasound transmission sequence. However, the plane-wave tracking sequence remained the same, apart from the PRF being increased to 15 kHz.

To fulfil the Lamb wave conditions, the specimens were placed in a water bath to ensure

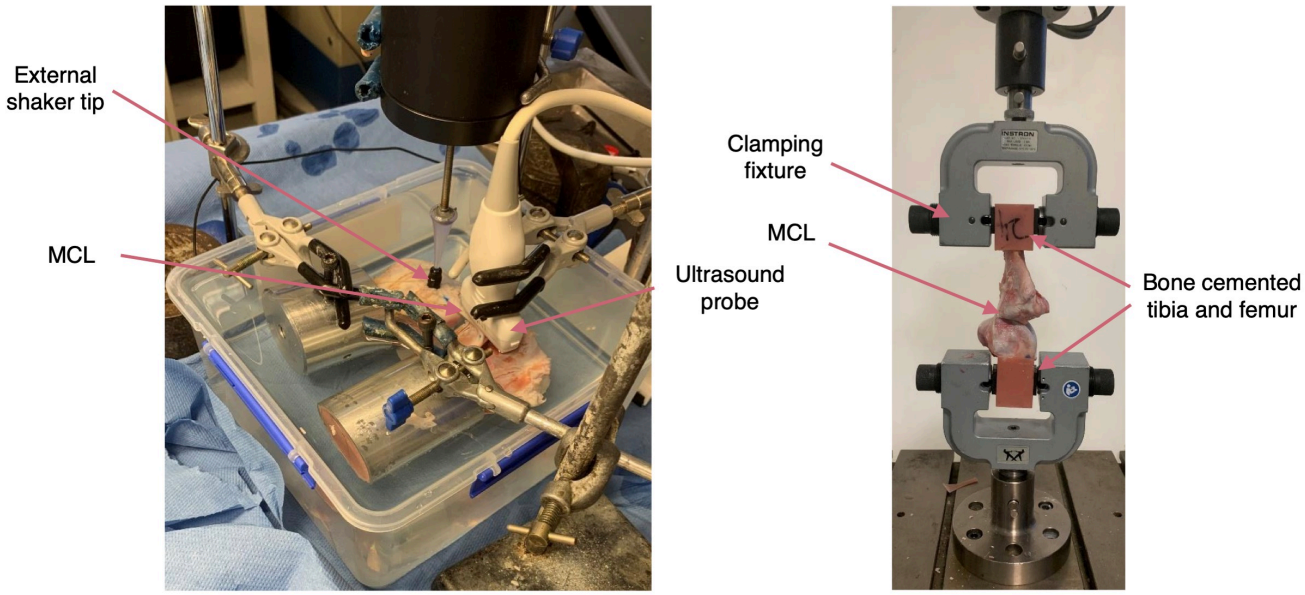


FIGURE 6.3 Experimental setup for the porcine MCL shear wave imaging measurements. Ultrasound measurements were performed in a water bath with the ligaments unloaded, and shear waves were generated using an external shaker **(left)**. A dynamic creep test was performed in a material testing machine to validate the viscoelastic properties of the ligaments **(right)**.

that the ligament was surrounded by a medium of similar density (Figure 6.3). The joint was positioned such that the MCL remained slack and unloaded to reduce variability in shear wave velocity measurements. The ultrasound transducer was clamped in place over the MCL with the linear array parallel to the ligament fibre direction. The transducer face was just submerged below the water surface, but was not in contact with the ligament. The external shaker tip was positioned as close to the edge of the transducer as possible, either near the femoral or tibial ligament attachment.

Shear waves were continuously generated by the external shaker at frequencies of $200 - 800\,\text{Hz}$, in $100\,\text{Hz}$ increments. For each specimen, five repeat ultrasound measurements were taken at each shear wave frequency.

Material mechanical testing

For this experimental series, the main aim was to validate the viscoelastic material properties measured using shear wave imaging. Viscoelastic properties are generally obtained through mechanical relaxation or creep testing [39]. However, the Voigt model chosen for this study cannot be described by stress relaxation. Thus, a dynamic creep test was performed instead: when a material is sinusoidally loaded in tension, the phase lag between the load and displacement curve will depend on the viscoelastic material properties. Equation 6.2 describes this relationship [39]:

$$tan(\delta) = \frac{\eta\omega}{\mu} = \tau\omega \tag{6.2}$$

δ = load-displacement phase lag

τ = Voigt time constant (shown in Equation 6.1)

ω = angular loading frequency

The sinusoidal mechanical tests were performed in a material testing machine (Model 8874, Instron, Norwood, MA). The femur and tibia were cemented into cubic moulds using polymethyl-methacrylate (PMMA), which allowed the specimens to be mounted in the testing machine using clamping fixtures (Figure 6.3). The specimens were preloaded to

$\sim$6 % tensile strain (estimated from the original ligament length measured using a Vernier calliper) and allowed to stress relax for 10 minutes prior to testing. Subsequently, specimens were sinusoidally loaded for 25 cycles in displacement control between strain amplitudes of approximately $\pm$1 % of the preloaded state. The first 20 cycles preconditioned the ligament; force and displacement measured by the material testing machine was recorded for the last 5 cycles. The sinusoidal test was performed at strain rates of 1, 3, 5, 7 and 10 Hz with three repeats each. The specimens were allowed to rest for 10 minutes between each test.

Data analysis

All ultrasound measurements were again processed using all six shear wave imaging post-processing methods, including the TOF, phase velocity and dispersion methods. For the dispersion methods, the experimental dispersion maps were compiled by combining measurements at the seven different excitation frequencies, resulting in five repeat dispersion maps for each specimen. For the remaining post-processing methods, the 35 collected measurements were processed individually, since these methods do not account for variations of shear wave velocity with frequency. Due to the anisotropy of ligamentous structures, Young's modulus cannot be reliably estimated from the shear modulus [160], and instead results are reported in terms of shear modulus.

For the dynamic creep tests, the phase lag between the collected force and displacement curves was obtained by taking the Fourier transform of the data (Matlab function `fft`) and finding the phase of the transform components at the loading frequency (Matlab function `angle`). The difference between the phase angles of the force and displacement response gave the phase lag. The Voigt time constant was then found from the gradient of the linear regression between the angular loading frequency and the tangent of the phase lag (Matlab function `fitlm`). The standard error (SE) of the linear regression gradient was used to quantify the uncertainty of the estimated time constants.

The reliability of the different shear wave imaging post-processing methods was assessed by computing the coefficient of variation (CV) of the calculated material properties. Furthermore, Voigt time constants obtained with shear wave imaging were validated

against the measures from the dynamic creep tests using RMSE and the Pearson's correlation coefficient (R).

Lastly, as was done for the agar plate specimens, a sensitivity analysis was performed for the multivariable dispersion models to quantify the uncertainty associated with the viscoelastic properties obtained with shear wave imaging.

6.2.3 Speckle tracking: porcine specimens

Given the highlighted challenges in measuring ligament strain, and the potential for clinical impact, speckle tracking validation focused on ligaments with different anatomy (porcine and human) in different loading conditions (quasi-static and dynamic). Since the exclusion of ground truth data when tuning the algorithm is a novel concept, the aim of this study was to develop and validate this approach for this specific application, verifying that results compare to established strain measurement techniques.

Specimens & test setup

The proposed speckle tracking optimisation routine was first tested on porcine MCLs during uniaxial loading, and the calculated strains were validated against digital image correlation (DIC) measurements. Three fresh-frozen porcine stifle ("knee") joints were thawed at room temperature and dissected free of soft tissue while carefully preserving the MCL. A metal pin was inserted perpendicular to the ligament fibres approximately $1\,\mathrm{cm}$ distal to the tibial plateau. This pin was visible on both the ultrasound and DIC images and therefore allowed the region of interest of the two strain measurement techniques to be standardised. The femur and tibia were cemented into aluminium bone pots using PMMA which enabled them to be mounted in a material testing machine for testing (Figure 6.4). A $10\,\mathrm{N}$ preload removed slackness from the ligament. The MCL was then preconditioned with 10 cycles of $0-3\,\%$ strain (estimated from the length of the MCL measured using a rule and the crosshead displacement) at $0.2\,\mathrm{Hz}$. The MCL was subsequently loaded between the preloaded state and $3\,\%$ strain at $0.2\,\mathrm{Hz}$ for all ultrasound and DIC acquisitions, which

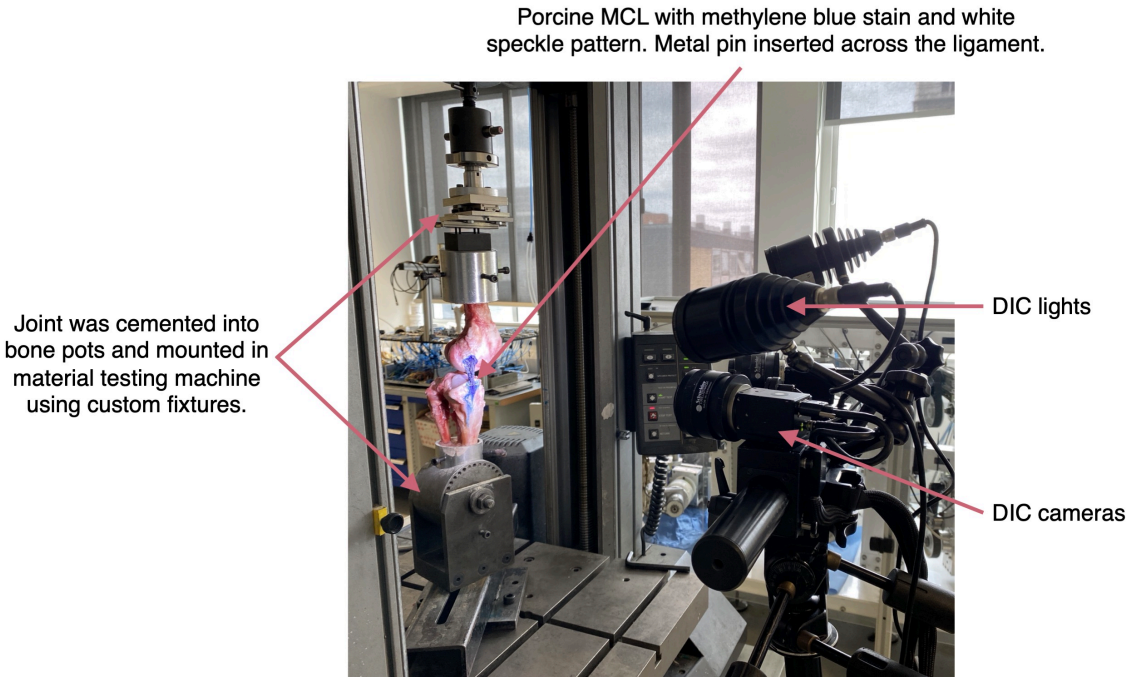


FIGURE 6.4 Experimental setup for the porcine MCL strain measurements. The porcine stifle joint was mounted in a material testing machine and loaded to 3 % strain. A speckle pattern was applied to the MCL, which enabled DIC strain measurements with the stereo cameras. The metal pin that was inserted perpendicular to the ligament fibres was visible in the ultrasound and DIC images and was used to match the region of interests for the two imaging modalities.

is comparable to the strains that ligaments and tendons were subjected to in previous speckle tracking studies [50, 166]. Note that all ultrasound and DIC strains subsequently calculated from the measurements were relative strains with respect to the preloaded ligament state. Regular water spray prevented tissues from drying out.

Ultrasound measurements

Ultrasound measurements were taken using the acquisition procedure outlined in Table 4.1 in Section 4.2 (page 91). In short, images were collected at 30 Hz using a high-frequency ultrasound machine (Vantage 128, Verasonics Inc., Kirkland, WA, USA) equipped with a L11-5v transducer (linear, 38 mm, 5 – 11 MHz bandwidth) operating at a central frequency of 7.6 MHz and with an ultrasound stand-off attached to the front of the transducer. During the measurements, the linear array was positioned over the joint space parallel to the assumed ligament fibre direction so that the imaging plane was a coronal slice through the ligament. RF data were collected using two imaging modes: the conventional scanline

imaging mode with focused beams and a coherent plane-wave compounding (CPWC) mode. For each specimen and imaging mode, at least 14 intervals that captured loading between $0\,\%$ to maximum strain were recorded. The Verasonics pixel-based beamforming technique was used to reconstruct the RF signal with a grid spacing of $0.05 \times 0.05\,\mathrm{mm}$ and the data were saved in IQ format, from which the envelope and log compressed B-mode data used for the speckle tracking algorithm could be calculated during post-processing.

Optical DIC measurements

DIC measurements were taken using a 3D DIC system (Aramis 5M, GOM, Braunschweig, Germany) equipped with two cameras with $50\,\mathrm{mm}$ lenses (Schneider Kreuznach, Bad Kreuznach, Germany). The measuring volume was $45 \times 50 \times 25\,\mathrm{mm}$ (height $\times$ width $\times$ depth) and the system was calibrated using a $30 \times 24\,\mathrm{mm}$ panel (resulting calibration deviation <0.03 pixel). A light-on-dark speckle pattern was used: the ligaments were stained using a $1\,\%$ methylene blue solution before spraying on a white acrylic paint speckle pattern [266, 267]. Data were captured at $9\,\mathrm{Hz}$. Simultaneous DIC and ultrasound measurement was not possible due to the line-of-sight requirement for the optical DIC. To verify that this did not affect the results, optical DIC acquisitions were taken both before and after the ultrasound acquisitions, with each capturing six loading intervals of $0\,\%$ to maximum strain.

Data analysis

For the DIC measurements, commercial software (Aramis Professional 2017, GOM, Braunschweig, Germany) was used to create a surface component over the complete ligament with point distance <15 pixels and facet size <30 pixels and the strain maps were calculated for each loading interval. A Matlab script was used to isolate the portion of the surface components aligned with the region of interest of the ultrasound measurements. To account for the fact that the ultrasound probe is not always placed in the same position and orientation on the ligament, strain was calculated along 1000 randomly placed lines that passed through this region of interest at varying angles. The mean across these

lines was used for the calculation of the overall mean strain data for comparison with the ultrasound results.

The ultrasound and DIC data were synchronised and split into intervals of minimum to maximum loading by manually identifying the frames in the video sequences in which the MCL was the most slack and taut, and a region ($\sim 30 \times 4.5\,\mathrm{mm}$) encompassing the ligament was selected on the first ultrasound image of each interval. A total of 120 intervals were available for analysis (Figure 6.5). For each specimen, 10 intervals for each imaging mode were randomly assigned to the training set. The remaining intervals were used for testing, with at least 4 available for each imaging mode for each specimen.

The training subset ($n = 60$) was first used for the displacement convergence check, which aimed to determine the minimum settings for which the full tissue motion is captured. Convergence was checked for the following settings: frame rates ($2 - 30\,\mathrm{Hz}$), non-rigid image registration (NRIR) pyramid levels ($1 - 6$), and block-matching axial/lateral maximum displacement settings ($0.1 - 0.5\,\mathrm{mm}$). Settings for which the lateral displacement field had not converged (relative errors above $5\,\%$) were excluded from the to-be-trialled optimisation

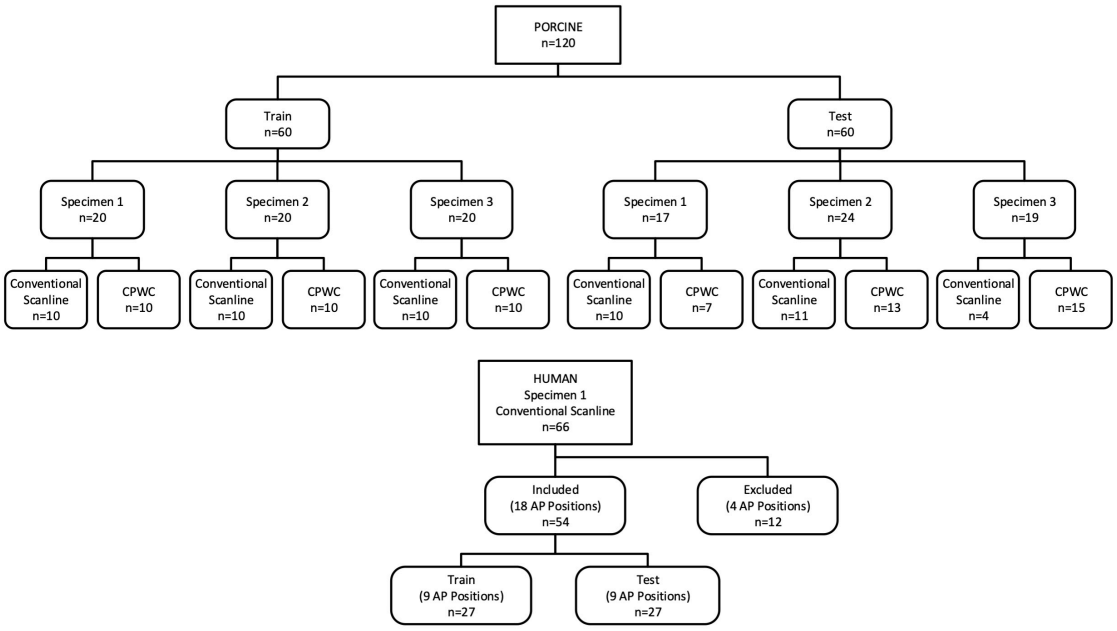


FIGURE 6.5 Flowchart of the *ex vivo* ultrasound speckle tracking measurements taken for the porcine and human specimens, illustrating the training/test split for the optimisation routine. Human measurements for which the transducer was not on the MCL or the anterior bundle of the posterior oblique ligament (POL) were excluded.

inputs.

The surrogate optimisation routine on the training subset was subsequently used to create the application-specific speckle tracking algorithm (without knowledge of the DIC result). The speckle tracking settings that were trialled during the optimisation routine are summarised in Table 6.1, and these were based on parameter values identified from the literature. To reduce computational requirements, possible sample points were limited to a range of settings with predefined step sizes. The performance of the tuned algorithm was verified through comparison to the optical DIC data using the independent test subset.

The calculated ultrasound and DIC strains were then quantitatively compared by calculating the average RMSE and Pearson's correlation coefficient (R) between the mean strain curves during the captured loading cycle. Since DIC is only able to capture the surface strains, the mean strain curves for the ultrasound measurements were calculated using just the row of nodes closest to the surface of the ligament.

To also enable comparison of the repeatability of the ultrasound and optical DIC techniques, the same metric used as quality penalty during the ultrasound optimisation, i.e. normalised standard deviation (Figure 4.4, page 100), was also calculated for the ultrasound test subset and the optical DIC: the final strain maps at maximum loading of different repeats of the same specimen were aligned and the normalised standard deviation of the maps at maximum strain was found. For the DIC measurements, this procedure was repeated for a range of median filter settings in the GOM software; results are reported for median filter $= 10$ since a convergence analysis revealed that the calculated quality penalties and strains converged at this point.

TABLE 6.1 Parameters of the speckle tracking algorithm that were tuned for all applications of this project, showing the settings used in previous studies, the range of settings tested here, and the final settings found by the surrogate optimisation routine (after 1500 iterations) for the *ex vivo* porcine, *ex vivo* human, and *in vivo* human ligaments. The *ex vivo* studies are discussed in Chapter 6, and the *in vivo* study is described in Chapter 7.

Optimisation parameters	Description	Settings used in previous studies	Settings tested in this study	Porcine MCL optimisation results	*Ex vivo* human medial knee ligaments optimisation results	*In vivo* human medial knee ligaments optimisation results
Imaging mode	Ultrasound transmission and acquisition method used to obtain the ultrasound images.	Most ultrasound scanners use conventional scanline imaging, but there is some evidence of improved performance with coherent plane-wave compounding (CPWC) [109]	**Porcine:** conventional scanlines and coherent plane-wave compounding ***Ex vivo* human:** conventional scanlines ***In vivo* human:** conventional scanlines	Conventional scanlines	Conventional scanlines	Conventional scanlines
Longitudinal node spacing (mm)	Node spacing along the selected region of interest.	**MCL:** 0.8 [51, 166] **LCL:** 0.5-0.8 [49, 51, 166] **Achilles tendon:** 0.5-0.83 [191, 193, 199] **Patellar tendon:** 2 [200, 201]	0.4, 0.6, 0.8, 1.0, 1.2, 1.4, 1.6, 1.8, 2.0	2.0	0.6	1.0
Transverse node spacing (mm)	Node spacing across the selected region of interest.	**LCL:** 0.5 [49] **Achilles tendon:** 0.2-0.5 [191, 193, 199]	0.10, 0.15, 0.20, 0.25, 0.30, 0.35, 0.40, 0.45, 0.50	0.35	0.30	0.25
Processing frame rate (Hz)	Frame rate of the ultrasound video. Original frame rate of the collected acquisitions was 30 fps (maximum achievable with the ultrasound machine and imaging modes used in this study). This was downsampled by a factor of 2 and 3 to obtain the lower frame rates of 15 and 10 fps.	**MCL:** 17.5-70 [51, 166] **LCL:** 17.5-70 [49, 51, 166] **Achilles tendon:** 42-155 [90, 93, 193, 199] **Patellar tendon:** 70 [201] **Flexor digitorum superficialis tendon:** 120 [197]	**Porcine:** 10, 15, 30 ***Ex vivo* human:** 30 ***In vivo* human:** 30	10	30	30
Displacement calculation method	Method used to find nodal displacements.	Block-matching [49, 89, 93, 95, 166, 191–193, 197, 199, 202] Non-rigid image registration (NRIR) [177, 190, 194, 195]	**Porcine:** Block-matching and NRIR ***Ex vivo* human:** Block-matching and NRIR ***In vivo* human:** NRIR only (displacement field convergence was not achieved with block-matching)	NRIR	NRIR	NRIR
Block-matching lateral kernel size (mm)	Kernel size in the lateral direction.	**MCL:** 0.4-1.6 [51, 166] **LCL:** 0.4-1.6 [49, 51, 166] **Achilles tendon:** 1-2 [90, 94, 95, 191, 193] **Patellar tendon:** 1.35 [200, 201] **Tibialis anterior tendon:** 0.5 [196] **Flexor digitorum superficialis tendon:** 4.3 [197]	**Porcine:** 0.4, 0.6, 0.8, 1.0, 1.2, 1.4, 1.6 ***Ex vivo* human:** 0.4, 0.6, 0.8, 1.0, 1.2, 1.4, 1.6 ***In vivo* human:** -	-	-	-
Block-matching axial kernel size (mm)	Kernel size in the axial direction.	**MCL:** 0.4-1.6 [51, 166] **LCL:** 0.6-3.2 [49, 51, 166] **Achilles tendon:** 0.4-1 [90, 94, 95, 191, 193] **Patellar tendon:** 1 [200, 201] **Tibialis anterior tendon:** 0.3 [196] **Flexor digitorum superficialis tendon:** 2.2 [197]	**Porcine:** 0.4, 0.6, 0.8, 1.0, 1.2, 1.4, 1.6 ***Ex vivo* human:** 0.4, 0.6, 0.8, 1.0, 1.2, 1.4, 1.6 ***In vivo* human:** -	-	-	-

Block-matching lateral maximum displacement (mm)	Maximum detectable frame-to-frame displacements in the lateral direction.	**MCL:** 0.8 [166] **LCL:** 0.6-1 [49, 166] **Achilles tendon:** 0.8-1 [95, 188] **Tibialis anterior tendon:** 1 [196] **Flexor digitorum superficialis tendon:** 4.3 [197]	**Porcine:** 0.1, 0.2, 0.3, 0.4, 0.5 ***Ex vivo* human:** 0.3, 0.4, 0.5 ***In vivo* human:** -	-	-	-
Block-matching axial maximum displacement (mm)	Maximum detectable frame-to-frame displacements in the axial direction.	**MCL:** 0.2 [166] **LCL:** 0.5-0.8 [49, 166] **Achilles tendon:** 0.4-0.8 [95, 188] **Tibialis anterior tendon:** 0.3 [196] **Flexor digitorum superficialis tendon:** 0.86 [197]	**Porcine:** 0.1, 0.2, 0.3, 0.4, 0.5 ***Ex vivo* human:** 0.3, 0.4, 0.5 ***In vivo* human:** -	-	-	-
Block-matching cross-correlation threshold	If the normalised cross-correlation between the reference and search kernel is below this threshold, displacements are interpolated from neighbouring nodes.	**MCL:** 0.5-0.95 [51, 166] **LCL:** 0.5-0.95 [51, 166] **Achilles tendon:** 0.7 [90, 188, 192] **Tibialis anterior tendon:** 0.7 [196] **Flexor digitorum superficialis tendon:** 0.7 [197]	**Porcine:** 0.50, 0.55, 0.60, 0.65, 0.70, 0.75, 0.80, 0.85, 0.90, 0.95 ***Ex vivo* human:** 0.50, 0.55, 0.60, 0.65, 0.70, 0.75, 0.80, 0.85, 0.90, 0.95 ***In vivo* human:** -	-	-	-
NRIR pyramid levels	Number of multi-resolution image pyramid levels used in the imregdemon Matlab function.	No settings published	**Porcine:** 1, 2, 3, 4, 5, 6 ***Ex vivo* human:** 3, 4, 5, 6 ***In vivo* human:** 3, 4, 5, 6	5	6	4
NRIR smoothing level	Amount of diffusion-like regularisation applied in the imregdemon Matlab function.	No settings published	1, 2, 3, 4, 5, 6, 7, 8, 9, 10	10	7	2
Regularisation order	Specifies whether regularisation is applied to the step displacements or the final cumulative displacements.	Step displacements [166, 168, 198, 268]	Step displacements Cumulative displacements	Step displacements	Step displacements	Cumulative displacements
Regularisation method	Type of regularisation used to remove noise in the displacement field and prevent noise amplification when calculating the strain field.	Median filter [49, 166, 168, 173, 188, 198, 240] 2^{nd} order polynomial surface fit [88, 94, 191, 199] 2D cubic smoothing spline [246] Median filter & 2^{nd} order polynomial surface fit [50, 51, 90]	Median filter 2^{nd} order polynomial surface fit 2D cubic smoothing spline 4^{th} order low-pass Butterworth filter 4^{th} order low-pass Butterworth filter & 2D cubic smoothing spline Median filter & 2^{nd} order polynomial surface fit Median filter & 2D cubic smoothing spline	Median filter & 2D cubic smoothing spline	4^{th} order low-pass Butterworth filter & 2D cubic smoothing spline	4^{th} order low-pass Butterworth filter & 2D cubic smoothing spline
Median filter longitudinal window size (mm)	Median filter window size along the selected region of interest.	2.5-3 [49, 188, 198]	1.0, 1.5, 2.0, 2.5, 3.0, 3.5, 4.0, 4.5, 5.0	2.5	-	-
Median filter transverse window size (mm)	Median filter window size across the selected region of interest.	1.5 [49, 188, 198]	0.5, 0.7, 0.9, 1.1, 1.3, 1.5	0.7	-	-
Cubic smoothing spline smoothing parameter	Amount of smoothing used in the spaps Matlab function.	No settings published	7.0, 7.5, 8.0, 8.5, 9.0, 9.5, 10.0	10.0	10.0	10.0
Butterworth filter longitudinal cut-off frequency (mm^{-1})	Cut-off frequency along the selected region of interest.	No settings published	400, 600, 800, 1000, 1200, 1400, 1600, 1800, 2000	-	400	400
Butterworth filter transverse cut-off frequency (mm^{-1})	Cut-off frequency across the selected region of interest.	No settings published	400, 600, 800, 1000, 1200, 1400, 1600, 1800, 2000	-	400	400

6.2.4 Speckle tracking: cadaveric human specimens

To verify that the optimisation routine is insensitive to anatomy and loading conditions, it was also tested for ultrasound measurements taken of the MCL and POL of a human cadaveric knee during a dynamic extension-flexion movement. During extension-flexion, these medial ligamentous structures strain due to the physiological motion. Previous studies have found that ligament structures anterior and posterior to the medial epicondyle experience opposing elongation behaviours during this movement: structures with posterior attachments (i.e., posterior MCL and POL) will shorten during flexion, while structures with anterior attachments (i.e., anterior MCL) will experience lengthening, with the effect becoming more apparent the further the attachments are located from the epicondyle [18, 47]. Thus, the speckle tracking algorithm was tested for this trend.

Specimens & test setup

Following ethics approval (Imperial College Healthcare Tissue Bank) and informed consent in line with the Declaration of Helsinki [269], an undissected fresh-frozen human cadaveric knee (female, 49 y old) was thawed for 24 h at room temperature and placed in an established, manually actuated extension-flexion kinematics rig [18, 270]. The knee was extended/flexed between 0° and 100° and a metronome was used to regulate the motion cycle to 0.25 Hz. Regular water spray prevented tissues from drying out.

Ultrasound measurements

The ultrasound transducer was attached to the tibia using a clamp (Figure 6.6); this reduced out-of-plane motion since the investigated ligament structures are close to parallel to the longitudinal axis of the tibia throughout extension and flexion. Ultrasound measurements were taken for 22 different anterior/posterior (AP) positions of the transducer spaced ∼1 mm using the same ultrasound acquisition system as before, but this time images were only collected using the conventional scanline imaging mode. For each AP position, three repeats of extension to flexion were recorded (Figure 6.5).

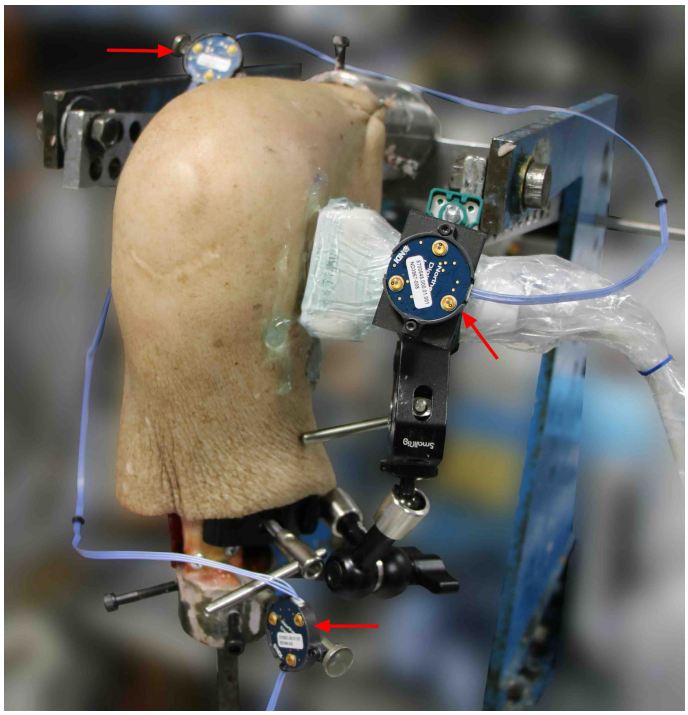


FIGURE 6.6 Experimental setup for the human ligament strain measurements. The cadaveric knee was mounted in an extension-flexion kinematics rig, the ultrasound transducer was attached to the tibia and held over the medial ligamentous structures, and the positions of the femur, tibia, and ultrasound probe were measured with a motion analysis system (arrows point to markers).

Motion analysis measurements

During all ultrasound acquisitions, the movement of the femur, tibia, and ultrasound transducer was tracked using an active marker motion analysis system with translational accuracy of $\pm 0.1\,\mathrm{mm}$ (Optotrak Certus, Northern Digital, Waterloo, ON, Canada) (Figure 6.6). After the ultrasound measurements were taken, the knee was dissected to expose the medial and lateral side of the joint, with the markers used for tracking remaining rigidly attached to the femur and tibia. The anterior and posterior edges of the tibial and femoral attachments of the MCL, and of anatomical landmarks that enabled adoption of a common knee joint coordinate system [271], were then digitised with respect to the tracking markers. This allowed for post-test calculation of the knee joint kinematics and movement of the ligament attachments using commonly applied rigid-body analysis techniques [272].

Data analysis

At the end of each measurement, the knee was held still for a couple of seconds before saving the ultrasound and motion analysis data; this allowed the implementation of a

Matlab algorithm which synchronised the two data streams by identifying the time point at which both the ultrasound images and motion analysis data became constant values with respect to time. Repeat ultrasound measurements were split into intervals of $0° - 100°$ of flexion and synchronised using the knee flexion angles, which were calculated with a Matlab algorithm used in previous motion analysis research [272]. The unconstrained kinematics, i.e., varus-valgus and internal-external rotation angles, were calculated as well, and the standard deviation of these across all measurements was computed to verify that the knee was subject to similar loading conditions throughout the experiment.

The motion analysis data was additionally used to determine the relative AP positions of the ultrasound transducer with respect to the ligaments using the tracked positions of the transducer and digitised MCL attachment points. This relative position was normalised to the MCL width, with zero set to the mid-portion of the MCL, -1 the posterior edge and 1 the anterior edge.

Ultrasound measurements for which the transducer was not located on the MCL or the anterior bundle of the POL were excluded, as determined from the calculated AP positions. This was due to the following: the POL gradually merges into the MCL, with its anterior fibres expected to be approximately in line with the MCL fibres and the longitudinal orientation of the ultrasound transducer. However, fibres located further posterior become increasingly more oblique and, thus, the collected ultrasound images do not capture the principal plane of motion in this region. Here, the cut-off was set to -1.5 of the normalised AP position, i.e., measurements for which the transducer extended beyond the posterior edge of the MCL by more than $25\,\%$ of its width were excluded.

For all remaining ultrasound measurements, the region of the ligament for which strains should be calculated was manually defined on the first ultrasound frame of the $0 – 100°$ of flexion intervals. Pilot tests indicated that processing strains in the region lying on the tibia yielded poor results. Thus, a region that started at the tibial plateau and spanned an area $\sim 20\,\mathrm{mm}$ proximally along the ligament (towards the femoral attachment) and $\sim 4.5\,\mathrm{mm}$ anteriorly across the thickness of the ligament was selected.

The ultrasound measurements were again split into a $50:50$ training and test subset (Figure 6.5), where the training data was used for the convergence check and to construct the application-specific algorithm. The Pearson's correlation coefficient (R) between AP position and ligament strain was computed. Furthermore, the mean strains at full flexion along the anterior and posterior borders of the MCL were estimated by calculating the length changes between the digitised anterior and posterior MCL attachments obtained from the motion analysis measurements. The motion analysis and ultrasound strains at full flexion were compared by interpolating the motion analysis strains to the AP positions at which ultrasound strains were obtained and calculating the RMSE between the two strain measures. Again, repeatability was analysed with the normalised standard deviation of the 2D strain maps between repeats of the same measurement. Note that, since the measurements were captured for knee flexion starting at $0°$, the strains calculated using the speckle tracking algorithm as well as the reference strains from the optically tracked attachment points were relative to the ligament state in full extension, rather than a measure of absolute strain.

6.3 Results

6.3.1 Shear wave imaging: agar phantom specimens

Agar cube specimens

The measured dimensions and weights of the agar cube specimens are summarised in Table 6.2.

The quasi-static compression tests on the agar cube specimens found that the initial apparent Young's modulus (first $10\,\%$ of loading) ranged from 37 to 64 kPa, increasing with higher agar concentrations (Figure 6.7).

The Young's moduli, Voigt viscosities and Voigt time constants calculated with the different post-processing methods are presented in Table 6.3. The Young's moduli were highly

TABLE 6.2 Dimensions and weights of the agar cube specimens, as measured using a Vernier calliper. Heights were used to calculate strains, and the width and depth gave the cross-sectional area for stress calculation. The standard deviation (±SD) is based on three repeat measurements. However, for the length measurements, an error of $\pm 1.0\,\mathrm{mm}$ is assumed when computing the upper and lower Young's modulus, since the non-rigidity of the cubes made it difficult to take the measurements.

	Specimen 1	Specimen 2	Specimen 3	Specimen 4
Height (mm)	32.6 ± 0.9	42.3 ± 0.7	45.2 ± 0.5	44.0 ± 0.5
Width (mm)	42.3 ± 0.4	43.3 ± 0.4	43.2 ± 0.2	39.0 ± 0.9
Depth (mm)	41.3 ± 0.4	41.2 ± 0.3	41.6 ± 0.4	44.8 ± 0.4
Weight (g)	59.9	75.0	83.0	79.2
Density ($\mathrm{kg/m^3}$)	1051.8	993.9	1021.8	1030.2

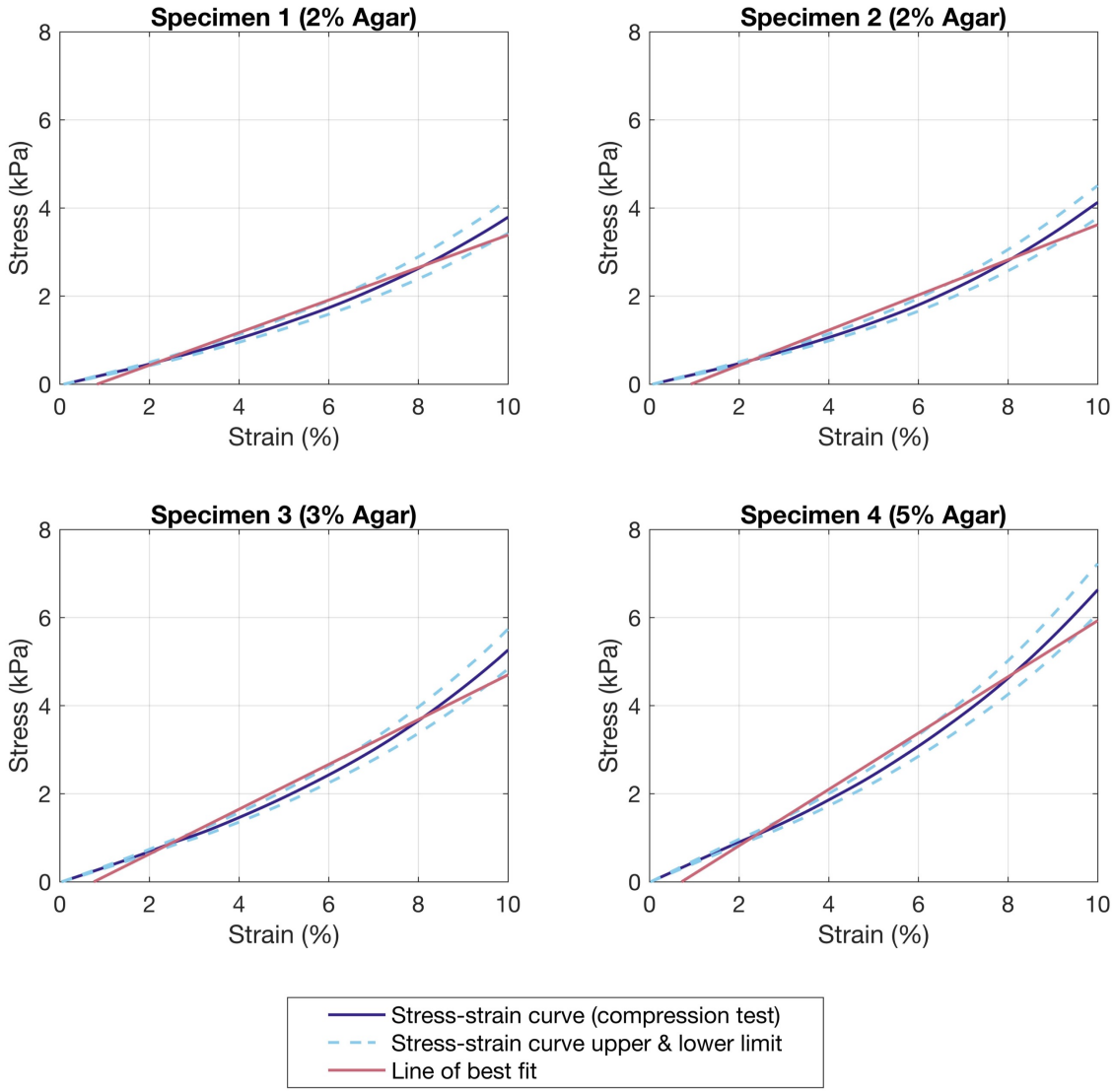


FIGURE 6.7 Quasi-static stress-strain curves during the initial response to loading for the large homogeneous agar cube samples of varying agar concentrations. The dashed lines show the upper and lower limit of the experimental stress-strain curves, which are based on the assumed $\pm 1\,\mathrm{mm}$ measurement errors for the dimensions of the agar cubes.

correlated with the initial apparent Young's moduli obtained from the mechanical compression tests ($R > 0.99$ for all four post-processing techniques) (Figure 6.8). The radon transform and linear regression time-of-flight (TOF) post-processing methods exhibited the largest errors (RMSE $= 7.72$ and $5.75\,\mathrm{kPa}$, respectively), with errors most prominent for specimens with higher Young's modulus. Young's moduli obtained with the phase velocity and viscoelastic dispersion analysis methods, on the other hand, agreed well with the mechanical testing results for all specimens (RMSE $= 2.44$ and $1.37\,\mathrm{kPa}$, respectively).

TABLE 6.3 Summary of the measured material properties for the agar cube specimens, obtained using ultrasound shear wave imaging and quasi-static material testing. For the shear wave imaging results, the data is based on six repeated measurements and presented as the mean ± standard deviation (SD), as the data was found to be normally distributed according to the Shapiro-Wilk test. Additionally, the range is provided (shown in square brackets). For the material testing results, the standard error (±SE) gives the uncertainty for the predicted gradient of the linear regression, while the range (shown in square brackets) is based on the upper and lower limit of the stress-strain curves.

		Specimen 1	Specimen 2	Specimen 3	Specimen 4
Young's modulus E (kPa)	Radon transform (TOF)	41.55 ± 1.78 [39.25 43.96]	41.12 ± 3.26 [38.15 46.64]	56.17 ± 1.86 [54.27 59.32]	77.58 ± 3.37 [73.66 82.18]
	Linear regression (TOF)	40.98 ± 1.93 [38.32 43.91]	40.35 ± 3.25 [36.84 45.89]	54.55 ± 1.94 [51.81 57.50]	74.00 ± 3.33 [70.83 80.00]
	Phase velocity method	39.60 ± 1.33 [38.25 42.08]	39.19 ± 3.32 [35.78 44.77]	52.18 ± 2.24 [48.89 54.57]	67.69 ± 3.67 [63.96 73.83]
	Viscoelastic dispersion analysis	38.43 ± 1.81 [36.83 41.76]	37.74 ± 2.96 [34.12 42.46]	50.86 ± 2.74 [47.19 54.06]	63.09 ± 3.05 [59.83 67.38]
	Material testing	36.93 ± 0.55 [33.50 40.85]	39.88 ± 0.70 [36.45 43.58]	50.85 ± 0.76 [46.68 55.26]	63.90 ± 0.95 [58.57 69.53]
Voigt shear viscosity η (Pa · s)	Viscoelastic dispersion analysis	0.82 ± 0.07 [0.74 0.93]	0.83 ± 0.12 [0.70 1.05]	1.00 ± 0.09 [0.85 1.10]	1.79 ± 0.17 [1.60 2.01]
Voigt time constant τ (µs)	Viscoelastic dispersion analysis	21.50 ± 1.92 [19.34 24.18]	21.85 ± 2.02 [19.13 24.71]	19.71 ± 2.50 [15.69 23.21]	28.48 ± 3.00 [25.43 33.62]

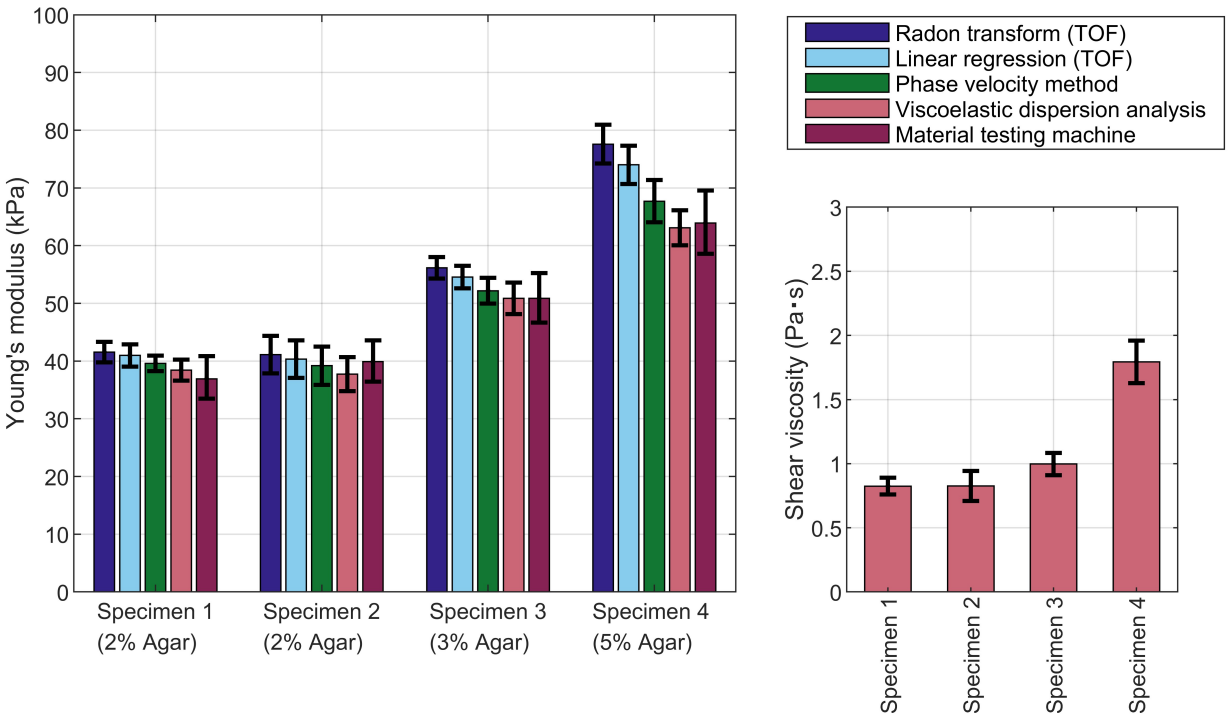


FIGURE 6.8 Bar chart of the measured material properties for the agar cube specimens, obtained using ultrasound shear wave imaging (four post-processing techniques), and quasi-static material testing. Error bars show ±SD for the shear wave imaging results, and the upper and lower limits for the material testing results. Shear wave imaging results were highly correlated with the Young's moduli obtained from the initial quasi-static stress-strain response, with the phase velocity and viscoelastic dispersion analysis post-processing methods providing the best accuracy.

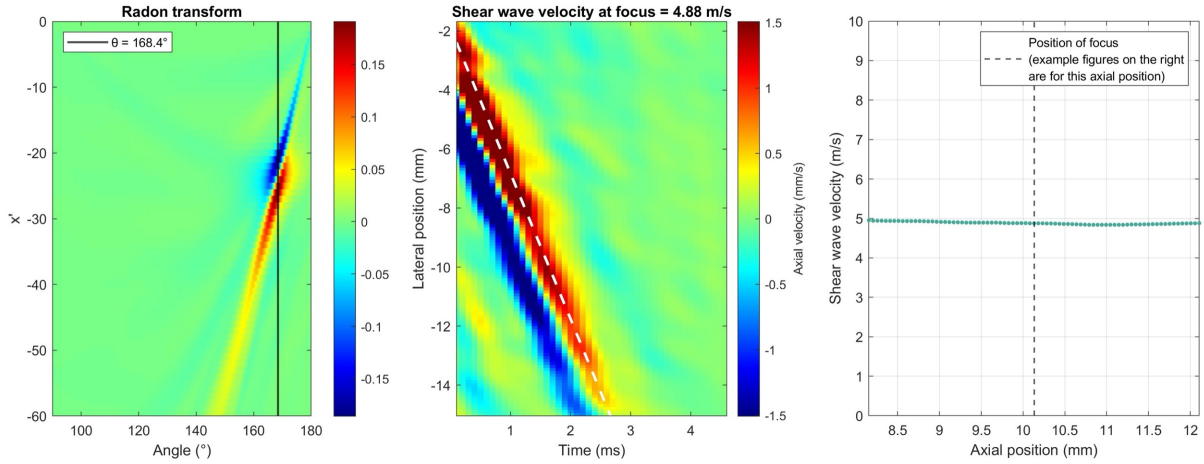


FIGURE 6.9 Radon transform (TOF) post-processing example for an agar cube specimen. The radon transform algorithm **(left)** calculates the sum along projections of different angles and offsets (x') and can thus detect lines in images. By applying the algorithm to the lateral-temporal axial velocity slice, the best projection (white dashed line) through the shear wave peaks/troughs can be found, the slope of which is equal to the shear wave velocity **(middle)**. This was repeated at a range of axial depths **(right)**.

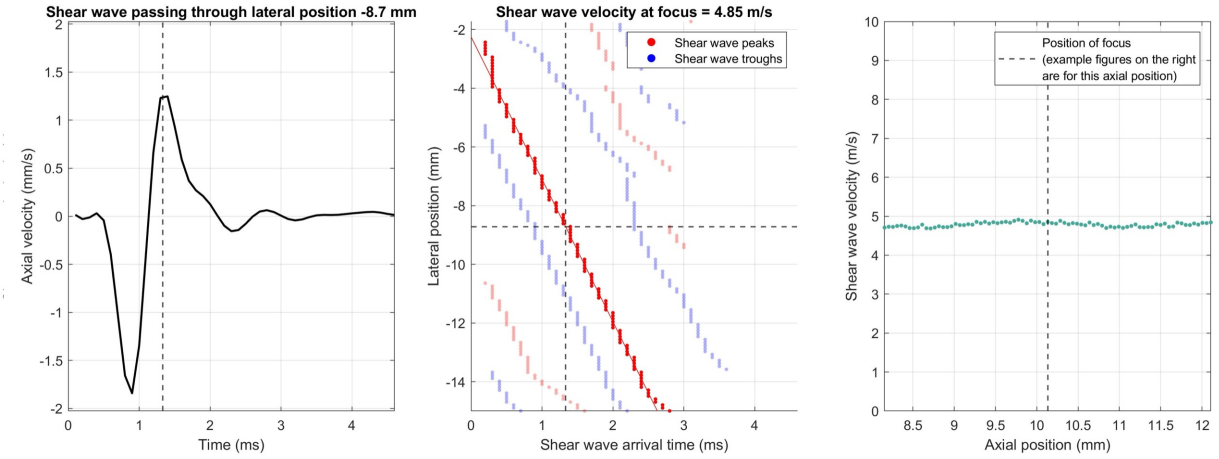


FIGURE 6.10 Linear regression (TOF) post-processing example for an agar cube specimen. Peaks/troughs were identified from the axial velocity vs time plot for each lateral position **(left)**. Thus, a line of best fit passing through the shear wave peaks or troughs can be found **(middle)**. This was repeated at a range of axial depths **(right)**.

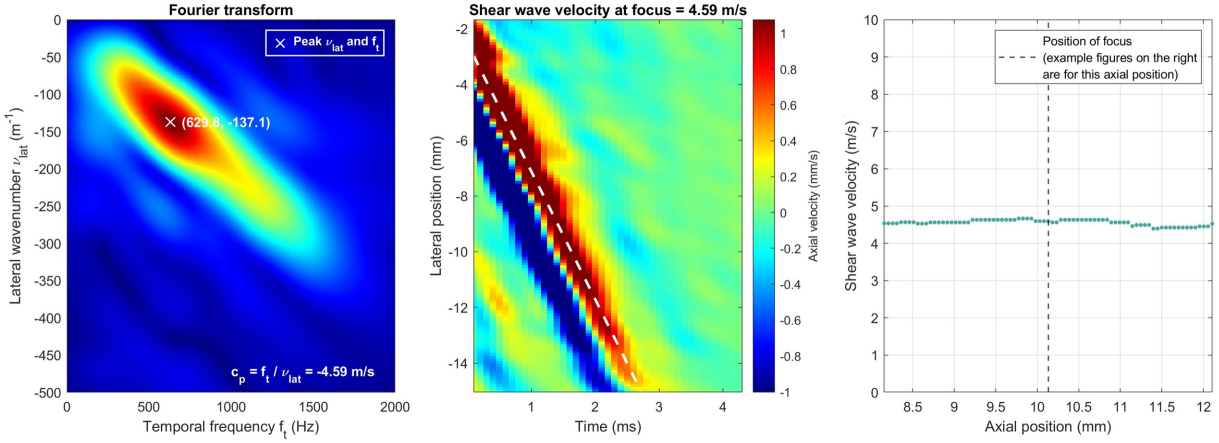


FIGURE 6.11 Phase velocity method post-processing example for an agar cube specimen. By finding the peak spatial and temporal frequencies in the Fourier domain of the axial velocity slice **(left)**, the shear wave trajectory (white dashed line) of the dominant phase component in the axial velocity slice was found **(middle)**. This was repeated at a range of axial depths **(right)**.

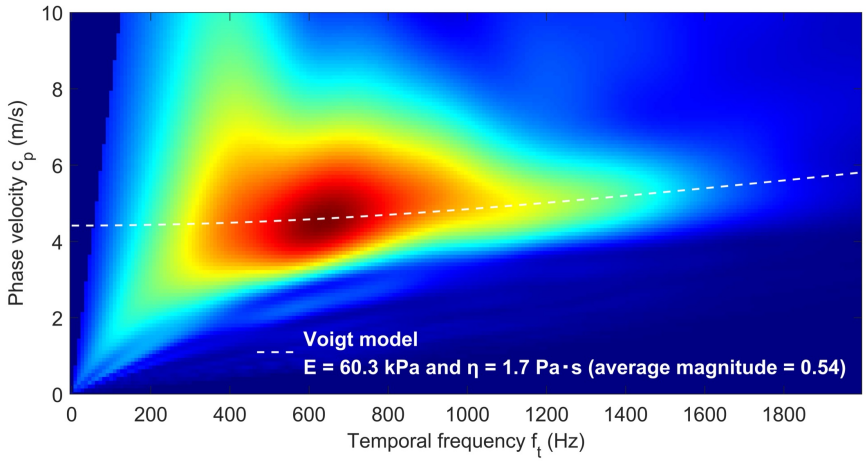


FIGURE 6.12 Viscoelastic dispersion analysis post-processing example for an agar cube specimen. The Voigt model was fit to the experimental dispersion map, which was obtained from the Fourier domain of the lateral-temporal axial velocities. Due to the increased computational cost of the fitting procedure, rather than obtaining a dispersion map at each axial position, an average axial-velocity slice for the $\pm 2\,\mathrm{mm}$ region above/below the push pulse focus was used.

Material properties measured for the two specimens made with the same agar concentration of $2\,\%$ w/w were in good agreement with one another, with the measured Young's moduli and Voigt viscosities obtained with shear wave imaging within $0.69\,\mathrm{kPa}$ and $0.01\,\mathrm{Pa \cdot s}$ of one another ($<2\,\%$ difference); for the mechanical compression test, the difference between the measured Young's moduli was $2.95\,\mathrm{kPa}$ ($\sim 8\,\%$ difference).

Figures 6.9 to 6.12 demonstrate how the shear wave imaging results were obtained for each of the four different post-processing methods for an example measurement of specimen 4.

Agar plate specimens

The measured dimensions and weights of the agar plate specimens are summarised in Table 6.4.

TABLE 6.4 Thicknesses of the agar plate specimens, as measured using a Vernier calliper. These were used for the Lamb wave models. The standard deviation (±SD) is based on four repeat measurements.

	Specimen 1	Specimen 2	Specimen 3	Specimen 4	Specimen 5	Specimen 6
Plate thickness (mm)	2.9 ± 0.6	3.8 ± 0.4	5.0 ± 0.4	5.7 ± 0.3	6.4 ± 0.2	7.2 ± 0.5

The shear wave imaging results for the agar plate specimens (5 % w/w) are shown in Table 6.5. The measured material properties varied greatly with plate thickness when using post-processing methods that did not consider Lamb wave dispersion, with the Young's moduli and Voigt viscosities exhibiting large coefficients of variations (CV $> 27\,\%$) and strong correlations with the plate thickness ($R > 0.7$) (Figure 6.13). Results from the Lamb wave and the combined Lamb wave & Voigt viscoelastic dispersion analysis were less affected by the specimen thickness, although variation was high for the viscosities of the combined model (Young's modulus: $R = 0.09$ and 0.40, CV $= 14.8\,\%$ and $11.7\,\%$, respectively; Voigt shear viscosity for Lamb wave & viscoelastic analysis: $R = -0.27$, CV $= 52.9\,\%$).

The combined Lamb wave & viscoelastic dispersion analysis yielded results that best matched the Young's modulus obtained from the compression test on the 5 % w/w agar

TABLE 6.5 Summary of the measured material properties for the agar plate specimens, obtained using ultrasound shear wave imaging. The results for all three repeat measurements for each specimen and post-processing method are presented.

		Specimen 1	Specimen 2	Specimen 3	Specimen 4	Specimen 5	Specimen 6
Young's modulus E (kPa)	Radon transform (TOF)	36.78, 37.84, 40.48	52.03, 51.92, 52.07	65.43, 54.28, 56.42	55.23, 49.21, 104.02	108.42, 69.17, 64.70	83.60, 82.78, 110.98
	Linear regression (TOF)	36.24, 35.26, 37.01	50.80, 50.00, 49.62	64.54, 57.92, 66.67	50.95, 51.22, 51.79	63.33, 73.08, 69.93	82.81, 86.31, 86.51
	Phase velocity method	19.66, 15.46, 18.01	38.15, 28.03, 32.15	47.51, 46.89, 48.07	29.24, 27.61, 31.35	31.20, 43.82, 46.65	68.03, 73.64, 73.11
	Viscoelastic dispersion analysis	17.96, 19.61, 19.51	29.67, 25.62, 27.84	27.36, 31.72, 33.78	22.70, 23.02, 23.62	28.92, 28.09, 32.00	59.68, 41.15, 43.01
	Lamb wave dispersion analysis	64.48, 64.48, 66.99	87.13, 86.38, 84.04	89.01, 81.88, 82.26	57.93, 53.53, 57.93	77.70, 76.65, 80.00	77.59, 80.23, 80.33
	Viscoelastic & Lamb wave dispersion analysis	52.88, 55.21, 55.05	72.66, 69.59, 68.37	69.22, 69.88, 65.57	57.93, 52.10, 57.93	68.37, 72.90, 76.73	66.62, 66.21, 69.31
Voigt shear viscosity η (Pa · s)	Viscoelastic dispersion analysis	1.34, 1.30, 1.33	1.74, 1.88, 1.75	2.24, 2.12, 2.17	1.89, 1.78, 1.93	2.20, 2.42, 2.43	2.02, 2.51, 2.46
	Viscoelastic & Lamb wave dispersion analysis	1.50, 1.35, 1.50	1.82, 2.09, 1.95	2.69, 2.71, 3.13	0.22, 0.42, 0.31	1.75, 1.00, 0.89	1.34, 1.55, 1.37
Voigt time constant τ (µs)	Viscoelastic dispersion analysis	74.77, 66.41, 68.33	58.73, 73.43, 62.79	81.86, 66.81, 64.28	83.45, 77.51, 81.74	76.22, 86.19, 75.91	33.82, 61.11, 57.27
	Viscoelastic & Lamb wave dispersion analysis	28.33, 24.46, 27.17	25.08, 30.09, 28.56	38.93, 38.84, 47.67	3.75, 8.06, 5.27	25.54, 13.68, 11.54	20.17, 23.38, 19.74

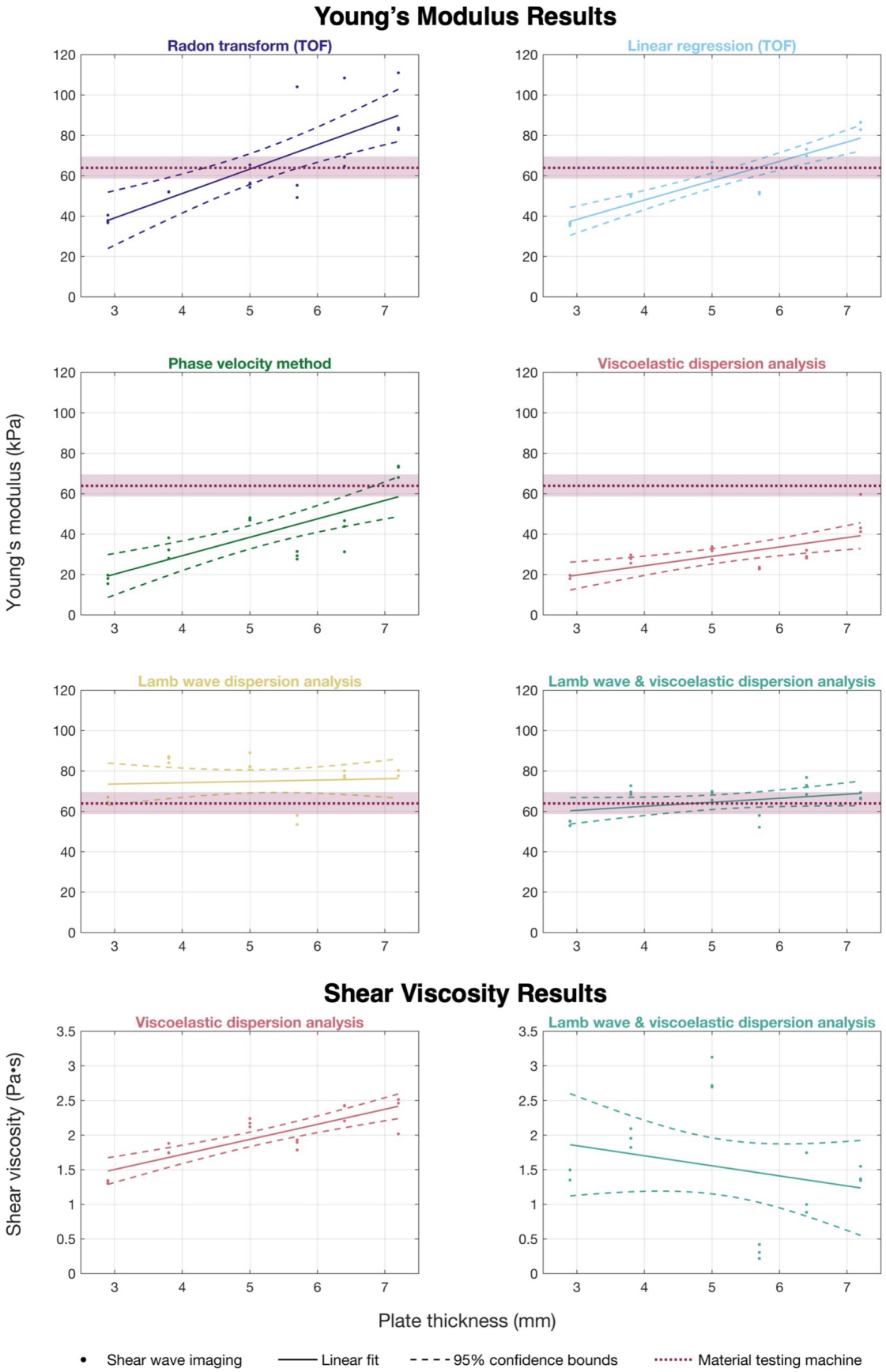


FIGURE 6.13 Material properties for the thin-layered agar plate specimens of varying thickness, obtained using ultrasound shear wave imaging (six post-processing techniques). All three repeats collected for each plate thickness are shown. Results were most comparable to the Young's modulus obtained from mechanical test on the $5\,\%\,\mathrm{w/w}$ agar cube when using the combined Lamb wave & viscoelastic dispersion analysis.

cube specimen (RMSE $= 7.41\,\mathrm{kPa}$). Results deviated most from the validation Young's modulus when using the viscoelastic dispersion analysis (RMSE $= 35.55\,\mathrm{kPa}$).

For plate thicknesses larger than $5\,\mathrm{mm}$, two modes were clearly visible on the dispersion maps, and the models that considered Lamb wave dispersion appeared to provide a better fit to these multiple modes (Figure 6.14).

The sensitivity analysis, which was performed on the two multi-variable viscoelastic dispersion models, showed that the combined Lamb wave & viscoelastic dispersion model resulted in slightly larger confidence regions (Figure 6.15). For the viscoelastic dispersion model, the goodness-of-fit (average magnitude along the curve) remained within $1\,\%$ of the curve of best fit for a range of shear moduli and viscosities of around $8\,\mathrm{kPa}$ and $0.7\,\mathrm{Pa}\cdot\mathrm{s}$. For the combined Lamb wave & viscoelastic model, the shear moduli and viscosities could vary around $9\,\mathrm{kPa}$ and $1.8\,\mathrm{Pa}\cdot\mathrm{s}$.

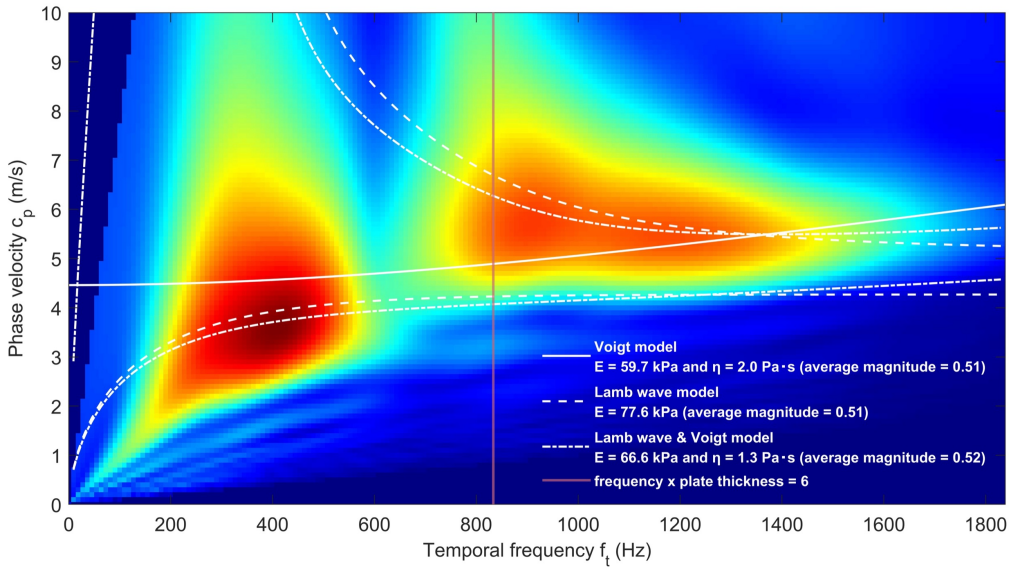


FIGURE 6.14 Dispersion analysis post-processing example for an agar plate specimen (thickness $= 7.2\,\mathrm{mm}$). The three dispersion models were fit to the experimental dispersion map, with the fit aiming to find the curves that best pass through the high-magnitude regions. For the Lamb wave models, the A0 mode was fit to the experimental dispersion map for frequencies below $6/(\text{plate thickness})$ (i.e., below $833\,\mathrm{Hz}$ for this specimen), and the A1 mode was used for frequencies above this threshold.

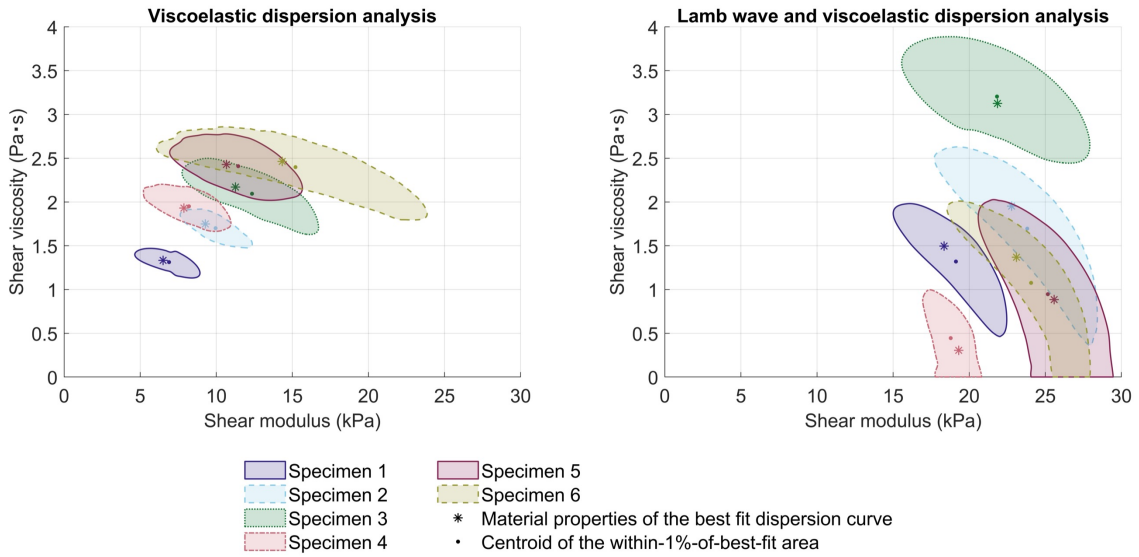


FIGURE 6.15 Sensitivity analysis for the multi-variable dispersion models applied to the agar plate measurements. The depicted confidence regions show the combinations of shear moduli and Voigt viscosities for which the goodness-of-fit of the dispersion curves are within $1\,\%$ of the best-fit dispersion curve. The $*$ markers show the material properties for the best fit, and the $\bullet$ markers show the material properties for the centroid of the confidence region. The goodness-of-fit was defined as the average magnitude of the experimental dispersion map along the fitted curve, which was also used as the optimisation parameter during the search for the curve of best fit.

6.3.2 Shear wave imaging: porcine specimens

The measured thicknesses of the four porcine MCL specimens used for the shear wave imaging validation are detailed in Table 6.6.

TABLE 6.6 Thicknesses of the porcine MCL specimens, as measured from the ultrasound images. These were used for the Lamb wave models. The standard deviation ($\pm$SD) is based on thicknesses measured from the 35 repeat ultrasound measurements for each specimen.

	Specimen 1	Specimen 2	Specimen 3	Specimen 4
Ligament thickness (mm)	4.30 ± 0.14	4.17 ± 0.03	6.70 ± 0.04	5.86 ± 0.78

All material properties measured from the mechanical sinusoidal loading test and ultrasound shear wave imaging procedure are shown in Table 6.7.

The dynamic sinusoidal tensile test found that the phase shift between the force and displacement response increased with loading frequency (Figure 6.16). The Voigt time constants computed from the gradients of the linear regression models ranged between $1.91 - 21.35$ ms. While the goodness-of-fit of the fitted Voigt time constant models ($tan(\delta) =$

TABLE 6.7 Summary of the measured material properties for the porcine MCL specimens, obtained using ultrasound shear wave imaging and dynamic material tensile testing. For the shear wave imaging time-of-flight (TOF) and phase velocity methods, the data did not follow a normal distribution due to its dependence on the shear wave excitation frequency. Therefore, results are presented as the range of material properties measured across 35 repeat measurements from seven excitation frequencies (shown in square brackets). For the shear wave imaging dispersion methods, results are based on 5 repeated dispersion maps, each constructed from a set of 7 measurements at different excitation frequencies. Normality was confirmed with the Shapiro-Wilk test, and thus, the mean ± standard deviation (SD) and the range (shown in square brackets) are provided. For the material testing results, the standard error (±SE) of the gradient from the linear regression is given.

		Specimen 1	Specimen 2	Specimen 3	Specimen 4
Voigt shear modulus μ (kPa)	Radon transform (TOF)	[17.66 89.49]	[41.51 166.49]	[6.69 162.40]	[15.88 118.37]
	Linear regression (TOF)	[30.87 95.78]	[77.82 193.56]	[31.63 161.48]	[19.13 111.15]
	Phase velocity method	[10.88 87.40]	[12.52 173.46]	[10.00 138.67]	[11.28 101.16]
	Viscoelastic dispersion analysis	4.15 ± 0.06 [4.07 4.22]	7.79 ± 0.09 [7.66 7.90]	5.63 ± 0.03 [5.58 5.66]	4.44 ± 0.05 [4.36 4.48]
	Lamb wave dispersion analysis	176.32 ± 0.38 [175.93 176.77]	484.26 ± 6.89 [473.39 490.40]	174.15 ± 4.96 [171.13 182.75]	145.22 ± 1.15 [143.99 146.79]
	Viscoelastic & Lamb wave dispersion analysis	5.20 ± 0.14 [5.03 5.42]	29.42 ± 1.86 [26.40 31.14]	10.16 ± 0.12 [10.01 10.31]	7.29 ± 0.09 [7.14 7.36]
Voigt shear viscosity η (Pa · s)	Viscoelastic dispersion analysis	8.32 ± 0.02 [8.29 8.34]	14.68 ± 0.15 [14.45 14.81]	10.64 ± 0.09 [10.57 10.79]	9.02 ± 0.04 [8.97 9.08]
	Viscoelastic & Lamb wave dispersion analysis	27.76 ± 0.07 [27.66 27.85]	86.95 ± 1.86 [84.01 88.85]	23.46 ± 0.15 [23.30 23.65]	21.66 ± 0.14 [21.53 21.87]
Voigt time constant τ (ms)	Viscoelastic dispersion analysis	2.01 ± 0.03 [1.98 2.04]	1.89 ± 0.02 [1.85 1.92]	1.89 ± 0.03 [1.87 1.93]	2.03 ± 0.01 [2.02 2.06]
	Viscoelastic & Lamb wave dispersion analysis	5.34 ± 0.13 [5.14 5.50]	2.97 ± 0.22 [2.70 3.31]	2.31 ± 0.03 [2.29 2.35]	2.97 ± 0.03 [2.94 3.02]
	Material testing	4.57 ± 0.70	3.02 ± 0.40	1.91 ± 0.30	21.35 ± 6.17

$\tau \times (2\pi f_{loading})$) was low ($R^2 < 0.75$), the standard error of the regression gradient remained below ± 0.70 ms for specimens 1 – 3. For the fourth specimen, longer phase lags with large standard deviations were observed, and the standard error of the regression gradient was also much higher (± 6.17 ms). This indicated that the specimen may have been damaged when cementing the tibia and femur, which was done between the shear wave imaging and mechanical test measurement; thus, the following results are presented both with and without this specimen.

Shear moduli measured using ultrasound shear wave imaging varied greatly depending on which post-processing method was used. Lamb wave dispersion analysis resulted in the highest measurements of 244.99 ± 160.14 kPa. The TOF and phase velocity methods all

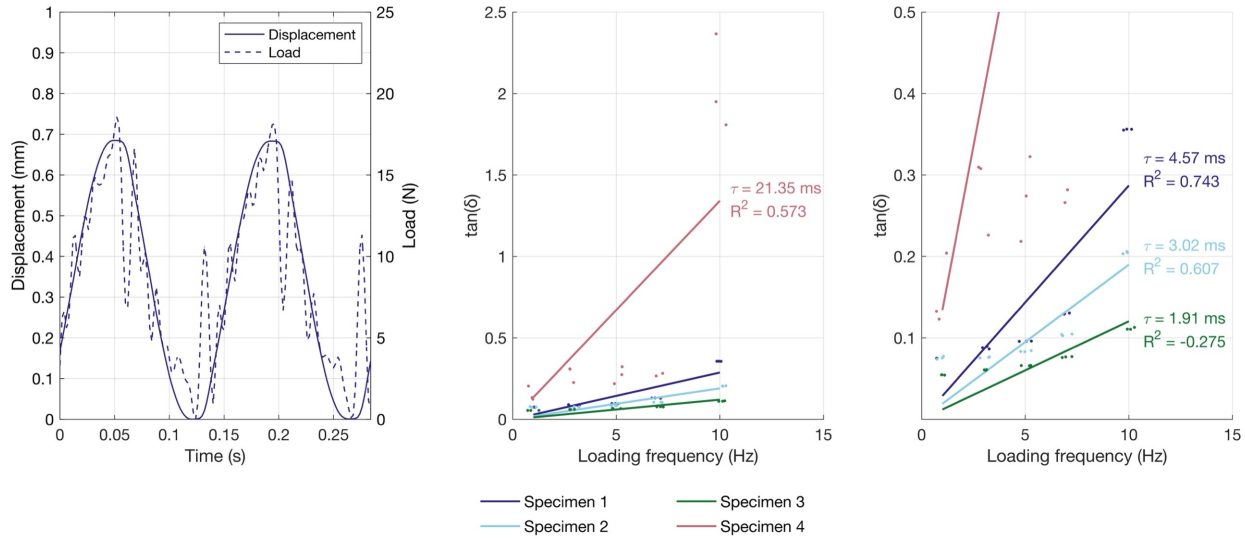


FIGURE 6.16 Viscoelastic behaviour of the porcine MCL specimens, measured using a dynamic tensile loading test. The force and displacement response are shown for an example measurement of specimen 1 loaded at 7 Hz **(left)**. While the phase lag (δ) was difficult to observe from the raw data, it could be derived from the frequency domain, and the results revealed that the tangent of the phase lag increased with loading frequency **(middle)**. An enlarged view with a smaller y-axis scale better shows this trend for specimens 1 – 3 **(right)**. The Voigt time constant (τ) was calculated from the gradient of the line of best fit.

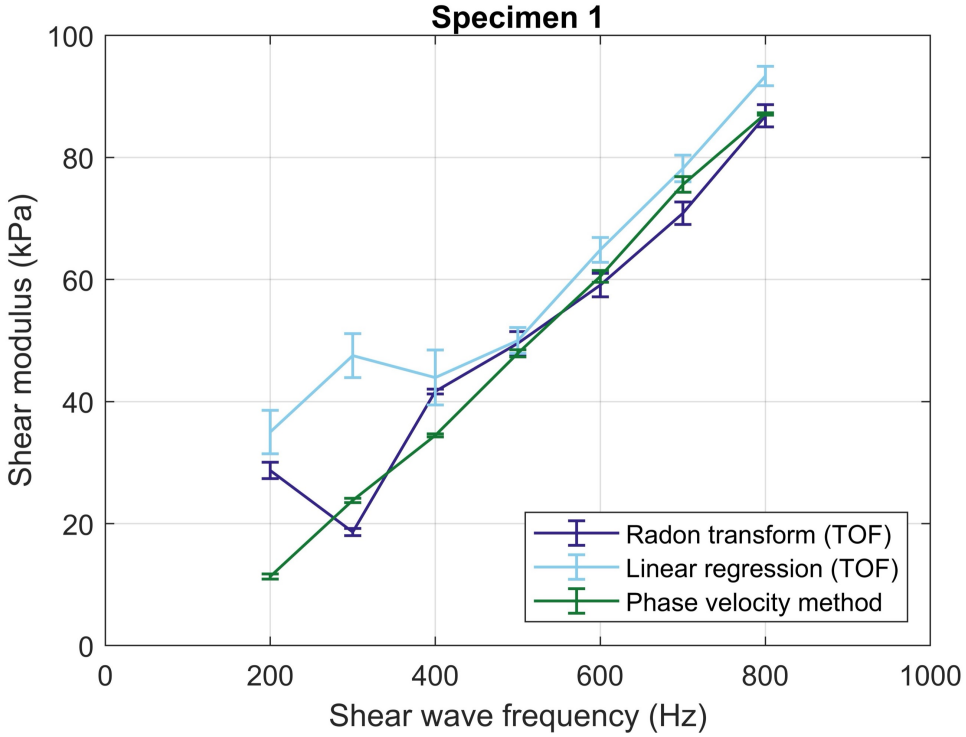


FIGURE 6.17 Example of how the shear modulus, obtained from shear wave imaging time-of-flight (TOF) or phase velocity post-processing methods, varied with different shear wave excitation frequencies (porcine MCL specimen 1). Error bars show ±SD of the 5 repeat measurements at each frequency. The overall shear modulus was calculated from the average of all measurements and, therefore, the results had large standard deviations.

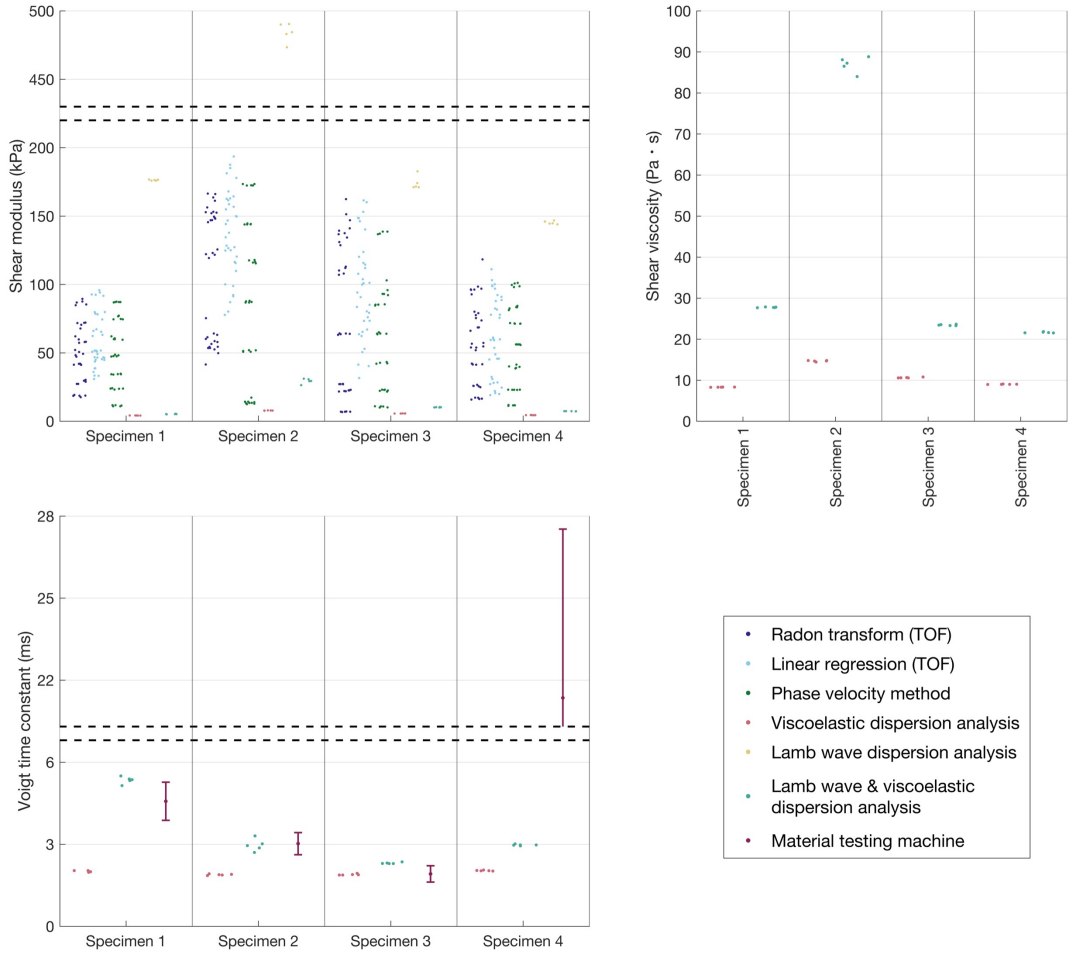


FIGURE 6.18 Scatter plot of the measured material properties for the porcine MCL specimens obtained using ultrasound shear wave imaging (six post-processing techniques), and dynamic sinusoidal tensile testing. Dashed black lines show a break in the y-axis. Error bars indicate ± standard error of the linear regression gradient for the material testing results. The shear modulus varied greatly for the different post-processing methods. Out of the two post-processing methods that also measured viscosity, the combined Lamb wave & viscoelastic dispersion analysis produced superior results that better matched the Voigt time constant from the material testing validation experiment.

produced similar measurements at a mid-range of $74.75 \pm 27.09\,\mathrm{kPa}$. These methods also resulted in the largest variability (CV $\approx 50\,\%$ vs $< 7\,\%$ for the other methods), since they calculate the shear modulus directly from the shear wave phase or group velocity, which varied greatly across the measurements of different excitation frequencies (Figure 6.17). Lastly, much lower shear moduli of $9.26 \pm 8.39\,\mathrm{kPa}$ were obtained when introducing viscous dispersion (Figure 6.18).

Comparison to the validation data showed that the viscoelasticity of the specimens was best captured when using the combined Lamb wave & viscoelastic dispersion analysis: the

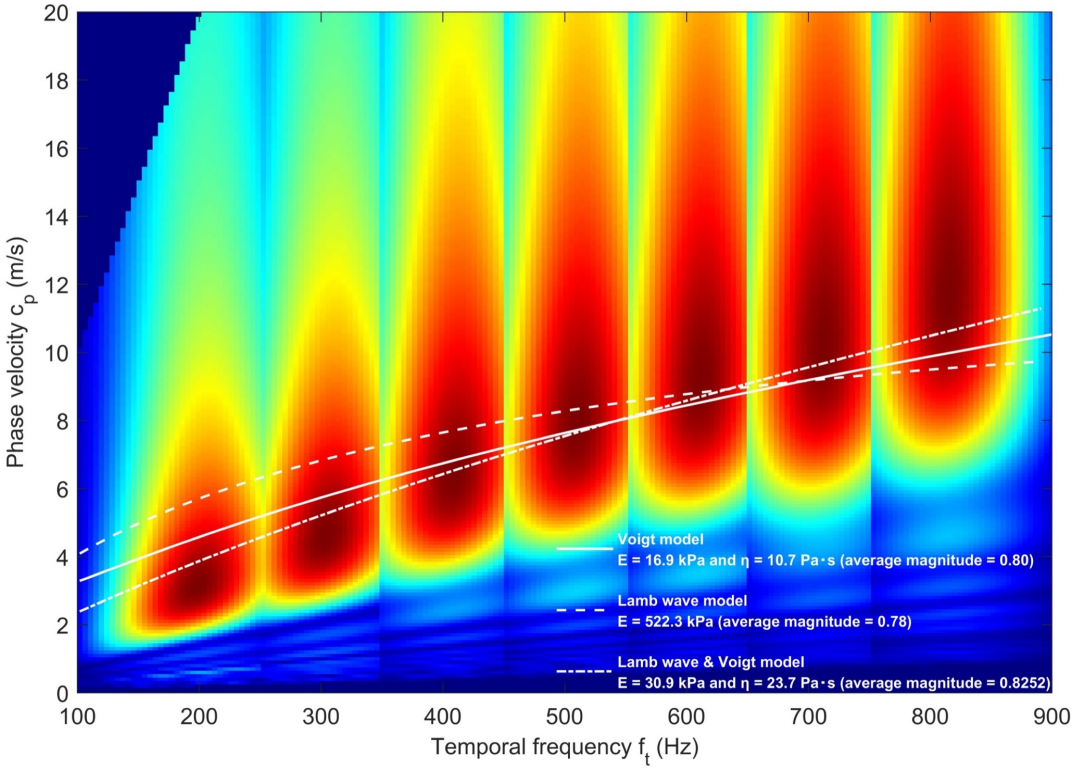


FIGURE 6.19 Dispersion analysis post-processing example for a porcine MCL specimen (thickness $= 6.7\,\mathrm{mm}$). Dispersion maps from seven different measurements, each utilising a different shear wave excitation frequency between $200 - 800\,\mathrm{Hz}$, were combined to produce one dispersion map with similarly strong magnitudes across the entire frequency range. All Lamb wave models only used the A0 mode, since the A0 to A1 switchover frequency was never reached.

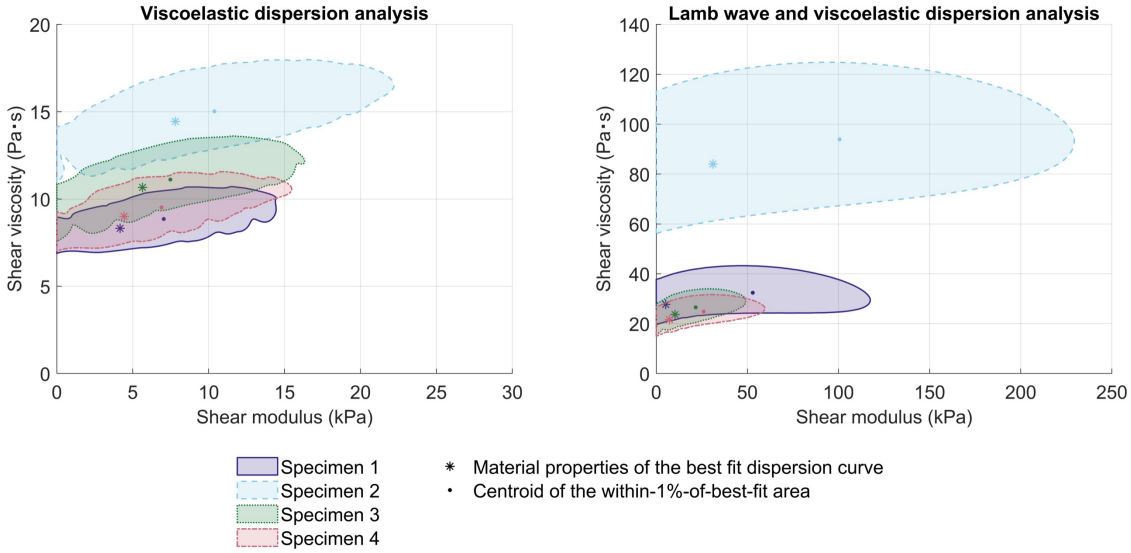


FIGURE 6.20 Sensitivity analysis for the multi-variable dispersion models applied to the porcine MCL measurements. The large confidence regions indicate a considerable level of uncertainty in the material properties found from the best fit, with a large range of shear moduli and viscosities producing similarly high goodness-of-fit measures. The $*$ markers show the material properties for the best fit, and the $\bullet$ markers show the material properties for the centroid of the confidence region.

Voigt shear modulus and viscosity of the fitted models resulted in Voigt time constants that best matched the results from the dynamic mechanical loading test (*without specimen* 4*:* $R = 0.98$, $RMSE = 0.50\,ms$; *with specimen* 4*:* $R = -0.10$, $RMSE = 9.20\,ms$). When using just the viscoelastic dispersion model without the Lamb wave component, the Voigt time constants were almost identical for all four specimen ($1.95 \pm 0.08\,ms$), which did not agree as well with the varying time constants measured during the mechanical test (*without specimen* 4*:* $R = 0.90$, $RMSE = 1.62\,ms$; *with specimen* 4*:* $R = 0.76$, $RMSE = 9.76\,ms$).

Only the A0 mode was utilised during the fitting of the Lamb wave model to the experimental dispersion map for all specimens. Since the thickness of all specimens was less than $6.7\,mm$, the A0 to A1 switchover frequency was expected to be over $900\,Hz$, which was above the maximum excitation frequency of $800\,Hz$. Visual inspection of the experimental dispersion maps confirmed that only one mode was active (Figure 6.19).

The sensitivity analysis revealed that there was a large level of uncertainty in the multivariable dispersion model results, with the goodness-of-fit of the dispersion models remaining high for a large range of shear moduli and viscosities (Figure 6.20). For the viscoelastic dispersion model, the goodness-of-fit remained within $1\,\%$ of the curve of best fit for a range of shear moduli and viscosities of around $15\,kPa$ and $\pm 5\,Pa \cdot s$. For the combined Lamb wave & viscoelastic model, the within-1-%-of-best-fit area spanned shear moduli and viscosities of up to $225\,kPa$ and $70\,Pa \cdot s$.

6.3.3 Speckle tracking: porcine specimens

For the quasi-static porcine MCL measurements, the pre-optimisation displacement convergence check found that frame rates had to be $\geq$9 Hz, NRIR pyramid levels $\geq$1, and block-matching axial/lateral maximum displacement $\geq$0.1 mm (Table 6.8, Figure 6.21). Thus, these settings were subsequently used during the surrogate optimisation routine (Table 6.1, page 153).

After running the surrogate optimisation routine for 1500 iterations, the quality penalty for the porcine training measurements reached a minimum of 0.19, with the strain maps visibly improving as the optimisation progressed and the quality penalty decreased (Figure 6.22). The strain maps were most repeatable when the displacement field was calculated using the non-rigid image registration method, followed by regularisation of the displacement field using a combination of a median filter and 2D cubic spline smoothing. All settings of the final tuned speckle tracking algorithm for the quasi-static porcine application are shown in Table 6.1, page 153).

Ultrasound and optical DIC strain measurements were strongly correlated (R $>$ 0.99, RMSE $<$ 0.59 %) (Figure 6.23). The average peak strains measured for the ultrasound test set and DIC acquisitions were 2.26 ± 0.60 % and 2.34 ± 0.28 %, respectively (Table 6.9). Furthermore, the ultrasound and DIC strain maps had comparable repeatability, with similar normalised standard deviation of repeat strain maps (US: $<$0.22, DIC: $<$0.22) (Figure 6.24).

TABLE 6.8 Results for the pre-optimisation convergence check on the porcine and human training sets, showing the settings for which convergence was tested, and the settings for which the lateral displacement field had converged to within relative errors of 5 %.

		Settings tested	Settings for which convergence was reached	
	Optimisation parameter	Human and porcine	Human	Porcine
NRIR	Frame rate (Hz)	$2-30$	≥ 20	≥ 9
	Pyramid levels	$1-6$	≥ 3	≥ 1
Block-matching	Frame rate (Hz)	$2-30$	≥ 23	≥ 9
	Axial/lateral maximum displacement (mm)	$0.1-0.5$	≥ 0.3	≥ 0.1

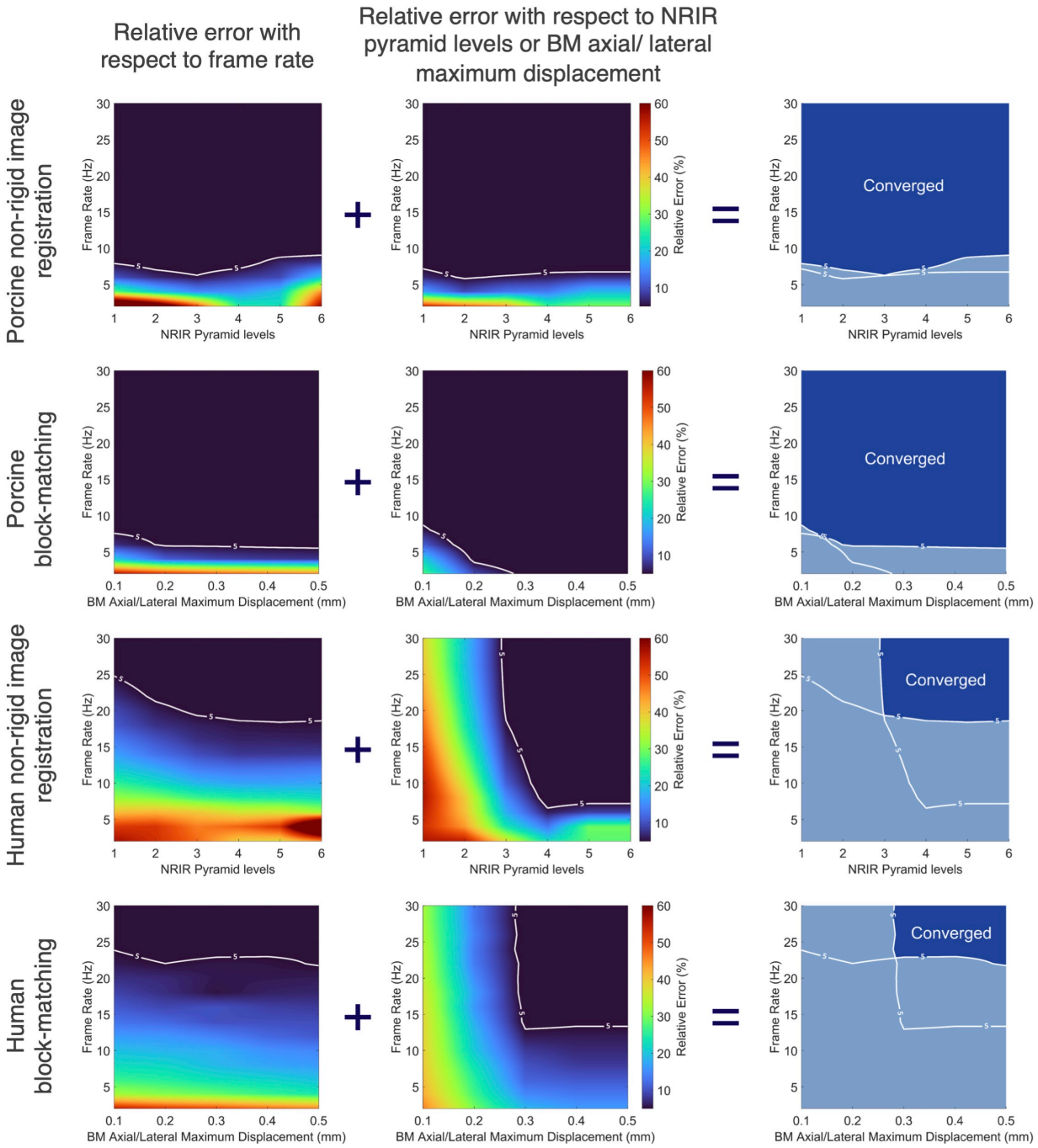


FIGURE 6.21 Displacement convergence results for the porcine and human training measurements. Relative errors for the lateral displacements were calculated both with respect to frame rate **(left column)** and NRIR pyramid levels or block-matching (BM) axial/lateral maximum displacement **(middle column)**. The white line shows the combination of settings at which the relative errors dropped below 5 %. Overall, convergence was then said to have been reached if both relative errors were below 5 % **(right column)**.

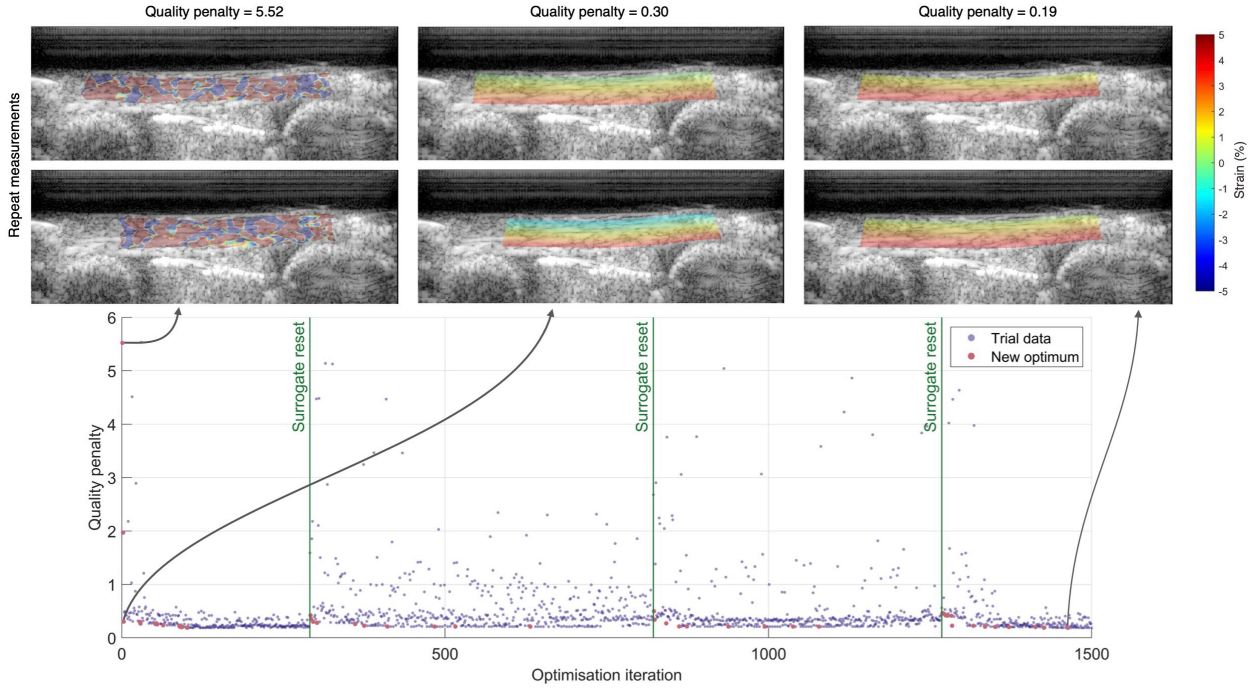


FIGURE 6.22 Convergence of the surrogate optimisation for the porcine measurements and example strain maps of repeats for different quality penalties. At each optimisation iteration, a different combination of parameter settings is trialled. After finding a local minimum, the surrogate optimisation resets with new starting points. As the quality penalty (normalised standard deviation of the strain maps) decreased, repeat strain maps became more similar.

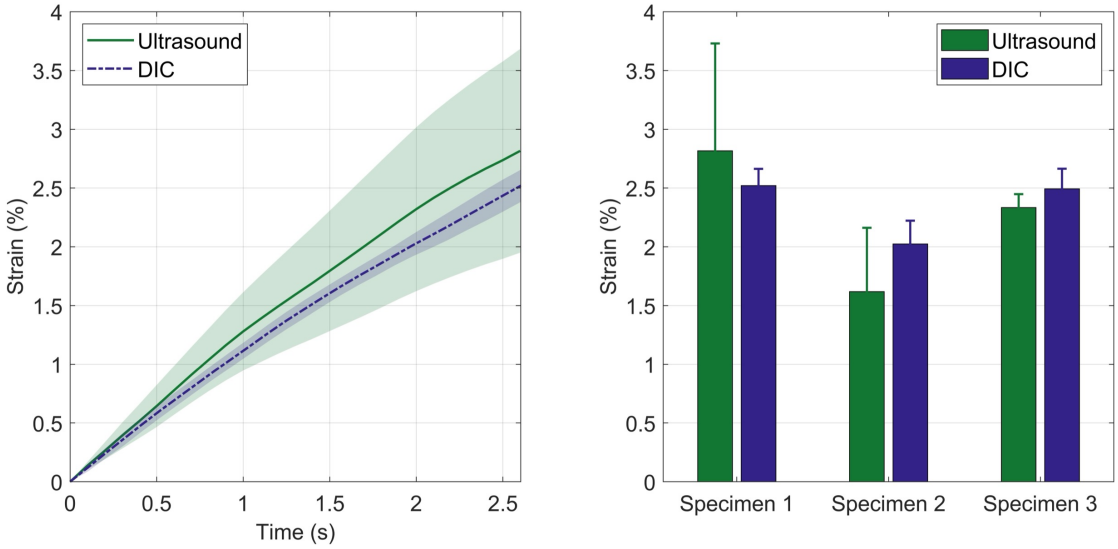


FIGURE 6.23 Porcine MCL surface strains measured by the tuned ultrasound speckle tracking algorithm (test set) and optical DIC. Example strain curves (mean $\pm$ SD) of porcine specimen 1 throughout the uniaxial tensile test show the strong correlation between ultrasound and DIC measurements **(left)**. Ultrasound speckle tracking and DIC measured comparable average strains at maximum loading for all porcine specimens **(right)**.

TABLE 6.9 Strain results for the three porcine specimens, obtained from the tuned ultrasound speckle tracking algorithm and the DIC measurements. The standard deviation is based on repeat measurements.

Specimen	Surface strains at maximum loading (%)			Normalised standard deviation of strain maps at maximum loading			RMSE between ultrasound and DIC strain curves (%)		R between ultrasound and DIC strain curves	
	Ultrasound training set	Ultrasound test set	DIC	Ultrasound training set	Ultrasound test set	DIC	Ultrasound training set	Ultrasound test set	Ultrasound training set	Ultrasound test set
1	2.72 ± 0.43	2.82 ± 0.91	2.52 ± 0.14	0.18	0.22	0.16	0.17	0.20	0.9996	0.9997
2	1.68 ± 0.66	1.62 ± 0.54	2.02 ± 0.20	0.18	0.20	0.22	0.15	0.23	0.9986	0.9995
3	1.40 ± 0.92	2.33 ± 0.11	2.49 ± 0.17	0.20	0.04	0.21	0.59	0.08	0.9918	0.9990
Average	1.93 ± 0.70	2.26 ± 0.60	2.34 ± 0.28	0.19 ± 0.01	0.15 ± 0.10	0.20 ± 0.03	0.30 ± 0.25	0.17 ± 0.08	0.9967 ± 0.0042	0.9994 ± 0.0003

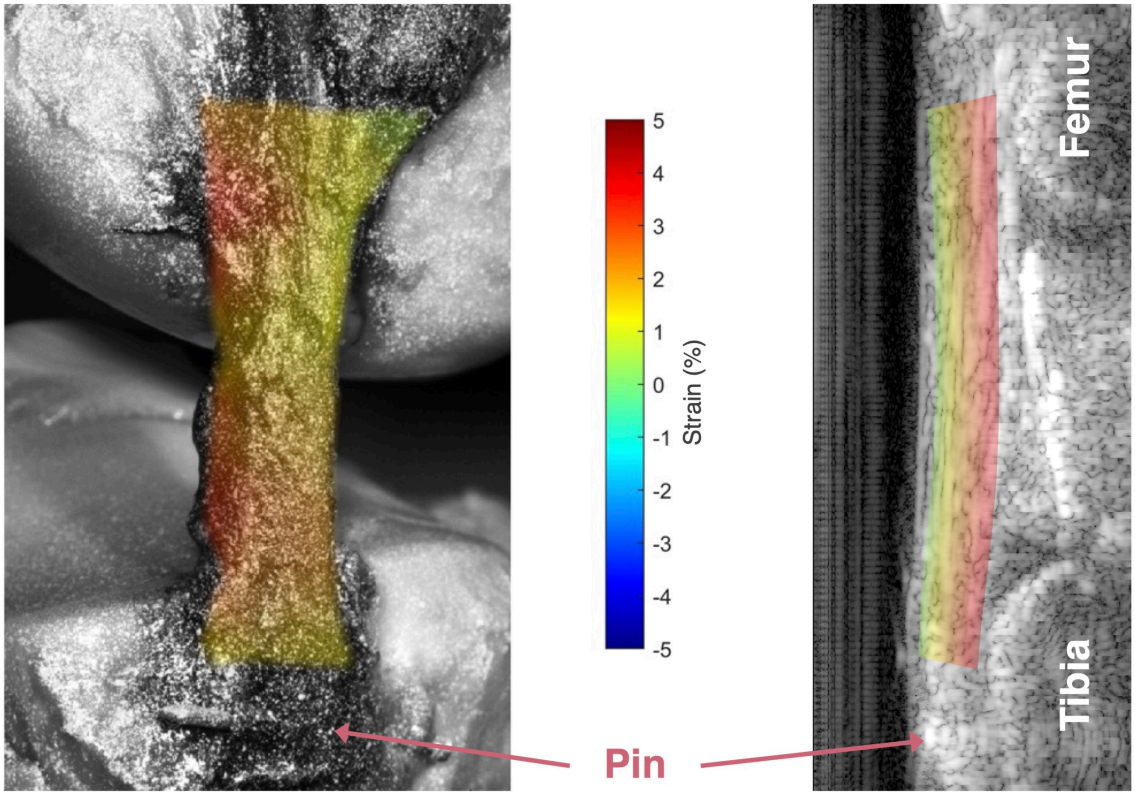


FIGURE 6.24 Example porcine strain maps at maximum loading obtained using DIC **(left)** and ultrasound **(right)**. The DIC strain map shows the MCL surface strain, while the ultrasound strain map shows strain in an orthogonal plane into the ligament.

6.3.4 Speckle tracking: cadaveric human specimens

The pre-optimisation convergence check found that higher settings were needed for the dynamic human knee tests: frame rate $\geq$23 Hz, NRIR pyramid levels $\geq$3, block-matching axial/lateral maximum displacement $\geq$0.3 mm (Table 6.8, Figure 6.21). The settings used as optimisation input were adjusted accordingly (see Table 6.1, page 153).

The surrogate optimisation routine reached a minimum quality penalty of 0.26 for the optimum speckle tracking settings shown in Table 6.1 (page 153). Similar to the quasi-static porcine implementation, a non-rigid image registration method was found to be preferable, followed by regularisation of the displacement field with a combined Butterworth filter and 2D cubic spline smoothing.

Out of the 22 collected AP positions, four were off the MCL and the anterior bundle of the POL and were excluded from further processing. Furthermore, it was found that the anterior bundle of the MCL had not been captured during the measurements, with the furthest anterior measurement located at a normalised AP position of -0.35. For the 18 included measurements, the kinematics were found to be consistent, with standard deviations for the varus-valgus and internal-external rotation angles of $0.68 \pm 0.17°$ and $1.57 \pm 0.38°$ (mean $\pm$ SD of loading range), respectively. The strains developed in the ligaments between $0°$ and $100°$ of flexion, as measured using the application-specific ultrasound speckle tracking algorithm, were highly correlated with the relative AP position ($R > 0.91$), and matched the strain estimates from the motion capture measurements (training set: RMSE $= 6.28\,\%$, test set: RMSE $= 5.76\,\%$) (Figure 6.25). Furthermore, similar normalised standard deviations of the strain maps were achieved as for the porcine specimens (training set: 0.26 ± 0.29, test set: 0.20 ± 0.39). From these strain maps, small strain variations between the superficial and deep portions of the ligaments could be detected (Figure 6.26).

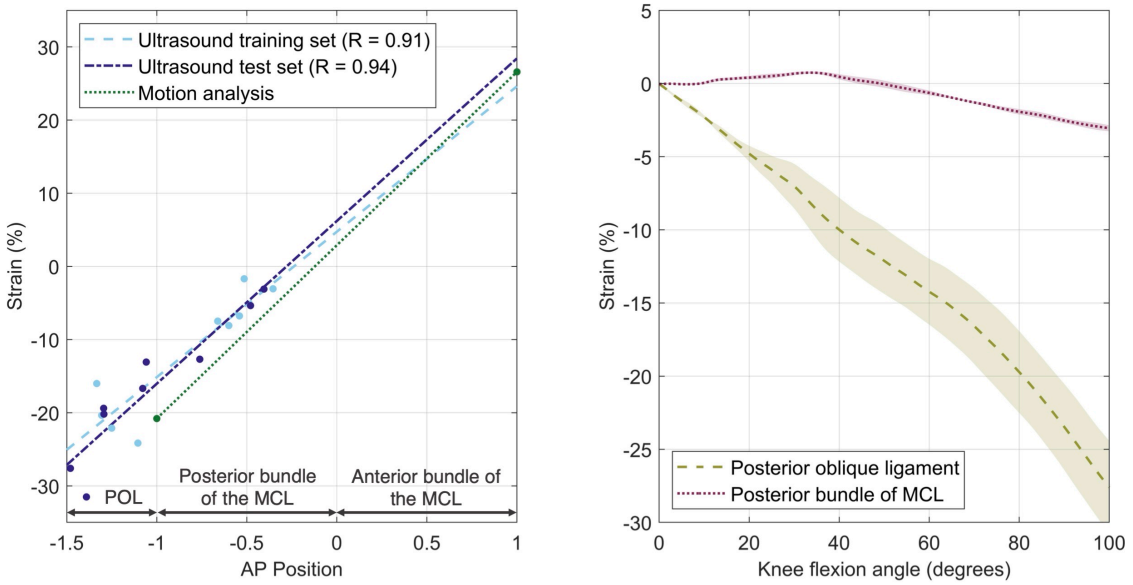


FIGURE 6.25 Strains in the medial ligaments of the cadaveric human knee during extension-flexion, as measured by the tuned speckle tracking algorithm. The MCL and POL strain measured using ultrasound was highly correlated with anterior/posterior (AP) position for both the training and test set, and matched the strain estimates from the optical motion analysis measurements **(left)**. Example strain curves are shown for the anterior bundle of the POL (AP position $= -1.48$) and the posterior bundle of the MCL (AP position $= -0.35$) **(right)**. AP position was normalised to MCL width (the dimension out of the imaging plane). The shaded region shows the $\pm$SD of the three repeat extension-flexion cycles.

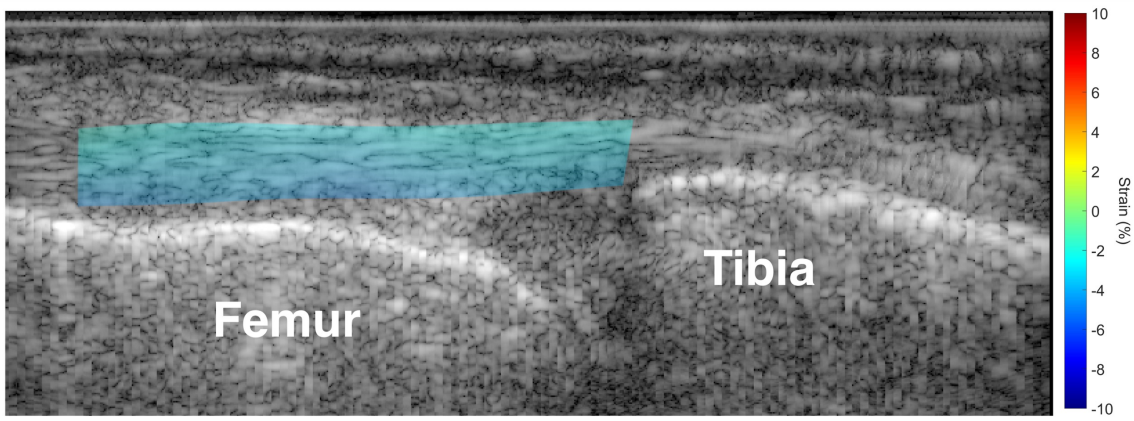


FIGURE 6.26 Example strain map for the posterior bundle of the MCL at 100° of flexion (AP position $= -0.35$).

6.4 Discussion

6.4.1 Shear wave imaging: most important findings

This study demonstrated that a combined viscoelastic and Lamb wave post-processing model most accurately measures the material properties for thin and viscoelastic soft tissue, finding material properties that match the properties obtained from mechanical testing to within $6 - 11\,\%$. This is the first time that ultrasound-based viscoelastic properties have been quantitatively linked to the mechanically tested properties of ligaments or tendons. With this post-processing approach, the dependency of the measured properties on the thickness of the ligament and the shear wave excitation frequency is eliminated and additional information about the viscous nature of the tissue is obtained. This notably improves the clinical usefulness of this ultrasound technique for assessing the function of orthopaedic connective tissue, providing more reliable and comprehensive measures that can be compared across patients with ligaments or tendons of different sizes and viscous properties.

Validation against the material properties obtained from mechanical testing confirmed the intuitive hypotheses set at the beginning of the chapter: while the viscoelastic dispersion model most accurately measured the material properties for the large agar cube specimens, the combined Voigt and Lamb wave model was needed for the thin agar and porcine ligament specimens. Using the correct model reduced the RMSE of the Young's modulus by up to $28\,\mathrm{kPa}$ (i.e., $44\,\%$ of the average mechanical testing result of $64\,\mathrm{kPa}$) and of the

Voigt time constant by up to 1.12 ms (i.e., 15 % of the average mechanical testing result of 7.71 ms).

6.4.2 Shear wave imaging: comparison to literature

The shear wave velocities of $\sim 3.5 - 5\,\mathrm{m/s}$ measured for the $2 - 5\,\%$ w/w agar cube specimens were slightly lower than those reported by previous studies ($\sim 1.4 - 11\,\mathrm{m/s}$ for agar concentrations of $0.9 - 2.7\,\%$ w/w) [41, 147, 150]. A possible reason for this discrepancy may be their addition of $MgCO_3$ or polymer instead of flour to create heterogeneity for ultrasonic scattering [41, 147]. Despite this, the elastic moduli calculated from the shear wave velocities corresponded well with the validation data from the mechanical compression tests, with high correlation and low RMSE values ($R > 0.99$ and RMSE $= 1.4\,\mathrm{kPa}$ when using a viscoelastic dispersion model). Similar accuracy was found by Xie et al. [145] and Khalitov et al. [148], whose shear wave results on CIRS elastography phantoms had correlations of $R > 0.99$ and RMSE $= 2.9 - 3.4\,\mathrm{kPa}$ when validated against the material property data provided by the manufacturer. Additionally, the variation between repeat shear wave velocity measurements on the agar cube phantoms was low (CV $\approx 1.7 - 4.2\,\%$) and within the range observed in previous measurements on homogeneous tissue-mimicking phantoms (CV $\approx 1.5 - 30\,\%$) [146, 147, 150], indicating similar robustness of the shear wave imaging procedure.

Material properties for *in vivo* human medial collateral ligaments have previously been quantified by Wu et al. [71] using the Aixplorer commercial shear wave imaging system and an elastic TOF model. Their shear moduli of $8 - 12\,\mathrm{kPa}$ were lower than the shear moduli of $50 - 140\,\mathrm{kPa}$ obtained from the elastic models applied to the porcine ligaments of this study. This could indicate that porcine MCLs have a higher shear stiffness than human MCLs. Alternatively, shear waves propagating through *in vivo* human MCLs may be subject to more dispersive effects that further slow down the wave, such as through interactions with the surrounding soft tissue [273]. A final reason could be that shear waves with different frequencies were used. In this study, shear moduli were the average from

measurements with external shaker frequencies between 200 – 800 Hz (Figure 6.17). Wu et al., on the other hand, used ARF-generated shear waves, in which case TOF methods measure the group velocity at the shear wave centre frequency [30]. Previous studies using the Aixplorer system have reported centre frequencies of around 200 – 400 Hz [30, 139, 141]. Here, when only including measurements at this lower frequency range, the shear moduli from the elastic models had a lower range of 10 – 60 kPa (Figure 6.16).

The Voigt viscosity has not previously been defined for the collateral ligaments. However, the viscosity of $\sim$40 Pa s measured for the porcine MCLs using the combined Voigt & Lamb wave model was within the range of viscosities previously reported for the Achilles and hamstring tendons (18 – 65 Pa s) [41]. Moreover, previous mechanical viscoelastic creep measurements on human and bovine MCLs reported values of 0.08 – 0.37 for $tan(\delta)$, i.e. the tangent of the phase lag between the force and displacement response, for loading rates of 0.1 – 10 Hz [72, 73]. This agrees well with the values of 0.05 – 0.36 found for specimens 1 – 3 of this study, and suggests that the large values of up to 2.04 measured for specimen 4 are likely invalid.

The results of this study demonstrated that choosing the correct material model during post-processing is especially important for thin specimens. For the agar plates, using an elastic model resulted in elastic moduli measurements up to one-third of those measured with the Lamb wave model, with the thinnest phantom specimen experiencing the largest underestimations. Similarly, for the porcine specimens, the moduli from the elastic models were up to a factor of two or three times lower than those from the Lamb wave model. These observations are in line with the results reported by Maksuti et al. [139], who measured two to five times lower moduli in their PVA phantoms when using an elastic model instead of a Lamb wave dispersion model.

While the addition of viscous effects to the Lamb wave model did not notably change the elastic modulus measurements for the agar plate specimens, it resulted in much lower shear moduli in the porcine specimens ($<$6 % of the shear moduli from the Lamb wave model and 10 – 30 % of the shear moduli from the elastic model). While no single study has directly investigated the effect of using a combined viscoelastic and Lamb wave model,

comparison of results from different studies on the Achilles tendon suggests a different behaviour to the one observed here: the shear modulus for the Achilles tendon found by Brum et al. [30] using a combined Lamb wave and Voigt model ($\mu \approx 920\,\text{kPa}$) was both higher than the shear modulus reported by Helfenstein-Didier et al. [29] using just a Lamb wave model ($\mu < 520\,\text{kPa}$), as well as the ones found by Aubry et al. [134] and Haen et al. [158] using elastic TOF models ($\mu < 300\,\text{kPa}$).

6.4.3 Shear wave imaging: limitations

While the Voigt and Lamb wave models aim to better approximate the true shear wave propagation behaviour in thin and viscoelastic structures, their increased complexity comes with limitations. Firstly, the fitting of complex dispersion curves leads to notably longer processing times compared to the TOF methods (>1 minute vs <10 seconds for each axial tracking location), limiting their suitability for real-time implementations.

Additionally, the models rely on several assumptions. (1) the simplicity of the Voigt model, consisting of a single spring and dashpot, fails to capture the full viscoelastic behaviour of tendons and ligaments. Most importantly, it is unable to accurately represent stress relaxation, modelling an instantaneous drop in stress after a load has been applied, rather than a gradual decay as is common for soft tissue [42]. More complex rheological models have previously been proposed for tendons and ligaments that aim to better represent the complex stress and strain response during mechanical testing [31, 42]. Furthermore, while the Voigt model predicts a linear relationship between the tangent of the time lag and loading frequency, the mechanical loading measurements of this study did not strictly follow this trend (Figure 6.16), indicating that additional viscoelastic mechanisms may be at play. Thus, even though it has been shown that the Voigt dispersion model produces equally accurate results as more complex models when studying tissue-mimicking phantoms [43], future research should verify whether this also applies to tendons and ligaments. (2) the Lamb wave model approximates the imaged medium as an infinite plate of constant thickness. In reality, the thickness of specimens often varied slightly along its length. In

tendons, thickness variations were estimated to result in errors in the measured material properties of around 5 % [30]. (3) the Lamb wave model also assumes that the plate boundaries are parallel to the direction of propagation. However, during *in situ* imaging of the porcine MCLs, the ligaments were not always perfectly aligned to the lateral ultrasound direction, since these structures take on a slightly curved shape as they wrap around the concave medial side of the knee. While curved boundaries have previously been found to have a negligible effect on the formation of guided waves in the cornea [212], they may have a greater effect in fibrous, anisotropic structures where the shear wave propagation behaviour depends on the direction of travel [160]. For substantial curvatures, an algorithm that tracks the shear wave around the curvature may need to be considered [139]. (4) the final assumption of the Lamb wave model is that the structure is surrounded by a medium of similar density. Removal of all tissue surrounding the porcine MCL, including the meniscus, meant that the joint could be opened up slightly such that most of the ligament was directly surrounded by water during the measurements. However, near the attachment sites, the ligament was still resting against bone. Interactions of the guided wave with an adjacent structure of notably higher density and stiffness could alter the propagation behaviour and invalidate the Lamb wave model [30, 273].

The validation procedures also had some shortcomings. Ultrasound-based material property measurements of the agar cubes were only performed in an unloaded state and validated against the initial gradient of the stress-strain curve. Previous research suggests that the measured shear moduli represent the instantaneous material properties [144, 159]. Thus, it would be valuable to validate properties over a range of loads by taking ultrasound measurements while the specimens are compressed in the materials testing machine. Furthermore, the dynamic creep test performed on the porcine specimens only allowed for validation of Voigt time constants, i.e. the ratio of shear viscosity to shear modulus, rather than specific values of the two properties. While a static creep test could have been performed instead, allowing the extensional elastic moduli and viscosities to be obtained by fitting the Voigt static creep equation to the strain-time response [39], these values may not be representative of the viscoelastic shear properties: Bonifasi-

Lista et al. [72] demonstrated that, while the viscoelastic phase lag is comparable during dynamic shear and extensional loading of human MCLs, the extensional stiffness is much larger than the shear stiffness. This indicates that shear Voigt time constants can be approximated by those obtained from longitudinal loading, while specific shear modulus and viscosities need to be evaluated under shear loading.

Finally, there were also limitations associated with the found results. The material properties found using multi-variable (viscosity and shear modulus) dispersion models had large confidence areas, especially for the higher material properties of the porcine MCLs (Figures 6.15 and 6.20). One factor contributing to this low specificity is the large spread of the high-magnitude regions in the experimental dispersion maps (Figures 6.14 and 6.19). The processing procedure used here aims to account for this source of uncertainty introduced by the experimental data: rather than extracting the phase velocities of maximum magnitude at each frequency and fitting the theoretical dispersion curves to these points, as is the conventional procedure [30, 139–141, 156], it finds the curve that, on average, best crosses through the high-magnitude region. This method also allows the uncertainty of the experimental dispersion map to be accounted for during the sensitivity analysis, illustrating how dispersion curves with notably different trajectories can still, on average, cross through points of similarly high magnitudes. A second source of uncertainty may be a low sensitivity of the theoretical dispersion curve to changes in material properties. The sensitivity analysis of this study showed that confidence areas increased with increasing shear moduli and viscosities, indicating reduced sensitivity with increasing material properties. For example, viscosities could be measured with a precision of around $2\,\mathrm{Pa\,s}$ for the agar plate specimens that had a shear modulus of $\sim$20 kPa, while the precision of the stiffer porcine ligaments increased to around $70\,\mathrm{Pa\,s}$. Brum et al. [30] made the same observation, describing that their combined Voigt & Lamb wave dispersion curves were insensitive to changes in Voigt viscosities when a large shear moduli is used. Specifically, Voigt viscosities $0,\ 1,\ 2,\ 3$ and $4\,\mathrm{Pa\,s}$ each resulted in a distinct dispersion curve when the shear modulus was set to $30\,\mathrm{kPa}$, but did not significantly change the curves for a shear modulus of $200\,\mathrm{kPa}$.

6.4.4 Speckle tracking: most important findings

The most important findings from the *ex vivo* speckle tracking studies was that it was possible to tune an ultrasound speckle tracking algorithm to calculate soft tissue strain that matches gold standard reference data without requiring a priori knowledge of the ground truth data. This was achieved by using an optimisation routine based on displacement field convergence and repeatability of results. In this work, the approach was validated for the medial structures of the knee, for both porcine and human knees under quasi-static and dynamic loading, demonstrating for the first time that ultrasound speckle tracking can be successfully tuned without ground truth data, thus providing a new avenue for ultrasound research where it is difficult or expensive to obtain these reference data.

The key advantage of this new approach is that it could potentially avoid the need for gold standard reference data. Instead, repeated acquisitions are required under the same loading/movement conditions. To measure strains due to physiological loading conditions, such as locomotion for orthopaedic applications or cyclic cardiovascular motion, this would require a brace to hold the transducer in a fixed location, as has been used in previous studies [274, 275]. To measure strains due to external loading conditions (i.e., when the clinician manually pushes the probe into the skin to create strain), as used to detect tumours and lesions, it would be important to control the force applied to ensure consistent repeats (which could be measured by placing a weight scale beneath the patient).

Closer inspection of the optimisation results revealed that, as the optimisation progressed and the quality penalty decreased, the average measured strain magnitude converged to a single strain level with relative errors dropping below $10\,\%$. It was found that the initial displacement field convergence check was an important step to reduce the risk of systematic bias and ensure that results converged to the correct level of strain. For the porcine MCLs, these strains closely matched the surface strain measured using DIC. For the cadaveric human specimen, the ultrasound strains also corresponded closely to strain estimates calculated from the motion analysis system, indicating that the optimisation enables strain to be calculated from dynamic movement as well.

6.4.5 Speckle tracking: comparison to literature

The correlation coefficient ($R = 0.99$) and differences (~ 0.1 percentage points) between strains found from DIC and the tuned algorithm, which inherently did not rely on the reference data, were similar to those from previous studies, even to those where the reference data were also used to tune the algorithm [49, 50, 166, 198] (these were outlined in detail in Table 2.5 of the literature review, page 48).

For the cadaveric human knee, there was a strong correlation between strain in the medial ligamentous structures and the AP position of the ultrasound transducer over the ligaments, with measured strains ranging between $-30\,\%$ and $0\,\%$. This corresponded well with previously reported length-change values in the posterior bundles of the MCL and the POL [14, 18, 19, 47, 96] (previously reported strains in the medial knee ligaments were summarised in Figure 2.2 of the literature review, page 24). Furthermore, the maximum strain magnitudes of $30\,\%$ exceeded the previously reported maximum strains in tendons and ligaments ($10\,\%$ along the fibres and $21\,\%$ across the fibres) [189]. These results support the hypothesis that an optimisation routine that is not given any ground-truth data can still generate a reliable speckle tracking algorithm, demonstrating its capability for a new application with larger range of motion and strain magnitudes than has been previously tested.

The normalised standard deviations across the repeat strain maps produced by ultrasound were equally low as those obtained using DIC, indicating that the strains within the ligament can be measured with similar reliability as optical DIC, which is often considered to be a gold standard. However, after averaging the strain within the region of interest, DIC strains had significantly lower standard deviations (Figure 6.23). This is in line with what has previously been observed by Dandois et al. [166]. This is possibly due to poor tracking performance in ultrasound measurements with poor image quality leading to outliers in the strain results. Excluding ultrasound measurements based on manual image quality assessment is very subjective [51]. Therefore, all measurements were used during post-processing, regardless of image quality, except for the measurements on the human

specimen for which motion analysis data revealed that the ultrasound transducer had not been over the MCL or the anterior bundle of the POL. While accurate strain measurements could still be obtained when averaging a high number of repeats, developing an automatic or objective method of excluding poor quality results, as suggested by Slane et al. [51], would improve the reliability of the speckle tracking algorithm when fewer repeat ultrasound acquisitions are available.

The settings chosen by the optimisation routine were notably different to previously used settings in the collateral ligaments. Thus far, only block-matching algorithms have been used for the collateral ligaments, but here a non-rigid image registration algorithm was found to be preferable. Similar success with non-rigid image registration was observed for other non-uniform soft tissue motion, such as in the Achilles tendon [177, 190, 194, 195, 242] or myocardium [276, 277]. Furthermore, displacement field regularisation is usually performed using median filtering and/or second order polynomial surface fits [49, 50, 191]. Here, the performance of a 2D cubic smoothing spline was additionally tested, which has previously been found to provide better results in discontinuous tissue such as the carotid artery [246]. The results of this study showed similar superiority for the inhomogeneous tissue of ligaments: 2D cubic smoothing spline regularisation significantly outperformed any other form of regularisation, producing much lower quality penalties. In addition, combining 2D cubic smoothing splines with either a median or fourth order low-pass Butterworth filter further improved the repeatability, especially for the dynamic human measurements.

6.4.6 Speckle tracking: limitations

The novel optimisation scheme had limitations. Firstly, it relies on controlled and repeatable loading conditions. Especially during *in vivo* applications where the soft tissue is loaded due to a physiological motion, it will require the test protocol to ensure that the same movement is performed every time. This becomes even more critical when the range of motion is small, for example when measuring MCL strain during varus-valgus loading

instead of extension-flexion [51].

Furthermore, since the objective function of the optimisation is based on reducing variance errors and does not contain any information on bias errors, there is a risk that results obtained with the found settings are biased. Since RMSE is dominated by variance when there are large outliers [278], this metric can be reduced significantly with regularisation even if results still contain a bias. Here, it was shown that the results had low RMSE with low bias and low variance. However, further analysis revealed that if the ultrasound acquisitions had too low a frame rate, displacements could not be captured fully. Since all repeat measurements were equally affected by the same error source, the optimisation routine produced results with low variance, but large bias errors. This error source was mitigated with the pre-optimisation displacement field convergence check. Other potential sources of bias errors are large out-of-plane motion [204, 279], poor overall speckle pattern quality [280], or artefacts that obscure the speckle pattern [279, 281].

Optimising based on repeatability may also lead to over-regularisation (i.e., a loss of sensitivity) of the deformation or strain maps: standard deviation of repeat deformation or strain maps naturally decreases the less variation there is within individual maps. While this may not affect the average deformation or strain within the region of interest, information about the non-uniform behaviour within the tissue may be lost, especially for inhomogeneous tissue composed of multi-level structures that slide relative to each other and have varying mechanical properties, such as the fascicles of ligaments and tendons [50, 51, 204]. This over-regularisation will be less prominent when strains are not needed and the optimisation is instead based on the deformation map, since the differentiation step to calculate strain amplifies any noise.

Additionally, there were limitations for the validation protocols. (i) for the porcine measurements, only the strains calculated at the top row of nodes closest to the top boundary of the porcine MCL were used for validation against the DIC strains. This is because notable variations between the superficial and deep portions of the ultrasound strain maps were observed, with deeper portions experiencing higher strains (Figure 6.24). DIC surface strains can only be used to validate the most superficial portion

of the ultrasound strain maps. The measured strain variation is likely due to the fact that, rather than clamping onto the ligament directly, the attachment sites were kept intact and the full joint was loaded in the material-testing machine (Figure 6.4). Since deeper fibres attach closer to the joint line, they are much shorter than superficial fibres (approximately $1/3$ the length for human MCLs) [55]. Thus, the strains arising in these fibres for the same crosshead displacement will be accordingly higher. It is inherently an advantage of this new approach that it is possible to quantify this elevated strain in the deeper fibres for the first time. Since repeated ultrasound measurements should still produce the same strain map, the full 2D maps were used when calculating the normalised standard deviations throughout the optimisation routine. (ii) for the human MCL and POL, DIC measurements were not possible since the ligaments deformed and twisted in such a way during extension and flexion that areas of the tissue surface started to overlap or rotate out of view. Also, the ligaments moved out of the DIC field of view during extension-flexion and the size and weight of the DIC camera system meant it was not possible to anchor it to the tibia, as was possible for the ultrasound transducer. Length change measures were used instead of DIC, which are widely reported in the field [18, 282]. (iii) furthermore, while the intention was to capture the full MCL during the human cadaveric measurements, it was found that the anterior portion of the MCL had not been captured as it was difficult to identify the anterior border from the ultrasound images. The use of a brace to collect a series of measures at regularly spaced AP positions could overcome this challenge. (iv) performance of the algorithm was only tested for ultrasound envelope data, since beamformed RF data were not readily available on the Verasonics research ultrasound machine. Since it has previously been shown that for some applications the speckle tracking algorithm performs better when using RF data [50, 173, 176], future studies that have access to different data types could include this in the optimisation routine as an additional optimisation parameter. (iv) lastly, it should also be noted that, during the displacement field convergence check, only low settings were investigated. Care should be taken when increasing the settings beyond an optimum mid-range [204]. For example, very high frame rate acquisitions require more frames to be processed and are thus more prone to error accumulations. Furthermore, small frame-to-frame displacements are more

sensitive to subpixel tracking inaccuracies [163, 236, 283]. Likewise, if the size of block-matching search kernels is increased to allow for larger frame-to-frame kernel displacements to be detected, the risk of false matching within the larger search kernel increases [163]. Thus, it would be interesting to explore whether the calculated displacements diverge again when these settings are increased further.

6.4.7 Conclusion

This study showed that ultrasound shear wave imaging and speckle tracking algorithms can be adapted for measuring the material properties and strain behaviour of ligaments. By using a material model that considers the viscous and thin nature of the tissue, the sensitivity of shear wave imaging measurements to the structure's thickness, which was observed with previous implementations of the technique, was removed. This allowed for accurate quantification of the viscoelastic properties, both for tissue-mimicking phantoms and porcine ligaments, demonstrating for the first time the link to the mechanical properties obtained from mechanical testing.

Additionally, the novel optimisation routine was able to produce custom speckle tracking algorithms without the need to collect ground-truth data. These algorithms were able to measure the tissue motion reliably and accurately, with results comparable to previous studies that relied on ground-truth data for algorithm tuning. The routine was equally effective for both quasi-static, uniaxially loaded porcine MCLs, and the medial ligamentous structures of the dynamic, physiologically moving human knee. Since the optimisation makes no assumptions about the underlying tissue or equipment, future studies could explore its applicability in different fields.

07

Validation: *In Vivo*

7.1 Introduction **194**
7.2 Materials and Methods **197**
7.3 Results **209**
7.4 Discussion **221**

I would like to acknowledge the help of Dr Richard van Arkel, Mr Gareth Jones and Mariam Al-Laith in obtaining ethical permissions for the clinical study. Furthermore, I would like to note that Jonah Leinwand contributed to the study with healthy volunteers by collecting the "rater 1" measurements for this study. All analyses were conducted by myself using the post-processing techniques developed in this PhD project.

Additionally, I would like to thank Dimitri Amiras for the loan of the Clarius ultrasound scanner used for the clinical pilot study, and the Research Divisional Workshop and Student Training Workshop for their help in modifying the orthotic knee braces.

List of Abbreviations

AP	Anterior/posterior
FDA	Food and Drug Administration
ICC	Intra-class correlation coefficient
IMU	Inertial measurement unit
LVDT	Linear variable displacement transducer
MCL	Medial collateral ligament
MSE	Mean squared error
NRIR	Non-rigid image registration
POL	Posterior oblique ligament
TKR	Total knee replacement

7.1 Introduction

Knee instability or stiffness due to abnormal collateral ligament function can severely impair daily living, leading to falls or restricted range of motion and pain [6, 8, 9]. Collateral ligament insufficiency may arise from traumatic events, such as tears or ruptures, with damage to the collateral ligaments accounting for $9\,\%$ of athletic injuries [284]. Alternatively, it can be a result of improper tensioning of the ligaments during a knee replacement surgery, with $20-35\,\%$ of total knee replacements (TKRs) failing due to instability or stiffness linked to collateral ligament imbalance [3, 13]. Given that every year in the UK around $125{,}000$ knee sprains are diagnosed during A&E visits and $100{,}000$ TKRs are performed, there are a vast number of patients suffering with complications associated with improper function of these ligaments [3, 285].

Despite this, there is currently no objective tool to assess and monitor the condition of these ligaments. Current assessment of the collateral ligaments is based on palpation to locate tender or swollen regions of the connective tissue, or through varus-valgus stress tests to detect laxity [44, 45, 51]. Ultrasound or magnetic resonance imaging may also be used to detect visible structural changes, including enlargement due to swelling, large tears, or ruptures [58].

Quantitative imaging techniques that measure the biomechanical response of these tissues to loading could provide additional, objective insights into pathological changes that are not visible on standard medical images [51, 166]. Such changes might include minute tears or alterations in tissue microstructure due to remodelling or overstraining. Additionally, these

techniques could detect non-physiological straining of ligaments, which may occur due to altered knee biomechanics following arthroscopic surgery [14].

The widespread availability of ultrasound machines in orthopaedic clinics, combined with their low cost and safety, positions ultrasound-based quantitative techniques as valuable tools for clinical practice [51]. One such method, speckle tracking, has already been validated for measuring *in situ* collateral ligament strain during physiological movement of cadaveric knees. For instance, Dandois et al. [166] demonstrated its reliability in assessing strain during varus-valgus loading. Additionally, the work of this project, presented in the previous chapters, showed that an optimisation routine can be used to tune the speckle tracking algorithm for additional knee motions, validating its effectiveness for measuring medial ligament strain during dynamic knee extension-flexion.

However, several challenges must be addressed before speckle tracking can be used for *in vivo* measurement of collateral ligament strain. In *ex vivo* experiments, controlled and repeatable movement was achieved through the use of a kinematics rig or motorised loading, and optical motion capture systems allowed for precise tracking of the kinematics [166, 231]. Furthermore, by optically tracking the transducer during measurements and subsequently digitising the ligament attachments post-testing after dissecting away surrounding tissue, strain measurements could be correlated with its anterior/posterior position over the ligament. Lastly, rigid fixation of the transducer to the tibia ensured consistent alignment with the ligament during motion. However, in *in vivo* clinical applications, these methods are unfeasible, necessitating the development of alternative solutions.

Here, to address these challenges, a custom knee brace was designed to hold the ultrasound transducer in place. This brace provides a semi-rigid fixation to the tibia, maintaining transducer alignment with the ligament during speckle tracking acquisitions. Integrated inertial measurement unit (IMU) sensors attached to the brace track the knee flexion angle, ensuring strain measurements can be compared across patients or over time within the same flexion range. Additionally, a positioning system enables controlled anterior/posterior movement of the transducer, allowing for pseudo-3D acquisitions and

allowing for the capture of strain variations across the ligament.

The aim of this study is to validate the use of ultrasound speckle tracking for measuring *in vivo* collateral ligament strain during dynamic extension-flexion. Specifically, it evaluates the inter-rater and intra-rater reliability of the technique when using the custom knee brace and the tuned speckle tracking algorithm developed in this project. Furthermore, a pilot study conducted on a total knee replacement patient demonstrates the use of the technique in a clinical setting.

7.2 Materials and Methods

7.2.1 Knee brace design

When collecting speckle tracking measurements, it is important to minimise out-of-plane motion. Maintaining a stable position over the medial ligaments is challenging during knee extension and flexion due to the large range of motion. During the *ex vivo* cadaveric experiment, the transducer was clamped to the tibial bone, which ensured that the imaging plane remained approximately stable and parallel to the ligament. An alternative solution was required for the *in vivo* measurements, and thus a knee brace was developed which held the transducer in place throughout the flexion cycle by providing a semi-rigid fixation to the tibia.

Knee brace specifications

The knee brace for holding the ultrasound transducer had to fulfil the following criteria:

1. Provide an almost-rigid fixation of the transducer to the tibia (mimicking the *ex vivo* experimental setup where the transducer was directly clamped to the tibia), thus ensuring that the transducer moves with the tibia and remains close to parallel to the ligaments during extension-flexion.

2. Enable incremental adjustments of the anterior/posterior (AP) position of the transducer, allowing a sweep of measurements to be taken across the full AP span of the medial

knee ligaments.

3. Allow for easy, quick and flexible initial positioning of the transducer.

4. Must pass ethical clearance to use during an *in vivo* study, i.e. must be comfortable and safe to wear.

5. Consist of readily available or simple-to-manufacture parts to enable the design to be reproduced easily.

Design iterations

The design of the knee brace underwent four iterations (Figure 7.1), described in detail below, with the third design used for the study with healthy volunteers and the fourth design used for the clinical pilot study. All 3D-printed parts were designed using computer-aided design software (SolidWorks Corp., Dassault Systèmes, Vélizy, France) and made with Onyx filament using a FDM printer (Onyx Pro, Markforged, MA, USA).

1. **Single-point fixation to lower leg:** the first design consisted of a simple 3D-printed block strapped to the lower leg, to which the ultrasound transducer attached via a ball head mount and spring-loaded clamp. A hot shoe rail printed into the block allowed medial/lateral movement of the transducer towards/away from the knee. While the simplicity of this design was attractive, the single-point fixation did not provide sufficient stability, and the tissue of interest moved out of the ultrasound field of view throughout knee flexion. Additionally, it did not allow for AP adjustments after fixation.

2. **Two-point fixation to lower leg:** the next design incorporated a longer 3D-printed part that strapped to the lower leg at two locations, with the additional fixation point located at a more distal position. The ultrasound transducer attached via a "magic arm" clamp, which could slide along a hot shoe rail of the 3D-printed part which wrapped around the medial side of the knee. This allowed great flexibility in adjusting the position and angle of the transducer such that it was over the ligaments. Compared to the first iteration, this design was significantly more stable, with the transducer remaining

approximately parallel to the ligament throughout knee flexion. However, the ultrasound images showed significant proximal/distal movement, with the tibia and femur visibly moving along the lateral direction of the images, indicating that rigid fixation with respect to the tibia was not fully achieved.

3. **Adapted orthotic knee brace for wired ultrasound transducer:** for the third design, an orthotic knee brace (Pluspoint3, Orthoservice AG, Chiasso, Switzerland) was adapted to hold the ultrasound transducer over the medial side of the knee. For this, the medial hinge of the brace was removed and a graduated mechanical XY stage was attached to the medial support bar of the lower leg. This mechanical stage was repurposed from a microscope stage used for positioning specimens under a microscope. Next, the transducer attached to the mechanical stage via an adjustable bracket, which allowed for movement of the transducer along and around the proximal/distal axis. An IMU sensor held within one of the lower leg straps enabled measurement of the knee flexion angle. This design fulfilled nearly all criteria: the orthotic knee brace improved stability, with its more conforming fit and additional fixation to the upper leg providing better constraint while also making it more comfortable to wear. The adjustable bracket allowed for initial positioning of the transducer over the ligament, after which all degrees of freedom apart from the AP position could then be locked for testing. Subsequently, during testing, the mechanical stage enabled precise adjustments of the AP position of the transducer in $1\,\mathrm{mm}$ increments. Lastly, all parts were quick to procure or 3D-print, with all parts and material costing just under £300.

4. **Adapted orthotic knee brace for the wireless ultrasound transducer:** finally, the third design was modified slightly to be compatible with the larger and heavier wireless ultrasound transducer used for the clinical study. Firstly, a more efficient positioning system was needed. While finding a suitable initial position of the transducer was possible with the adjustable bracket of the previous design, the process was too time-consuming and cumbersome for a clinical setting. The added size and weight would make manoeuvring of the probe even more challenging. Thus, a magic-arm was reintroduced, which allowed for much more flexible positioning of the transducer. The

magic arm attached to the brace via a "nato rail", which enabled variable proximal/distal placement of the transducer. The transducer was securely mounted to the linear stage using a custom 3D-printed clamp, designed to conform to the transducer's shape based on a 3D scan. This provided a more stable fixation compared to using cable ties. Lastly, two IMU sensors that attached to the lateral support bars of the brace of the upper and lower leg were implemented in this design, improving the accuracy of knee flexion angle measurements. The additional IMU sensor, and the nato rail and magic clamp (common camera equipment) increased the cost slightly to just under £350.

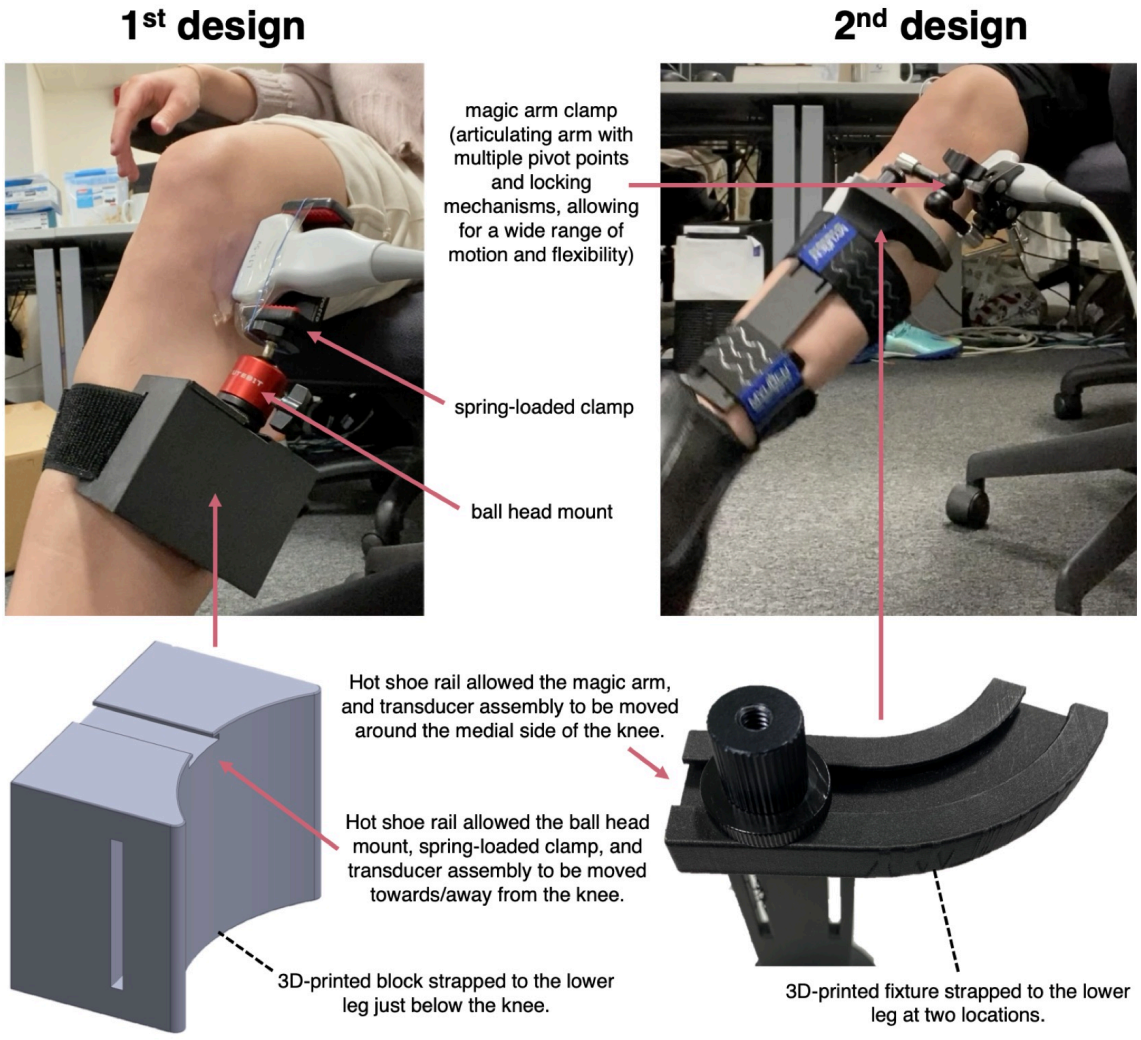


FIGURE 7.1 Iterations of the knee brace design for *in vivo* measurements of medial knee ligament strain during extension-flexion using ultrasound. The design had to hold the ultrasound transducer over the medial side of the knee, maintaining a stable position over the ligaments throughout the full flexion cycle. Furthermore, an incremental AP positioning system was implemented, allowing the strain variation for different ligament bundles to be captured. The first two designs were prototypes, and the third and fourth designs were used for *in vivo* measurements with healthy participants and a clinical pilot study, respectively.



FIGURE 7.1 (cont.)

7.2.2 Speckle tracking: healthy volunteers

Participants

This study was approved by the Imperial College Research Ethics Committee (ICREC) (reference number: 22IC7520, letter of favourable opinion included in Appendix A), and informed consent was obtained from each participant. Fourteen healthy volunteers without previous knee/leg injury or disease were recruited (7F 7M). For each participant, speckle tracking measurements were taken of their medial ligamentous complex of the right knee during active dynamic flexion-extension. Two participants (1F 1M) were assigned to the "optimisation training set": they attended a single session to collect measurements to tune the speckle tracking algorithm for this *in vivo* study. The remaining twelve participants (6F 6M) made up the "reliability test set": to allow for assessment of inter-rater and intra-rater reliability of the tuned speckle tracking algorithm, these participants were invited to three sessions each. The first two sessions were performed on the same day by two different raters, and the third session was conducted by the first rater less than a month later.

Ultrasound measurements

All ultrasound measurements were obtained using the same ultrasound system, transducer, and conventional imaging mode used for the *ex vivo* experiments (Verasonics Vantage 128, L11-5v transducer). The acoustic outputs produced by this equipment and imaging mode were measured with a hydrophone wave tank setup, which was described in detail in Chapter 5. Based on the results of these measurements, a maximum transducer voltage of $10\,\mathrm{V}$ was hard-coded into the Verasonics script, which ensured that the acoustic output remained within safe thresholds set by regulatory bodies [219] (MI<0.7, TI<0.01, $I_{sppa}<82\,\mathrm{W/cm^2}$, $I_{spta}<1.3\,\mathrm{mW/cm^2}$).

Participants were asked to sit on a table with the back of their right knee aligned with the edge of the table, such that the upper leg was fully resting on the table and the lower leg was hanging off the edge. Next, the custom-adapted brace (Figure 7.1, 3$^{\mathrm{rd}}$ design) was placed on their knee and the ultrasound transducer was positioned over the medial

ligament complex of the right knee. The most anterior position for which fibrous tissue was still clearly visible on the ultrasound images was determined and, to ensure that the anterior border of the ligament complex would be captured, the initial measurement location was set to $\sim$5 mm anterior from this position.

The participants were asked to actively move their knee between full extension and $\sim$90° of flexion to the beat of a metronome set to 25 bpm, resulting in an approximately sinusoidal loading rate of $\sim$0.2 Hz. The ligament motion was captured using 8 s ultrasound acquisitions, which included $\sim 2-3$ intervals of extension to flexion. For the two participants whose measurements were used to tune the speckle tracking algorithm, five repeats were collected at three AP positions spaced 4 mm apart, where the transducer AP position was adjusted using the linear stage of the knee brace. For the remaining participants, a measurement was taken at $\sim$21 AP positions, where the transducer was incrementally moved 1 mm further posterior with each measurement.

IMU measurements

During all ultrasound measurements, the angle of the lower leg in the sagittal plane was measured using a Bluetooth IMU sensor (BWT901CL, WitMotion, Shenzhen, China), held within the lower leg strap of the knee brace; since the femur remained almost stationary, the lower leg angle gave an approximation of the knee flexion angle. The IMU angle at full extension was recorded at the beginning of each session and, by assuming that this corresponded to 0° of flexion, this datum point was used to calibrate the IMU angles to match the knee flexion angles. Data were subsequently captured at 100 Hz for each 8 s ultrasound acquisition.

Data analysis

To start, the average motion throughout the ultrasound acquisitions was calculated using the non-rigid image registration (NRIR) algorithm (Matlab function `imregdemons`) applied to the full field of view; this allowed the approximately sinusoidal motion of the soft tissue to

be matched to the loading curve from knee flexion angles for automated synchronisation of the two data streams.

Intervals for different knee flexion ranges were then extracted from the ultrasound acquisitions (Table 7.1). Since full flexion/extension was not achieved for all measurements, reducing the flexion range yielded more intervals available for analysis. Ultimately, a flexion range of 20° – 75° was selected.

The training measurements were used as input to the optimisation routine to tune the speckle tracking algorithm. First, the displacement field convergence check was performed on all extension to flexion intervals collected at the three AP positions for the two participants of the training set ($n = 73$). Next, the surrogate optimisation scheme was executed, with results from the convergence check informing the input range for some of the settings (e.g., frame rate). To reduce computational cost, only one extension to flexion interval from each measurement (i.e., 5 repeats per AP position, overall $n = 30$) were used in the optimisation (Figure 7.2).

Initial positioning of the transducer over the ligament can vary between sessions, potentially

TABLE 7.1 Number of measurements captured during the *in vivo* study with healthy participants for different knee flexion ranges. The second column indicates the average number of anterior/posterior (AP) positions per session (out of a total of $\sim$21) for which at least one interval for the given flexion range was captured. The third column shows the overall number of intervals (n) available for the given flexion range for all participants and sessions of the test group. Since full extension/flexion was not reached during all sessions, the investigated flexion range for which medial ligament strains were calculated was reduced to $20° - 75°$ of flexion.

Knee flexion range	Average number of AP positions per session for which at least one interval with the given flexion range was achieved	Total number of intervals for the test group (n)
$5° - 70°$	11	864
$10° - 70°$	17	1322
$15° - 70°$	19	1520
$20° - 70°$	19	1647
$20° - 75°$	19	1637
$20° - 80°$	19	1585
$20° - 85°$	18	1457
$20° - 90°$	15	1194

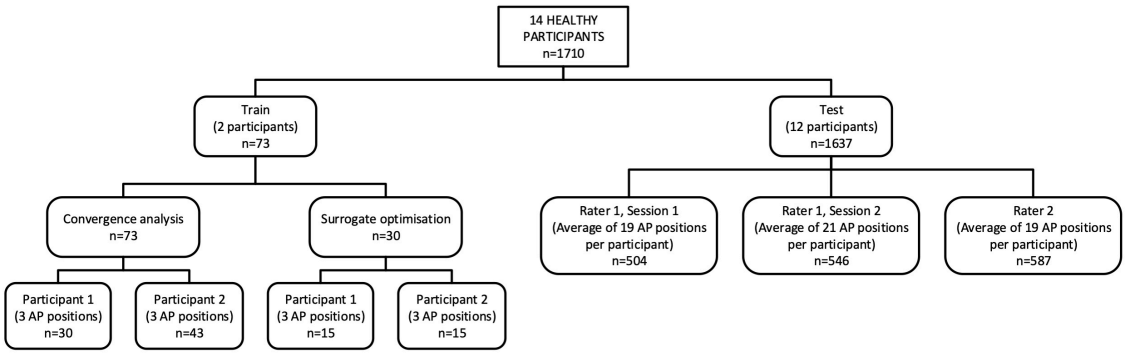


FIGURE 7.2 Flowchart of the *in vivo* ultrasound speckle tracking measurements taken for the healthy participants, illustrating the training group for tuning the speckle tracking algorithm, and the test group for the inter-rater and intra-rater reliability study. n indicates the number of $20^\circ - 75^\circ$ flexion intervals available from all ultrasound measurements.

capturing slightly different proximal/distal and anterior/posterior regions of the ligament. To enable comparison across the three different sessions for each participant in the test set, the ultrasound acquisitions were spatially registered (Figure 7.3). For each session, the first ultrasound frames from the intervals collected at each AP position (corresponding to $\sim 20^\circ$ of flexion) were arranged into a 3D matrix (lateral $\times$ axial $\times$ AP position). The femur and tibia edges at each AP position were then manually identified in the ultrasound images. Next, a surrogate optimisation algorithm with $10{,}000$ function evaluations was applied to align the 3D matrices of the three sessions. The to-be-minimised objective function combined equally weighted contributions from the distance between the selected bone edges and the mean squared error (MSE) of the greyscale ultrasound data. At each function evaluation, different rigid transformations were tested, allowing for maximum lateral, axial and AP shifts of $\pm 20\,\mathrm{mm}$, $\pm 4\,\mathrm{mm}$ and $\pm 15\,\mathrm{mm}$, respectively, and rotations in the coronal plane of up to $\pm 10^\circ$. The result was co-registered images for each participant, with the acquisitions from the three sessions aligned such that, on average, the objective function at the matched AP positions was minimised.

The tuned speckle tracking algorithm was subsequently used to calculate the ligament strains for the reliability test set. To assess the dependency of calculated strains on the selected ligament region, strain calculations were repeated for a range of regions of interest spanning different lengths of the ligament ($5 - 25\,\mathrm{mm}$), and placed at varying positions along the ligament. These positions were defined by a proximal offset ($-5 - 15\,\mathrm{mm}$) of the

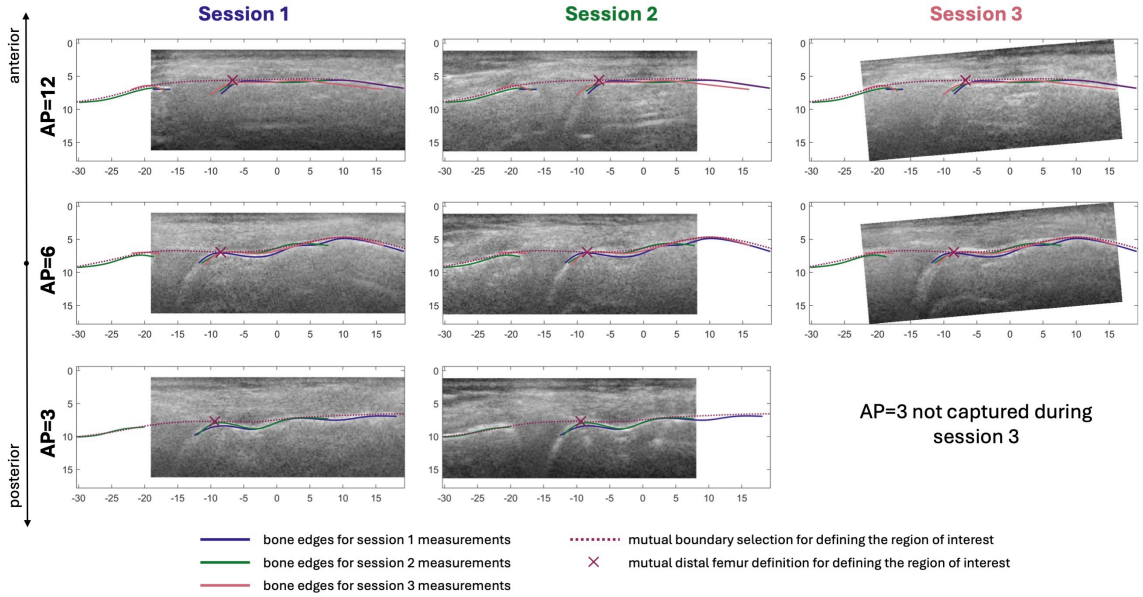


FIGURE 7.3 Spatial registration of the *in vivo* ultrasound acquisitions obtained at the three different sessions for each participant. Three example anterior/posterior (AP) positions are shown, where acquisitions from the second and third session are plotted with respect to the coordinate system of the first session, and AP$=1$ is the most posterior location collected during all sessions. The registration was based on matching the greyscale ultrasound data and minimising the distance between the manually defined bone edges (solid lines). A mutual deep ligament boundary (dotted line) and the most distal extra-articular point of the femur ($\times$) were manually selected on the registered images, which were used to define the ligament region of interests.

most distal point of the region of interest with respect to the most distal extra-articular point of the femur, i.e. a manually selected point that corresponded to approximately the last bit of bone before the cartilage. The region of interest extended $4\,\mathrm{mm}$ superficially from the deep ligament boundaries which, along with the distal femur points, were manually selected from the registered ultrasound images, such that the points and boundaries were identical across the three sessions (Figure 7.3).

Inter-rater and intra-rater reliabilities of the measured strains were quantified with intra-class correlation coefficients (ICCs) using a two-way random effects model based on absolute agreement, i.e. ICC(2,1). Inter-rater reliability was calculated with results from the first session conducted by rater 1 and the single session conducted by rater 2, while intra-rater reliability was based on the first and second sessions performed by rater 1. Reliability calculations included results from all registered AP positions of all participants for which a data point was available from both sessions, and was repeated for the different region of interest selections. Reliability was also visualised using Bland-Altman plots.

Repeatability for repeat measures ($2-3$ consecutive extension-flexion intervals captured in a single ultrasound acquisition) was again reported using the normalised standard deviation of the 2D strain maps.

7.2.3 Speckle tracking: clinical pilot study

Participant

This clinical study was approved by a Research Ethics Committee (REC) of the UK Health Research Authority (HRA) (REC reference number: 23/WM/0162, IRAS project ID: 323566, REC and HRA letter of favourable opinion and approval included in Appendix B and C). The study was conducted in accordance with the Declaration of Helsinki [269], and informed consent was obtained from all participants in the study.

The pilot study was conducted on a patient undergoing knee replacement surgery. Ultrasound images of the medial ligament structures of the knee receiving the replacement were collected pre- and post-operatively. Since patients often experience pain and limited range of motion directly before and after the surgery, all measurements were taken in the operating theatre with the patient under anaesthesia (before the start of the surgery and after completion once the sterile dressing had been applied over the incision).

Ultrasound measurements

Ultrasound measurements were collected using a commercial wireless ultrasound scanner using the settings shown in Table 4.2 in Section 4.2 (page 91). In short, B-mode images were collected at a frame rate of $16\,\text{Hz}$ using a high-frequency ultrasound transducer (Clarius 1st generation L7-38, linear, $38.5\,\text{mm}$, $4-13\,\text{MHz}$ bandwidth) operating at $10\,\text{MHz}$. Data were saved in DICOM format with a resolution of $0.07 \times 0.07\,\text{mm}$.

The custom-adapted knee brace (Figure 7.1, 4^{th} design) was used to position the wireless ultrasound transducer over the medial ligament structures of the knee. The patient was positioned laying supine, and passive knee extension and flexion was achieved by moving

the patient's foot along the operating table. Ultrasound images captured the motion of the medial ligaments throughout this motion. Measurements were obtained at 10 AP positions spaced 2 mm apart, with ∼4 intervals of extension to flexion captured at each position.

IMU measurements

Two Bluetooth IMU sensors were used to measure the knee flexion angle during the ultrasound acquisitions. The sensors were mounted on the side of the knee brace, with their x-axes aligned parallel to the knee's mediolateral axis. This setup ensured that the primary rotation detected by the sensors occurred around the x-axis (flexion/extension movement), with minimal interference from other rotational axes. The knee flexion angle was then calculated as the difference in rotation around the x-axis between the two sensors. Before the brace was fitted to the patient, the sensors were calibrated with the knee brace in full extension, setting the flexion angle to 0°. The advantage of using two IMU sensors over a single sensor, as was done in the study with healthy volunteers, is that it allows for both limbs to move. This gives the clinician freedom to move the knee as they would in a routine clinical examination test.

Data analysis

The tuned speckle tracking algorithm from the healthy volunteer study was used to calculate the strains in the ligaments for flexion ranges of 20° – 75°. Strains were measured in the portion of the ligament adjacent to the femur, as this region produced the most repeatable results during the study with healthy participants (i.e., regions starting at the most distal extra-articular femoral point and spanning 10 – 15 mm towards the femoral attachment).

Repeatability for the four repeat extension-flexion intervals collected at each AP position was assessed with the normalised standard deviation of the strain maps. Furthermore, the correlation of ligament strain with AP position was determined using the Pearson's correlation coefficient (R).

7.3 Results

7.3.1 Speckle tracking: healthy volunteers

The pre-optimisation displacement convergence check revealed that only the NRIR method was able to achieve convergence for frame rates $\geq$30 Hz and NRIR pyramid levels $\geq$3 (Table 7.2, Figure 7.4). Therefore, the block-matching method was excluded from the surrogate optimisation scheme, and the speckle tracking algorithm was tuned for NRIR implementations with the found minimum settings (Table 6.1, page 153).

The surrogate optimisation routine reached a minimum quality penalty of 0.23 after 1500 function evaluations, finding similar tuned settings of the speckle tracking algorithm as for the human *ex vivo* application (Table 6.1, page 153). The main differences were a lower NRIR smoothing level (2 vs 7) and regularisation on the cumulative instead of step displacements.

TABLE 7.2 Results for the pre-optimisation convergence check on the *in vivo* optimisation training set, showing the settings for which convergence was tested, and the settings for which the lateral displacement field had converged to within relative errors of $5\,\%$.

	Optimisation parameter	Settings tested	Settings for which convergence was reached
NRIR	Frame rate (Hz)	$2-30$	≥ 30
	Pyramid levels	$1-6$	≥ 3
Block-matching	Frame rate (Hz)	$2-30$	no convergence
	Axial/lateral maximum displacement (mm)	$0.1-0.5$	no convergence

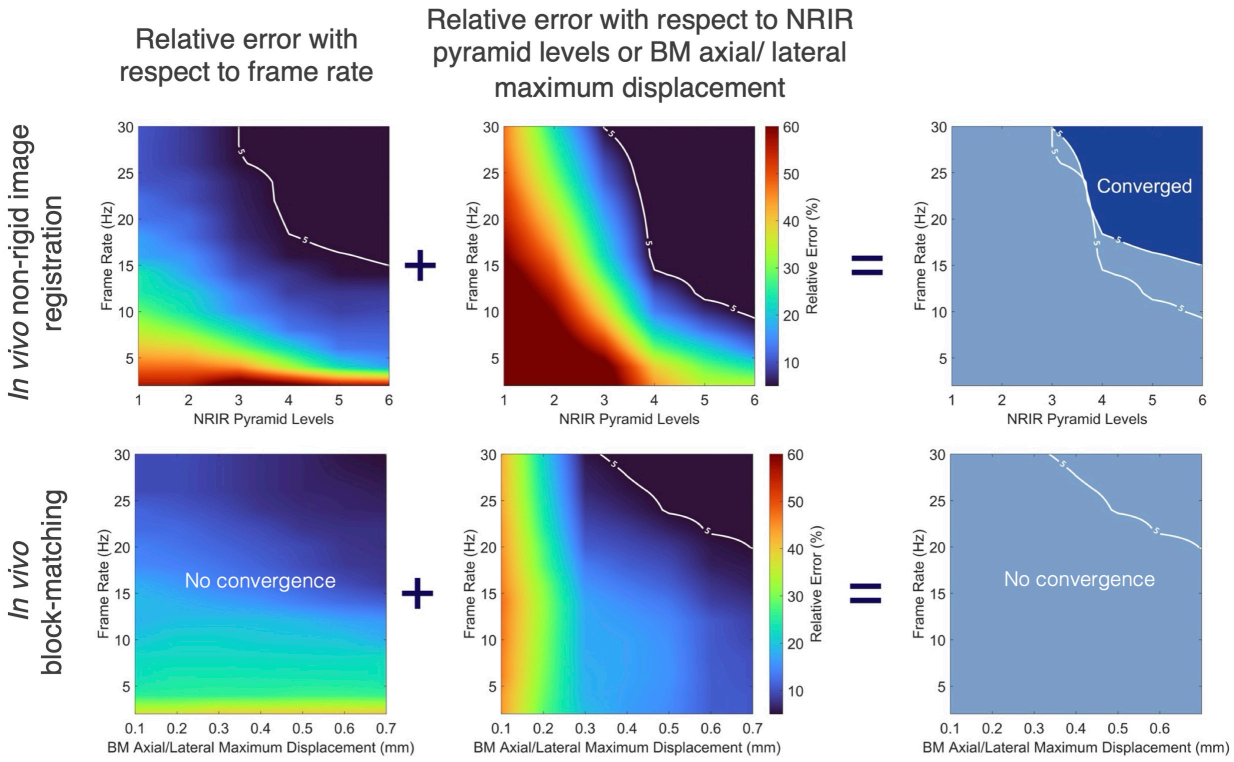


FIGURE 7.4 Displacement convergence results for the *in vivo* training measurements of the healthy participants, both with respect to frame rate **(left column)** and NRIR pyramid levels or block-matching (BM) axial/lateral maximum displacement **(middle column)**. The white line shows the combination of settings for which convergence was reached, with relative errors dropping below $5\,\%$. Overall, convergence was then said to have been reached if both relative errors were below $5\,\%$ **(right column)**. Results show that the block-matching method did not converge for the tested settings.

Spatial registration showed that, on average, there was a $10 \pm 4\,\mathrm{mm}$ difference in the range of AP positions captured for the three sessions of each participant. Overall, inter-rater acquisitions overlapped at 136 AP positions and intra-rater acquisitions at 156 AP positions across all participants. However, the requirement of measuring strain within a common region of interest further reduced the number of AP positions available for the reliability measurements (especially for long regions of interest with a large proximal offset from the distal femur point), since the position of the transducer along the ligament varied slightly from session to session. Out of the regions of interest for which at least 20 AP positions were available across at least four participants, a region of interest length of $15\,\mathrm{mm}$ with no offset from the distal extra-articular femur point (proximal offset $= 0\,\mathrm{mm}$) was found to result in the highest inter- and intra-rater reliabilities (inter-rater: ICC $= 0.78$, n $= 21$;

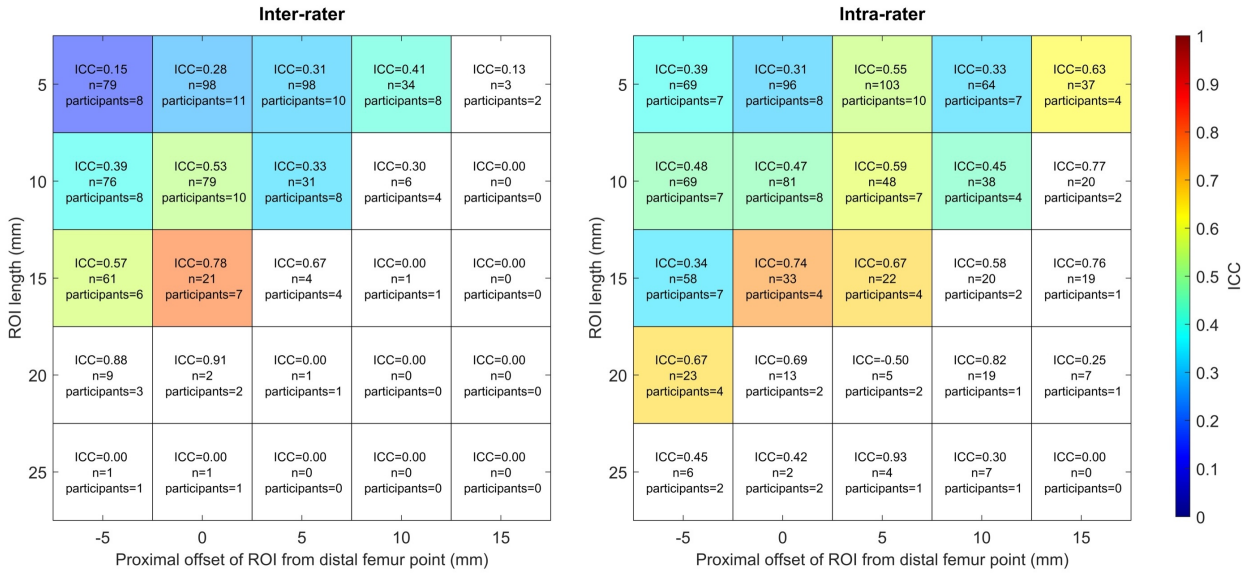


FIGURE 7.5 Inter-rater (**left**) and intra-rater (**right**) reliabilities for the *in vivo* ultrasound strain measurements of the medial ligaments of healthy participants. ICC metrics were calculated for different region of interest selections of the ligament in the first ultrasound image of the loading cycle (knee flexion angle $= 20°$). n corresponds to the number of anterior/posterior (AP) positions across all participants that were included in the ICC measure, i.e. positions for which a strain measure was available from both sessions. The number of participants for which a data point from at least one AP position was available and used in the ICC calculation is shown as well. Results based on <20 AP positions across <4 participants were considered unreliable; for all other results, the colormap visually depicts the strength of the ICC.

intra-rater: ICC $=$ 0.74, n $=$ 33) (Figure 7.5). Reliabilities remained moderately high for a shorter region of interest (proximal offset $=$ 0 mm, length $=$ 10 mm) and, with more than double the data points available, this result may be considered a more dependable outcome metric (inter-rater: ICC $=$ 0.53, n $=$ 79; intra-rater: ICC $=$ 0.47, n $=$ 81). The agreements for both regions of interest are visualised with correlation and Bland-Altman plots (Figure 7.6 and Figure 7.7), which show a reasonably strong correlation with mean difference values close to zero (R $>$ 0.54, mean difference $= -5.60 - 0.57\,\%$).

The strain variation with AP position was plotted for all participants and sessions (Figure 7.8 and Figure 7.9), which revealed that the strains ligaments experienced after 20° to 75° of flexion varied up to $\sim$37 % for the different bundles of the medial knee ligament complex located within the captured AP range (for 10 mm long ROI: minimum strain $= -11.12 \pm 7.21\,\%$, maximum strain $= 26.26 \pm 9.89\,\%$; for 15 mm long ROI: minimum strain $= -14.35 \pm 8.76\,\%$, maximum strain $= 22.64 \pm 15.55\,\%$). Example 2D strain maps

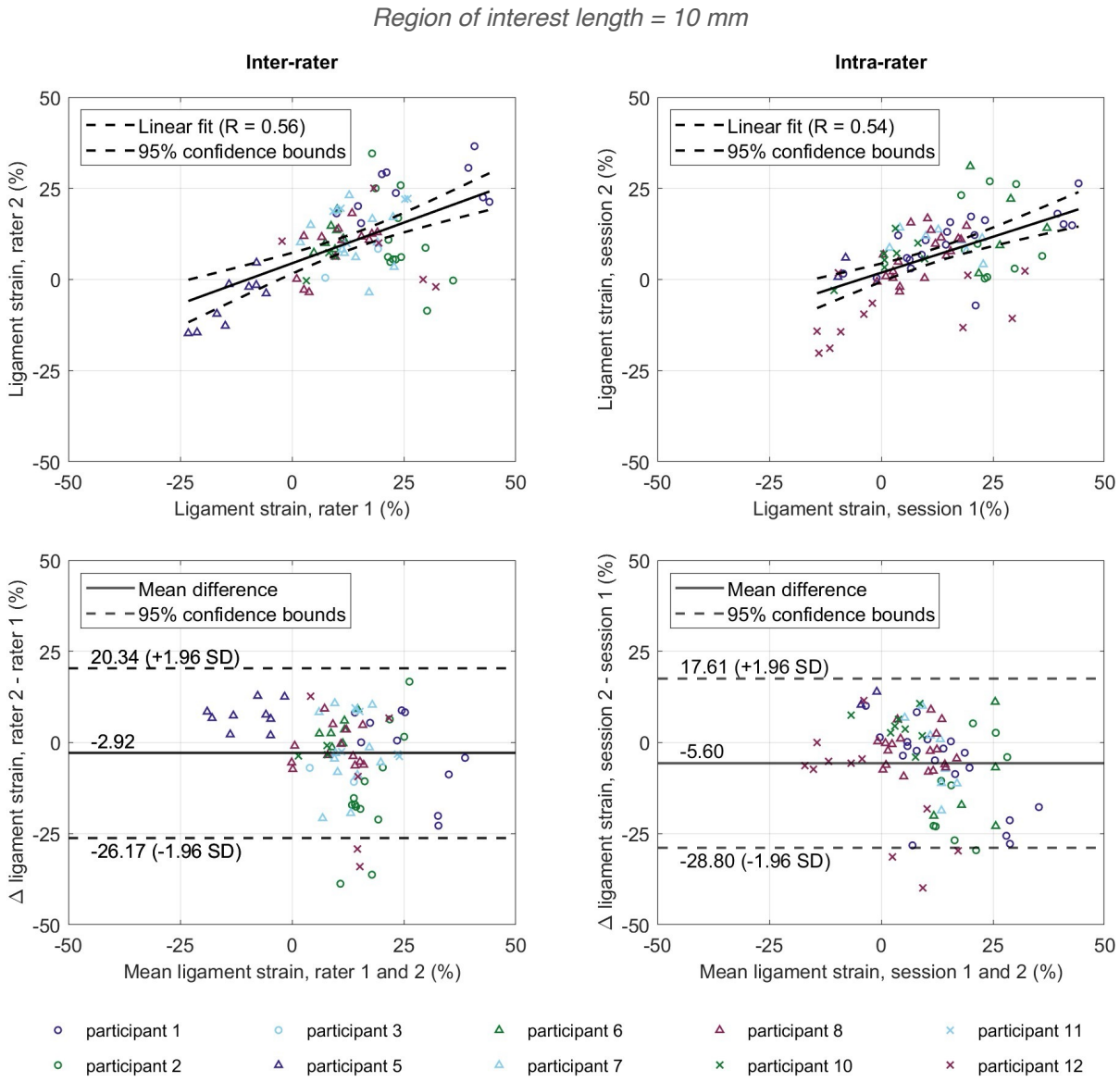


FIGURE 7.6 Correlation (**top row**) and Bland-Altman (**bottom row**) plots showing the agreement of the inter-rater (**left column**) and intra-rater (**right column**) *in vivo* ultrasound strain measurements when a ligament region of interest of $\mathbf{10\,mm}$ length and $0\,\mathrm{mm}$ proximal offset from the distal femur is selected.

and strain curves for an anterior medial ligament bundle are shown in Figure 7.10 and Figure 7.11.

The mean normalised standard deviation of repeat strain maps (consecutive intervals extracted from the same ultrasound acquisition) were found to be high (for $10\,\mathrm{mm}$ long ROI: 2.78 ± 17.24; for $15\,\mathrm{mm}$ long ROI: 0.75 ± 1.34). Closer inspection of the data revealed a non-

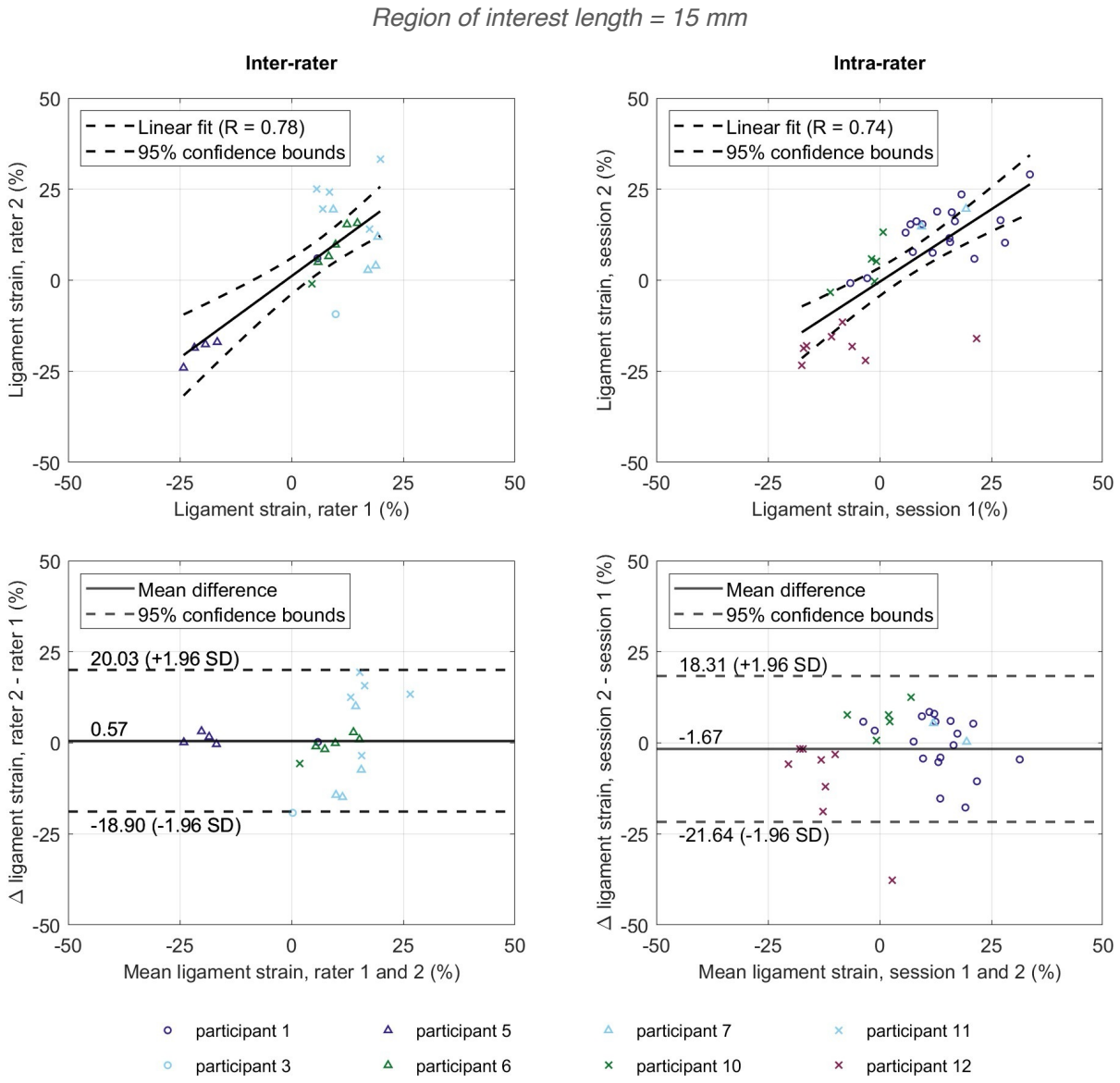


FIGURE 7.7 Correlation (**top row**) and Bland-Altman (**bottom row**) plots showing the agreement of the inter-rater (**left column**) and intra-rater (**right column**) *in vivo* ultrasound strain measurements when a ligament region of interest of $\mathbf{15\,mm}$ length and $0\,\mathrm{mm}$ proximal offset from the distal femur is selected.

normal distribution. Specifically, for maps with average strains close to zero, normalising the standard deviation produced large outliers, resulting in a highly left-skewed distribution with a wide spread. Thus, median values were found to be much lower and more in line with the results from the *ex vivo* experiments (for $10\,\mathrm{mm}$ long ROI: 0.39; for $15\,\mathrm{mm}$ long ROI: 0.36).

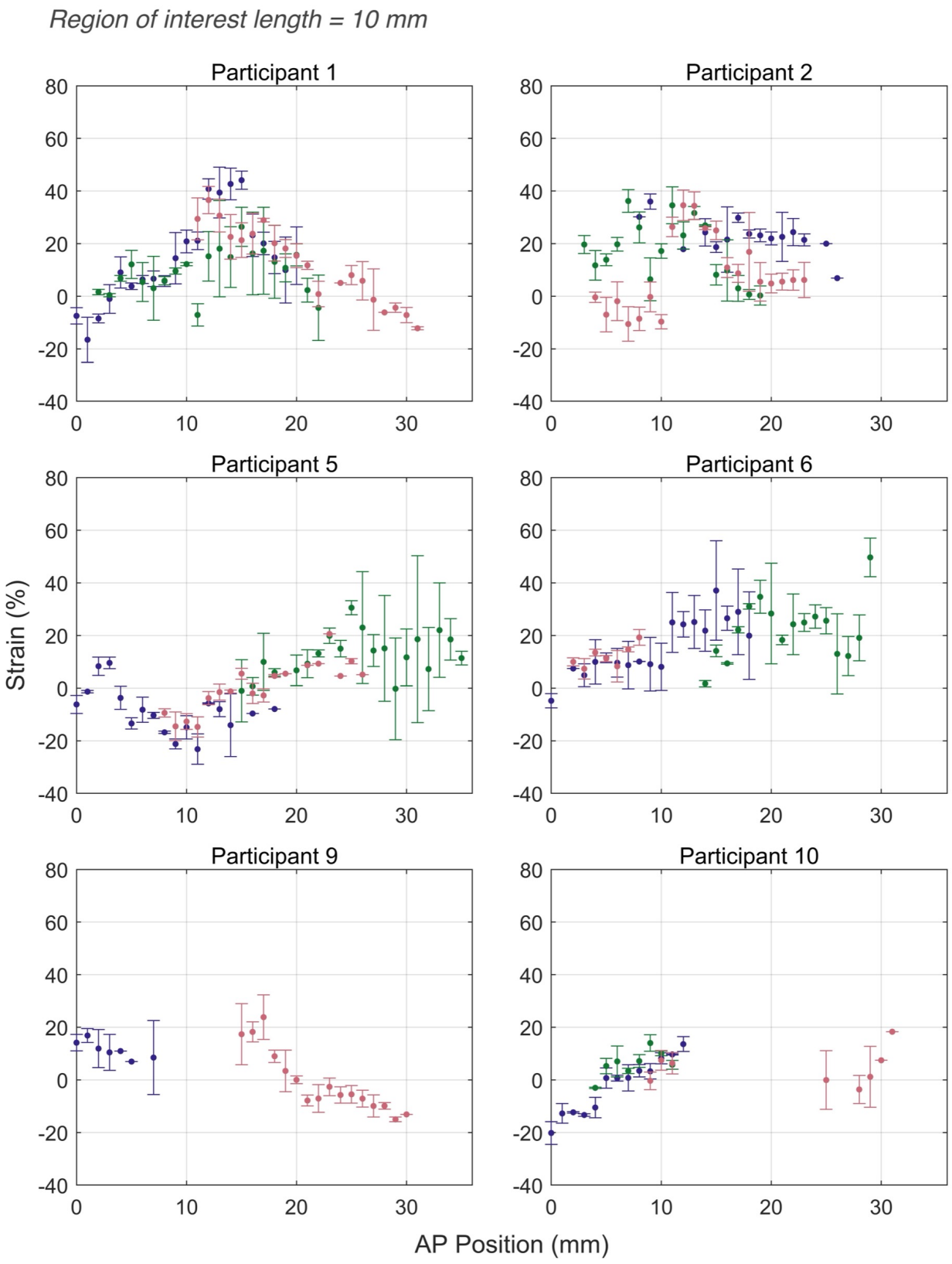


FIGURE 7.8 Strains that developed in the medial knee ligaments of 12 healthy participants during 20° to 75° of flexion, as measured by the tuned *in vivo* speckle tracking algorithm for a region of interest extending $\mathbf{10\,mm}$ proximally from the distal femur. Plots show the variation of strain with anterior/posterior (AP) position, calculated from the ultrasound images collected by two raters over three sessions. The AP axis for each participant was defined such that $0\,\mathrm{mm}$ was the most posterior position collected during the three sessions (based on the spatial registration) and more positive values indicated more anterior positions.

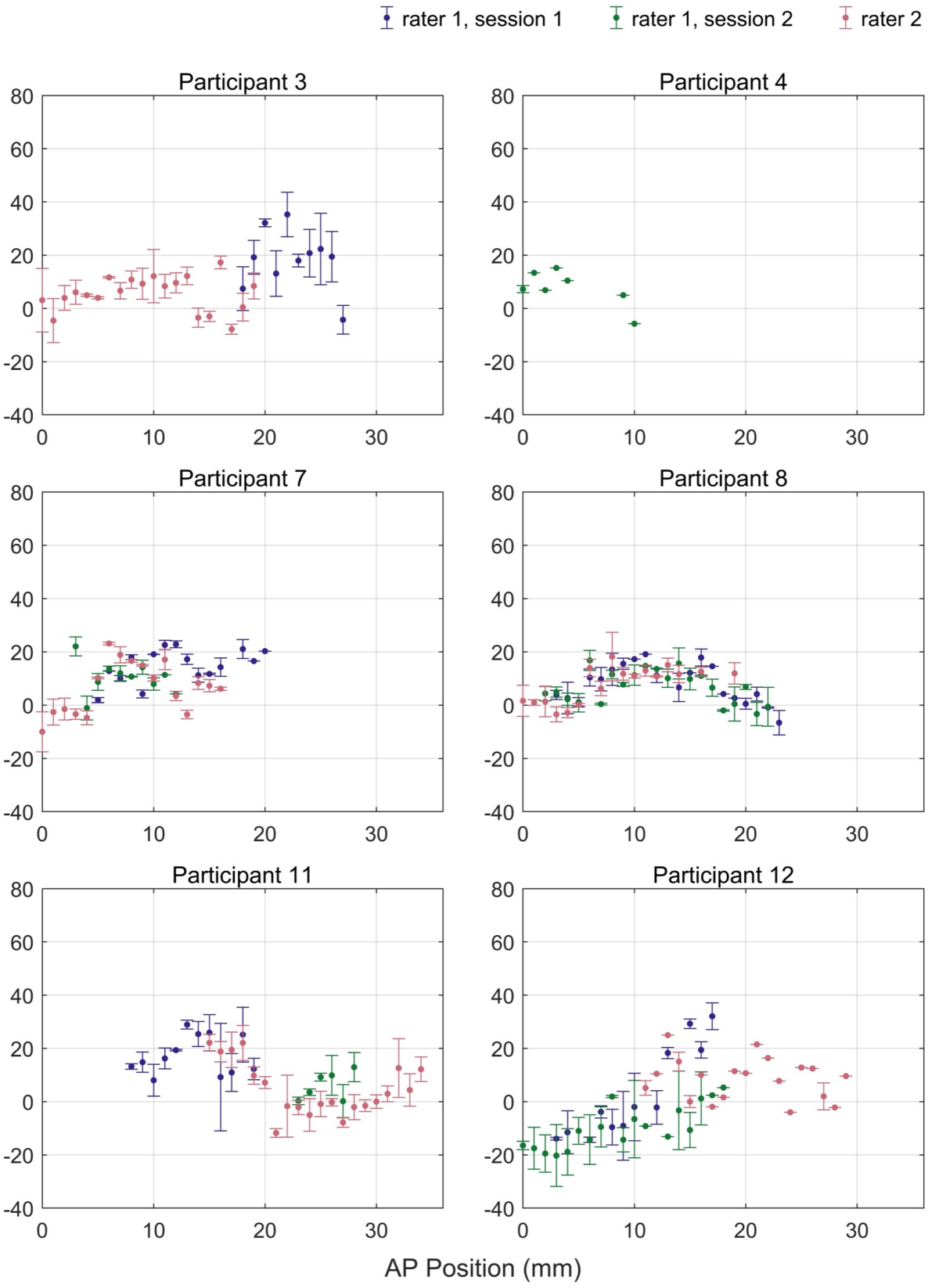


FIGURE 7.8 (cont.)

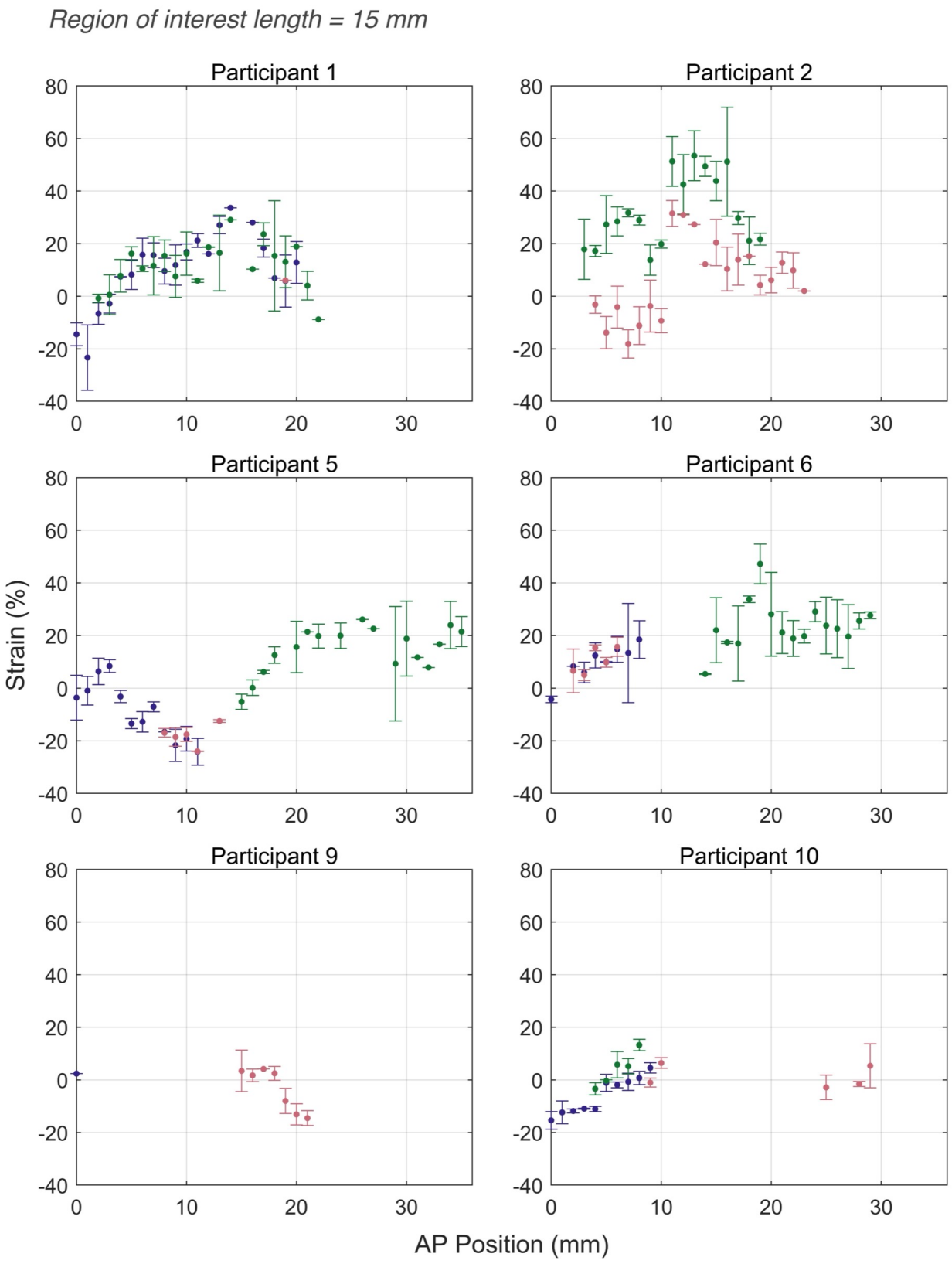


FIGURE 7.9 Strains that developed in the medial knee ligaments of 12 healthy participants during 20° to 75° of flexion, as measured by the tuned *in vivo* speckle tracking algorithm for a region of interest extending $\mathbf{15\ mm}$ proximally from the distal femur. Plots show the variation of strain with anterior/posterior (AP) position, calculated from the ultrasound images collected by two raters over three sessions. The AP axis for each participant was defined such that $0\ \mathrm{mm}$ was the most posterior position collected during the three sessions (based on the spatial registration) and more positive values indicated more anterior positions.

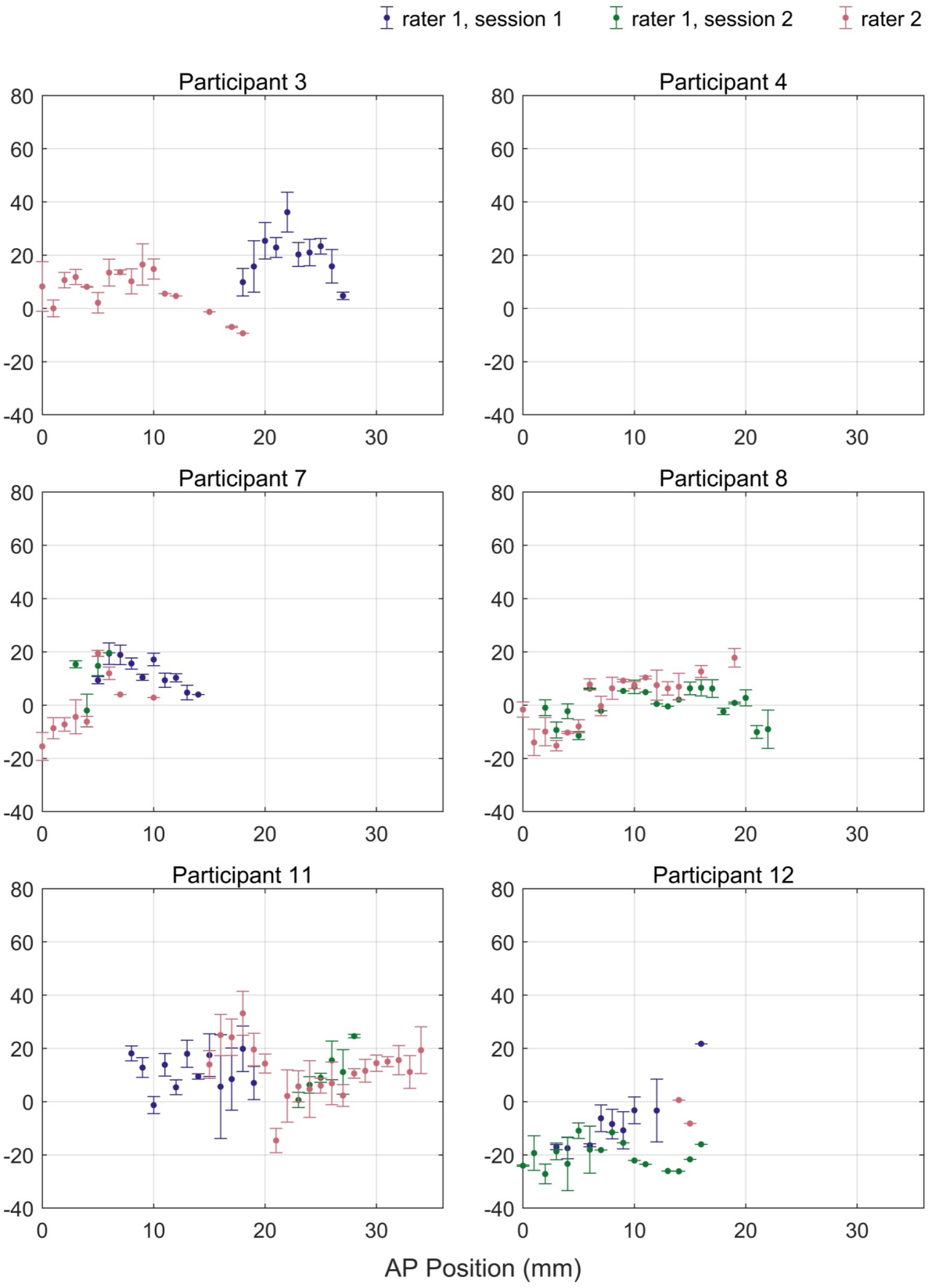


FIGURE 7.9 (cont.)

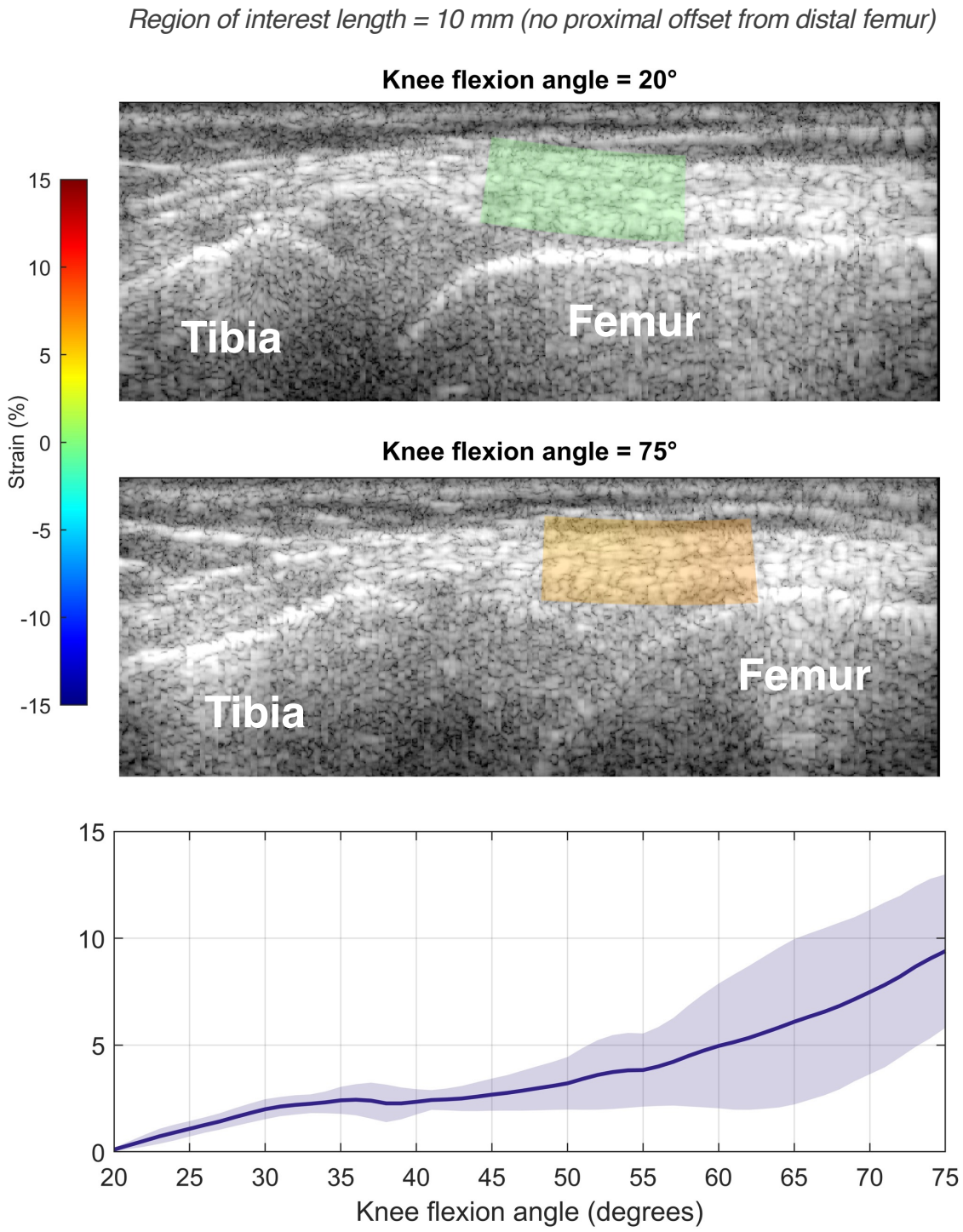


FIGURE 7.10 Example *in vivo* strain map for the anterior bundle of the medial ligament complex after knee flexion from 20° to 75° for a ligament region of interest extending $\mathbf{10\ mm}$ proximally from the distal femur (**top and middle**), and the strain curve showing how average strains in this region of interest evolved throughout knee flexion (**bottom**). Note that the ligament state at 20° is taken as the reference point, i.e. $0\,\%$ strain, and the map at 75° shows how the ligament strained relative to this state.

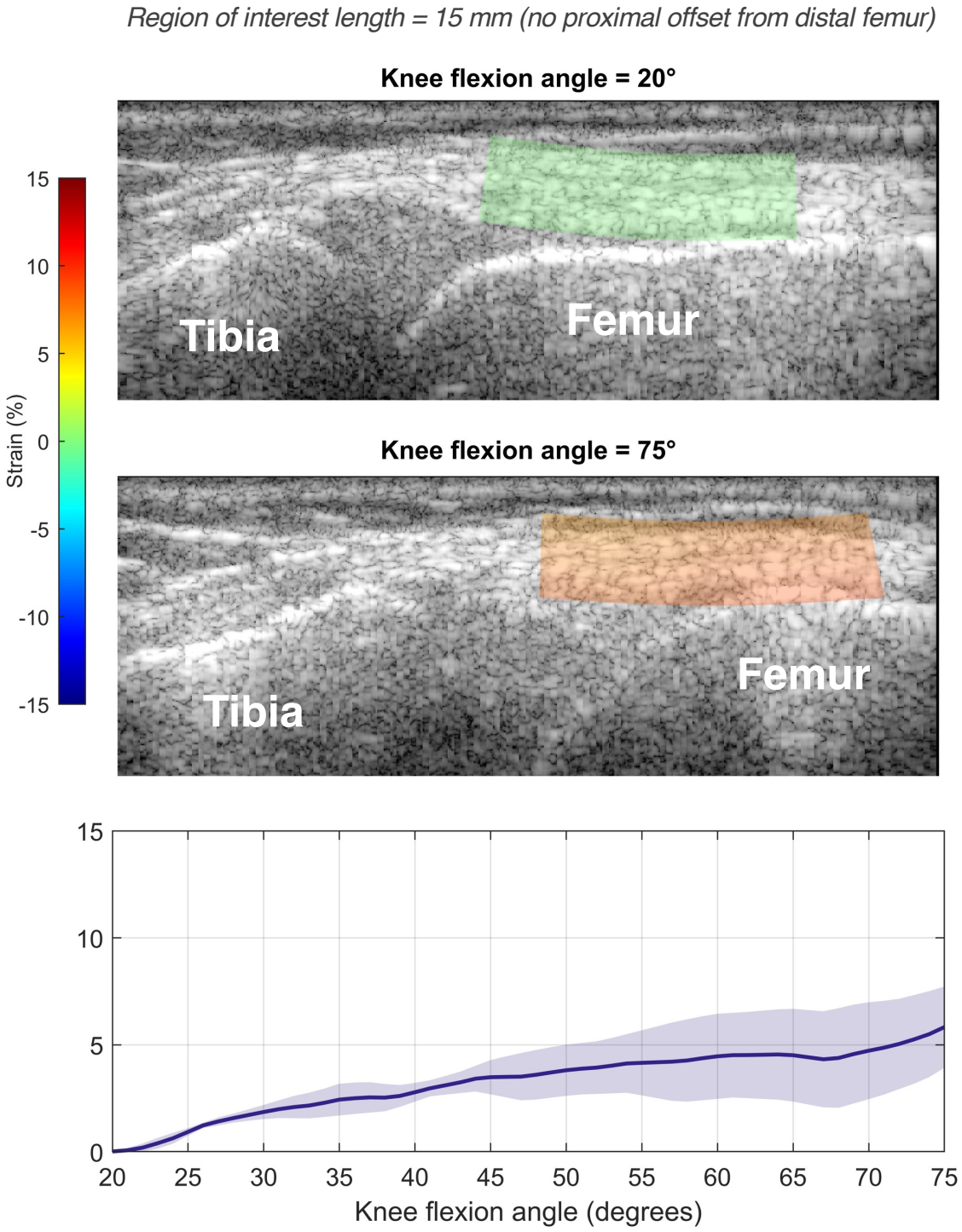


FIGURE 7.11 Example *in vivo* strain map for the anterior bundle of the medial ligament complex after knee flexion from 20° to 75° for a ligament region of interest extending $\mathbf{15\ mm}$ proximally from the distal femur (**top and middle**), and the strain curve showing how average strains in this region of interest evolved throughout knee flexion (**bottom**). Again, note that the ligament state at 20° is taken as the reference point, i.e. $0\,\%$ strain, and the map at 75° shows how the ligament strained relative to this state.

7.3.2 Speckle tracking: clinical pilot study

The pre-operative strain measurements of the medial ligament structures were highly correlated with AP position (R >0.89), with positive strains up to around $30\,\%$ measured for the anterior bundles, and strains dropping to around $-30\,\%$ in the posterior bundles (Figure 7.12). Again, the mean normalised standard deviation was higher than for the *ex vivo* experiments (for $10\,\mathrm{mm}$ long ROI: 1.07 ± 0.72; for $15\,\mathrm{mm}$ long ROI: 4.01 ± 8.65) due to low strains being measured in the mid-portion of the medial ligament complex, leading to division with values close to zero. Median normalised standard deviations were again lower (for $10\,\mathrm{mm}$ long ROI: 0.77; for $15\,\mathrm{mm}$ long ROI: 0.56).

During the post-operative measurements, the medial ligaments of the knee could not be visualised on the ultrasound images. Usually, the femur and tibia appear as bright boundaries in the ultrasound images, which can be used as landmarks to locate the ligament. It was expected that the metal implant would appear as a similarly bright feature in the image. However, neither bone, implant nor fibrous tissue could be identified in the images. Thus, no speckle tracking measurements were collected after the surgery.

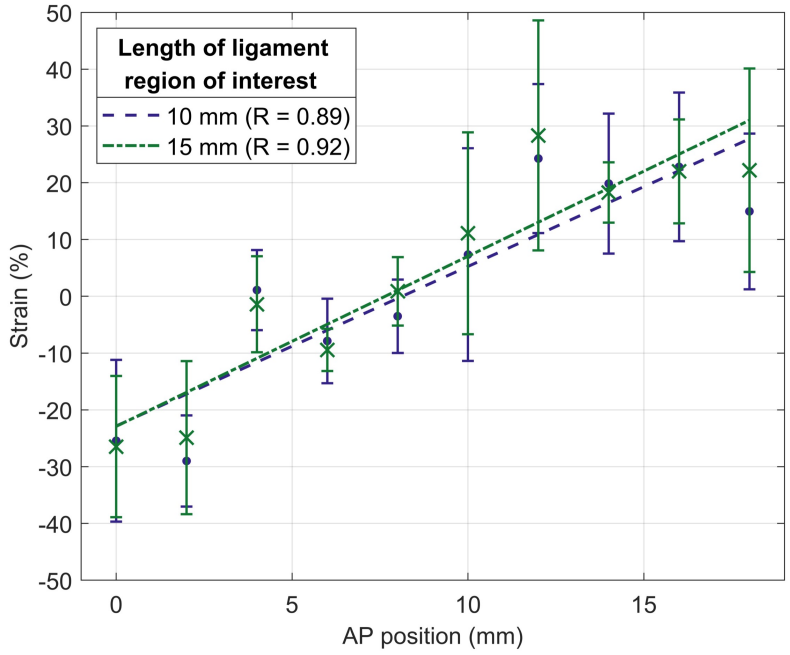


FIGURE 7.12 Pre-operative strains in the medial ligaments during extension-flexion in a knee replacement patient, as measured by the tuned speckle tracking algorithm. Strains were calculated for two regions of interest capturing different lengths along the ligament. AP position was defined such that values increased for more anterior positions, and $0\,\mathrm{mm}$ was the most posterior position at which ultrasound images were collected. Strains were highly correlated with AP position for both regions.

7.4 Discussion

7.4.1 Most important findings

This study represents the first *in vivo* application of ultrasound speckle tracking to ligaments, quantifying the technique's inter-rater and intra-rater reliability in measuring the ligament strain behaviour during dynamic knee extension-flexion. This leap from *ex vivo* to *in vivo* implementation was underpinned by a range of advancements: (i) the design of a custom-adapted knee brace that enables stable fixation of the transducer over the ligaments across a range of incrementally varied anterior/posterior (AP) positions, allowing full characterisation of the non-uniform strain behaviour, (ii) the development of a registration algorithm which aligns the ultrasound images collected at different sessions and allows comparison between strains measured at different time points, and (iii) the novel optimisation scheme that produced application-specific settings of the ultrasound speckle tracking algorithm. This produced a speckle tracking procedure that can non-invasively assess collateral ligament function using low acoustic output levels that strictly adhere to the thresholds set by the Food and Drug Administration (FDA).

During tuning of the algorithm, the objective function converged to similarly low quality penalties as in the previous *ex vivo* optimisations (*ex vivo*: 0.26, *in vivo*: 0.23). Additionally, the tuned algorithm was comparable to the one found for the *ex vivo* cadaveric measurements. This indicates that the *in vivo* measurement procedure using the knee brace was able to replicate the *ex vivo* test setup, resulting in ultrasound images with

comparable speckle appearance and motion.

The region of interest for which strain is calculated was found to play an important role in reliably measuring the strain in the ligaments. It was found that intra-class correlations could be improved by avoiding the area over the joint space (proximal offset $\geq 0\,\mathrm{mm}$). Additionally, longer regions of interest that encompassed more of the ligament resulted in higher intra-class correlations. Here, reliabilities could only be analysed for regions of interest up to a length of $15\,\mathrm{mm}$; for longer lengths too few data points were available for comparison, since too many acquisitions for which the region extended out of the field of view had to be excluded. Despite this, results were able to demonstrate that using the longest length of $15\,\mathrm{mm}$, an inter-rater reliability of 0.78 can be obtained, indicating good agreement between the measurements [286, 287]. Even for the slightly shorter region of $10\,\mathrm{mm}$, the inter-rater reliability remained moderately high at 0.53; since this result is based on a larger number of data points across more participants, this value may represent a more conservative measure of the intra-class correlation.

7.4.2 Comparison to literature

Bogaerts et al. [190] previously measured an inter-day reliability of 0.72 when using a speckle tracking algorithm to measure strains in the Achilles tendon. Despite the challenges associated with measuring strains in the collateral ligaments compared to large energy-storing tendons [51], the measurement protocol and post-processing procedure implemented in this study led to comparable reliability, with a best-case inter- and intra-rater ICC of 0.78 and 0.74, respectively. Even the more conservative measures of ~ 0.5 indicate moderate reliability that is comparable to other diagnostic measurements performed with ultrasound or MRI imaging. For example, the intra-rater reliability for measuring the stiffness of malignant breast masses with shear wave imaging was found to lie between $0.51 - 0.71$ [25], and ICCs of 0.41 were still considered acceptable in MRI scoring of abnormalities in the brain [288].

For the healthy participants, strains measured in the medial ligaments ranged, on average,

between -14 to $23\,\%$. A slightly larger range of around -30 to $30\,\%$ was measured during the clinical pilot study. These values agree well with the *ex vivo* measurements on the cadaveric knee of the previous chapter, as well as previously reported medial collateral ligament (MCL) and posterior oblique ligament (POL) elongation behaviours measured using linear variable displacement transducers (LVDTs) or fluoroscopy [14, 18, 19, 47, 96] (see Figure 2.2 of the literature review, page 24). Additionally, the pre-operative strains measured during the clinical study were strongly correlated with the transducer AP position ($R > 0.89$), which is comparable to the correlation found in the cadaveric *ex vivo* study ($R > 0.91$). However, this observation could not be made for the results of the reliability study, since too many data points needed to be excluded during post-processing.

7.4.3 Limitations

The main limitation of the reliability study was that a large number of data points had to be excluded during post-processing when calculating the reliability metrics. There were several factors that contributed to this.

Firstly, during the calculation of intra-class correlation, it is important that strains from different sessions are compared for the same amount of ligament loading, i.e. the same extension-flexion range of motion. However, not all participants achieved the same range of knee flexion. This may have been due to a limitation of the measurement procedure: strains for the reliability study were obtained for active flexion with the participant sitting at the edge of a table. In this position, more muscle force and conscious thought was needed during the last 20° of extension to move the knee into a fully straight position, while for the last 20° of flexion, soft tissue around the knee appeared to interfere with the edge of the table. Thus, it was difficult for the participants to consistently achieve the full flexion range over the course of the 30 minute measurement session. As a result, not all recorded extension-flexion intervals covered the full 0° – 90° flexion range. Even after reducing the range to 20° – 75° during analysis, around $25\,\%$ of the collected intervals did not achieve this range and had to be excluded (Table 7.1). To achieve a larger range of motion, the

measurement procedure used in the clinical pilot study could be used, which has the patient lying in a supine position on an examination bed with their foot sliding along the bed to achieve knee flexion; here, this was only tested for passive knee flexion, but it could work equally for an active motion controlled by the patient.

Next, since the collateral ligaments are characterised by a non-uniform strain behaviour during knee extension-flexion, it is crucial that strains are compared for the same regions in the ligament. This was achieved by spatially aligning the ultrasound acquisitions obtained at the different sessions using the registration algorithm during post-processing. This enabled strains at the different time points to be compared for a common region of interest, located in the same anterior/posterior bundle and at the same position along the ligament. However, this spatial registration procedure uncovered inconsistencies across sessions in the AP positioning of the transducer over the medial ligaments, which meant that, on average, only half of the collected measurements captured a mutual AP range. Additionally, while individual ultrasound images captured an approximately $40\,\mathrm{mm}$ long section of the ligament, variations in proximal/distal positioning of the transducer meant that the common ligament section available across sessions was much shorter. Thus, strains could often only be compared for a smaller ligament region of interest, which is why fewer data points became available for an increasing region of interest length (Figure 7.5). It is evident that a protocol is needed that allows for more consistent positioning of the transducer across raters and at different time points. The meniscus, tibia, and femur, which are often visible in the ultrasound images, can be used as reference points to standardise the proximal/distal transducer position; with the results of this study showing that strains are most reliably measured for a region adjacent to the femur, future studies could aim to position the transducer such that the ligament section from the joint space to the femoral attachment is captured. However, setting the AP position as well as the inclination of the transducer may be more challenging. While subtle changes of the bone shape in the ultrasound images can be detected by the spatial registration algorithm in post-processing, these are unique to each patient and are difficult to identify in practice while taking the measurements. A real-time implementation of the spatial registration algorithm could address this issue by

providing immediate feedback on transducer positioning, ensuring that the same region of the ligament is captured as in previous sessions.

Another factor limiting the maximum length of the regions of interest was that part of the ligament moved out of the ultrasound field of view throughout knee flexion, meaning that a smaller portion of the ligament could be tracked throughout the full motion. This lateral shift out of the image was higher than in the *ex vivo* experiments and indicated that the brace did not provide a fully rigid fixation to the tibia, resulting in some relative proximal/distal movement with respect to the knee throughout flexion. While the source of this relative movement could not be determined with certainty, one possibility is that the soft tissue that the knee brace rests against moves during extension-flexion due to, for example, tensing and relaxing of muscles. Thus, the knee brace could benefit from further adaptations to improve transducer stability. To accurately quantify the amount of relative motion between the transducer and the ligament, both proximally/distally as well as in other directions, the knee brace and transducer assembly could be tested on a cadaveric knee, where the position of the transducer and ligament bone attachments can be tracked with a motion capture system. This could help guide the development of future brace adaptations.

There is also a limitation regarding the implementation of this procedure into clinical practice. To capture the non-uniform 3D strain behaviour of the medial ligaments using a 2D imaging modality, multiple repeat measurements at different AP positions need to be captured. This procedure is time-consuming. By using the improved brace design (Figure 7.1, 4th design) that facilitated initial transducer positioning and by reducing the number of AP positions from 20 to 10, the measurement time was reduced from approximately 30 to 10 minutes. While this is a notable improvement, 10 minutes is still a significant length of time for a clinical diagnostic tool, and this time would be doubled if both the medial and lateral collateral ligaments need to be imaged to fully assess knee stability. A 3D ultrasound transducer could be an alternative since the full ligament could be captured with one measurement. However, with current technology, 3D transducers come with trade-offs such as a much smaller field of view, lower image resolution, or decreased frame rates [51, 289], and thus are likely unable to capture the intricate speckle

pattern of ligaments during dynamic knee motion.

Lastly, it should also be noted that there was a limited time window available to conduct the clinical pilot study. Thus, results could only be obtained for one patient at the time of surgery. This time constraint also meant that the speckle tracking algorithm could not be newly tuned for the Clarius ultrasound transducer used in the clinical study; instead, the tuned settings for *in vivo* measurements with the Verasonics ultrasound machine were used. For further clinical measurements, machine-specific settings should be found by applying the optimisation routine to images obtained with the Clarius ultrasound system. Additionally, it would be interesting to investigate how the strain behaviour in the medial knee ligaments changes post-surgery. While here the ultrasound images collected immediately post-surgery exhibited significant artefacts that obscured the ligaments, it might be possible to obtain clearer images at the patients' follow-up appointments once the soft tissue around the knee has recovered from surgery.

7.4.4 Conclusion

In conclusion, ultrasound speckle tracking can be used to non-invasively measure the *in vivo* strain behaviour of the medial ligaments of the knee with moderate to good reliability. The feasibility of using this imaging procedure in a clinical setting was demonstrated with measurements performed on a knee replacement patient. This quantitative ultrasound technique could, therefore, provide a safe and inexpensive tool to monitor the function of the collateral ligaments, with changes in the strain behaviour indicating ligament injury or imbalance.

08

Conclusions and Future Work

8.1 Discussion 230
8.2 Recommendations for future work 235

List of Abbreviations

AP	Anterior/posterior
ARF	Acoustic radiation force
DIC	Digital image correlation
MCL	Medial collateral ligament
PWI	Plane wave imaging
TKR	Total knee replacement

8.1 Discussion

8.1.1 Most important findings

The principal takeaway from the work produced throughout this PhD is that quantitative ultrasound techniques previously used for large and homogeneous tissue can be adapted to accurately and reliably assess the biomechanical function of thin and fibrous connective tissue.

The success of applying the shear wave imaging technique to these structures primarily depends on selecting a tissue model that can accurately assess the material properties of the tissue based on the shear wave propagation behaviour (Chapter 3). For the thin and viscoelastic medial ligaments of the knee, a combined Voigt & Lamb wave model best captures the complex shear wave propagation behaviour in ligaments by considering the dispersive effects arising from the tissue's thinness and viscosity. Using this model, accurate material properties of the ligaments can be obtained that quantitatively match those from mechanical testing and that do not fluctuate based on the ligament's thickness. Additionally, unlike conventional post-processing approaches, it provides insight into the viscous properties of the tissue, providing an additional metric to assess ligament function (Chapter 6).

Applying the speckle tracking technique to these structures requires careful tuning of the many algorithmic settings. An optimisation routine based on convergence and repeatability of the calculated tissue motion can be used to find application-specific settings without

the need for ground truth reference data (Chapter 4 and 6). With a tuned algorithm, the strain behaviour can be measured in the medial ligaments of the knee, both *ex vivo* and *in vivo*, capturing the non-uniform strain distribution that arises in the ligaments as the knee is flexed, with positive strains in the anterior bundles and negative strains in the posterior bundles (Chapter 6 and 7). Additionally, by using a custom-adapted knee brace to hold the ultrasound transducer and spatially registering the ultrasound images obtained at different sessions, the strain distribution can be compared across time points with moderate to good reliability, allowing changes in ligament function over time to be detected (Chapter 7).

Ultrasound transmissions that produce an acoustic radiation force (ARF) strong enough to generate shear waves can produce acoustic outputs that are close to or exceed the recommendations set by regulatory bodies (Chapter 5). An external shaker is a suitable alternative to safely generate shear waves when used for *in vivo* applications. It additionally enables shear wave propagation to be investigated for a larger range of shear wave frequencies, which can be beneficial when analysing the frequency-dependent dispersive effect in ligaments (Chapter 6). Ultrasound imaging modes used for speckle tracking result in much lower acoustic outputs that are within the safe thresholds, allowing for easy adoption of the technique to *in vivo* applications (Chapter 5).

Lastly, all acquisition and post-processing methods have been outlined in detail, describing how these can be used for a range of tissues with different material characteristics, not just ligaments and tendons. All used Matlab functions are shared throughout to ensure easy reproducibility (Chapter 3 and 4).

8.1.2 Clinical relevance

The viscoelastic properties measured with ultrasound shear wave imaging, along with the strain behaviour obtained from ultrasound speckle tracking, can reveal damage or abnormal loading in tendons and ligaments. Current assessment of these structures is either unreliable, such as palpation or laxity tests [44, 45], or can only detect large structural changes, such as conventional ultrasound or MRI imaging [58]. Thus, these

ultrasound techniques can provide an objective diagnostic tool to uncover changes in the composition or microstructure of these tissues, as well as abnormal loading behaviours [94].

In the collateral ligaments, tears or ruptures commonly occur due to overstraining due to eccentric loading, with footballers and skiers affected most frequently. The resulting damage to the structures can manifest as a reduction in elastic modulus and viscosity [41, 84], as well as a change in the strain distribution [89, 94]. Thus, non-invasive ultrasound shear wave imaging and speckle tracking could be used as a diagnostic tool to detect injury to the ligament and, additionally, monitor and guide the recovery process. For instance, it has been shown that tissue can regenerate and heal in response to regular loading, which has been linked to an increase in elastic modulus [33]. Thus, the elastic modulus measured with shear wave imaging could, for example, be used to monitor the effectiveness of a physiotherapy regimen in restoring ligament function.

Additionally, these techniques can help detect non-physiological function of the collateral ligaments following knee replacement surgery, which may be contributing to complications such as instability or stiffness [6]. For instance, it has been shown that total knee replacement (TKR) surgery alters the strain behaviour in ligaments [14, 19, 47]. Reduced levels of strains could indicate that the ligaments are slack and are not engaged properly during knee movement, limiting their ability to provide support through restraining forces [31], which may lead to instability. Conversely, elevated levels of strains could suggest that the ligaments are providing excessive restraining force, resulting in knee stiffness. Non-invasive monitoring of these effects can help define the post-operative recovery plan to either strengthen or loosen the ligaments. For example, it has been shown that stiffness can be reduced through regular stretching [40]. Furthermore, these techniques will facilitate research into how surgical techniques or implant designs impact post-operative collateral ligament function, allowing for more informed decisions in future designs.

8.1.3 Limitations

The main limitation of the shear wave imaging validation is that it was only performed on simplified tissue models, i.e. agar phantoms and *ex vivo* porcine MCLs with the surrounding tissue removed. The results might therefore not be representative of the accuracy of the technique when applied to *in vivo* ligaments, where the multiple assumptions made by the used viscoelastic and guided wave models may no longer be valid. Furthermore, the large confidence area on the measured shear moduli and viscosities could limit the reliability and usefulness of the technique in practice. Lastly, the shear wave imaging push pulse used in this project cannot be safely used *in vivo* with ARF-generated shear waves, and finding safe transmission settings may be challenging since acoustic outputs produced by new settings need to be measured with time-consuming hydrophone experiments.

The main limitation of the speckle tracking technique is the difficulty in collecting ultrasound acquisitions of sufficient quality, i.e. acquisitions that contain the same amount of loading, with the transducer staying aligned with the ligament during the motion, and with the images capturing the same area of the ligament at repeat sessions. An additional limitation is that the optimisation routine may result in overly regularised strain maps; however, whether this is actually the case is difficult to verify, since obtaining validation data for the strain distribution in the coronal plane is challenging.

Lastly, it should also be noted that the diagnostic value of these techniques in the collateral ligaments is not guaranteed and was only assumed based on their previous use to detect damage in other ligaments or tendons [41, 86, 87, 89, 94]. Therefore, the ability to assess the health and function of the collateral ligaments needs to be tested with clinical studies with affected patients, verifying whether changes in the ligament's shear moduli, viscosity, or strain behaviour measured with ultrasound can be linked to injury or improper balancing after knee replacement surgery.

8.1.4 Final conclusions

Knee instability or stiffness are common complications arising from improper function of the collateral ligaments due to injury or inadequate tensioning of these tissues during knee replacement surgery. By making adaptations to non-invasive ultrasound techniques conventionally used for large and homogeneous tissues, such as shear wave imaging and speckle tracking, their performance in assessing collateral ligaments can be improved. Thus, quantitative measures that could provide insight into the ligament's health and function can be obtained, such as its viscoelastic material properties and its strain behaviour during knee movement.

8.2 Recommendations for future work

8.2.1 Shear wave imaging

Determining the role of ligament and tendon anisotropy

The results from this study and previous measurements by Bonifasi-Lisa et al. [72] on the human medial collateral ligament (MCL) showed that the viscoelastic time constant is comparable for shear and extensional loading, despite the anisotropic nature of ligaments. However, Bonifasi-Lisa et al. also demonstrated that the extensional stiffness was more than three orders of magnitude greater than the shear stiffness. This highlights how the assumption of incompressibility and isotropy, which allows the extensional Young's modulus to be approximated from three times the shear modulus, most certainly does not apply to the collateral ligaments.

Since the mechanical function of ligaments and tendons is classically described in terms of their tensile stress-strain response, future studies could attempt to derive the relationship between the shear material properties obtained with ultrasound and the Young's modulus obtained from tensile testing. Previous analysis performed by Royer et al. [160] suggests that the extensional Young's modulus cannot be accurately determined from just the shear moduli along the fibres in transversely isotropic materials. However, if the level of anisotropy is known, an estimate of the Young's modulus could be obtained if both the shear modulus along and across the fibres is measured (Equation 13 in Royer et al. [160]). Thus, this will require the following additional work: (1) measurement of the anisotropy

of the collateral ligaments and verification whether this value is constant across different people, and (2) validating whether the shear wave imaging procedure can capture the wave propagation across the ligament. Brum et al. [30] previously demonstrated this in the Achilles tendon. However, the collateral ligaments span a much smaller width, which limits the distance across which the propagation behaviour in the transverse direction can be tracked.

Despite this, calculating Young's modulus from the shear modulus might ultimately rely on a number of approximations that lead to uncertainty in the measurements. Additionally, it might not even be necessary: while the extensional Young's modulus is a more intuitive metric that has been used for decades, the shear modulus itself has previously been found to be sufficient to detect injury in ligaments and tendons [41, 86, 87]. Therefore, rather than estimating Young's modulus from the shear wave measurements, future work could focus on improving the viscoelastic validation by performing a mechanical test under shear loading. Furthermore, by performing both dynamic and static creep tests, specific values for the shear modulus and viscosity could be obtained, rather than just their ratio, i.e. viscoelastic time constant [39].

Improve the sensitivity of the viscoelastic properties obtained from the multi-variable dispersion analyses

Shear wave dispersion does not only lead to frequency-dependent phase velocities, but also results in frequency-dependent attenuation of shear waves, a phenomenon that was not fully utilised during this project. Thus, the confidence of the measured material properties could likely be improved by fitting both the phase velocity and attenuation dispersion curves to the experimental data. The theoretical attenuation dispersion curves can be obtained by considering the imaginary contributions of the shear and Lamb wavenumbers (i.e. solving the imaginary parts of Equation 3.16 and 3.22) [229]. In fact, these attenuation dispersion curves were already obtained as a by-product when fitting the combined Voigt & Lamb wave model, since the complexity of the equation meant that phase velocity and attenuation dispersive effects could not be separated by decomposing

the equation into its real and imaginary parts.

Consideration of attenuation may be particularly beneficial for large shear moduli and viscosities. While the phase velocity dispersion curves display little variance when material properties are high, Brum et al. [30] found that the attenuation dispersion curves retain a much higher sensitivity. This could remove one source of uncertainty, leading to smaller confidence areas for the goodness-of-fit of the fitted dispersion curves. Thus, future studies could look into methods for calculating the attenuation from the experimental data, i.e. measuring the decay of axial velocity magnitude with propagation distance. However, during such analysis, other effects that may be contributing to the magnitude of the axial velocities must be considered, such as diffraction of the wave and filtering applied during post-processing [30].

In situ and *in vivo* application

Having demonstrated the validity of this technique in *ex vivo* porcine specimens with the surrounding soft tissue removed, future work should test the technique in intact cadaveric knee specimens. The *in situ* conditions may lead to new challenges. As has been demonstrated through the strain measurements of this study, the ligament is subject to complex and non-uniform loading behaviours during knee motion, with different bundles of the ligaments engaged to provide the required restraining forces in different knee positions. Since it has previously been shown that the material properties measured with shear wave imaging are highly dependent on the load applied to the tissue [144, 159], it is anticipated that measurements may vary greatly at different knee angles. Thus, future research with cadaveric knees could investigate how measured properties vary at different extension-flexion, varus-valgus, and internal-external rotation angles, as well as the effect of muscle loading. Based on these results, a recommendation can be made for the knee position for which material properties best match those from mechanical testing, which will allow for more accurate comparison across patients and different time points.

Additionally, it would be interesting to test the power of the technique *in vivo*, verifying whether it can detect ligament damage or abnormalities based on changes in the

viscoelastic properties. The current implementation using the external shaker can be directly translated to *in vivo* use, since the plane wave imaging (PWI) ultrasound transmissions used to track the shear waves are well within the safe acoustic output range. However, while a significant benefit of using an external shaker is the larger range of shear wave frequencies available for the dispersion analysis, there are still several arguments for using shear waves ARF-generated shear waves in a clinical setting. Most importantly, the full shear wave imaging procedure can be performed using only ultrasound equipment and does not require the purchase, management, and maintenance of an external vibration device. Additionally, shear waves generated using an acoustic radiation force (ARF) push pulse have a broadband frequency spectrum. While analysis may be limited to this range of frequencies, the dispersion behaviour in this range can be obtained from a single shear wave, thus reducing the data collection and processing time. Therefore, it would be valuable to test both types of excitation methods for *in vivo* use. This will require adjustments of the ARF push pulse such that sufficiently strong shear waves can be generated while remaining below the acoustic output thresholds. A study that simulates the formation of ultrasound beams could help optimise the transmission settings, such as focal configurations and push duration, by investigating the relationship between the settings, the strength of the acoustic radiation force and the resulting acoustic safety metrics [249].

Tissue model development

It is possible that generating shear waves *in situ* may result in different propagation behaviours than in the tested porcine ligaments, where the surrounding soft tissue had been removed. Thus, further adaptations to the tissue models applied during post-processing may be needed.

While the Voigt & Lamb wave model provided a good approximation for the shear wave measurements of this project, it still relies on several tissue approximations that may not be valid during *in situ* or *in vivo* measurements of the collateral ligaments. For instance, it is anticipated that the introduction of surrounding tissue will affect the propagation behaviour

of the shear wave. This may be complicated by the fact that the collateral ligaments border multiple different structures with varying levels of stiffnesses, such as the meniscus, fat, and bone. Since it has previously been demonstrated that the formation of guided waves greatly depends on the stiffness mismatch at the boundaries [273], a custom guided wave model may need to be developed that considers the varying stiffness of surrounding structures at different positions along the ligament.

Furthermore, while this study focused on the propagation of antisymmetric guided wave modes in ligaments, previous research has not explicitly justified the absence of symmetric modes. It remains unclear whether this is due to the excitation conditions, boundary constraints, or the intrinsic mechanical properties of the tissue. Future studies could investigate the propagation of both symmetric and antisymmetric modes by generating theoretical velocity and attenuation curves for different mode types in ligamentous tissue. This analysis could help determine whether symmetric modes are inherently suppressed or if their detection is limited by experimental constraints. Incorporating such insights into tissue models may further refine the interpretation of shear wave measurements in both *ex vivo* and *in vivo* settings.

Additionally, future studies could test the effect of using different viscoelastic models, such as a standard linear solid (SLS) or a fractional Voigt model, which may better represent both the time-dependent creep and stress relaxation behaviour of ligaments [43]. These models define the viscoelastic material properties with an additional parameter (an additional elastic spring parameter for the SLS model and a fractional exponent for the fractional Voigt model). Thus, while the theoretical dispersion curves of these models may be able to provide a better fit to the experimental data, the confidence of the found properties may be reduced due to the dependency on three variables. This trade-off could be investigated using the sensitivity analysis developed in this project.

8.2.2 Speckle tracking

Further investigate the effect of initial region of interest selection

The effect of placing the tissue region of interest for which strains are calculated at different positions along the ligament was already investigated in the *in vivo* study of this project. However, the initial region of interest also dictates the fibre direction along which strains are calculated, with fibres assumed to follow the non-uniform nodal grid of the selected region. Further analysis could investigate how deviations from this assumed initial fibre orientation affects the final strain measurements. The equations derived from a ligament-specific deformation gradient decomposition (Equations 4A.11-4A.14 in Addendum 4A of Chapter 4) should facilitate this analysis, since these allow strains to be calculated along different directions (θ_F) regardless of the shape of the region of interest and nodal grid.

Improve optimisation routine

Here, validation of the measured strains in the porcine ligaments was only based on the average strains within the final ultrasound and digital image correlation (DIC) strain maps at the end of the loading cycle. Thus, the ability of the speckle tracking algorithm to pick out strain variations within the strain map (i.e., in the coronal plane) is not captured. In general, the strain maps produced in this project were characterised by relatively smooth and gradual strain variations within the map. Since DIC measurements can only capture the ligament surface strains, it is challenging to validate whether this represents the true variation in this plane (i.e., along and across the thickness of the ligament). However, it could indicate that the optimisation routine prefers settings that over-regularise the deformation or strain field, as uniform maps are more likely to be repeatable. It could be tested whether a better balance between repeatability and over-regularisation can be achieved by making modifications to the objective function of the optimisation. For example, the quality penalty could be adjusted such that larger normalised standard deviations are allowed for results that capture more non-uniform strain or deformation distributions.

Improve knee brace design

Future studies could improve the design of the knee brace that holds the ultrasound transducer during the *in vivo* measurements to provide additional rigidity and ensure that the same region of the ligament is captured throughout knee movement. Testing the adapted knee braces on cadaveric knees in a testing laboratory could guide future modifications of the brace: by tracking the position of the transducer and ligament using a motion capture system, the alignment of the transducer throughout different knee movements can be quantified. Future designs should prioritise a stable alignment over the ligament with minimal out-of-plane movement [51, 204], while still allowing flexible initial positioning of the transducer and incremental variation in anterior/posterior (AP) position.

Allow for variable focal depths of the conventional imaging mode

The hydrophone safety measurements for the conventional imaging mode were only performed for a single focal depth. Since the depth at which the collateral ligaments are located in the ultrasound images can vary greatly between patients depending on the amount of soft tissue around the knee, future *in vivo* studies would benefit from adjustable focal settings such that the focal depth can be set to coincide with the ligament. Most of the tissue motion tracking is in the lateral direction, and thus it is likely that capturing the tissue of interest with a higher lateral resolution will improve the performance of the speckle tracking algorithm [106]. Since changes in the focal configuration will change the maximum acoustic pressures and intensities in the field, future studies could measure how these acoustic outputs vary with different focal depth settings, ensuring that these remain within safe levels for *in vivo* use.

Clinical study with knee replacement patient

The clinical pilot study presented in Chapter 7 aimed to demonstrate the readiness of the technique for clinical research. Such a study could assess whether knee replacement surgery alters the native strain behaviour, and whether post-operative ligament healing

and adaptation can lead to changes in ligament balance and function. This would involve taking measurements on the collateral ligaments both before surgery, as well as at different time points after the surgery. It would, furthermore, be interesting to assess whether there is a link between the ligament strain behaviour and patient reported outcome metrics, such as pain, instability and stiffness.

09

References

[1] A. Judge, N. K. Arden, C. Cooper, M. Kassim Javaid, A. J. Carr, R. E. Field, and P. A. Dieppe, “Predictors of outcomes of total knee replacement surgery,” *Rheumatology (United Kingdom)*, vol. 51, no. 10, pp. 1804–1813, 2012.

[2] A. Heikkilä, N. Sevander Kreus, A. Häkkinen, M. Vuorenmaa, P. Salo, P. Konsta, and J. Ylinen, “Effect of total knee replacement surgery and postoperative 12 month home exercise program on gait parameters,” *Gait and Posture*, vol. 53, pp. 92–97, 2017.

[3] Y. Ben-Shlomo *et al.*, “The national joint registry 17th annual report 2020,” National Joint Registry, London, Tech. Rep., 2020.

[4] R. Gunaratne, D. N. Pratt, J. Banda, D. P. Fick, R. J. K. Khan, and B. W. Robertson, “Patient dissatisfaction following total knee arthroplasty: a systematic review of the literature,” *Journal of Arthroplasty*, vol. 32, no. 12, pp. 3854–3860, 2017.

[5] D. C. Ayers, M. Yousef, H. Zheng, W. Yang, and P. D. Franklin, “The prevalence and predictors of patient dissatisfaction 5-years following primary total knee arthroplasty,” *Journal of Arthroplasty*, vol. 37, no. 6S, S121–S128, 2022.

[6] S. Babazadeh, J. D. Stoney, K. Lim, and P. F. Choong, “The relevance of ligament balancing in total knee arthroplasty: how important is it? A systematic review of the literature,” *Orthopedic Reviews*, vol. 1, no. 2, Art. no. e26, 2009.

[7] A. Kappel, M. Laursen, P. T. Nielsen, and A. Odgaard, “Relationship between outcome scores and knee laxity following total knee arthroplasty: a systematic review,” *Acta Orthopaedica*, vol. 90, no. 1, pp. 46–52, 2019.

[8] E. Aunan, T. J. Kibsgård, L. M. Diep, and S. M. Röhrl, “Intraoperative ligament laxity influences functional outcome 1 year after total knee arthroplasty,” *Knee Surgery, Sports Traumatology, Arthroscopy*, vol. 23, no. 6, pp. 1684–1692, 2015.

[9] S. Matsuda and H. Ito, “Ligament balancing in total knee arthroplasty - Medial stabilizing technique,” *Asia-Pacific Journal of Sports Medicine, Arthroscopy, Rehabilitation and Technology*, vol. 2, no. 4, pp. 108–113, 2015.

[10] K. K. Athwal, H. El Daou, E. Inderhaug, W. Manning, A. J. Davies, D. J. Deehan, and A. A. Amis, “An in vitro analysis of medial structures and a medial soft tissue reconstruction in a constrained condylar total knee arthroplasty,” *Knee Surgery, Sports Traumatology, Arthroscopy*, vol. 25, no. 8, pp. 2646–2655, 2017.

[11] F. Völlner, T. Weber, M. Weber, T. Renkawitz, S. Dendorfer, J. Grifka, and B. Craiovan, “A simple method for determining ligament stiffness during total knee arthroplasty in vivo,” *Scientific Reports*, vol. 9, no. 1, Art. no. 5261, 2019.

[12] K. A. Gustke, G. J. Golladay, M. W. Roche, L. C. Elson, and C. R. Anderson, “A new method for defining balance: promising short-term clinical outcomes of sensor-guided TKA,” *Journal of Arthroplasty*, vol. 29, no. 5, pp. 955–960, 2014.

[13] D. H. Le, S. B. Goodman, W. J. Maloney, and J. I. Huddleston, “Current modes of failure in TKA: infection, instability, and stiffness predominate,” *Clinical Orthopaedics and Related Research*, vol. 472, no. 7, pp. 2197–2200, 2014.

[14] S. H. Hosseini Nasab, C. R. Smith, P. Schütz, B. Postolka, R. List, and W. R. Taylor, “Elongation patterns of the collateral ligaments after total knee arthroplasty are dominated by the knee flexion angle,” *Frontiers in Bioengineering and Biotechnology*, vol. 7, Art. no. 323, 2019.

[15] P. P. Provenzano, D. Heisey, K. Hayashi, R. Lakesand, and R. Vanderby, “Subfailure damage in ligament: a structural and cellular evaluation,” *Journal of Applied Physiology*, vol. 92, no. 1, pp. 362–371, 2002.

[16] D. Cosgrove, F. Piscaglia, J. Bamber, J. Bojunga, J. M. Correas, O. H. Gilja, A. S. Klauser, I. Sporea, F. Calliada, V. Cantisani, M. D’Onofrio, E. E. Drakonaki, M. Fink, M. Friedrich-Rust, J. Fromageau, R. F. Havre, C. Jenssen, R. Ohlinger, A. Săftoiu, F. Schaefer, and C. F. Dietrich, “EFSUMB guidelines and recommendations on the clinical use of ultrasound elastography. Part 2: Clinical applications,” *Ultraschall in der Medizin*, vol. 34, no. 3, pp. 238–253, 2013.

[17] R. Prado-Costa, J. Rebelo, J. Monteiro-Barroso, and A. S. Preto, “Ultrasound elastography: compression elastography and shear-wave elastography in the assessment of tendon injury,” *Insights into Imaging*, vol. 9, no. 5, pp. 791–814, 2018.

[18] L. Willinger, S. Shinohara, K. K. Athwal, S. Ball, A. Williams, and A. A. Amis, “Length-change patterns of the medial collateral ligament and posterior oblique ligament in relation to their function and surgery,” *Knee Surgery, Sports Traumatology, Arthroscopy*, vol. 28, no. 12, pp. 3720–3732, 2020.

[19] S. H. Hosseini Nasab, C. R. Smith, P. Schütz, P. Damm, A. Trepczynski, R. List, and W. R. Taylor, “Length-change patterns of the collateral ligaments during functional activities after total knee arthroplasty,” *Annals of Biomedical Engineering*, vol. 48, no. 4, pp. 1396–1406, 2020.

[20] G. Ferraioli, C. Tinelli, B. Dal Bello, M. Zicchetti, G. Filice, C. Filice, and Liver Fibrosis Study Group, “Accuracy of real-time shear wave elastography for assessing liver fibrosis in chronic hepatitis C: a pilot study,” *Hepatology*, vol. 56, no. 6, pp. 2125–2133, 2012.

[21] É. Bavu, J. L. Gennisson, M. Couade, J. Bercoff, V. Mallet, M. Fink, A. Badel, A. Vallet-Pichard, B. Nalpas, M. Tanter, and S. Pol, “Noninvasive in vivo liver fibrosis evaluation using supersonic shear imaging: a clinical study on 113 hepatitis C virus patients,” *Ultrasound in Medicine and Biology*, vol. 37, no. 9, pp. 1361–1373, 2011.

[22] L. Sandrin, B. Fourquet, J. M. Hasquenoph, S. Yon, C. Fournier, F. Mal, C. Christidis, M. Ziol, B. Poulet, F. Kazemi, M. Beaugrand, and R. Palau, “Transient elastography: a new noninvasive method for assessment of hepatic fibrosis,” *Ultrasound in Medicine and Biology*, vol. 29, no. 12, pp. 1705–1713, 2003.

[23] E. Brusseau, J. Kybic, J. F. Déprez, and O. Basset, “2-D locally regularized tissue strain estimation from radio-frequency ultrasound images: theoretical developments and results on experimental data,” *IEEE Transactions on Medical Imaging*, vol. 27, no. 2, pp. 145–160, 2008.

[24] M. Tanter, J. Bercoff, A. Athanasiou, T. Deffieux, J. L. Gennisson, G. Montaldo, M. Muller, A. Tardivon, and M. Fink, “Quantitative assessment of breast lesion viscoelasticity: initial clinical results using supersonic shear imaging,” *Ultrasound in Medicine and Biology*, vol. 34, no. 9, pp. 1373–1386, 2008.

[25] D. O. Cosgrove, W. A. Berg, C. J. Doré, D. M. Skyba, J. P. Henry, J. Gay, C. Cohen-Bacrie, and BE1 Study Group, “Shear wave elastography for breast masses is highly reproducible,” *European Radiology*, vol. 22, no. 5, pp. 1023–1032, 2012.

[26] I. Céspedes, J. Ophir, H. Ponnekanti, and N. Maklad, “Elastography: elasticity imaging using ultrasound with application to muscle and breast in vivo,” *Ultrasonic Imaging*, vol. 15, no. 2, pp. 73–88, 1993.

[27] C. Pellot-Barakat, F. Frouin, M. F. Insana, and A. Herment, “Ultrasound elastography based on multiscale estimations of regularized displacement fields,” *IEEE Transactions on Medical Imaging*, vol. 23, no. 2, pp. 153–163, 2004.

[28] G. Y. Li, Y. Zheng, Y. X. Jiang, Z. Zhang, and Y. Cao, “Guided wave elastography of layered soft tissues,” *Acta Biomaterialia*, vol. 84, pp. 293–304, 2019.

[29] C. Helfenstein-Didier, R. J. Andrade, J. Brum, F. Hug, M. Tanter, A. Nordez, and J. L. Gennisson, “In vivo quantification of the shear modulus of the human Achilles tendon during passive loading using shear wave dispersion analysis,” *Physics in Medicine and Biology*, vol. 61, no. 6, pp. 2485–2496, 2016.

[30] J. Brum, M. Bernal, J. L. Gennisson, and M. Tanter, “In vivo evaluation of the elastic anisotropy of the human Achilles tendon using shear wave dispersion analysis,” *Physics in Medicine and Biology*, vol. 59, no. 3, pp. 505–523, 2014.

[31] D. L. Butler, E. S. Grood, F. R. Noyes, and R. F. Zernicke, “Biomechanics of ligaments and tendons.,” *Exercise and sport sciences reviews*, vol. 6, pp. 125–81, 1978.

[32] H.-J. Jung, M. B. Fisher, and S. L.-Y. Woo, “Role of biomechanics in the understanding of normal, injured, and healing ligaments and tendons,” *BMC Sports Science, Medicine and Rehabilitation*, vol. 1, Art. no. 9, 2009.

[33] C.-K. Cheng and S. L.-Y. Woo, *Frontiers in orthopaedic biomechanics*. Springer Singapore, 2020.

[34] P. Kannus, “Structure of the tendon connective tissue,” *Scandinavian Journal of Medicine & Science in Sports*, vol. 10, no. 6, pp. 312–320, 2000.

[35] J. Kastelic, A. Galeski, and E. Baer, “The multicomposite structure of tendon,” *Connective Tissue Research*, vol. 6, no. 1, pp. 11–23, 1978.

[36] A. Viidik, “Functional properties of collagenous tissues,” *International Review of Connective Tissue Research*, vol. 6, pp. 127–215, 1973.

[37] M. J. Mienaltowski and D. E. Birk, “Structure, physiology, and biochemistry of collagens,” in *Progress in heritable soft connective tissue diseases*, 2014, pp. 5–29.

[38] K. M. Quapp and J. A. Weiss, “Material characterization of human medial collateral ligament,” *Journal of Biomechanical Engineering*, vol. 120, no. 6, pp. 757–763, 1998.

[39] B. R. Gupta, *Rheology applied in polymer processing*. CRC Press, 2022.

[40] K. Kubo, H. Kanehisa, Y. Kawakami, and T. Fukunaga, “Influence of static stretching on viscoelastic properties of human tendon structures in vivo,” *Journal of Applied Physiology*, vol. 90, no. 2, pp. 520–527, 2001.

[41] D. H. Cortes, S. M. Suydam, K. G. Silbernagel, T. S. Buchanan, and D. M. Elliott, “Continuous shear wave elastography: a new method to measure viscoelastic properties of tendons in vivo,” *Ultrasound in Medicine and Biology*, vol. 41, no. 6, pp. 1518–1529, 2015.

[42] W. Zhang, A. Capilnasiu, and D. Nordsletten, “Comparative analysis of nonlinear viscoelastic models across common biomechanical experiments,” *Journal of Elasticity*, vol. 145, pp. 117–152, 2021.

[43] B. Zhou and X. Zhang, “Comparison of five viscoelastic models for estimating viscoelastic parameters using ultrasound shear wave elastography,” *Journal of the Mechanical Behavior of Biomedical Materials*, vol. 85, pp. 109–116, 2018.

[44] J. L. Cook, K. M. Khan, Z. S. Kiss, C. R. Purdam, and L. Griffiths, “Reproducibility and clinical utility of tendon palpation to detect patellar tendinopathy in young basketball players,” *British Journal of Sports Medicine*, vol. 35, no. 1, pp. 65–69, 2001.

[45] G. A. Malanga, S. Andrus, S. F. Nadler, and J. McLean, “Physical examination of the knee: a review of the original test description and scientific validity of common orthopedic tests,” *Archives of Physical Medicine and Rehabilitation*, vol. 84, no. 4, pp. 592–603, 2003.

[46] R. D’Ambrosi, K. Corona, G. Guerra, S. Cerciello, C. Ursino, N. Ursino, and M. Hantes, “Posterior oblique ligament of the knee: state of the art,” *EFORT Open Reviews*, vol. 6, no. 5, pp. 364–371, 2021.

[47] S. H. Hosseini Nasab, C. R. Smith, B. Postolka, P. Schütz, R. List, and W. R. Taylor, “In vivo elongation patterns of the collateral ligaments in healthy knees during functional activities,” *The Journal of Bone and Joint Surgery*, vol. 103, no. 17, pp. 1620–1627, 2021.

[48] Q. Zhang, N. C. Adam, S. H. Hosseini Nasab, W. R. Taylor, and C. R. Smith, “Techniques for in vivo measurement of ligament and tendon strain: a review,” *Annals of Biomedical Engineering*, vol. 49, no. 1, pp. 7–28, 2021.

[49] K. Gijsbertse, A. Sprengers, H. Naghibi Beidokhti, M. Nillesen, C. de Korte, and N. Verdonschot, “Strain imaging of the lateral collateral ligament using high frequency and conventional ultrasound imaging: An ex-vivo comparison,” *Journal of Biomechanics*, vol. 73, pp. 233–237, 2018.

[50] L. C. Slane and D. G. Thelen, “The use of 2D ultrasound elastography for measuring tendon motion and strain,” *Journal of Biomechanics*, vol. 47, no. 3, pp. 750–754, 2014.

[51] L. C. Slane, J. A. Slane, J. D’hooge, and L. Scheys, “The challenges of measuring in vivo knee collateral ligament strains using ultrasound,” *Journal of Biomechanics*, vol. 61, pp. 258–262, 2017.

[52] N. Otake, H. Chen, X. Yao, and S. Shoumura, “Morphologic study of the lateral and medial collateral ligaments of the human knee,” *Okajimas Folia Anatomica Japonica*, vol. 83, no. 4, pp. 115–122, 2007.

[53] E. S. Grood, S. F. Stowers, and F. R. Noyes, “Limits of movement in the human knee. Effect of sectioning the posterior cruciate ligament and posterolateral structures,” *The Journal of Bone and Joint Surgery*, vol. 70, no. 1, pp. 88–97, 1988.

[54] J. D. Hassebrock, M. T. Gulbrandsen, W. L. Asprey, J. L. Makovicka, and A. Chhabra, “Knee ligament anatomy and biomechanics,” *Sports Medicine and Arthroscopy Review*, vol. 28, no. 3, pp. 80–86, 2020.

[55] J. R. Robinson, J. Sanchez-Ballester, A. M. J. Bull, R. d. W. M. Thomas, and A. A. Amis, “The posteromedial corner revisited. An anatomical description of the passive restraining structures of the medial aspect of the human knee.,” *The Journal of Bone and Joint Surgery*, vol. 86-B, no. 5, pp. 674–681, 2004.

[56] S. Bollen, “Epidemiology of knee injuries: diagnosis and triage,” *British Journal of Sports Medicine*, vol. 34, no. 3, pp. 227–228, 2000.

[57] K. Andrews, A. Lu, L. Mckean, and N. Ebraheim, “Review: Medial collateral ligament injuries,” *Journal of Orthopaedics*, vol. 14, no. 4, pp. 550–554, 2017.

[58] R. J. Hodgson, P. J. O’Connor, and A. J. Grainger, “Tendon and ligament imaging,” *British Journal of Radiology*, vol. 85, no. 1016, pp. 1157–1172, 2012.

[59] B. Grawe, A. J. Schroeder, R. Kakazu, and M. S. Messer, “Lateral collateral ligament injury about the knee: anatomy, evaluation, and management,” *Journal of the American Academy of Orthopaedic Surgeons*, vol. 26, no. 6, e120–e127, 2018.

[60] H. J. Cho and D. S. Kwak, “Mechanical properties and characteristics of the anterolateral and collateral ligaments of the knee,” *Applied Sciences*, vol. 10, no. 18, Art. no. 6266, 2020.

[61] D. L. Butler, M. D. Kay, and D. C. Stouffer, “Comparison of material properties in fascicle-bone units from human patellar tendon and knee ligaments,” *Journal of Biomechanics*, vol. 19, no. 6, pp. 425–432, 1986.

[62] R. F. LaPrade, T. S. Bollom, F. A. Wentorf, N. J. Wills, and K. Meister, “Mechanical properties of the posterolateral structures of the knee,” *American Journal of Sports Medicine*, vol. 33, no. 9, pp. 1386–1391, 2005.

[63] W. T. Wilson, A. H. Deakin, A. P. Payne, F. Picard, and S. C. Wearing, “Comparative analysis of the structural properties of the collateral ligaments of the human knee,” *Journal of Orthopaedic and Sports Physical Therapy*, vol. 42, no. 4, pp. 345–351, 2012.

[64] J. R. Kerrigan, B. J. Ivarsson, D. Bose, N. J. Madeley, S. A. Millington, K. S. Bhalla, and J. R. Crandall, “Rate-sensitive constitutive and failure properties of human collateral knee ligaments,” in *IRCOBI Conference*, 2003, pp. 177–190.

[65] T. J. Lujan, C. J. Underwood, H. B. Henninger, B. M. Thompson, and J. A. Weiss, “Effect of dermatan sulfate glycosaminoglycans on the quasi-static material properties of the human medial collateral ligament,” *Journal of Orthopaedic Research*, vol. 25, no. 7, pp. 894–903, 2007.

[66] K. Smeets, J. Slane, L. Scheys, S. Claes, and J. Bellemans, “Mechanical analysis of extra-articular knee ligaments. Part one: native knee ligaments,” *The Knee*, vol. 24, no. 5, pp. 949–956, 2017.

[67] S. L. Woo, M. A. Gomez, T. J. Sites, P. O. Newton, C. A. Orlando, and W. H. Akeson, “The biomechanical and morphological changes in the medial collateral ligament of the rabbit after immobilization and remobilization,” *The Journal of Bone and Joint Surgery*, vol. 69, no. 8, pp. 1200–1211, 1987.

[68] S. L.-Y. Woo, C. A. Orlando, M. A. Gomez, C. B. Frank, and W. H. Akeson, “Tensile properties of the medial collateral ligament as a function of age,” *Journal of Orthopaedic Research*, vol. 4, no. 2, pp. 133–141, 1986.

[69] T. Q. Lee, J. Dettling, M. D. Sandusky, and P. J. McMahon, “Age related biomechanical properties of the glenoid-anterior band of the inferior glenohumeral ligament-humerus complex,” *Clinical Biomechanics*, vol. 14, no. 7, pp. 471–476, 1999.

[70] C. Wan, Z. Hao, S. Wen, and H. Leng, “A quantitative study of the relationship between the distribution of different types of collagen and the mechanical behavior of rabbit medial collateral ligaments,” *PLoS One*, vol. 9, no. 7, Art. no. e103363, 2014.

[71] J. Wu, Z. Qian, W. Liang, J. Liu, L. Ren, and L. Ren, “In vivo assessment of material properties of muscles and connective tissues around the knee joint based on shear wave elastography,” *Journal of the Mechanical Behavior of Biomedical Materials*, vol. 109, Art. no. 103829, 2020.

[72] C. Bonifasi-Lista, S. P. Lake, M. S. Small, and J. A. Weiss, “Viscoelastic properties of the human medial collateral ligament under longitudinal, transverse and shear loading,” *Journal of Orthopaedic Research*, vol. 23, no. 1, pp. 67–76, 2005.

[73] A. Ristaniemi, L. Stenroth, S. Mikkonen, and R. K. Korhonen, “Comparison of elastic, viscoelastic and failure tensile material properties of knee ligaments and patellar tendon.,” *Journal of Biomechanics*, vol. 79, pp. 31–38, 2018.

[74] A. Chawla, S. Mukherjee, H. Warhatkar, and R. Malhotra, “Dynamic characterization of bovine medial collateral ligaments,” in *IRCOBI Conference*, International Research Council on Biomechanics of Injury, 2009, pp. 109–112.

[75] S. G. Cone, H. E. Piercy, E. P. Lambeth, H. Ru, J. A. Piedrahita, J. T. Spang, L. A. Fordham, and M. B. Fisher, “Tissue-specific changes in size and shape of the ligaments and tendons of the porcine knee during post-natal growth,” *PLoS One*, vol. 14, no. 10, Art. no. e0219637, 2019.

[76] J. L. Blank, D. G. Thelen, and J. D. Roth, “Shear wave speeds track axial stress in porcine collateral ligaments,” *Journal of the Mechanical Behavior of Biomedical Materials*, vol. 105, Art. no. 103704, 2020.

[77] L. Peck, K. Billiar, and M. Ray, “Dynamic failure properties of the porcine medial collateral ligament-bone complex for predicting injury in automotive collisions,” *The Open Biomedical Engineering Journal*, vol. 4, pp. 77–84, 2010.

[78] N. M. Germscheid, G. M. Thornton, D. A. Hart, and K. A. Hildebrand, “A biomechanical assessment to evaluate breed differences in normal porcine medial collateral ligaments,” *Journal of Biomechanics*, vol. 44, no. 4, pp. 725–731, 2011.

[79] G. M. Thornton, T. D. Schwab, and T. R. Oxland, “Fatigue is more damaging than creep in ligament revealed by modulus reduction and residual strength,” *Annals of Biomedical Engineering*, vol. 35, no. 10, pp. 1713–1721, 2007.

[80] G. M. Thornton, D. B. Lemmex, Y. Ono, C. J. Beach, C. R. Reno, D. A. Hart, and I. K. Lo, “Aging affects mechanical properties and lubricin/PRG4 gene expression in normal ligaments,” *Journal of Biomechanics*, vol. 48, no. 12, pp. 3306–3311, 2015.

[81] S. M. Strickland, T. W. Belknap, S. A. Turner, T. M. Wright, and J. A. Hannafin, “Lack of hormonal influences on mechanical properties of sheep knee ligaments,” *American Journal of Sports Medicine*, vol. 31, no. 2, pp. 210–215, 2003.

[82] K. K. Athwal, H. E. Daou, C. Kittl, A. J. Davies, D. J. Deehan, and A. A. Amis, “The superficial medial collateral ligament is the primary medial restraint to knee laxity after cruciate-retaining or posterior-stabilised total knee arthroplasty: effects of implant type and partial release,” *Knee Surgery, Sports Traumatology, Arthroscopy*, vol. 24, no. 8, pp. 2646–2655, 2016.

[83] M. Maes, T. Luyckx, and J. Bellemans, “Does a conservative tibial cut in conventional total knee arthroplasty violate the deep medial collateral ligament?” *Knee Surgery, Sports Traumatology, Arthroscopy*, vol. 22, no. 11, pp. 2735–2739, 2014.

[84] S. Aubry, J. P. Nueffer, M. Tanter, F. Becce, C. Vidal, and F. Michel, “Viscoelasticity in Achilles tendonopathy: quantitative assessment by using real-time shear-wave elastography,” *Radiology*, vol. 274, no. 3, pp. 821–829, 2015.

[85] X. Chen, Y. Shen, Y. Zheng, H. Lin, Y. Guo, Y. Zhu, X. Zhang, T. Wang, and S. Chen, “Quantification of liver viscoelasticity with acoustic radiation force: a study of hepatic fibrosis in a rat model,” *Ultrasound in Medicine and Biology*, vol. 39, no. 11, pp. 2091–2102, 2013.

[86] C.-Y. Lin, S. Sadeghi, D. A. Bader, and D. H. Cortes, “Ultrasound shear wave elastography of the elbow ulnar collateral ligament: reliability test and a preliminary case study in a baseball pitcher,” *Journal of Engineering and Science in Medical Diagnostics and Therapy*, vol. 1, no. 1, Art. no. 011004, 2018.

[87] S. Sadeghi, C.-Y. Lin, D. A. Bader, and D. H. Cortes, “Evaluating changes in shear modulus of elbow ulnar collateral ligament in overhead throwing athletes over the course of a competitive season,” *Journal of Engineering and Science in Medical Diagnostics and Therapy*, vol. 1, no. 4, Art. no. 041008, 2018.

[88] W. H. Clark and J. R. Franz, “Triceps surae muscle-subtendon interaction differs between young and older adults,” *Connective Tissue Research*, vol. 61, no. 1, pp. 104–113, 2020.

[89] C. Couppé, R. B. Svensson, C. O. Josefsen, E. Kjeldgaard, and S. P. Magnusson, “Ultrasound speckle tracking of Achilles tendon in individuals with unilateral tendinopathy: a pilot study,” *European Journal of Applied Physiology*, vol. 120, no. 3, pp. 579–589, 2020.

[90] W. H. Clark and J. R. Franz, “Age-related changes to triceps surae muscle-subtendon interaction dynamics during walking,” *Scientific Reports*, vol. 11, no. 1, Art. no. 21264, 2021.

[91] R. M. Khair, L. Stenroth, A. Péter, N. J. Cronin, A. Reito, J. Paloneva, and T. Finni, “Non-uniform displacement within ruptured Achilles tendon during isometric contraction,” *Scandinavian Journal of Medicine and Science in Sports*, vol. 31, no. 5, pp. 1069–1077, 2021.

[92] R. M. Khair, L. Stenroth, N. J. Cronin, A. Reito, J. Paloneva, and T. Finni, “In vivo localized gastrocnemius subtendon representation within the healthy and ruptured human Achilles tendon,” *Journal of Applied Physiology*, vol. 133, no. 1, pp. 11–19, 2022.

[93] R. Beyer, A.-S. Agergaard, S. P. Magnusson, and R. B. Svensson, “Speckle tracking in healthy and surgically repaired human Achilles tendons at different knee angles - a validation using implanted tantalum beads,” *Translational Sports Medicine*, vol. 1, no. 2, pp. 79–88, 2018.

[94] L. C. Slane and D. G. Thelen, “Achilles tendon displacement patterns during passive stretch and eccentric loading are altered in middle-aged adults,” *Medical Engineering and Physics*, vol. 37, no. 7, pp. 712–716, 2015.

[95] J. R. Franz and D. G. Thelen, “Depth-dependent variations in Achilles tendon deformations with age are associated with reduced plantarflexor performance during walking,” *Journal of Applied Physiology*, vol. 119, no. 3, pp. 242–249, 2015.

[96] K. Kono, S. Konda, T. Yamazaki, S. Tanaka, K. Sugamoto, and T. Tomita, “In vivo length change of ligaments of normal knees during dynamic high flexion,” *BMC Musculoskeletal Disorders*, vol. 21, no. 1, Art. no. 552, 2020.

[97] D. A. Dennis, R. D. Komistek, R. H. Kim, and A. Sharma, “Gap balancing versus measured resection technique for total knee arthroplasty,” in *Clinical Orthopaedics and Related Research*, vol. 468, 2010, pp. 102–107.

[98] N. P. Sheth, A. Husain, and C. L. Nelson, “Surgical techniques for total knee arthroplasty: measured resection, gap balancing, and hybrid,” *Journal of the American Academy of Orthopaedic Surgeons*, vol. 25, no. 7, pp. 499–508, 2017.

[99] G.-R. She and Z.-G. Zha, “Gap balancing versus measured resection in primary total knee arthroplasty: A retrospective cohort study protocol,” *Medicine*, vol. 99, no. 20, Art. no. e20017, 2020.

[100] A. Gordon, G. Golladay, T. L. Bradbury, I. Fernandez-Madrid, V. E. Krebs, P. Patel, C. Higuera, W. Barsoum, and J. Suarez, “Are patients more satisfied with a balanced total knee arthroplasty?” In *Orthopaedic Proceedings*, vol. 101-B, International Society for Technology in Arthroplasty (ISTA), 2019, p. 116.

[101] T. L. Szabo, *Diagnostic ultrasound imaging: Inside out*, 2nd ed. Academic press, 2013.

[102] H. Shankar and P. S. Pagel, “Potential adverse ultrasound-related biological effects: a critical review,” *Anesthesiology*, vol. 115, no. 5, pp. 1109–1124, 2011.

[103] G. Haar, *The safe use of ultrasound in medical diagnosis*, 3rd ed. British Institute of Radiology, 2012.

[104] R. de Luca, L. Forzoni, F. Gelli, and J. Bamber, “An educational overview of ultrasound probe types and their fields of application,” *Archives of Acoustics*, vol. 46, no. 1, pp. 3–15, 2021.

[105] L. Demi, “Practical guide to ultrasound beam forming: Beam pattern and image reconstruction analysis,” *Applied Sciences*, vol. 8, no. 9, Art. no. 1544, 2018.

[106] A. Ng and J. Swanevelder, “Resolution in ultrasound imaging,” *Continuing Education in Anaesthesia, Critical Care and Pain*, vol. 11, no. 5, pp. 186–192, 2011.

[107] J. Bercoff, “Ultrafast Ultrasound Imaging,” in *Ultrasound Imaging - Medical Applications*, InTech, 2011, pp. 3–24.

[108] Y. Deng, N. C. Rouze, M. L. Palmeri, and K. R. Nightingale, “Ultrasonic shear wave elasticity imaging sequencing and data processing using a Verasonics research scanner,” *IEEE Transactions on Ultrasonics, Ferroelectrics, and Frequency Control*, vol. 64, no. 1, pp. 164–176, 2017.

[109] H. Li, Y. Guo, and W. N. Lee, “Systematic performance evaluation of a cross-correlation-based ultrasound strain imaging method,” *Ultrasound in Medicine and Biology*, vol. 42, no. 10, pp. 2436–2456, 2016.

[110] G. Montaldo, M. Tanter, J. Bercoff, N. Benech, and M. Fink, “Coherent plane-wave compounding for very high frame rate ultrasonography and transient elastography,” *IEEE Transactions on Ultrasonics, Ferroelectrics, and Frequency Control*, vol. 56, no. 3, pp. 489–506, 2009.

[111] M. Smallcomb and J. C. Simon, “Histotripsy in collagenous tendons,” in *Proceedings of Meetings on Acoustics*, vol. 39, AIP Publishing, 2019, Art. no. 020004.

[112] J. Bercoff, M. Tanter, and M. Fink, “Supersonic shear imaging: a new technique for soft tissue elasticity mapping,” *IEEE Transactions on Ultrasonics, Ferroelectrics and Frequency Control*, vol. 51, no. 4, pp. 396–409, 2004.

[113] W. F. Bynum and R. Porter, *Medicine and the Five Senses*. Cambridge University Press, 1993.

[114] J. Ophir, I. Céspedes, H. Ponnekanti, Y. Yazdi, and X. Li, “Elastography: a quantitative method for imaging the elasticity of biological tissues,” *Ultrasonic Imaging*, vol. 13, no. 2, pp. 111–134, 1991.

[115] D. S. Hughes and J. L. Kelly, “Second-order elastic deformation of solids,” *Physical Review*, vol. 92, no. 5, pp. 1145–1149, 1953.

[116] S. Duenwald, H. Kobayashi, K. Frisch, R. Lakes, and R. Vanderby, “Ultrasound echo is related to stress and strain in tendon,” *Journal of Biomechanics*, vol. 44, no. 3, pp. 424–429, 2011.

[117] S. Duenwald-Kuehl, R. Lakes, and R. Vanderby, “Strain-induced damage reduces echo intensity changes in tendon during loading,” *Journal of Biomechanics*, vol. 45, no. 9, pp. 1607–1611, 2012.

[118] C. S. Chamberlain, S. E. Duenwald-Kuehl, G. Okotie, S. H. Brounts, G. S. Baer, and R. Vanderby, “Temporal healing in rat achilles tendon: ultrasound correlations,” *Annals of Biomedical Engineering*, vol. 41, no. 3, pp. 477–487, 2013.

[119] R. M. Lerner, S. R. Huang, and K. J. Parker, “"Sonoelasticity" images derived from ultrasound signals in mechanically vibrated tissues,” *Ultrasound in Medicine and Biology*, vol. 16, no. 3, pp. 231–239, 1990.

[120] A. P. Sarvazyan, O. V. Rudenko, S. D. Swanson, J. B. Fowlkes, and S. Y. Emelianov, “Shear wave elasticity imaging: a new ultrasonic technology of medical diagnostics,” *Ultrasound in Medicine and Biology*, vol. 24, no. 9, pp. 1419–1435, 1998.

[121] K. Nightingale, S. McAleavey, and G. Trahey, “Shear-wave generation using acoustic radiation force: in vivo and ex vivo results,” *Ultrasound in Medicine and Biology*, vol. 29, no. 12, pp. 1715–1723, 2003.

[122] H. Zhao, P. Song, D. D. Meixner, R. R. Kinnick, M. R. Callstrom, W. Sanchez, M. W. Urban, A. Manduca, J. F. Greenleaf, and S. Chen, “External vibration multi-directional ultrasound shearwave elastography (EVMUSE): application in liver fibrosis staging,” *IEEE Transactions on Medical Imaging*, vol. 33, no. 11, pp. 2140–2148, 2014.

[123] R. M. Lerner, K. J. Parker, J. Holen, R. Gramiak, and R. C. Waag, “Sono-elasticity: medical elasticity images derived from ultrasound signals in mechanically vibrated targets,” in *Acoustical Imaging*, vol. 16, Boston: Springer, 1988, pp. 317–327.

[124] S. A. McAleavey, M. Menon, and J. Orszulak, “Shear-modulus estimation by application of spatially-modulated impulsive acoustic radiation force,” *Ultrasonic Imaging*, vol. 29, no. 2, pp. 87–104, 2007.

[125] S. M. Lee, J. M. Lee, H. J. Kang, H. K. Yang, J. H. Yoon, W. Chang, S. J. An, K. B. Lee, and S. Y. Baek, “Liver fibrosis staging with a new 2D-shear wave elastography using comb-push technique: Applicability, reproducibility, and diagnostic performance,” *PLoS One*, vol. 12, no. 5, Art. no. e0177264, 2017.

[126] H. Zhao, P. Song, M. W. Urban, J. F. Greenleaf, and S. Chen, “Robust shear wave speed measurement using comb-push ultrasound radiation force,” in *IEEE International Ultrasonics Symposium, IUS*, IEEE, 2011, pp. 1270–1273.

[127] S. S. Yengul, P. E. Barbone, and B. Madore, “Application of a forward model of axisymmetric shear wave propagation in viscoelastic media to shear wave elastography,” *The Journal of the Acoustical Society of America*, vol. 143, no. 6, pp. 3266–3277, 2018.

[128] D. Larsson, “Accuracy assessment of shear wave elastography for arterial applications by mechanical testing,” M.S. thesis, KTH Royal Institute of Technology, School of Engineering Science, Stockholm, 2014.

[129] P. Song, H. Zhao, A. Manduca, M. W. Urban, J. F. Greenleaf, and S. Chen, “Comb-push ultrasound shear elastography (CUSE): a novel method for two-dimensional shear elasticity imaging of soft tissues,” *IEEE Transactions on Medical Imaging*, vol. 31, no. 9, pp. 1821–1832, 2012.

[130] J. R. Doherty, G. E. Trahey, K. R. Nightingale, and M. L. Palmeri, “Acoustic radiation force elasticity imaging in diagnostic ultrasound,” *IEEE Transactions on Ultrasonics, Ferroelectrics, and Frequency Control*, vol. 60, no. 4, pp. 685–701, 2013.

[131] M. W. Urban, “Production of acoustic radiation force using ultrasound: methods and applications,” *Expert Review of Medical Devices*, vol. 15, no. 11, pp. 819–834, 2018.

[132] K. J. Parker, J. Ormachea, and Z. Hah, “Group versus phase velocity of shear waves in soft tissues,” *Ultrasonic Imaging*, vol. 40, no. 6, pp. 343–356, 2018.

[133] L. Brillouin, *Wave propagation and group velocity*. Academic Press, 2013, vol. 8.

[134] S. Aubry, J. R. Risson, A. Kastler, B. Barbier-Brion, G. Siliman, M. Runge, and B. Kastler, “Biomechanical properties of the calcaneal tendon in vivo assessed by transient shear wave elastography,” *Skeletal Radiology*, vol. 42, no. 8, pp. 1143–1150, 2013.

[135] S. Sadeghi and D. H. Cortes, “Measurement of the shear modulus in thin-layered tissues using numerical simulations and shear wave elastography,” *Journal of the Mechanical Behavior of Biomedical Materials*, vol. 102, Art. no. 103502, 2020.

[136] M. J. Lowe, “Matrix techniques for modeling ultrasonic waves in multilayered media,” *IEEE Transactions on Ultrasonics, Ferroelectrics, and Frequency Control*, vol. 42, no. 4, pp. 525–542, 1995.

[137] X. Xiang, F. Yan, Y. Yang, Y. Tang, L. Wang, J. Zeng, and L. Qiu, “Quantitative assessment of healthy skin elasticity: reliability and feasibility of shear wave elastography,” *Ultrasound in Medicine and Biology*, vol. 43, no. 2, pp. 445–452, 2017.

[138] C. Payne, P. Watt, and N. Webborn, “Shear wave elastography measures of the Achilles tendon: Influence of time of day, leg dominance and the impact of an acute 30-minute bout of running,” *Applied Sciences*, vol. 8, no. 7, Art. no. 1170, 2018.

[139] E. Maksuti, E. Widman, D. Larsson, M. W. Urban, M. Larsson, and A. Bjällmark, “Arterial stiffness estimation by shear wave elastography: validation in phantoms with mechanical testing,” *Ultrasound in Medicine and Biology*, vol. 42, no. 1, pp. 308–321, 2016.

[140] M. Bernal, I. Nenadic, M. W. Urban, and J. F. Greenleaf, “Material property estimation for tubes and arteries using ultrasound radiation force and analysis of propagating modes,” *The Journal of the Acoustical Society of America*, vol. 129, no. 3, pp. 1344–1354, 2011.

[141] E. Widman, E. Maksuti, D. Larsson, M. W. Urban, A. Bjällmark, and M. Larsson, “Shear wave elastography plaque characterization with mechanical testing validation: a phantom study,” *Physics in Medicine and Biology*, vol. 60, no. 8, pp. 3151–3174, 2015.

[142] C. C. Luo, L. X. Qian, G. Y. Li, Y. Jiang, S. Liang, and Y. Cao, “Determining the in vivo elastic properties of dermis layer of human skin using the supersonic shear imaging technique and inverse analysis,” *Medical Physics*, vol. 42, no. 7, pp. 4106–4115, 2015.

[143] S. Sadeghi, M. Johnson, D. A. Bader, and D. H. Cortes, “Change in shear modulus of healthy lower leg muscles after treadmill running: Toward a noninvasive diagnosis of chronic exertional compartment syndrome,” *Journal of Engineering and Science in Medical Diagnostics and Therapy*, vol. 2, no. 3, Art. no. 031004, 2019.

[144] S. M. H. Ahmadzadeh, X. Chen, H. Hagemann, M. X. Tang, and A. M. J. Bull, “Developing and using fast shear wave elastography to quantify physiologically-relevant tendon forces,” *Medical Engineering and Physics*, vol. 69, pp. 116–122, 2019.

[145] H. Xie, V. Shamdasani, H. Zhao, P. Song, S. Zhou, J. L. Robert, J. Greenleaf, and S. Chen, “A phantom study to cross-validate multimodality shear wave elastography techniques,” in *IEEE International Ultrasonics Symposium*, IEEE, 2012, pp. 1858–1861.

[146] T. Nordenfur, “Comparison of pushing sequences for shear wave elastography,” M.S. thesis, KTH Royal Institute of Technology, Stockholm, 2013.

[147] J. K. Jang, K. Kondo, T. Namita, M. Yamakawa, and T. Shiina, “Comparison of techniques for estimating shear-wave velocity in arterial wall using shear-wave elastography - FEM and phantom study,” in *2015 IEEE International Ultrasonics Symposium, IUS*, Taipei, Taiwan, 2015, pp. 1–4.

[148] R. S. Khalitov, S. N. Gurbatov, and I. Y. Demin, “The use of the Verasonics ultrasound system to measure shear wave velocities in CIRS phantoms,” *Physics of Wave Phenomena*, vol. 24, pp. 73–76, 2016.

[149] R. P. Carbente, J. M. Maia, and A. A. Assef, “Image reconstruction utilizing median filtering applied to elastography,” *BioMedical Engineering Online*, vol. 18, Art. no. 22, 2019.

[150] S. Sadeghi, “Evaluation of muscle function and pathologies using ultrasound shear wave elastography,” Ph.D. dissertation, The Pennsylvania State University, 2019.

[151] X. Zhang, Q. Wang, Z. Lyu, X. Gao, P. Zhang, H. Lin, Y. Guo, T. Wang, S. Chen, and X. Chen, “Noninvasive assessment of age-related stiffness of crystalline lenses in a rabbit model using ultrasound elastography,” *BioMedical Engineering Online*, vol. 17, Art. no. 75, 2018.

[152] S. Sadeghi, M. Johnson, D. A. Bader, and D. H. Cortes, “The shear modulus of lower-leg muscles correlates to intramuscular pressure,” *Journal of Biomechanics*, vol. 83, pp. 190–196, 2019.

[153] S. Sadeghi, C. Newman, and D. H. Cortes, “Change in skeletal muscle stiffness after running competition is dependent on both running distance and recovery time: a pilot study,” *PeerJ*, vol. 6, Art. no. e4469, 2018.

[154] S. Sadeghi, K. Quinlan, K. E. Eilertson, G. G. Billy, J. Bible, J. M. Sions, and D. H. Cortes, “Changes in shear modulus of the lumbar multifidus muscle during different body positions,” *Journal of Biomechanical Engineering*, vol. 141, no. 8, Art. no. 081003, 2019.

[155] S. Sadeghi, J. E. Bible, and D. H. Cortes, “Quantifying dysfunction of the lumbar multifidus muscle after radiofrequency neurotomy and fusion surgery: a preliminary study,” *Journal of Engineering and Science in Medical Diagnostics and Therapy*, vol. 3, no. 4, Art. no. 041001, 2020.

[156] I. Z. Nenadic, M. W. Urban, S. Aristizabal, S. A. Mitchell, T. C. Humphrey, and J. F. Greenleaf, “On Lamb and Rayleigh wave convergence in viscoelastic tissues,” *Physics in Medicine and Biology*, vol. 56, no. 20, pp. 6723–6738, 2011.

[157] M. W. Urban, C. Pislaru, I. Z. Nenadic, R. R. Kinnick, and J. F. Greenleaf, “Measurement of viscoelastic properties of in vivo swine myocardium using lamb wave dispersion ultrasound vibrometry (LDUV),” *IEEE Transactions on Medical Imaging*, vol. 32, no. 2, pp. 247–261, 2013.

[158] T. X. Haen, A. Roux, M. Soubeyrand, and S. Laporte, “Shear waves elastography for assessment of human Achilles tendon’s biomechanical properties: an experimental study,” *Journal of the Mechanical Behavior of Biomedical Materials*, vol. 69, pp. 178–184, 2017.

[159] M. C. A. Brandão, G. C. Teixeira, C. R. C. Fontenelle, A. Fontenelle, L. F. Oliveira, and L. L. Menegaldo, “Correlation between the shear modulus measured by elastography (SSI) and tangent modulus from tensile tests of in vitro fresh-frozen human tendons,” *Journal of Biomechanics*, vol. 160, Art. no. 111826, 2023.

[160] D. Royer, J.-L. Gennisson, T. Deffieux, and M. Tanter, “On the elasticity of transverse isotropic soft tissues (L),” *The Journal of the Acoustical Society of America*, vol. 129, no. 5, pp. 2757–2760, 2011.

[161] C. N. Maganaris and J. P. Paul, “In vivo human tendon mechanical properties,” *The Journal of Physiology*, vol. 521, no. 1, pp. 307–313, 1999.

[162] T. Varghese, M. Bilgen, and J. Ophir, “Multiresolution imaging in elastography,” *IEEE Transactions on Ultrasonics, Ferroelectrics, and Frequency Control*, vol. 45, no. 1, pp. 65–75, 1998.

[163] J.-W. H. Korstanje, R. W. Selles, H. J. Stam, S. E. R. Hovius, and J. G. Bosch, “Dedicated ultrasound speckle tracking to study tendon displacement,” *Medical Imaging 2009: Ultrasonic Imaging and Signal Processing*, vol. 7265, pp. 44–45, 2009.

[164] T. Varghese, “Chapter 8 - Lateral and shear strain imaging for ultrasound elastography,” in *Tissue Elasticity Imaging*, Elsevier, 2020, pp. 167–183.

[165] M. A. Lubinski, S. Y. Emelianov, K. R. Raghavan, A. E. Yagle, A. R. Skovoroda, and M. O’Donnell, “Lateral displacement estimation using tissue incompressibility,” *IEEE Transactions on Ultrasonics, Ferroelectrics, and Frequency Control*, vol. 43, no. 2, pp. 247–256, 1996.

[166] F. Dandois, O. Taylan, J. Bellemans, J. D’Hooge, H. Vandenneucker, L. Slane, and L. Scheys, “Validated ultrasound speckle tracking method for measuring strains of knee collateral ligaments in-situ during varus/valgus loading,” *Sensors*, vol. 21, no. 5, Art. no. 1895, 2021.

[167] E. E. Konofagou, T. Harrigan, and J. Ophir, “Shear strain estimation and lesion mobility assessment in elastography,” *Ultrasonics*, vol. 38, no. 1-8, pp. 400–404, 2000.

[168] H. H. G. Hansen, R. G. P. Lopata, T. Idzenga, and C. L. de Korte, “Full 2D displacement vector and strain tensor estimation for superficial tissue using beam-steered ultrasound imaging,” *Physics in Medicine and Biology*, vol. 55, no. 11, pp. 3201–3218, 2010.

[169] R. Al Mukaddim, N. H. Meshram, and T. Varghese, “Locally optimized correlation-guided Bayesian adaptive regularization for ultrasound strain imaging,” *Physics in Medicine and Biology*, vol. 65, no. 6, Art. no. 065008, 2020.

[170] W.-n. Lee, C. M. Ingrassia, S. D. Fung-kee-fung, K. D. Costa, J. W. Holmes, and E. E. Konofagou, “Theoretical quality assessment of myocardial elastography with in vivo validation,” *IEEE Transactions on Ultrasonics, Ferroelectrics, and Frequency Control*, vol. 54, no. 11, pp. 2233–2245, 2007.

[171] K. Gijsbertse, A. M. Sprengers, M. M. Nillesen, H. H. Hansen, R. G. Lopata, N. Verdonschot, and C. L. de Korte, “Three-dimensional ultrasound strain imaging of skeletal muscles,” *Physics in Medicine and Biology*, vol. 62, no. 2, pp. 596–611, 2017.

[172] H. Chen, H. Shi, and T. Varghese, “Improvement of elastographic displacement estimation using a two-step cross-correlation method,” *Ultrasound in Medicine and Biology*, vol. 33, no. 1, pp. 48–56, 2007.

[173] R. G. Lopata, M. M. Nillesen, H. H. Hansen, I. H. Gerrits, J. M. Thijssen, and C. L. de Korte, “Performance evaluation of methods for two-dimensional displacement and strain estimation using ultrasound radio frequency data,” *Ultrasound in Medicine and Biology*, vol. 35, no. 5, pp. 796–812, 2009.

[174] H. Chen and T. Varghese, “Multilevel hybrid 2D strain imaging algorithm for ultrasound sector/phased arrays,” *Medical Physics*, vol. 36, no. 6, pp. 2098–2106, 2009.

[175] K. F. Kvåle, “Investigation of methods for 2D strain imaging of brain tumors,” M.S. thesis, Norwegian University of Science and Technology, Trondheim, 2014.

[176] M. S. Richards and M. M. Doyley, “Non-rigid image registration based strain estimator for intravascular ultrasound elastography,” *Ultrasound in Medicine and Biology*, vol. 39, no. 3, pp. 515–533, 2013.

[177] R. L. Chimenti, A. S. Flemister, J. Ketz, M. Bucklin, M. R. Buckley, and M. S. Richards, “Ultrasound strain mapping of Achilles tendon compressive strain patterns during dorsiflexion,” *Journal of Biomechanics*, vol. 49, no. 1, pp. 39–44, 2016.

[178] J.-P. Thirion, “Image matching as a diffusion process: an analogy with Maxwell’s demons,” *Medical Image Analysis*, vol. 2, no. 3, pp. 243–260, 1998.

[179] M. McCormick, N. Rubert, and T. Varghese, “Bayesian regularization applied to ultrasound strain imaging,” *IEEE Transactions on Biomedical Engineering*, vol. 58, no. 6, pp. 1612–1620, 2011.

[180] T. M. Mutala, G. N. Mwango, A. Aywak, D. Cioni, and E. Neri, “Determining the elastography strain ratio cut off value for differentiating benign from malignant breast lesions: systematic review and meta-analysis,” *Cancer Imaging*, vol. 22, no. 1, p. 12, 2022.

[181] A. Itoh, E. Ueno, E. Tohno, H. Kamma, H. Takahashi, T. Shiina, M. Yamakawa, and T. Matsumura, “Breast disease: clinical application of US elastography for diagnosis,” *Radiology*, vol. 239, no. 2, pp. 341–350, 2006.

[182] R. G. Barr, K. Nakashima, D. Amy, D. Cosgrove, A. Farrokh, F. Schafer, J. C. Bamber, L. Castera, B. I. Choi, Y. H. Chou, C. F. Dietrich, H. Ding, G. Ferraioli, C. Filice, M. Friedrich-Rust, T. J. Hall, K. R. Nightingale, M. L. Palmeri, T. Shiina, S. Suzuki, I. Sporea, S. Wilson, and M. Kudo, “WFUMB guidelines and recommendations for clinical use of ultrasound elastography: Part 2: Breast,” *Ultrasound in Medicine and Biology*, vol. 41, no. 5, pp. 1148–1160, 2015.

[183] G. Ferraioli, C. Filice, L. Castera, B. I. Choi, I. Sporea, S. R. Wilson, D. Cosgrove, C. F. Dietrich, D. Amy, J. C. Bamber, R. Barr, Y. H. Chou, H. Ding, A. Farrokh, M. Friedrich-Rust, T. J. Hall, K. Nakashima, K. R. Nightingale, M. L. Palmeri, F. Schafer, T. Shiina, S. Suzuki, and M. Kudo, “WFUMB guidelines and recommendations for clinical use of ultrasound elastography: Part 3: Liver,” *Ultrasound in Medicine and Biology*, vol. 41, no. 5, pp. 1161–1179, 2015.

[184] K. Tajiri, K. Kawai, and T. Sugiyama, “Strain elastography for assessment of liver fibrosis and prognosis in patients with chronic liver diseases,” *Journal of Gastroenterology*, vol. 52, no. 6, pp. 724–733, 2017.

[185] J. Jiang and T. J. Hall, “A generalized speckle tracking algorithm for ultrasonic strain imaging using dynamic programming,” *Ultrasound in Medicine and Biology*, vol. 35, no. 11, pp. 1863–1879, 2009.

[186] D. Cosgrove, R. Barr, J. Bojunga, V. Cantisani, M. C. Chammas, M. Dighe, S. Vinayak, J. M. Xu, and C. F. Dietrich, “WFUMB guidelines and recommendations on the clinical use of ultrasound elastography: part 4. Thyroid,” *Ultrasound in Medicine and Biology*, vol. 43, no. 1, pp. 4–26, 2017.

[187] R. G. Barr, D. Cosgrove, M. Brock, V. Cantisani, J. M. Correas, A. W. Postema, G. Salomon, M. Tsutsumi, H. X. Xu, and C. F. Dietrich, “WFUMB guidelines and recommendations on the clinical use of ultrasound elastography: Part 5. Prostate,” *Ultrasound in Medicine and Biology*, vol. 43, no. 1, pp. 27–48, 2017.

[188] J. R. Franz, L. C. Slane, K. Rasske, and D. G. Thelen, “Non-uniform in vivo deformations of the human Achilles tendon during walking,” *Gait and Posture*, vol. 41, no. 1, pp. 192–197, 2015.

[189] R. L. Chimenti, M. Bucklin, M. Kelly, J. Ketz, A. S. Flemister, M. S. Richards, and M. R. Buckley, “Insertional achilles tendinopathy associated with altered transverse compressive and axial tensile strain during ankle dorsiflexion,” *Journal of Orthopaedic Research*, vol. 35, no. 4, pp. 910–915, 2017.

[190] S. Bogaerts, C. De Brito Carvalho, L. Scheys, K. Desloovere, J. D’Hooge, F. Maes, P. Suetens, and K. Peers, “Evaluation of tissue displacement and regional strain in the Achilles tendon using quantitative high-frequency ultrasound,” *PLoS One*, vol. 12, no. 7, Art. no. e0181364, 2017.

[191] W. H. Clark and J. R. Franz, “Do triceps surae muscle dynamics govern non-uniform Achilles tendon deformations?” *PeerJ*, vol. 6, Art. no. e5182, 2018.

[192] L. Stenroth, D. Thelen, and J. Franz, “Biplanar ultrasound investigation of in vivo Achilles tendon displacement non-uniformity,” *Translational Sports Medicine*, vol. 2, no. 2, pp. 73–81, 2019.

[193] N. L. Lehr, W. H. Clark, M. D. Lewek, and J. R. Franz, “The effects of triceps surae muscle stimulation on localized Achilles subtendon tissue displacements,” *Journal of Experimental Biology*, vol. 224, no. 15, Art. no. jeb242135, 2021.

[194] A. N. Aggouras, R. L. Chimenti, A. Samuel Flemister, J. Ketz, L. C. Slane, M. R. Buckley, and M. S. Richards, “Impingement in insertional Achilles tendinopathy occurs across a larger range of ankle angles and is associated with increased tendon thickness,” *Foot and Ankle International*, vol. 43, no. 5, pp. 683–693, 2022.

[195] K. E. Mora, S. J. Mlawer, A. J. Bae, M. S. Richards, A. E. Loiselle, and M. R. Buckley, “Ultrasound strain mapping of the mouse Achilles tendon during passive dorsiflexion,” *Journal of Biomechanics*, vol. 132, Art. no. 110920, 2022.

[196] J. Farron, T. Varghese, and D. G. Thelen, “Measurement of tendon strain during muscle twitch contractions using ultrasound elastography,” *IEEE Transactions on Ultrasonics, Ferroelectrics, and Frequency Control*, vol. 56, no. 1, pp. 27–35, 2009.

[197] J.-W. H. Korstanje, R. W. Selles, H. J. Stam, S. E. Hovius, and J. G. Bosch, “Development and validation of ultrasound speckle tracking to quantify tendon displacement,” *Journal of Biomechanics*, vol. 43, no. 7, pp. 1373–1379, 2010.

[198] L. A. Chernak and D. G. Thelen, “Tendon motion and strain patterns evaluated with two-dimensional ultrasound elastography,” *Journal of Biomechanics*, vol. 45, no. 15, pp. 2618–2623, 2012.

[199] L. C. Slane and D. G. Thelen, “Non-uniform displacements within the Achilles tendon observed during passive and eccentric loading,” *Journal of Biomechanics*, vol. 47, no. 12, pp. 2831–2835, 2014.

[200] L. C. Slane, F. Dandois, S. Bogaerts, H. Vandenneucker, and L. Scheys, “Non-uniformity in the healthy patellar tendon is greater in males and similar in different age groups,” *Journal of Biomechanics*, vol. 80, pp. 16–22, 2018.

[201] L. C. Slane, S. Bogaerts, D. G. Thelen, and L. Scheys, “Nonuniform deformation of the patellar tendon during passive knee flexion,” *Journal of Applied Biomechanics*, vol. 34, no. 1, pp. 14–22, 2018.

[202] V. J. M. M. Schrier, S. Evers, J. G. Bosch, R. W. Selles, and P. C. Amadio, “Reliability of ultrasound speckle tracking with singular value decomposition for quantifying displacement in the carpal tunnel,” *Journal of Biomechanics*, vol. 85, pp. 141–147, 2019.

[203] Å. Fröberg, M. Mårtensson, M. Larsson, B. Janerot-Sjöberg, J. D’Hooge, and A. Arndt, “High variability in strain estimation errors when using a commercial ultrasound speckle tracking algorithm on tendon tissue,” *Acta Radiologica*, vol. 57, no. 10, pp. 1223–1229, 2016.

[204] R. B. Svensson, L. C. Slane, S. P. Magnusson, and S. Bogaerts, “Ultrasound-based speckle-tracking in tendons: a critical analysis for the technician and the clinician,” *Journal of Applied Physiology*, vol. 130, no. 2, pp. 445–456, 2021.

[205] S. Chen, M. Fatemi, and J. F. Greenleaf, “Quantifying elasticity and viscosity from measurement of shear wave speed dispersion,” *The Journal of the Acoustical Society of America*, vol. 115, no. 6, pp. 2781–2785, 2004.

[206] Y.-C. Fung, *Biomechanics: mechanical properties of living tissues*. New York, NY: Springer, 1993.

[207] J. H. Langdon, E. Elegbe, and S. A. McAleavey, “Single tracking location acoustic radiation force impulse viscoelasticity estimation (STL-VE): A method for measuring tissue viscoelastic parameters,” *IEEE Transactions on Ultrasonics, Ferroelectrics, and Frequency Control*, vol. 62, no. 7, pp. 1225–1244, 2015.

[208] N. Salameh, F. Peeters, R. Sinkus, J. Abarca-Quinones, L. Annet, L. C. Ter Beek, I. Leclercq, and B. E. Van Beers, “Hepatic viscoelastic parameters measured with MR elastography: correlations with quantitative analysis of liver fibrosis in the rat,” *Journal of Magnetic Resonance Imaging*, vol. 26, no. 4, pp. 956–962, 2007.

[209] L. Huwart, F. Peeters, R. Sinkus, L. Annet, N. Salameh, L. C. ter Beek, Y. Horsmans, and B. E. Van Beers, “Liver fibrosis: non-invasive assessment with MR elastography,” *NMR in Biomedicine*, vol. 19, no. 2, pp. 173–179, 2006.

[210] C. T. Barry, B. Mills, Z. Hah, R. A. Mooney, C. K. Ryan, D. J. Rubens, and K. J. Parker, “Shear wave dispersion measures liver steatosis,” *Ultrasound in Medicine and Biology*, vol. 38, no. 2, pp. 175–182, 2012.

[211] P. Garteiser, S. Doblas, J. L. Daire, M. Wagner, H. Leitao, V. Vilgrain, R. Sinkus, and B. E. Van Beers, “MR elastography of liver tumours: value of viscoelastic properties for tumour characterisation,” *European Radiology*, vol. 22, no. 10, pp. 2169–2177, 2012.

[212] M. Tanter, D. Touboul, J. L. Gennisson, J. Bercoff, and M. Fink, “High-resolution quantitative imaging of cornea elasticity using supersonic shear imaging,” *IEEE Transactions on Medical Imaging*, vol. 28, no. 12, pp. 1881–1893, 2009.

[213] T. M. Nguyen, J. F. Aubry, M. Fink, J. Bercoff, and M. Tanter, “In vivo evidence of porcine cornea anisotropy using supersonic shear wave imaging,” *Investigative Ophthalmology and Visual Science*, vol. 55, no. 11, pp. 7545–7552, 2014.

[214] J. Ormachea, K. J. Parker, and R. G. Barr, “An initial study of complete 2D shear wave dispersion images using a reverberant shear wave field,” *Physics in Medicine and Biology*, vol. 64, no. 14, Art. no. 145009, 2019.

[215] M. Bayat, S. Adabi, V. Kumar, A. Gregory, J. Webb, M. Denis, B. Kim, A. Singh, L. Mynderse, D. Husmann, A. Alizad, and M. Fatemi, “Acoustoelasticity analysis of transient waves for non-invasive in vivo assessment of urinary bladder,” *Scientific Reports*, vol. 9, no. 1, Art. no. 2441, 2019.

[216] Q. He, G. Y. Li, F. F. Lee, Q. Zhang, Y. Cao, and J. Luo, “Novel method for vessel cross-sectional shear wave imaging,” *Ultrasound in Medicine and Biology*, vol. 43, no. 7, pp. 1520–1532, 2017.

[217] H. Xu, J. Q. Mo, S. Chen, K. N. An, and Z. P. Luo, “Elasticity measurements by shear wave elastography: Comparison and selection of shear wave, rayleigh wave and Lamb Wave theory,” *Journal of Mechanics in Medicine and Biology*, vol. 18, no. 1, Art. no. 1750119, 2018.

[218] The Safety Group of the British Medical Ultrasound Society, “Guidelines for the safe use of diagnostic ultrasound equipment,” *Ultrasound*, vol. 18, no. 2, pp. 52–59, 2010.

[219] US Food and Drug Administration, *Marketing clearance of diagnostic ultrasound systems and transducers: Guidance for industry and Food and Drug Administration staff*. Silver Spring, MD: Center for Devices and Radiological Health, 2019.

[220] T. Loupas, J. T. Powers, and R. W. Gill, “An axial velocity estimator for ultrasound blood flow imaging, based on a full evaluation of the Doppler equation by means of a two-dimensional autocorrelation approach,” *IEEE Transactions on Ultrasonics, Ferroelectrics, and Frequency Control*, vol. 42, no. 4, pp. 672–688, 1995.

[221] S. L. Lipman, N. C. Rouze, M. L. Palmeri, and K. R. Nightingale, “Evaluating the improvement in shear wave speed image quality using multidimensional directional filters in the presence of reflection artifacts,” *IEEE Transactions on Ultrasonics, Ferroelectrics, and Frequency Control*, vol. 63, no. 8, pp. 1049–1063, 2016.

[222] R. C. Gonzalez and R. E. Woods, *Digital image processing*, 3rd ed. Pearson International, 2008.

[223] K. Brown, K. Streit, L. Hoban, and R. Gaddi, *2D Frequency Domain Filtering and the 2D DFT*. [Online]. Available: `https://www.clear.rice.edu/elec301/Projects01/image_filt/filter.html`.

[224] B. R. Chintada, R. Rau, and O. Goksel, “Nonlinear characterization of tissue viscoelasticity with acoustoelastic attenuation of shear waves,” *IEEE Transactions on Ultrasonics, Ferroelectrics, and Frequency Control*, vol. 69, no. 1, pp. 38–53, 2022.

[225] F. C. Meral, T. J. Royston, and R. L. Magin, “Rayleigh-Lamb wave propagation on a fractional order viscoelastic plate,” *The Journal of the Acoustical Society of America*, vol. 129, no. 2, pp. 1036–1045, 2011.

[226] P. H. S. Torr and A. Zisserman, “MLESAC: A new robust estimator with application to estimating image geometry,” *Computer Vision and Image Understanding*, vol. 78, no. 1, pp. 138–156, 2000.

[227] S. Rabinowitz, “How to find the square root of a complex number,” *Mathematics and Informatics Quarterly*, vol. 3, pp. 54–56, 1993.

[228] X. Sun, X. Ding, F. Li, S. Zhou, Y. Liu, N. Hu, Z. Su, Y. Zhao, J. Zhang, and M. Deng, “Interaction of Lamb wave modes with weak material nonlinearity: Generation of symmetric zero-frequency mode,” *Sensors*, vol. 18, no. 8, Art. no. 2451, 2018.

[229] M. Šofer, P. Ferfecki, and P. Šofer, “Numerical solution of Rayleigh-Lamb frequency equation for real, imaginary and complex wavenumbers,” in *MATEC Web of Conferences*, vol. 157, EDP Sciences, 2018, Art. no. 08011.

[230] M. H. Wang, M. L. Palmeri, V. M. Rotemberg, N. C. Rouze, and K. R. Nightingale, “Improving the robustness of time-of-flight based shear wave speed reconstruction methods using RANSAC in human liver in vivo,” *Ultrasound in Medicine and Biology*, vol. 36, no. 5, pp. 802–813, 2010.

[231] I. M. Kuder, M. Rock, G. G. Jones, A. A. Amis, F. B. Cegla, and R. J. van Arkel, “An optimization approach for creating application-specific ultrasound speckle tracking algorithms,” *Ultrasound in Medicine and Biology*, vol. 50, no. 8, pp. 1108–1121, 2024.

[232] S. Sitia, L. Tomasoni, and M. Turiel, “Speckle tracking echocardiography: A new approach to myocardial function,” *World Journal of Cardiology*, vol. 2, no. 1, pp. 1–5, 2010.

[233] P. Joos, J. Porée, H. Liebgott, D. Vray, M. Baudet, J. Faurie, F. Tournoux, G. Cloutier, B. Nicolas, and D. Garcia, “High-frame-rate speckle-tracking echocardiography,” *IEEE Transactions on Ultrasonics, Ferroelectrics, and Frequency Control*, vol. 65, no. 5, pp. 720–728, 2018.

[234] M. Orlowska, A. Ramalli, A. Petrescu, M. Cvijic, S. Bezy, P. Santos, J. Pedrosa, J. U. Voigt, and J. D’Hooge, “A novel 2-D speckle tracking method for high-frame-rate echocardiography,” *IEEE Transactions on Ultrasonics, Ferroelectrics, and Frequency Control*, vol. 67, no. 9, pp. 1764–1775, 2020.

[235] Å. Fröberg, A. S. Cissé, M. Larsson, M. Mårtensson, M. Peolsson, T. Movin, and A. Arndt, “Altered patterns of displacement within the Achilles tendon following surgical repair,” *Knee Surgery, Sports Traumatology, Arthroscopy*, vol. 25, no. 6, pp. 1857–1865, 2017.

[236] R. S. Bandaru, S. Evers, R. W. Selles, A. R. Thoreson, P. C. Amadio, S. E. Hovius, and J. G. Bosch, “Speckle tracking of tendon displacement in the carpal tunnel: improved quantification using singular value decomposition,” *IEEE Journal of Biomedical and Health Informatics*, vol. 23, no. 2, pp. 817–824, 2019.

[237] B. Cruz Perez, E. Pavlatos, H. J. Morris, H. Chen, X. Pan, R. T. Hart, and J. Liu, “Mapping 3D strains with ultrasound speckle tracking: method validation and initial results in porcine scleral inflation,” *Annals of Biomedical Engineering*, vol. 44, no. 7, pp. 2302–2312, 2016.

[238] A. Arndt, A. S. Bengtsson, M. Peolsson, A. Thorstensson, and T. Movin, “Non-uniform displacement within the Achilles tendon during passive ankle joint motion,” *Knee Surgery, Sports Traumatology, Arthroscopy*, vol. 20, no. 9, pp. 1868–1874, 2012.

[239] E. Kelly, R. Ellis, and W. Hing, “Ultrasound assessment of extensor pollicis brevis tendon excursion in different wrist positions in healthy people,” *Journal of Hand Therapy*, vol. 32, no. 3, pp. 375–381, 2019.

[240] P. Brown, J. Alsousou, M. Thompson, and A. Noble, “Controlled motion strain measurement using lateral speckle tracking in Achilles tendons during healing,” in *9th IEEE International Symposium on Biomedical Imaging (ISBI)*, IEEE, 2012, pp. 1104–1107.

[241] U. Techavipoo, Q. Chen, T. Varghese, and J. A. Zagzebski, “Estimation of displacement vectors and strain tensors in elastography using angular insonifications,” *IEEE Transactions on Medical Imaging*, vol. 23, no. 12, pp. 1479–1489, 2004.

[242] S. Bogaerts, C. De Brito Carvalho, A. De Groef, P. Suetens, and K. Peers, “Non-uniformity in pre-insertional Achilles tendon is not influenced by changing knee angle during isometric contractions,” *Scandinavian Journal of Medicine and Science in Sports*, vol. 28, no. 11, pp. 2322–2329, 2018.

[243] V. J. M. M. Schrier, S. Evers, J. R. Geske, W. K. Kremers, H. R. Villarraga, R. W. Selles, S. E. R. Hovius, R. Gelfman, and P. C. Amadio, “Relative motion of the connective tissue in carpal tunnel syndrome: the relation with disease severity and clinical outcome,” *Ultrasound in Medicine and Biology*, vol. 46, no. 9, pp. 2236–2244, 2020.

[244] T. Zakaria, Z. Qin, and R. L. Maurice, “Optical-flow-based B-mode elastography: application in the hypertensive rat carotid,” *IEEE Transactions on Medical Imaging*, vol. 29, no. 2, pp. 570–578, 2010.

[245] R. Z. Azar, O. Goksel, and S. E. Salcudean, “Sub-sample displacement estimation from digitized ultrasound RF signals using multi-dimensional polynomial fitting of the cross-correlation function,” *IEEE Transactions on Ultrasonics, Ferroelectrics, and Frequency Control*, vol. 57, no. 11, pp. 2403–2420, 2010.

[246] H. Shi and T. Varghese, “Two-dimensional multi-level strain estimation for discontinuous tissue,” *Physics in Medicine and Biology*, vol. 52, no. 2, pp. 389–401, 2007.

[247] B. McGinty, *Continuum Mechanics*, 2012. [Online]. Available: `https://www.continuummechanics.org`.

[248] M. W. Miller and M. C. Ziskin, “Biological consequences of hyperthermia,” *Ultrasound in Medicine and Biology*, vol. 15, no. 8, pp. 707–722, 1989.

[249] T. Marhenke, S. J. Sanabria, B. R. Chintada, R. Furrer, J. Neuenschwander, and O. Goksel, “Acoustic field characterization of medical array transducers based on unfocused transmits and single-plane hydrophone measurements,” *Sensors*, vol. 19, no. 4, Art. no. 863, 2019.

[250] International Electrotechnical Commission, *IEC 62359: Ultrasonics - Field characterization - Test methods for the determination of thermal and mechanical indices related to medical diagnostic ultrasonic fields*. Switzerland: International Electrotechnical Commission, 2005.

[251] N. Phipps, “Acoustic intensity measurement system: Application in localized drug delivery,” M.S. thesis, San Jose State University, San Jose, 2010.

[252] International Electrotechnical Commission, *IEC 62127: Ultrasonics - Hydrophones, Part 1: Measurement and characterization of medical ultrasonic fields up to 40 MHz*. Switzerland: International Electrotechnical Commission, 2007.

[253] R. B. Thompson and E. F. Lopes, “The effects of focusing and refraction on Gaussian ultrasonic beams,” *Journal of Nondestructive Evaluation*, vol. 4, no. 2, pp. 107–123, 1984.

[254] P. Jiang, “Application Note. MI Data - L11-5v HIQ Scripts,” Verasonics Inc., Kirkland, Tech. Rep., 2019.

[255] P. Kijanka and M. W. Urban, “Local phase velocity based imaging of viscoelastic phantoms and tissues,” *IEEE Transactions on Ultrasonics, Ferroelectrics, and Frequency Control*, vol. 68, no. 3, pp. 389–405, 2021.

[256] M. M. Karzova, P. V. Yuldashev, O. A. Sapozhnikov, V. A. Khokhlova, B. W. Cunitz, W. Kreider, and M. R. Bailey, “Shock formation and nonlinear saturation effects in the ultrasound field of a diagnostic curvilinear probe,” *The Journal of the Acoustical Society of America*, vol. 141, no. 4, pp. 2327–2337, 2017.

[257] H. L. Birch, C. T. Thorpe, and A. P. Rumian, “Specialisation of extracellular matrix for function in tendons and ligaments,” *Muscles, Ligaments and Tendons*, vol. 3, no. 1, pp. 12–22, 2013.

[258] L. C. Slane, J. Martin, R. DeWall, D. Thelen, and K. Lee, “Quantitative ultrasound mapping of regional variations in shear wave speeds of the aging Achilles tendon,” *European Radiology*, vol. 27, no. 2, pp. 474–482, 2017.

[259] B. Frankewycz, L. Henssler, J. Weber, N. P. B. da Silva, M. Koch, E. M. Jung, D. Docheva, V. Alt, and C. G. Pfeifer, “Changes of material elastic properties during healing of ruptured Achilles tendons measured with shear wave elastography: a pilot study,” *International Journal of Molecular Sciences*, vol. 21, no. 10, Art. no. 3427, 2020.

[260] B. K. Coombes, K. Tucker, B. Vicenzino, V. Vuvan, R. Mellor, L. Heales, A. Nordez, and F. Hug, “Achilles and patellar tendinopathy display opposite changes in elastic properties: A shear wave elastography study,” *Scandinavian Journal of Medicine and Science in Sports*, vol. 28, no. 3, pp. 1201–1208, 2018.

[261] T. Dirrichs, V. Quack, M. Gatz, M. Tingart, C. K. Kuhl, and S. Schrading, “Shear wave elastography (SWE) for the evaluation of patients with tendinopathies,” *Academic Radiology*, vol. 23, no. 10, pp. 1204–1213, 2016.

[262] T. Dirrichs, S. Schrading, M. Gatz, M. Tingart, C. K. Kuhl, and V. Quack, “Shear wave elastography (SWE) of asymptomatic achilles tendons: a comparison between semiprofessional athletes and the nonathletic general population,” *Academic Radiology*, vol. 26, no. 10, pp. 1345–1351, 2019.

[263] F. M. Gonzalez, C. A. Gleason, K. S. Lee, S. A. Labid, L. N. Nazarian, W. B. Morrison, and D. A. Reiter, “Shear wave elastography assessment and comparison study of the Achilles tendons in optimally conditioned asymptomatic young collegiate athletes,” *Skeletal Radiology*, vol. 50, no. 12, pp. 2381–2392, 2021.

[264] L. N. Zhang, W. B. Wan, Y. X. Wang, Z. Y. Jiao, L. H. Zhang, Y. K. Luo, and P. F. Tang, “Evaluation of elastic stiffness in healing Achilles tendon after surgical repair of a tendon rupture using in vivo ultrasound shear wave elastography,” *Medical Science Monitor*, vol. 22, pp. 1186–1191, 2016.

[265] M. Earle, G. De Portu, and E. DeVos, “Agar ultrasound phantoms for low-cost training without refrigeration,” *African Journal of Emergency Medicine*, vol. 6, no. 1, pp. 18–23, 2016.

[266] G. Lionello, C. Sirieix, and M. Baleani, “An effective procedure to create a speckle pattern on biological soft tissue for digital image correlation measurements,” *Journal of the Mechanical Behavior of Biomedical Materials*, vol. 39, pp. 1–8, 2014.

[267] T. Luyckx, M. Verstraete, K. De Roo, W. De Waele, J. Bellemans, and J. Victor, “Digital image correlation as a tool for three-dimensional strain analysis in human tendon tissue,” *Journal of Experimental Orthopaedics*, vol. 1, no. 1, p. 7, 2014.

[268] P. G. Brown, J. Alsousou, A. Cooper, M. S. Thompson, and J. A. Noble, “The AutoQual ultrasound elastography method for quantitative assessment of lateral strain in post-rupture Achilles tendons,” *Journal of Biomechanics*, vol. 46, no. 15, pp. 2695–2700, 2013.

[269] World Medical Association, “World Medical Association Declaration of Helsinki. Ethical principles for medical research involving human subjects,” *Bulletin of the World Health Organization*, vol. 79, no. 4, p. 373, 2001.

[270] A. J. Garner, O. W. Dandridge, A. A. Amis, J. P. Cobb, and R. J. van Arkel, “Partial and combined partial knee arthroplasty: greater anterior-posterior stability than posterior cruciate–retaining total knee arthroplasty,” *Journal of Arthroplasty*, vol. 36, no. 11, pp. 3765–3772, 2021.

[271] E. S. Grood and W. J. Suntay, “A joint coordinate system for the clinical description of three-dimensional motions: application to the knee,” *Journal of Biomechanical Engineering*, vol. 105, no. 2, pp. 136–144, 1983.

[272] O. Dandridge, A. Garner, A. A. Amis, J. P. Cobb, and R. J. van Arkel, “Variation in the patellar tendon moment arm identified with an improved measurement framework,” *Journal of Orthopaedic Research*, vol. 40, no. 4, pp. 799–807, 2022.

[273] M. Couade, M. Pernot, C. Prada, E. Messas, J. Emmerich, P. Bruneval, A. Criton, M. Fink, and M. Tanter, “Quantitative Assessment of Arterial Wall Biomechanical Properties Using Shear Wave Imaging,” *Ultrasound in Medicine & Biology*, vol. 36, no. 10, pp. 1662–1676, 2010.

[274] O. A. E. Salden, W. M. van Everdingen, R. Spee, P. A. Doevendans, and M. J. Cramer, “How I do it: feasibility of a new ultrasound probe fixator to facilitate high quality stress echocardiography,” *Cardiovascular Ultrasound*, vol. 16, no. 1, p. 6, 2018.

[275] L. Li, L. Zhao, R. Hassan, and H. Ren, “Review on wearable system for positioning ultrasound scanner,” *Machines*, vol. 11, no. 3, p. 325, 2023.

[276] B. Chakraborty, Z. Liu, B. Heyde, J. Luo, and J. D’Hooge, “2-D myocardial deformation imaging based on RF-based nonrigid image registration,” *IEEE Transactions on Ultrasonics, Ferroelectrics, and Frequency Control*, vol. 65, no. 6, pp. 1037–1047, 2018.

[277] B. Heyde, R. Jasaityte, D. Barbosa, V. Robesyn, S. Bouchez, P. Wouters, F. Maes, P. Claus, and J. D’Hooge, “Elastic image registration versus speckle tracking for 2-D myocardial motion estimation: a direct comparison in vivo,” *IEEE Transactions on Medical Imaging*, vol. 32, no. 2, pp. 449–459, 2012.

[278] B. A. Walther and J. L. Moore, “The concepts of bias, precision and accuracy, and their use in testing the performance of species richness estimators, with a literature review of estimator performance,” *Ecography*, vol. 28, no. 6, pp. 815–829, 2005.

[279] N. Azarmehr, X. Ye, J. D. Howes, B. Docking, J. P. Howard, D. P. Francis, and M. Zolgharni, “An optimisation-based iterative approach for speckle tracking echocardiography,” *Medical and Biological Engineering and Computing*, vol. 58, pp. 1309–1323, 2020.

[280] X. Hu, Z. Xie, and F. Liu, “Assessment of speckle pattern quality in digital image correlation from the perspective of mean bias error,” *Measurement*, vol. 173, Art. no. 108618, 2021.

[281] L. Al Saikhan, C. Park, T. Tillin, G. Lloyd, J. Mayet, N. Chaturvedi, and A. Hughes, “Relationship between image quality and bias in 3D echocardiographic measures: data from the SABRE (southall and brent revisited) study,” *Journal of the American Heart Association*, vol. 11, no. 9, Art. no. e019183, 2022.

[282] K. M. Ghosh, A. M. Merican, F. Iranpour, D. J. Deehan, and A. A. Amis, “Length-change patterns of the collateral ligaments after total knee arthroplasty,” *Knee Surgery, Sports Traumatology, Arthroscopy*, vol. 20, pp. 1349–1356, 2012.

[283] S. Kim, S. R. Aglyamov, S. Park, M. O’Donnell, and S. Y. Emelianov, “An autocorrelation-based method for improvement of sub-pixel displacement estimation in ultrasound strain imaging,” *IEEE Transactions on Ultrasonics, Ferroelectrics, and Frequency Control*, vol. 58, no. 4, pp. 838–843, 2011.

[284] M. Majewski, H. Susanne, and S. Klaus, “Epidemiology of athletic knee injuries: A 10-year study,” *Knee*, vol. 13, no. 3, pp. 184–188, 2006.

[285] D. Gair and Secondary Care Analytical Team, “Hospital Accident & Emergency Activity 2020-21,” NHS Digital, Tech. Rep., 2021.

[286] J. R. Landis and G. G. Koch, “The Measurement of Observer Agreement for Categorical Data,” Tech. Rep. 1, 1977, pp. 159–174.

[287] T. K. Koo and M. Y. Li, “A Guideline of Selecting and Reporting Intraclass Correlation Coefficients for Reliability Research,” *Journal of Chiropractic Medicine*, vol. 15, no. 2, pp. 155–163, 2016.

[288] Y. Rolland, M. Verin, C. A. Payan, S. Duchesne, E. Kraft, T. K. Hauser, J. Jarosz, N. Deasy, L. Defevbre, C. Delmaire, D. Dormont, A. C. Ludolph, G. Bensimon, and P. N. Leigh, “A new MRI rating scale for progressive supranuclear palsy and multiple system atrophy: validity and reliability,” *Journal of Neurology, Neurosurgery & Psychiatry*, vol. 82, no. 9, pp. 1025–1032, 2011.

[289] Q. Huang and Z. Zeng, “A Review on Real-Time 3D Ultrasound Imaging Technology,” *BioMed Research International*, vol. 2017, 2017.

10

Appendices

A ICREC letter of favourable opinion for the study with healthy volunteers **272**

B REC letter of favourable opinion for the clinical study **273**

C HRA letter of approval for the clinical study **280**

Appendix A: ICREC letter of favourable opinion for the study with healthy volunteers

Imperial College London

Imperial College Research Ethics Committee
Imperial College London
Room 221
Medical School Building
St Marys Campus
London
W2 1PG
Tel: +44 (0)207 594 1862

researchethicscommittee@imperial.ac.uk

28 April 2022

Dear Dr Richard van Arkel

Study Title: Ultrasonic Techniques for In Vivo Measurement of Collateral Ligament Function

ICREC reference number: 22IC7520

The above study was reviewed by the Imperial College Research Ethics Committee on 12/04/22.

This study was given a favourable opinion subject to revisions reviewed by the Research Governance and Integrity Team (RGIT). Following the review of your revised documents submitted on the 27/04/2022, the RGIT would like to grant full RGIT approval to the study on the basis described in the revised documents:

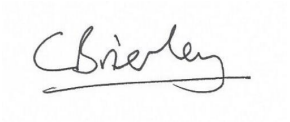
Documents
The documents reviewed were:

- Application (v2.2 27/04/2022)
- Consent (v2.2 27/04/2022)
- Participant information sheet (v2.2 27/04/2022)
- Protocol (v2.2 27/04/2022)
- Questionnaire (v2.2 27/04/2022)
- Recruitment Email (v2 27/04/2022)
- Recruitment Slide
- Verasonics Risk Analysis (29/05/2018)
- Verasonics Safety Guidelines for Imaging Human Subjects (v2.8 9/07/2014)

Membership of the Committee

The members of the Ethics Committee who reviewed the study were:
Shona Blair
Diana Varaden
Jennifer Wallis
Ruth Nicholson
Simon Noyce
Biddy Passmore
Sungano Chigogora

Yours sincerely,



Appendix B: REC letter of favourable opinion for the clinical study

Health Research Authority

West Midlands - Black Country Research Ethics Committee
2 Redman Place
Stratford
London
E20 1JQ

Telephone: 0207 104 8388

Please note: This is the favourable opinion of the REC only and does not allow you to start your study at NHS sites in England until you receive HRA Approval

13 July 2023

Mr Gareth G Jones
Department of Surgery and Cancer
2nd Floor, Sir Michael Uren Hub, Imperial College London
86 Wood Lane, London
W12 0BZ

Dear Mr Jones

Study title:	**In Vivo measurement of MCL strain pre and post knee arthroplasty using ultrasound.**
REC reference:	**23/WM/0162**
Protocol number:	**23CX8281**
IRAS project ID:	**323566**

The Proportionate Review Sub-committee of the West Midlands - Black Country Research Ethics Committee reviewed the above application on 11 July 2023.

Ethical opinion

On behalf of the Research Ethics Committee (REC), the sub-committee gave a favourable ethical opinion of the above research on the basis described in the application form, protocol and supporting documentation, subject to the conditions specified below.

Health Research Authority

Good practice principles and responsibilities

The UK Policy Framework for Health and Social Care Research sets out principles of good practice in the management and conduct of health and social care research. It also outlines the responsibilities of individuals and organisations, including those related to the four elements of research transparency:

1. registering research studies
2. reporting results
3. informing participants
4. sharing study data and tissue

Conditions of the favourable opinion

The REC favourable opinion is subject to the following conditions being met prior to the start of the study.

Number	Conditions
1.	Please provide clarification on whether the post-operative (6wks and 6 months) will be part of routine care. If it is not, please amend last section on page 2 of the PIS to clarify to the patients.
2.	The following changes should be made to the information sheet: a) Information regarding excluding people who were involved in any other clinical study in the last 4 months should be clearly defined in the protocol and/or PIS. b) Please confirm if email facility to return the consent form is possible. If yes, add this information where relevant (e.g. protocol and the PIS). c) Please make it clear if the research has no effect on the patient's overall care i.e., will not influence treatment decisions on the first page. d) Information regarding Governance section was confusing as it seems to imply that if needed will transfer patient identifiable information to other researchers and internationally. Please reword this section to make it clearer for the reader. e) Please add a telephone contact number in addition to the email address of the CI for any complaints. f) Include PALS in the complaints section and in the section on "what if something goes wrong".

Health Research Authority

	g) Explain clearly what incidental findings there might be and include these in the information sheet. h) Remove "I" in the following sentence of the PIS – "Where can I you find out more about how your information is used".
3.	The following changes should be made to the consent form: a) Please amend or remove the term 'gift' in item 6 of the consent form as the participants data is not a gift to Imperial College as such i.e. usage will still be subject to research data related restrictions.

You should notify the REC once all conditions have been met (except for site approvals from host organisations) and provide copies of any revised documentation with updated version numbers. Revised documents should be submitted to the REC electronically from IRAS. The REC will acknowledge receipt and provide a final list of the approved documentation for the study, which you can make available to host organisations to facilitate their permission for the study. Failure to provide the final versions to the REC may cause delay in obtaining permissions.

Confirmation of Capacity and Capability (in England, Northern Ireland and Wales) or NHS management permission (in Scotland) should be sought from all NHS organisations involved in the study in accordance with NHS research governance arrangements. Each NHS organisation must confirm through the signing of agreements and/or other documents that it has given permission for the research to proceed (except where explicitly specified otherwise).

Guidance on applying for HRA and HCRW Approval (England and Wales)/ NHS permission for research is available in the Integrated Research Application System.

For non-NHS sites, site management permission should be obtained in accordance with the procedures of the relevant host organisation.

Sponsors are not required to notify the Committee of management permissions from host organisations.

Registration of Clinical Trials

All research should be registered in a publicly accessible database and we expect all researchers, research sponsors and others to meet this fundamental best practice standard.

It is a condition of the REC favourable opinion that **all clinical trials are registered** on a publicly accessible database within six weeks of recruiting the first research participant. For this purpose, 'clinical trials' are defined as:

- clinical trial of an investigational medicinal product
- clinical investigation or other study of a medical device
- combined trial of an investigational medicinal product and an investigational medical device

Health Research Authority

- other clinical trial to study a novel intervention or randomised clinical trial to compare interventions in clinical practice.

Failure to register a clinical trial is a breach of these approval conditions, unless a deferral has been agreed by the HRA (for more information on registration and requesting a deferral see: Research registration and research project identifiers).

If you have not already included registration details in your IRAS application form you should notify the REC of the registration details as soon as possible.

Publication of Your Research Summary

We will publish your research summary for the above study on the research summaries section of our website, together with your contact details, no earlier than three months from the date of this favourable opinion letter.

Should you wish to provide a substitute contact point, make a request to defer, or require further information, please visit: https://www.hra.nhs.uk/planning-and-improving-research/application-summaries/research-summaries/

N.B. If your study is related to COVID-19 we will aim to publish your research summary within 3 days rather than three months.

During this public health emergency, it is vital that everyone can promptly identify all relevant research related to COVID-19 that is taking place globally. If you haven't already done so, please register your study on a public registry as soon as possible and provide the REC with the registration detail, which will be posted alongside other information relating to your project. We are also asking sponsors not to request deferral of publication of research summary for any projects relating to COVID-19. In addition, to facilitate finding and extracting studies related to COVID-19 from public databases, please enter the WHO official acronym for the coronavirus disease (COVID-19) in the full title of your study. Approved COVID-19 studies can be found at: https://www.hra.nhs.uk/covid-19-research/approved-covid-19-research/

It is the responsibility of the sponsor to ensure that all the conditions are complied with before the start of the study or its initiation at a particular site (as applicable).

After ethical review: Reporting requirements

The attached document "After ethical review – guidance for researchers" gives detailed guidance on reporting requirements for studies with a favourable opinion, including:

- Notifying substantial amendments
- Adding new sites and investigators
- Notification of serious breaches of the protocol
- Progress and safety reports
- Notifying the end of the study, including early termination of the study
- Final report
- Reporting results

The latest guidance on these topics can be found at https://www.hra.nhs.uk/approvals-amendments/managing-your-approval/.

Health Research Authority

Ethical review of research sites

The favourable opinion applies to all NHS sites taking part in the study, subject to management permission being obtained from the NHS/HSC R&D office prior to the start of the study (see "Conditions of the favourable opinion").

Approved documents

The documents reviewed and approved were:

Document	*Version*	*Date*	
GP/consultant information sheets or letters [GP Letter]		22 May 2023	
IRAS Application Form [IRAS_Form_26062023]		26 June 2023	
Participant consent form [ICF]		22 May 2023	
Participant information sheet (PIS) [PIS]		22 May 2023	
Research protocol or project proposal [Ultrasonic MCL strain monitoring]	1	22 May 2023	
Summary CV for Chief Investigator (CI) [Gareth Jones CV]		21 February 2023	
Summary CV for student [Student CV]			
Summary CV for supervisor (student research) [Richard Van Arkel Supervisor CV]			
Validated questionnaire [OKS]			

Membership of the Proportionate Review Sub-Committee

The members of the Sub-Committee who took part in the review are listed on the attached sheet.

Statement of compliance

The Committee is constituted in accordance with the Governance Arrangements for Research Ethics Committees and complies fully with the Standard Operating Procedures for Research Ethics Committees in the UK.

User Feedback

The Health Research Authority is continually striving to provide a high quality service to all applicants and sponsors. You are invited to give your view of the service you have received and the application procedure. If you wish to make your views known please use the feedback form

NHS
Health Research Authority

available on the HRA website: http://www.hra.nhs.uk/about-the-hra/governance/quality-assurance/

HRA Learning

We are pleased to welcome researchers and research staff to our HRA Learning Events and online learning opportunities– see details at: https://www.hra.nhs.uk/planning-and-improving-research/learning/

With the Committee's best wishes for the success of this project.

IRAS project ID: 323566	**Please quote this number on all correspondence**

Yours sincerely



On Behalf Of
Dr Clare Eddy
Chair

Email: blackcountry.rec@hra.nhs.uk

Health Research Authority

West Midlands - Black Country Research Ethics Committee

Attendance at PRS Sub-Committee of the REC meeting on 11 July 2023

Committee Members:

Name	*Profession*	*Present*	*Notes*
Dr Clare Eddy	Senior Research Fellow	Yes	Chair
Mrs Lynne Gray	Retired Senior Biomedical Scientist	Yes	
Dr Giridharan Rajaratnam	Deputy Regional Director	Yes	

Also in attendance:

Name	*Position (or reason for attending)*
Mr Taimoor Hassan	Approvals Administrator

Appendix C: HRA letter of approval for the clinical study

Ymchwil Iechyd a Gofal Cymru
Health and Care Research Wales

NHS
Health Research Authority

Mr Gareth G Jones
Department of Surgery and Cancer
2nd Floor, Sir Michael Uren Hub,
Imperial College London
86 Wood Lane, London
W12 0BZ

Email: approvals@hra.nhs.uk

10 August 2023

Dear Mr Jones

HRA and Health and Care Research Wales (HCRW) Approval Letter

Study title:	**In Vivo measurement of MCL strain pre and post knee arthroplasty using ultrasound.**
IRAS project ID:	**323566**
Protocol number:	**23CX8281**
REC reference:	**23/WM/0162**
Sponsor	**Imperial College London**

I am pleased to confirm that **HRA and Health and Care Research Wales (HCRW) Approval** has been given for the above referenced study, on the basis described in the application form, protocol, supporting documentation and any clarifications received. You should not expect to receive anything further relating to this application.

Please now work with participating NHS organisations to confirm capacity and capability, in line with the instructions provided in the "Information to support study set up" section towards the end of this letter.

How should I work with participating NHS/HSC organisations in Northern Ireland and Scotland?
HRA and HCRW Approval does not apply to NHS/HSC organisations within Northern Ireland and Scotland.

If you indicated in your IRAS form that you do have participating organisations in either of these devolved administrations, the final document set and the study wide governance report (including this letter) have been sent to the coordinating centre of each participating nation. The relevant national coordinating function/s will contact you as appropriate.

Please see IRAS Help for information on working with NHS/HSC organisations in Northern Ireland and Scotland.

How should I work with participating non-NHS organisations?
HRA and HCRW Approval does not apply to non-NHS organisations. You should work with your non-NHS organisations to obtain local agreement in accordance with their procedures.

What are my notification responsibilities during the study?

The standard conditions document "*After Ethical Review – guidance for sponsors and investigators*", issued with your REC favourable opinion, gives detailed guidance on reporting expectations for studies, including:

- Registration of research
- Notifying amendments
- Notifying the end of the study

The HRA website also provides guidance on these topics, and is updated in the light of changes in reporting expectations or procedures.

Who should I contact for further information?
Please do not hesitate to contact me for assistance with this application. My contact details are below.

Your IRAS project ID is **323566**. Please quote this on all correspondence.

Yours sincerely,
Helen Penistone
Approvals Manager

Email: approvals@hra.nhs.uk

Copy to: *Ms Becky Ward*

List of Documents

The final document set assessed and approved by HRA and HCRW Approval is listed below.

Document	*Version*	*Date*
Evidence of Sponsor insurance or indemnity (non NHS Sponsors only)		01 August 2023
GP/consultant information sheets or letters [GP Letter]		22 May 2023
IRAS Application Form [IRAS_Form_26062023]		26 June 2023
Organisation Information Document [OID]	1.6	16 June 2023
Other [Protocol Clean]	2	18 July 2023
Other [PIS Clean]	2	18 July 2023
Participant consent form [ICF]		22 May 2023
Summary CV for Chief Investigator (CI) [Gareth Jones CV]		21 February 2023
Summary CV for student [Student CV]		
Summary CV for supervisor (student research) [Richard Van Arkel Supervisor CV]		
Validated questionnaire [OKS]		

IRAS project ID	323566

Information to support study set up

The below provides all parties with information to support the arranging and confirming of capacity and capability with participating NHS organisations in England and Wales. This is intended to be an accurate reflection of the study at the time of issue of this letter.

Types of participating NHS organisation	Expectations related to confirmation of capacity and capability	Agreement to be used	Funding arrangements	Oversight expectations	HR Good Practice Resource Pack expectations
Research activities and procedures as per the protocol and other study documents will take place at participating NHS organisations.	Research activities should not commence at participating NHS organisations in England or Wales prior to their formal confirmation of capacity and capability to deliver the study in accordance with the contracting expectations detailed.	An Organisation Information Document has been submitted and the sponsor is not requesting and does not expect any other agreement to be used with participating NHS organisations of this type.	Study funding arrangements are detailed in the Organisation Information Document.	A Principal Investigator should be appointed at participating NHS organisations.	Where an external individual who does not already hold an NHS employment contract will be conducting any of the research activities that will be undertaken at this site type then they would be expected to hold an Honorary Research Contract. This should be issued be on the basis of a Research Passport (if university employed) or an NHS to NHS confirmation of pre-engagement checks letter (if NHS employed). These should confirm Occupational Health Clearance. These should confirm enhanced DBS checks and appropriate barred list checks. External staff holding pre-existing NHS employment contracts, or staff only

					undertaking questionnaires, should obtain a Letter of Access. This should be issued be on the basis of a Research Passport (if university employed) or an NHS to NHS confirmation of pre-engagement checks letter (if NHS employed). These should confirm Occupational Health Clearance. These should confirm standard DBS checks.

Other information to aid study set-up and delivery

This details any other information that may be helpful to sponsors and participating NHS organisations in England and Wales in study set-up.
The applicant has indicated that they intend to apply for inclusion on the NIHR CRN Portfolio.

Health Research Authority

West Midlands - Black Country Research Ethics Committee
2 Redman Place
Stratford
London
E20 1JQ

Telephone: 0207 104 8388

Please note: This is an acknowledgement letter from the REC only and does not allow you to start your study at NHS sites in England until you receive HRA Approval

10 August 2023

Miss Isabelle Kuder
PhD student
Student at Imperial College London
Department of Mechanical Engineering, City and Guilds Building
Imperial College London, Exhibition Road
South Kensington, London
SW7 2BX

Dear Miss Kuder

Study title:	**In Vivo measurement of MCL strain pre and post knee arthroplasty using ultrasound.**
REC reference:	**23/WM/0162**
Protocol number:	**23CX8281**
IRAS project ID:	**323566**

Thank you for your letter. I can confirm the REC has received the documents listed below and that these comply with the approval conditions detailed in our letter dated 13 July 2023.

Health Research Authority

Documents received

The documents received were as follows:

Document	*Version*	*Date*
Other [Protocol Tracked]	2	18 July 2023
Other [Protocol Clean]	2	18 July 2023
Other [PIS Tracked]	2	18 July 2023
Other [PIS Clean]	2	18 July 2023

Approved documents

The final list of approved documentation for the study is therefore as follows:

Document	*Version*	*Date*
GP/consultant information sheets or letters [GP Letter]	1	22 May 2023
IRAS Application Form [IRAS_Form_26062023]		26 June 2023
Other [Protocol Tracked]	2	18 July 2023
Other [Protocol Clean]	2	18 July 2023
Other [PIS Tracked]	2	18 July 2023
Other [PIS Clean]	2	18 July 2023
Participant consent form [ICF]	1	22 May 2023
Summary CV for Chief Investigator (CI) [Gareth Jones CV]		21 February 2023
Summary CV for student [Student CV]		
Summary CV for supervisor (student research) [Richard Van Arkel Supervisor CV]		
Validated questionnaire [OKS]	1	17 April 2023

You should ensure that the sponsor has a copy of the final documentation for the study. It is the sponsor's responsibility to ensure that the documentation is made available to R&D offices at all participating sites.

IRAS Project ID: 323566 **Please quote this number on all correspondence**

Yours sincerely



Taimoor Hassan
Approvals Administrator

E-mail: blackcountry.rec@hra.nhs.uk